



universität
wien

DISSERTATION

Titel der Dissertation

Petrological, geochemical and Os-Hf-Nd-Sr isotopic
characterization of the Subcontinental Lithospheric
Earth Mantle beneath Patagonia

Verfasserin

Mag.rer.nat. Andrea Mundl Bakk.rer.nat.

angestrebter akademischer Grad

Doktorin der Naturwissenschaften (Dr.rer.nat.)

Wien, 2015

Studienkennzahl lt. Studienblatt: A 796 605 426

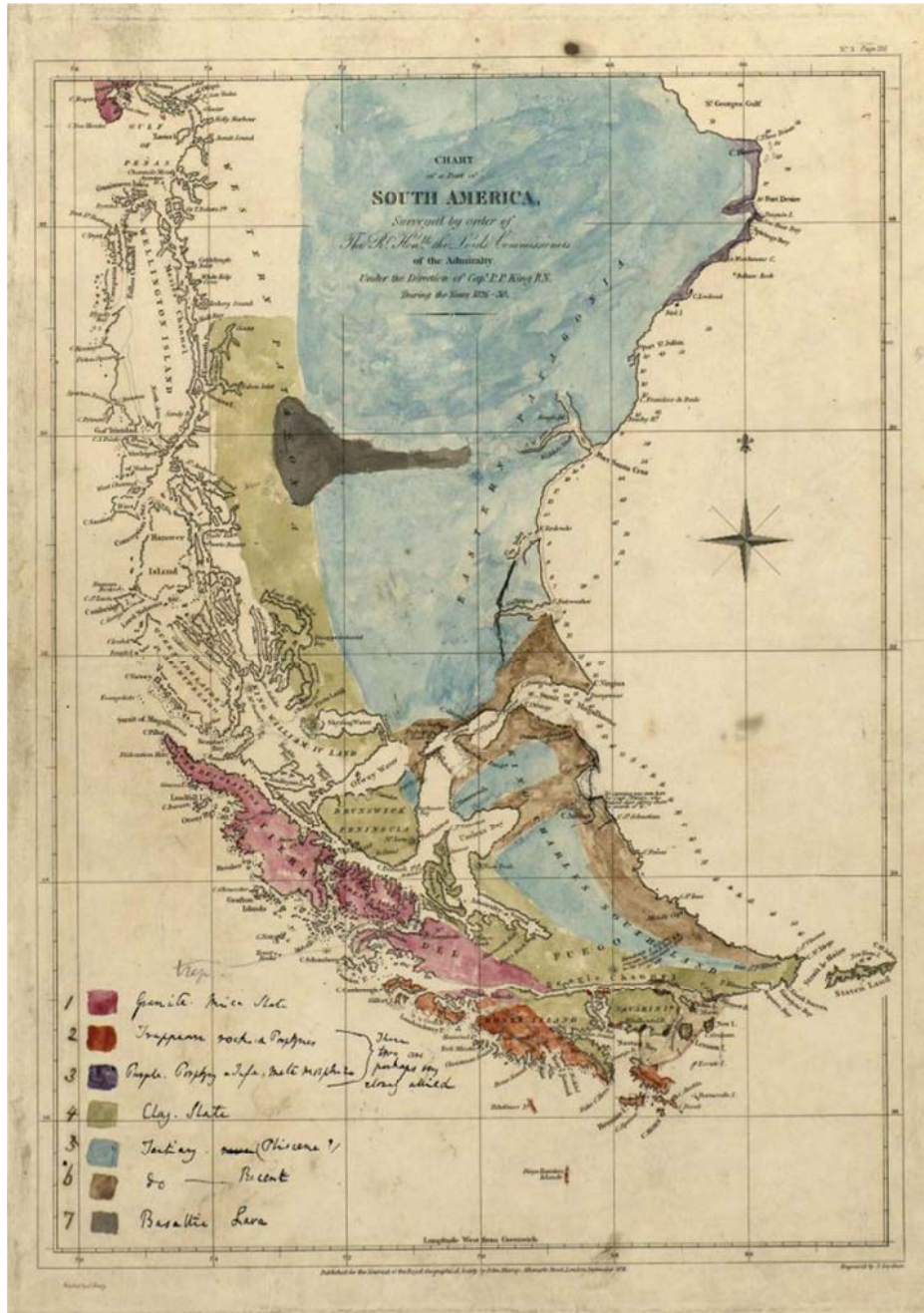
Dissertationsgebiet lt. Studienblatt: Erdwissenschaften

Betreuer: Ao. Univ. Prof. Dr. Theodoros Ntaflos

To Leo,

“Nothing can be more improving to a young naturalist,
than a journey in a distant country.”

- Charles Darwin



Geological map of southern Patagonia by Charles Darwin (ca. 1840)

TABLE OF CONTENTS

Acknowledgements	I
Abstract	III
Zusammenfassung	V
Introduction	
I. Project aims	1
II. Methods	3
III. Isotope systems	4
IV. Geological setting	8
Synthesis	
I. Bulk rock major and trace element compositions	13
II. Clinopyroxene major and trace element compositions	14
III. Highly siderophile element concentrations	16
IV. Isotopic compositions	17
V. Patagonian SCLM formation ages	19
Conclusions	21
References	23
Chapter I — South Patagonia	27
Mundl, A., Ntaflos, T., Ackerman, L., Bizimis, M., Bjerg, E.A. & Hauzenberger, C.A. (2015). Mesoproterozoic and Paleoproterozoic subcontinental lithospheric mantle domains beneath southern Patagonia: Isotopic evidence for its connection to Africa and Antarctica: <i>Geology</i> , v. 49, p. 39-42.	29
Data Repository	33
Additional Data	55

Chapter II — North Patagonia	73
Mundl, A., Ntaflos, T., Ackerman, L., Bizimis, M., Bjerg, E.A., Wegner, W. & Hauzenberger, C.A. (accepted). Geochemical and Os-Hf-Nd-Sr isotopic characterization of north Patagonian mantle xenoliths: Implications for extensive melt extraction and percolation processes: <i>Journal of Petrology — 6th Orogenic Lherzolite Conference Thematic Issue</i> .	75
Curriculum Vitae	123

ACKNOWLEDGEMENTS

The project was funded by the Austrian Science Fund (FWF grant P 23557). I am grateful for their financial support.

First and foremost, I would like to thank my supervisor, Prof. Theo Ntaflos for giving me the opportunity to become a part of this project. I am very thankful for the confidence in my abilities and the trust in me to work independently. The numerous (sometimes endless) discussions incredibly helped to improve my knowledge in a lot of ways. Thank you for all your support!

Big thanks go to Ernesto Bjerg from Universidad Nacional del Sur, for making the sample collection in Patagonia possible and such a fun time. I want to thank Lukas Ackerman of the Academy of Sciences of the Czech Republic for the time and patience for passing on his knowledge on the geochemistry of the Re-Os isotopic and PGE systems. I am grateful to Michael Bizimis, University of South Carolina, for teaching me the Hafnium isotope geochemistry. Thank you to Christoph Hauzenberger for numerous (LA-) ICP-MS analyses. Last but not least, to Wencke Wegner, for putting so much time and effort into analyzing samples for Sr and Nd isotopic composition. Thank you to all my co-authors, Theo, Ernesto, Lukas, Michael, Christoph and Wencke for the very helpful reviews and constructive discussions.

I am very grateful to Franz Kiraly (microprobe), Sigrid Hrabe (thin sections), Peter Nagl (XRF), Marianne Schwarzingger (sample preparation) and Monika Horschinegg (clean lab) for their assistance and help.

I'd like to thank my friends and colleagues for supporting me and making this journey such a positive and – most of the time – fun experience.

My biggest thanks go out to my family for their unconditional love and encouragement throughout the years! I am very grateful for all your support!

ABSTRACT

Mantle xenoliths – fragments of the subcontinental lithospheric mantle (SCLM) – from beneath Patagonia were petrographically and geochemically characterized and analyzed for their Os-Hf-Nd-Sr isotopic composition. Ten different mantle xenolith outcrops, spread all across Patagonia, were chosen and samples were carefully selected to obtain new insights into the origin and evolution of the lithospheric mantle underneath the southern part of Argentina. These SCLM fragments provide the opportunity to determine estimates on the formation age of continental terranes. An evolutionary link of crust and its underlying mantle makes dating continental fragments possible, even in areas where crustal basement rocks are scarce or completely inaccessible, as is the case for the southern part of Patagonia. The Re-Os isotopic system represents a useful and reliable tool to determine lithospheric mantle stabilization ages and subsequently provides information on the timing of formation of continental terranes.

Our study shows that Patagonia is made up of multiple continental fragments with Neo- to early Paleoproterozoic formation ages. The southernmost part, known as the Pali Aike area, represents the oldest part of southern Argentina and its early Paleoproterozoic (2.5 Ga) formation age indicates an evolutionary connection to parts of western Antarctica. The Deseado Massif area yields distinctly younger lithospheric mantle stabilization ages (1.3 Ga) and suggests a common origin with parts of South Africa. These new age determinations clearly show that the southern part of Patagonia (the Santa Cruz Province) is made up of at least two lithospheric fragments. A third fragment could be represented by the region of Tres Lagos, located southwest of the Deseado Massif. Re-Os SCLM formation ages indicate a mid Paleoproterozoic (1.9 Ga) origin. Age determinations from northern Patagonia, an area known as the North Patagonian Massif (NPM), are more difficult to interpret as the SCLM in this region has undergone extensive metasomatic overprinting. Minimum mantle stabilization ages suggest a Mesoproterozoic (1.0 to 1.3 Ga) evolution of the SCLM beneath the western part of the NPM. The lithospheric mantle

underneath Prahuaníyeyu, located roughly in the center of the NPM yields older, late Paleoproterozoic (1.7 Ga) formation ages. This suggests at least two variably old continental fragments beneath the northern part of Patagonia.

Petrographic and geochemical studies revealed distinct differences between mantle xenoliths from the South and the North of Patagonia. While the SCLM beneath the southern areas of Patagonia exhibits a wide range of fertility represented by abundant lherzolites and harzburgites, the northern part of Patagonia yields exclusively highly depleted mantle xenoliths. Clinopyroxene trace element and isotopic studies indicate that the lithospheric Earth mantle beneath the NPM has experienced reactions with a chromatographically fractionated melt after the initial melt depletion event. These melt-rock reactions lead to a compositionally evolving melt and variably altered mantle sections, which is strongly reflected in primitive mantle normalized clinopyroxene trace element patterns. Bulk rock and mineral compositions, on the contrary, suggest that this melt percolation event has not significantly affected major element systematics. Isotope and highly siderophile element (HSE) compositions, on the other hand, also suggest melt-rock reactions. Platinum group element systematics of samples from southern Patagonia suggest that metasomatic processes have not had impact on the iridium-group PGEs (Os, Ir and Ru). In contrast, bulk rock analyses of north Patagonian mantle xenoliths reveal a fractionation of IPGEs, also a strong sign for percolating melt-rock reactions in the SCLM beneath the NPM.

ZUSAMMENFASSUNG

Mantelxenolithe – Fragmente des subkontinentalen lithosphärischen Erdmantels (SCLM) – aus Patagonien wurden petrografisch und geochemisch beschrieben und deren Os-Hf-Nd-Sr Isotopenzusammensetzung bestimmt. Proben von zehn Aufschlüssen, verteilt in ganz Patagonien, wurden gesammelt und Mantelxenolithe wurden sorgfältig ausgewählt um neue Erkenntnisse über die Herkunft und Evolution des lithosphärischen Erdmantels unterhalb des südlichen Teils Argentiniens zu gewinnen. Diese Fragmente des SCLM ermöglichen es uns, Auskunft über den Stabilisierungszeitpunkt des lithosphärischen Erdmantels und folglich Informationen über den Entstehungszeitpunkt der darüber liegenden kontinentalen Kruste zu erhalten. Ein Zusammenhang der Bildung von Kruste und der Stabilisierung des darunter liegenden Erdmantels ermöglicht die Datierung der kontinentalen Lithosphäre, auch in Regionen, wo krustale Basements nicht zugänglich oder wie im Fall von Süd-Patagonien, mit Sedimenten und jungen Vulkangesteinen überlagert sind. Das Re-Os Isotopensystem ist ein wichtiges und verlässliches Werkzeug für die Datierung von SCLM-Bereichen und gibt in Folge Aufschluss über die Entstehung von kontinentalen Krustenbereichen.

Unsere Untersuchungen zeigen, dass Patagonien aus mehreren neo- bis paläoproterozoischen kontinentalen Fragmenten zusammengesetzt ist. Der südlichste Teil, das sogenannte Pali Aike, repräsentiert den ältesten Teil von Südargentinien. Das früh paläoproterozoische Alter (2,5 Ga) deutet auf eine gemeinsame Entstehung mit Bereichen der westlichen Antarktis hin. Der Erdmantel unterhalb des Deseado Massivs hingegen zeigt ein deutlich jüngeres Stabilisierungsalter von 1,3 Ga und lässt auf eine gemeinsame Entstehung mit Bereichen des südlichen Afrikas schließen. Diese neuen Erkenntnisse deuten darauf hin, dass der südliche Teil von Patagonien, die Provinz von Santa Cruz, aus mindestens zwei Teilen aufgebaut ist. Die Region von Tres Lagos im Südwesten des Deseado Massivs zeigt mit 1,9 Ga ein paläoproterozoisches Entstehungsalter und könnte somit ein drittes Fragment darstellen. Die Re-Os Isotopenergebnisse von Proben aus dem nördlichen Patagonien,

dem sogenannten Nord Patagonischen Massiv (NPM), sind schwieriger zu interpretieren, da der SCLM unterhalb dieses Bereichs stark von Metasomatose überprägt wurde. Mindestalter der Stabilisierung des lithosphärischen Erdmantels deuten auf eine mesoproterozoische Entstehung (1,0 bis 1,3 Ga) des westlichen Teils des NPM hin. Das Gebiet um Prahuaniyeu, im Zentrum des NPM gelegen, zeigt ein deutlich älteres, paläoproterozoisches (1,7 Ga) Entstehungsalter und lässt darauf schließen, dass der Norden von Patagonien aus mindestens zwei kontinentalen Fragmenten aufgebaut ist.

Petrographische und geochemische Untersuchungen an Mantelxenolithen zeigten deutliche Unterschiede zwischen dem Norden und dem Süden von Patagonien. Während der SCLM im südlichen Bereich unterschiedlich verarmte Proben von Lherzoliten bis Harzburgiten aufweist, findet man im Norden ausschließlich stark verarmte Harzburgite. Klinopyroxen-Spurenelementanalysen und Isotopenuntersuchungen zeigen, dass der Erdmantel unterhalb des NPM nach dem initialen Aufschmelzprozess eine Reaktion mit einer chromatografisch fraktionierten Schmelze erfahren hat. Diese Reaktion einer perkolierenden Schmelze mit Teilen des Erdmantels führt zu einer kompositionellen Veränderung der Schmelze und in Folge dessen zu unterschiedlich überprägten Erdmantelbereichen, was sich vor allem in der Spurenelementzusammensetzung widerspiegelt. Gesamtgesteins- und Mineralzusammensetzungen zeigen jedoch, dass diese Reaktion des Erdmantels mit einer darin perkolierenden Schmelze keine Auswirkung auf die Hauptelementsystematik hatte. Isotopen- und HSE-Zusammensetzungen weisen ebenfalls darauf hin, dass der Erdmantel mit einer Schmelze reagiert hat. Während Platinum Group Element Untersuchungen zeigen, dass metasomatische Prozesse, wenn vorhanden, im SCLM des südlichen Patagoniens keine Auswirkungen auf die Iridium-Gruppe der Platinum Group Elements (IPGE) hatten, zeigen manche Proben aus dem Norden von Patagonien eine Fraktionierung der IPGEs und somit eine deutliche Überprägung des SCLM unterhalb des NPM.

INTRODUCTION

I. Project aims

The aim of this project was to understand geochemical processes taking place in the subcontinental lithospheric mantle (SCLM) underneath Patagonia. The geodynamic situation of Patagonia has been the topic of discussions for decades. Whether Patagonia is composed of multiple lithospheric fragments with different origins and stabilization ages or whether all of Patagonia was formed simultaneously and hence, is comprised of one single tectonic plate has been a fundamental question for the past few decades (e.g. Stern et al., 1999; Pankhurst et al., 2006; Ramos, 2008; Schilling et al., 2008; Wang et al., 2008). In order to shed light into this ongoing debate, we have undertaken extensive geochemical and isotopic investigations of mantle rock samples from various areas throughout Patagonia.

Commonly, age determination of lithospheric fragments is carried out on crustal rock samples. Generally, isotopic dating of crustal basements can provide a good estimation on the timing of formation of continental terranes. It is however difficult to date crustal sections in Patagonia, especially in the southern part. Basement rock outcrops are scarce and large areas are covered with thick sedimentary sequences. Hence, direct access to the oldest basement rocks in those regions is impossible. Our approach to nonetheless get a good idea and a close approximation on the timing of the formation of the Patagonian continental terrane, was to look more closely at the lithospheric mantle beneath. The stabilization of this underlying subcontinental lithospheric mantle is, in principle, directly linked to the formation of its overlying crust. This link has been described by many authors (e.g. Griffin et al., 1999a, and references therein; Pearson, 1999) in other parts of the world, where isotopic dating of lithospheric mantle sections as well as their overlying crustal basement rocks reveal similar formation ages. This coupled origin of crust and underlying lithospheric mantle provides us a good opportunity to detect

a close approximation on the formation of continental terranes by studying mantle xenoliths, even without access to crustal basement outcrops.

In addition to the determination of the timing of SCLM stabilization, a further aim of this study was to detect and characterize metasomatic processes taking place in the mantle. It is a known fact, that various lithospheric mantle sections beneath Patagonia have been strongly affected by metasomatism (e.g. Stern et al., 1999; Gorring & Kay, 2000; Laurora et al., 2001; Rivalenti et al., 2004; Bjerg et al., 2005, 2009; Ntaflos et al., 2006; Wang et al., 2008; Alani et al., 2009; Dantas et al., 2009; Faccini et al., 2013) This is especially relevant in areas located close to the Andes cordillera in the western part of Patagonia. Modally metasomatized mantle xenoliths containing fluid derived phases such as amphibole or phlogopite in mantle peridotites are a known phenomenon from subcontinental lithospheric mantle sections located close to subduction zones. We have focused our study mainly on samples that have experienced cryptic metasomatism, hence samples that show no obvious signs of secondarily added mineral phases, such as the above mentioned H₂O-carrying minerals amphibole and/or phlogopite.

The main task of this dissertation was to petrographically and geochemically characterize the subcontinental lithospheric mantle beneath Patagonia. Based on these results, various mantle xenolith samples were further chosen for isotopic analyses in order to potentially determine the origin and timing of the formation of the Patagonian terrane and/or to provide isotopic evidence for metasomatic processes taking place within the mantle.

Chapter I focuses on mantle xenolith samples from Santa Cruz Province, the southern part of Patagonia. New insights into the origin of the south Patagonian continental region are presented and conclusions of evolutionary connections to continental terranes in other places of the world are drawn.

Chapter II deals with SCLM samples from beneath the North Patagonian Massif collected in the Rio Negro Province. In addition to the attempt to determine the stabilization age of the SCLM in north Patagonia, this chapter primarily describes the

cryptic metasomatic processes taking place within the lithospheric mantle in this area.

II. Methods

The selected analytical methods to advance in solving the above described problems were as follows:

Microscope - Leica

An optical microscope was used to get an overview of mineral phases and to determine textures of the mantle xenoliths. After preliminary studies of thin sections, the samples were further investigated by electron microprobe.

Electron

Microprobe - Cameca SX 100 (University of Vienna)

Polished carbon coated thin sections were investigated by microprobe to determine mineral major element compositions and detect potential micro-scale mineral occurrences.

XRF - Phillips PW 2400 (University of Vienna)

Fused disks (major elements) and pressed disks (trace elements) were prepared and analyzed for bulk rock compositions.

ICP-MS - Agilent 7500 (University of Graz); Element 2 (Thermo) with

Aridus IITM (CETAC) (Academy of Science, Prague)

Bulk rock powders were analyzed for trace element composition (Graz).

Bulk rock platinum group element and rhenium concentrations were determined (Prague).

- LA-ICP-MS - ESI NWR193 (Laser), Agilent 7500 (ICP-MS) (University of Graz)
Separated, embedded clinopyroxenes and thin sections were analyzed to determine mineral trace element compositions.
- MC-ICP-MS - Neptune + APEX (ESI,USA)
Hafnium isotopic ratios were determined on digested clinopyroxene separates.
- TIMS - Finnigan MAT 262 (Academy of Science, Prague);
Thermo Finnigan Triton (University of Vienna)
Osmium isotopic compositions of bulk rock sample powders were analyzed (Prague).
Strontium and neodymium isotopic ratios were determined on clinopyroxene separates (Vienna).

III. Isotope systems

Below is a brief description of the isotopic systems used in this dissertation to help answering the project's main questions. These isotopic systems are excellent tools to get a better idea on the timing of the SCLM stabilization and on potential metasomatic processes taking place in the lithospheric mantle beneath Patagonia.

The following isotopic systems used in mantle rock geochemistry are based on the different behavior of their parent and daughter isotopes during partial melting or metasomatic processes. I.e., in the event of partial melting of a mantle rock, one isotope acts more incompatible, hence prefers to go into the melt, while the other isotope remains in the residue. This fractionation of parent and daughter isotopes leads to a specific signature in mantle samples and enables us to reveal certain petrological and geochemical processes and/or to determine the timing of partial melting events leading to lithospheric mantle stabilization age estimates.

The Sm-Nd isotopic system

^{147}Sm decays to ^{143}Nd by α -decay with a half-life of 106 Ga., resulting in a decay constant of $\lambda = 6.54 \times 10^{-12} \text{yr}^{-1}$ (Lugmair and Marti, 1978). Sm and Nd, both rare earth elements (REE), fractionate during partial melting processes. Sm behaves more compatibly during melting of a mantle rock and hence, largely remains in the residue, while Nd prefers to go into the melt. With time, as a result of the decay of ^{147}Sm to ^{143}Nd , the depleted mantle's $\frac{^{143}\text{Nd}}{^{144}\text{Nd}}$ ratio increases continuously [1]. The stable ^{144}Nd isotope is used as a reference isotope.

$$[1] \quad \left(\frac{^{143}\text{Nd}}{^{144}\text{Nd}}\right)_{\text{sample}} = \left(\frac{^{143}\text{Nd}}{^{144}\text{Nd}}\right)_{\text{initial}} + \frac{^{147}\text{Sm}}{^{144}\text{Nd}} (e^{\lambda t} - 1)$$

The deviation of a sample's analyzed $\frac{^{143}\text{Nd}}{^{144}\text{Nd}}$ from the present day bulk earth ratio, $\left(\frac{^{143}\text{Nd}}{^{144}\text{Nd}}\right)_{\text{chon}} = 0.512638$ (Bouvier et al., 2008) is defined as the ϵ_{Nd} -notation [2].

$$[2] \quad \epsilon_{\text{Nd}} = \left[\frac{\left(\frac{^{143}\text{Nd}}{^{144}\text{Nd}}\right)_{\text{sample}}}{\left(\frac{^{143}\text{Nd}}{^{144}\text{Nd}}\right)_{\text{chon}}} - 1 \right] \times 10^4$$

The Rb-Sr isotopic system

The generally accepted constant for the β^- -decay of ^{87}Rb to ^{86}Sr is $\lambda = 1.42 \times 10^{-11} \text{yr}^{-1}$ (Steiger and Jäger, 1977) [3].

$$[3] \quad \left(\frac{^{87}\text{Sr}}{^{86}\text{Sr}}\right)_{\text{sample}} = \left(\frac{^{87}\text{Sr}}{^{86}\text{Sr}}\right)_{\text{initial}} + \frac{^{87}\text{Rb}}{^{86}\text{Sr}} (e^{\lambda t} - 1)$$

Rubidium and strontium both belong to the group of LILE (large ion lithophile elements) and are in geochemistry considered as mobile. However, their behavior during partial melting processes is somewhat contrary. Rb acts highly incompatibly during mantle melting, while Sr is in comparison more compatible and largely remains in the residual mantle. Hence, this fractionation leads to a very small Rb/Sr ratio in the residue. As a consequence, the radiogenic Sr production from the decay of ^{87}Rb is roughly terminated in the residue. Due to the mobile nature of these two elements, the Rb-Sr isotopic system is susceptible to disturbance during

metasomatism in the mantle. Hence, determined formation ages using the Rb-Sr system are often precarious. However, this system is an important tool when used as tracer for metasomatic processes in the mantle.

The Lu-Hf isotopic system

The Lu-Hf isotopic system is based on the β^- -decay of ^{176}Lu to ^{176}Hf . The system's decay constant is specified as $\lambda = 1.87 \times 10^{-11} \text{yr}^{-1}$ (Scherer et al., 2001). ^{177}Hf , a stable Hf isotope, is used as reference isotope. Present day chondrite values used for calculations are $\left(\frac{^{176}\text{Hf}}{^{177}\text{Hf}}\right)_{\text{chon}} = 0.282785$ and $\left(\frac{^{176}\text{Lu}}{^{177}\text{Hf}}\right)_{\text{chon}} = 0.0334$ (Bouvier et al., 2008). The Lu-Hf system applied to mantle xenolith samples can be considered reliable as both elements are rather immobile and fractionate during partial melting events. This fractionation of Lu, which remains in the mantle, and Hf, which prefers to go into the melt, leads to a high Lu/Hf ratio in the residue. Due to the rather short half-life of Lu (37 Ga), this in turn results in a continuously and fast growing $\frac{^{176}\text{Hf}}{^{177}\text{Hf}}$ ratio with time [4].

$$[4] \quad \left(\frac{^{176}\text{Hf}}{^{177}\text{Hf}}\right)_{\text{sample}} = \left(\frac{^{176}\text{Hf}}{^{177}\text{Hf}}\right)_{\text{initial}} + \frac{^{176}\text{Lu}}{^{177}\text{Hf}} (e^{\lambda t} - 1)$$

Comparing $\left(\frac{^{176}\text{Hf}}{^{177}\text{Hf}}\right)_{\text{sample}}$ with $\left(\frac{^{176}\text{Hf}}{^{177}\text{Hf}}\right)_{\text{chon}}$ enables us to determine the deviation of the analyzed ratios with present day bulk earth values. This can be expressed, analogous to the Sm-Nd system, as the ϵ_{Hf} - notation [5].

$$[5] \quad \epsilon_{\text{Hf}} = \left[\frac{\left(\frac{^{176}\text{Hf}}{^{177}\text{Hf}}\right)_{\text{sample}}}{\left(\frac{^{176}\text{Hf}}{^{177}\text{Hf}}\right)_{\text{chon}}} - 1 \right] \times 10^4$$

The Re-Os isotopic system

Contrary to the elements of the previously described isotopic systems, Re and Os are siderophile elements and belong to the group of HSE (highly siderophile elements). In the Earth's mantle, they preferentially reside in sulfides rather than in silicates. ^{187}Re decays to ^{187}Os by β^- -decay with a half-life of 41.6 Ga and a decay constant of $\lambda = 1.66 \times 10^{-11} \text{yr}^{-1}$ (Smoliar et al., 1996). The stable ^{188}Os is generally

used as reference isotope. The Re-Os isotopic system has become an important tool to determine the stabilization age of subcontinental lithospheric mantle sections as it remains relatively stable during metasomatism. The system is based on the very compatible behavior of Os and the moderately incompatible nature of Re during mantle melting. Ideally, partial melting of a mantle sample results in the complete removal of Re from the residual mantle and the subsequent retardation of the radiogenic Os production. Based on the assumption that all Re analyzed in the mantle samples is primary, a model age for the initial partial melting event, and hence the timing of SCLM stabilization, can be calculated [6].

$$[6] \quad T_{MA} = \frac{1}{\lambda} \times \ln \left\{ \left[\frac{\left(\frac{^{187}\text{Os}}{^{188}\text{Os}} \right)_{PM} - \left(\frac{^{187}\text{Os}}{^{188}\text{Os}} \right)_{sample}}{\left(\frac{^{187}\text{Re}}{^{188}\text{Os}} \right)_{PM} - \left(\frac{^{187}\text{Re}}{^{188}\text{Os}} \right)_{sample}} \right] + 1 \right\}$$

A more significant model age for mantle xenolith samples is the ‘Rhenium depletion age’ (T_{RD} ; Shirey and Walker, 1998). This model age is based on the assumption that during mantle melting, all Re is removed from the residual mantle. Hence, the radiogenic Os production is fully terminated. All Re analyzed in the sample is assumed to have been brought in by the host basalt, that carried the mantle xenoliths to the surface. Consequently, the $\frac{^{187}\text{Os}}{^{188}\text{Os}}$ ratio is calculated back to the eruption age (EA) of the mantle sample [7]. All determined T_{RDs} must be considered minimum.

$$[7] \quad T_{RD} = \frac{1}{\lambda} \times \ln \left\{ \left[\frac{\left(\frac{^{187}\text{Os}}{^{188}\text{Os}} \right)_{PM} - \left(\frac{^{187}\text{Os}}{^{188}\text{Os}} \right)_{sample(EA)}}{\left(\frac{^{187}\text{Re}}{^{188}\text{Os}} \right)_{PM}} \right] + 1 \right\}$$

An average primitive mantle (PM) value of $\frac{^{187}\text{Re}}{^{188}\text{Os}} = 0.4353$ and $\frac{^{187}\text{Os}}{^{188}\text{Os}} = 0.1296$ (Meisel et al., 2001) are used for calculation of Re-Os model ages. The λ_{Os} notation [8] is defined as the percentage difference between the analyzed $\frac{^{187}\text{Os}}{^{188}\text{Os}}$ ratio and the average defined primitive mantle $\frac{^{187}\text{Os}}{^{188}\text{Os}}$ ratio.

$$[8] \quad \lambda_{Os} = \left[\frac{\left(\frac{^{187}\text{Os}}{^{188}\text{Os}} \right)_{sample}}{\left(\frac{^{187}\text{Os}}{^{188}\text{Os}} \right)_{PM}} - 1 \right] \times 100$$

IV. Geological setting

As previously mentioned, the evolution and origin of Patagonia has been the focus of numerous debates for decades. Its geology on the other hand, is well known and numerous studies on crustal rocks provide extensive information on more recent (post-Gondwana) geological processes. The following is a brief overview on the existing data of Patagonia's geology.

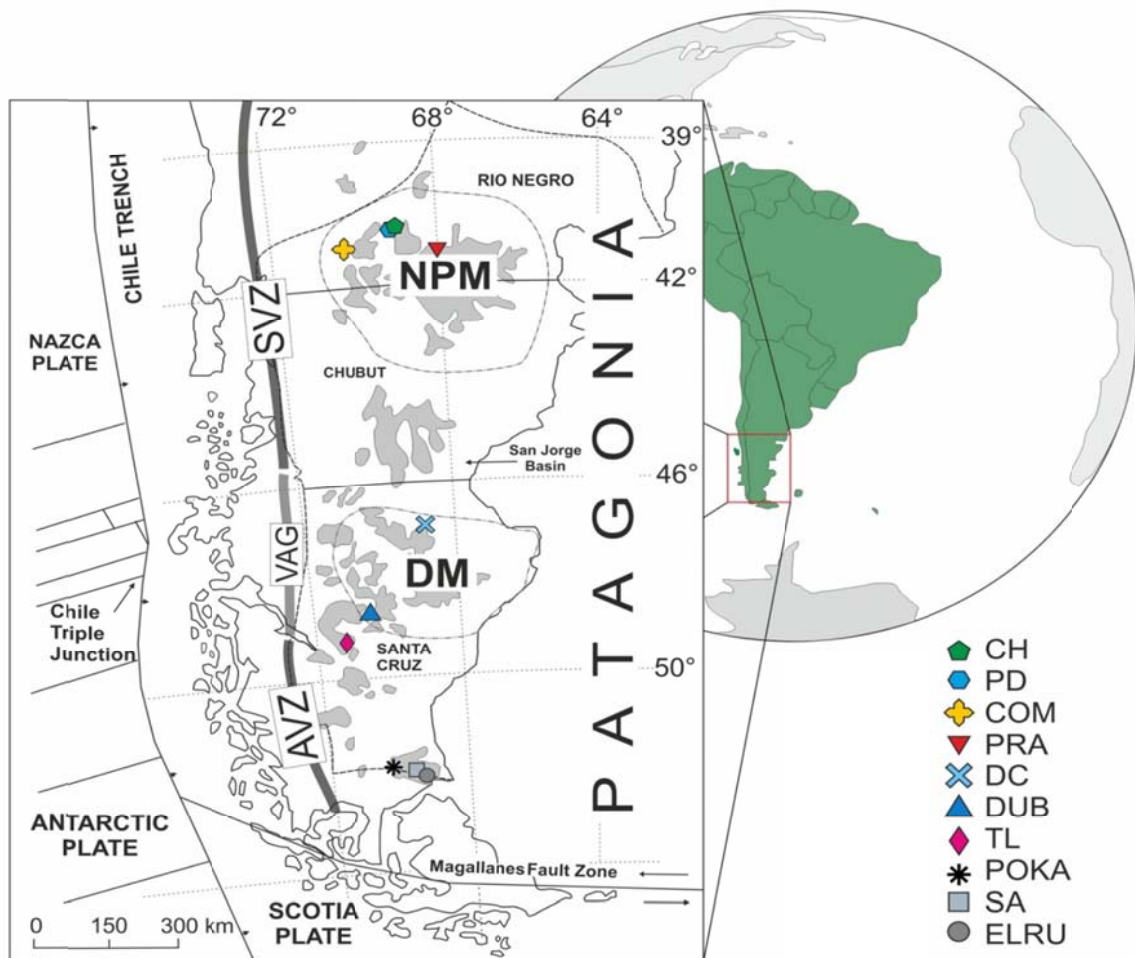


Fig. 1. Map of Patagonia, modified after Bjerg et al., 2009. Mantle sample outcrops of this study: CH – Cerro Chenque; PD – Puesto Diaz; COM – Comallo; PRA – Prahuanieyu; DC – Don Camilo; DUB – Gobernador Gregores; TL – Tres Lagos; POKA – Potrok Aike; SA – Salsa; ELRU – El Ruido.

Patagonia in southernmost Argentina stretches from $\sim 39^\circ$ S to $\sim 52^\circ$ S (Fig. 1) and is considered as the continental region south of Río Colorado. Geologically, Patagonia is referred to as the back-arc region east of the Andes Cordillera. The Andean cordillera can be divided in two major regions: The southern volcanic zone

(SVZ) extends to 46° S and is followed by a gap in volcanic activity (VAG). This volcanic gap separates the SVZ from the Austral volcanic zone (AVZ) which extends from 49° to 53° S. The subduction of the Antarctic plate in the south and the Nazca plate in the north underneath the South American plate results in the active volcanism of the Andes mountain chain. The gap in volcanic activity (VAG) is a consequence of the subduction of the Chile Triple Junction which according to Ramos and Kay (1992) and Gorring et al. (1997) induced a slab window in the subducted plate. Different motion speeds of the two subducting plates results in a northward migration of the VAG (e.g. Ramos and Kay, 1992; Stern and Kilian, 1996).

Patagonia consists of 3 provinces: Rio Negro in the North, Chubut and Santa Cruz in the South. The North Patagonian Massif (NPM), also known as the Somuncura Massif, located in the Rio Negro and Chubut Provinces, extends from 40° S to 44° S (Fig. 1). It is separated from the Deseado Massif (DM), in the Santa Cruz Province, by the San Jorge basin, which is filled with Meso-Cenozoic sedimentary rocks.

The North Patagonian Massif

Ramos (2008) divided the NPM into two Phanerozoic magmatic belts, a Northern and a Western Belt. Based on geochronological data, Pankhurst et al. (2006) suggested 4 distinct crustal formation stages for the Northern magmatic Belt at 530-500 Ma, 485-470 Ma, ~300 Ma and 290-250 Ma. Similar crust formation stages were described for the Western magmatic Belt at ~400 Ma, 320-310 Ma, 290-270 Ma and 270-250 Ma. Martínez Dopico et al. (2011) introduced Paleoproterozoic (up to 1.7 Ga) Sm-Nd model ages for low-grade metasedimentary rocks in the Northern magmatic Belt. These T_{DM} (Nd) model ages imply that those sediments had a Paleoproterozoic crustal source. Model ages from i.a. the Yaminué Complex and the Permian La Esperanza granites in the Northern Belt of the NPM indicate a Mesoproterozoic (1.3-1.6 Ga) crustal source and suggest an additional Proterozoic magmatic period. Neodymium model ages for metamorphic rocks from the Colohuincul Complex, located in the Western Belt range from 1.4 to 2.1 Ga. In

the southern part of the Western Belt, Martínez Dopico et al. (2011) introduce T_{DM} around 1.6 Ga. These authors also suggest at least three metamorphic episodes of Paleozoic rocks from the NPM.

The basement of the NPM consists of the above mentioned pre-Permian metamorphic rocks, late Permian to Early Triassic granites, granodiorites, ignimbrites, Triassic sedimentary and pyroclastic rocks, Late Triassic to Early Jurassic rhyolites, Late Jurassic andesites and Pliocene sediments.

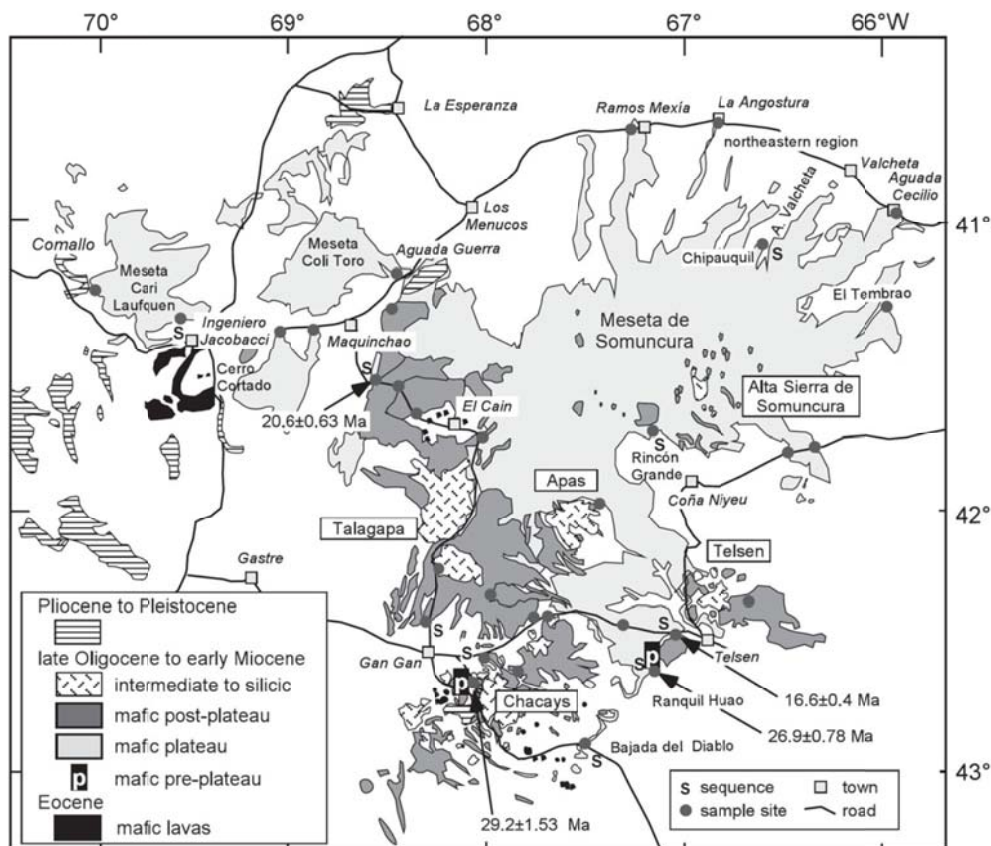


Fig. 2. Map of the Somuncura volcanic province from Kay et al. (2007)

The late Oligocene to early Miocene Somuncura Massif comprises basaltic, trachybasaltic, basaltic andesitic and trachyandesitic plateau basalts and continental sediments and covers an area of ca. 120,000 km² (Fig. 2). The alkali basalts that host the mantle xenoliths investigated in this study erupted in the Pleistocene and in recent times (Bjerg et al., 2009 and references therein).

The Deseado Massif

The Deseado Massif (DM), stretching from 47° S to 49° S, east of the VAG, located between the Deseado and the Chico River in the Santa Cruz Province, comprises an area of ~60.000 km² (Fig. 3). It is bounded in the north by the San Jorge Basin and in the south by the Magallane Basin.

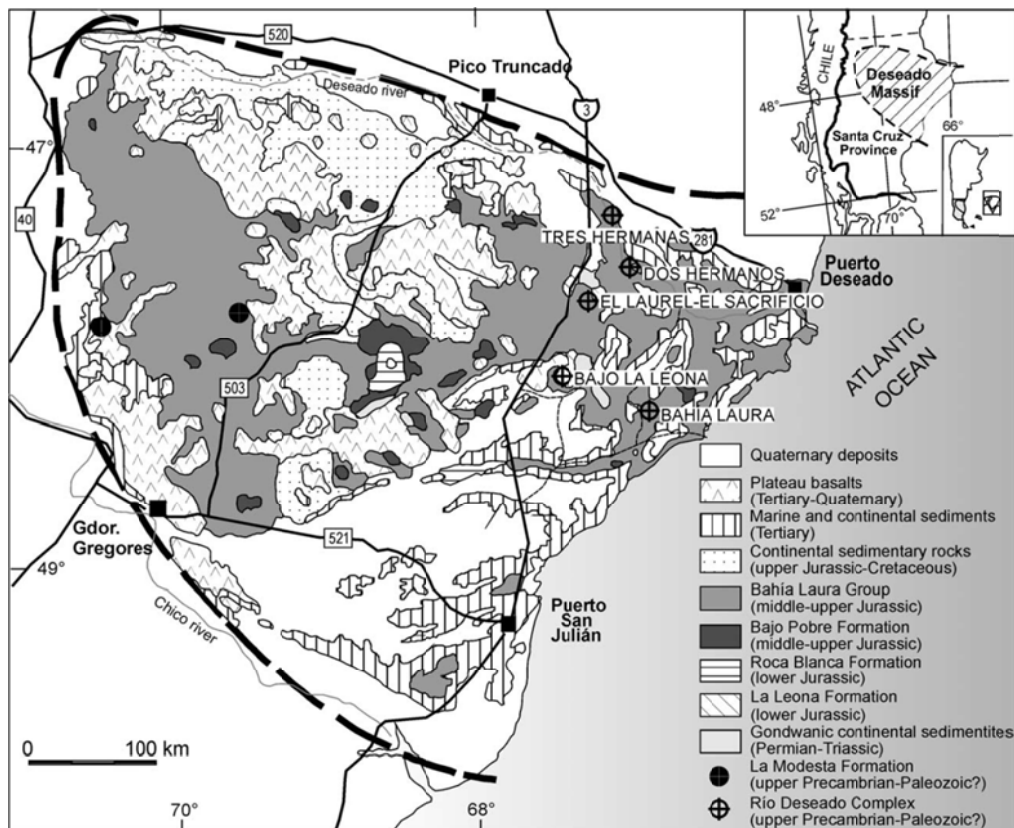


Fig. 3. Geological map of the Deseado Massif from Guido et al. (2004)

The oldest dated rocks in the DM are the Mesoproterozoic basement rocks of Dos Hermanos (Pankhurst et al., 2003). This basement consist of low-grade metamorphic rocks (Giacosa et al., 2002) and is covered by a Permian-Triassic Gondwanine sedimentary sequence, lower plutonic rocks and middle-upper Jurassic volcanic and volcano-sedimentary rocks (Guido et al., 2004; Fig. 3). According to T_{RDs} obtained from mantle xenolith samples by Schilling at al. (2008), the SCLM underneath the DM was formed in Meso- to late Paleoproterozoic times, in good agreement with the proposed Nd mantle separation ages obtained by Pankhurst et

al. (2003). Mantle xenolith carrying alkali basaltic magmatism occurred in the Pliocene to Quaternary.

The southern south of Patagonia

The area south of the DM, east of the Andean Cordillera is covered by successions of up to 7 km of sediments and young volcanic rocks. Hence, no basement outcrops are accessible in this area. Therefore, crustal rocks cannot be used to date the formation of the southernmost continental area of Patagonia. Based on the Re-Os isotopic study of mantle xenoliths from Pali Aike, Stern et al. (1999), Schilling et al. (2008) and Wang et al. (2008) proposed a young Phanerozoic lithosphere in southernmost Patagonia. However, this study rebuts these author's results and shows that the very South of Argentina was formed at least in early Paleoproterozoic times (Chapter I) and thus represents the oldest part of Patagonia.

SYNTHESIS

The following paragraphs represent a synthesis of all data obtained during this PhD project. Comparisons of subcontinental lithospheric mantle fragments from southern Patagonia (Chapter I) and mantle xenoliths from northern Patagonia (Chapter II) are drawn and the main differences are emphasized. Detailed information and results can be found in the respective chapters.

I. Bulk rock major and trace element compositions

Determined modal compositions of Patagonian mantle xenoliths reveal distinct differences between samples from the North and samples from the South (Fig. 4; PRA). With the exception of samples from Prahuanियeu locality (Bjerg et al., 2009),

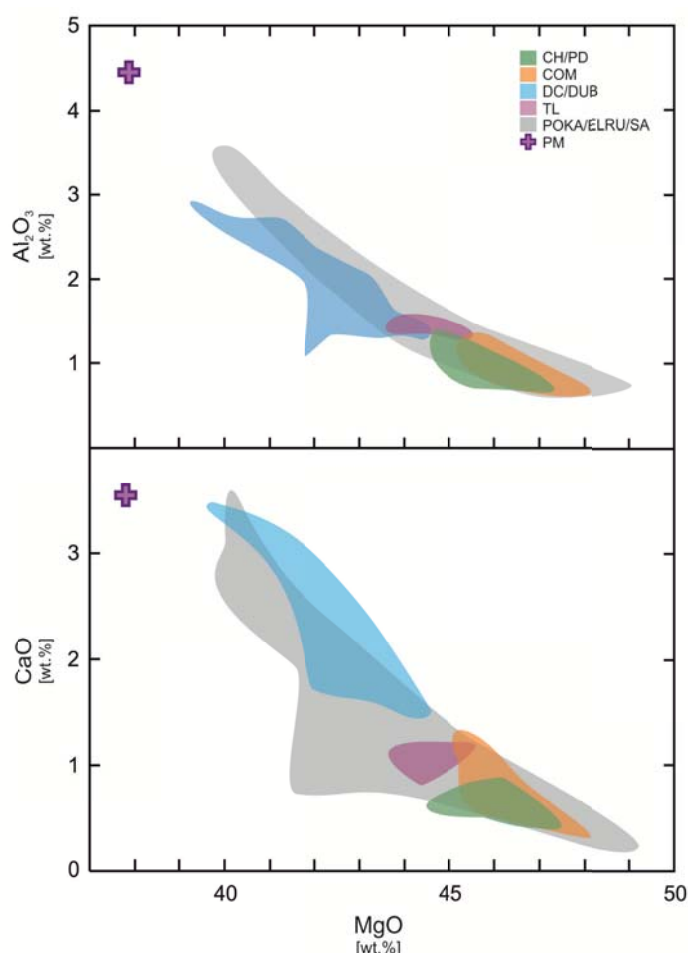


Fig. 5. Bulk rock MgO vs. Al₂O₃ and CaO.
PM – primitive mantle from McDonough & Sun (1995)

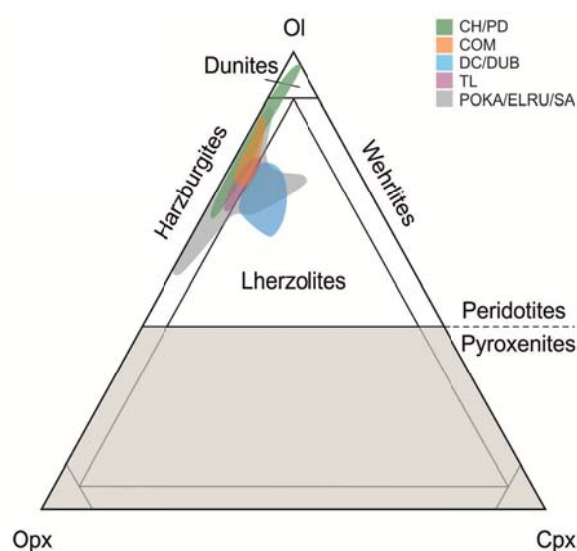


Fig. 4. Modal composition of Patagonian mantle xenoliths plotted in a triangle with the endmembers: Ol – olivine, Cpx – clinopyroxene and Opx – orthopyroxene. Legend as in Fig. 1.

mantle xenoliths from the northwestern part of Patagonia (CH, PD, COM) are represented by harzburgites and dunites (Table 1 Chapter II). The southern Patagonian outcrops (DC, DUB, TL, POKA, ELRU, SA) comprise dunites, harzburgites as

well as lherzolites (Table AD1 Chapter I). Hence, samples from the Northwest reveal an overall strongly depleted subcontinental lithospheric mantle (SCLM), while mantle xenoliths from southern Patagonia represent a SCLM that displays a large range of fertility. These differences in fertility of north and south Patagonian mantle xenoliths also become apparent in bulk rock major element compositions. MgO contents of northwestern Patagonian mantle samples range from 44.7 to 47.2 wt. % with Al₂O₃ and CaO ranging from 0.7 to 1.3 and 0.5 to 1.3 wt. %, respectively (Table 2 Chapter II). Samples from the South on the other hand, yield a much larger range of MgO contents from 39.2 to 49.0 wt. % (Table 2 and Table AD2, Chapter I). Bulk rock Al₂O₃ and CaO concentrations vary between 0.6 and 3.6 wt. % and 0.2 and 4.0 wt. %, respectively, for southern Patagonian mantle xenoliths (Fig. 5).

Bulk rock primitive-mantle normalized rare earth element (REE) patterns from north Patagonian mantle samples reveal lower HREE abundances (0.03 – 0.14 x PM; Table 2 Chapter II) compared to peridotites from southern Patagonia (0.07 – 0.79 x PM; Table 2 and Table AD2 Chapter I). Mantle xenoliths from the South display a wider and generally higher range in LREE compositions with 0.06 to 11.26 x PM. In comparison, samples from the northwestern part of Patagonia reveal a more uniform enrichment in LREE ranging from 0.12 to 1.38 x PM (Fig. 6).

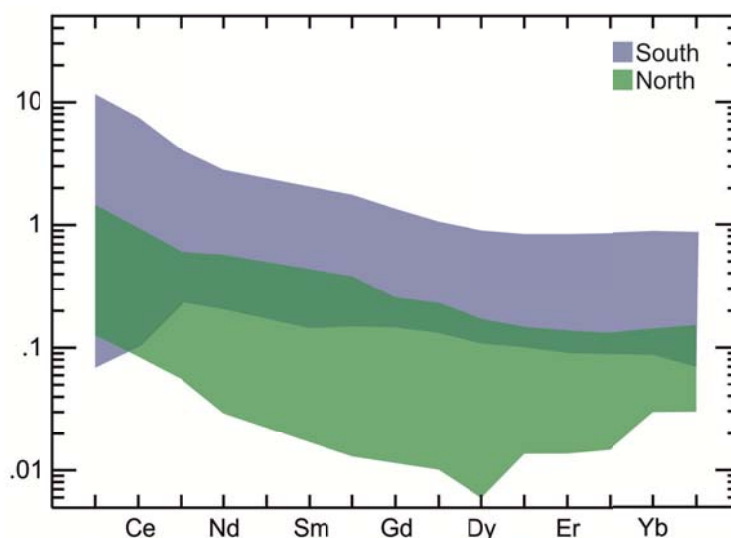


Fig. 6. Bulk rock PM-normalized rare earth element (REE) patterns of north (COM, PD, CH) and south (DC, DUB, TL, POKA, ELRU, SA) mantle xenoliths. PM from McDonough & Sun (1995)

II. Clinopyroxene major and trace element compositions

Radiogenic Hf, Nd and Sr isotopic ratios were determined from clinopyroxene (cpx) separates. Distinct differences also became apparent in the

composition of cpx from the South and the North of Patagonia. All microprobe clinopyroxene analyses from southern and northern Patagonia are given in Table 3 and Table AD5 Chapter I and Table 5 Chapter II, respectively.

All primary cpx are Cr-diopsides with compositions $\text{En}_{47-51}\text{Wo}_{45-50}\text{Fs}_{3-5}$ for south Patagonian and $\text{En}_{48-50}\text{Wo}_{46-49}\text{Fs}_{3-4}$ for north Patagonian mantle xenoliths. Cr_2O_3 and TiO_2 contents of cpx from the South range from 0.82 to 1.63 wt. % and 0.04 to 0.51 wt. %, respectively and in cpx from north Patagonia from 0.71 to 1.24 wt. % and 0.01 to 0.64 wt. %, respectively. Mg# and Al_2O_3 contents of primary cpx from southern Patagonian spinel-peridotites vary greatly between 0.91 and 0.94, and between 2.25 and 6.51 wt. %, respectively. Cpx from mantle xenoliths sampled at Comallo (COM), Puesto Diaz (PD) and Cerro Chenque (CH), on the other hand, are more depleted and with Mg# between 0.92 and 0.95 and a narrower range in Al_2O_3 contents ranging from 1.97 to 4.17 wt. %.

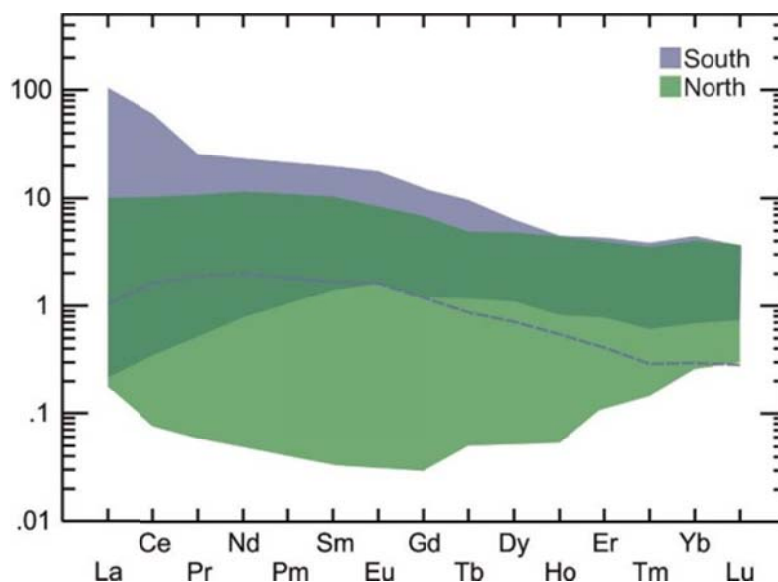


Fig. 7. Clinopyroxene PM-normalized REE patterns of South (Chapter I) and north (Chapter II) Patagonian mantle xenoliths. Dashed blue line represents the exception from southern Patagonian cpx (sample SA03). PM from McDonough & Sun (1995).

Clinopyroxene trace element compositions further underline the differences between mantle samples from the South and the North of Patagonia (Table 3 and Table AD7 Chapter I and Table 6 Chapter II, respectively). With the exception of one sample from the Pali Aike region (SA03), cpx from southern Patagonia yield narrower and overall lower HREE concentrations than cpx from northern Patagonia (Fig. 7). In contrast to cpx from south Patagonian sp-peridotites cpx from north Patagonia show a strong variation in MREE. Southern Patagonian cpx reveal a stronger enrichment in LREE compared to clinopyroxenes from north

Patagonian mantle samples. While some samples from the Tres Lagos region in southern Patagonia have cpx that show a depletion in LREE, all samples from the North have experienced an enrichment in these elements.

III. Highly siderophile element concentrations

A further distinct difference between samples from the North and samples from the South becomes apparent in the plot of chondrite normalized platinum group element (PGE) + rhenium compositions of analyzed bulk rock mantle

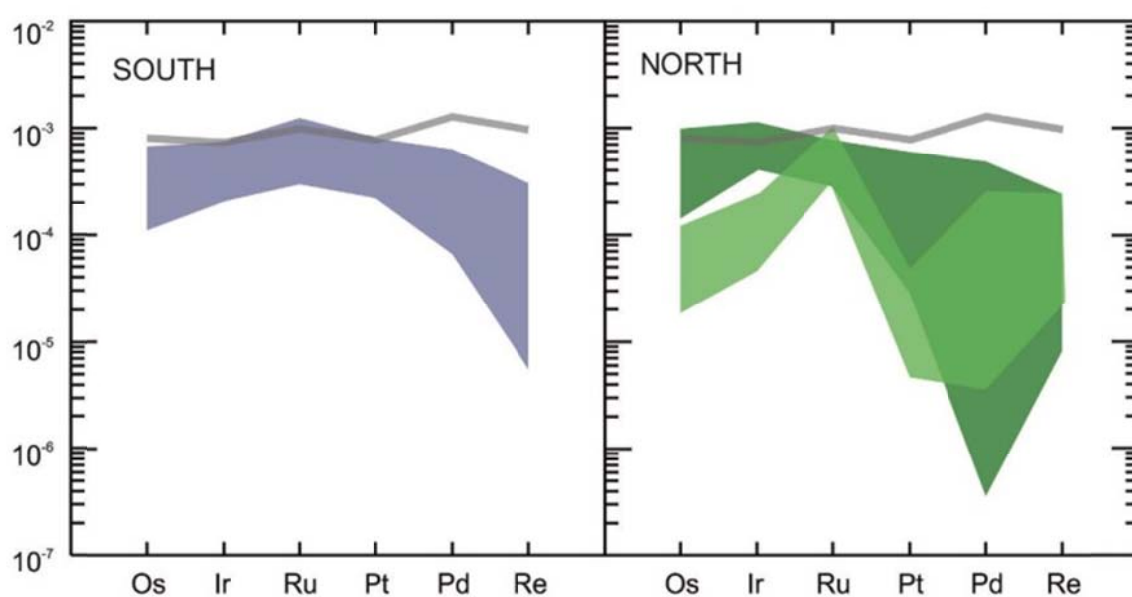


Fig. 8. Bulk rock chondrite-normalized highly siderophile element patterns of south (left) and north (right) Patagonian mantle xenoliths. CI from Anders & Grevesse (1989). Grey line represents PM of Becker et al. (2006).

xenoliths (Fig. 8). Samples from southern Patagonia (Table 1 Chapter I) exhibit no fractionation in the iridium-group PGEs (IPGEs) and exhibit more uniform chondrite normalized PGE+Re distribution patterns (Fig. 8, left). The majority of mantle samples from the northern part of Patagonia (Table 11 Chapter II), on the other hand, display a wide range in the more incompatible elements Pd and Re (Fig. 8, right, dark green area). Many mantle xenoliths from the North show a fractionation of Ru from Os and Ir (and Pt) (Fig. 8, right, light green area). This is likely due to the more depleted nature of north Patagonian mantle xenoliths, which results in the formation of Os-Ir(-Pt) alloys and laurite, a Ru-sulfide, after

extensive partial melting. As these elements are presumably hosted by different phases, percolation of a (sulfur saturated) melt can likely be a cause for a fractionation within the IPGEs in highly depleted samples. Overall, platinum group element abundances in mantle xenoliths from the southern part of Patagonia range from 7.1 to 25.1 ppb and are higher than PGE+Re concentrations in north Patagonian mantle samples ranging from 2.8 to 19.8 ppb.

IV. Isotopic compositions

Clinopyroxene Nd-Sr-Hf isotopic analyzes of all studied Patagonian mantle xenoliths (Table 1 Chapter I and Table 10 Chapter II) reveal a wide range of isotopic compositions. $^{143}\text{Nd}/^{144}\text{Nd}$ and $^{87}\text{Sr}/^{86}\text{Sr}$ ratios are more homogeneous within the studied north Patagonian sample suite (0.5127 to 0.5130 and 0.7027 to 0.7048, respectively) compared to mantle xenoliths from the South (0.5121 to 0.5133 and 0.7023 to 0.7077, respectively) (Fig. 9). In southern Patagonian mantle samples, radiogenic Sr ratios correlate well with radiogenic Nd compositions. In contrast, mantle xenoliths from the North display a weak decoupling of Sr from Nd (Fig. 9, a). Unlike mantle xenoliths from the South, samples from

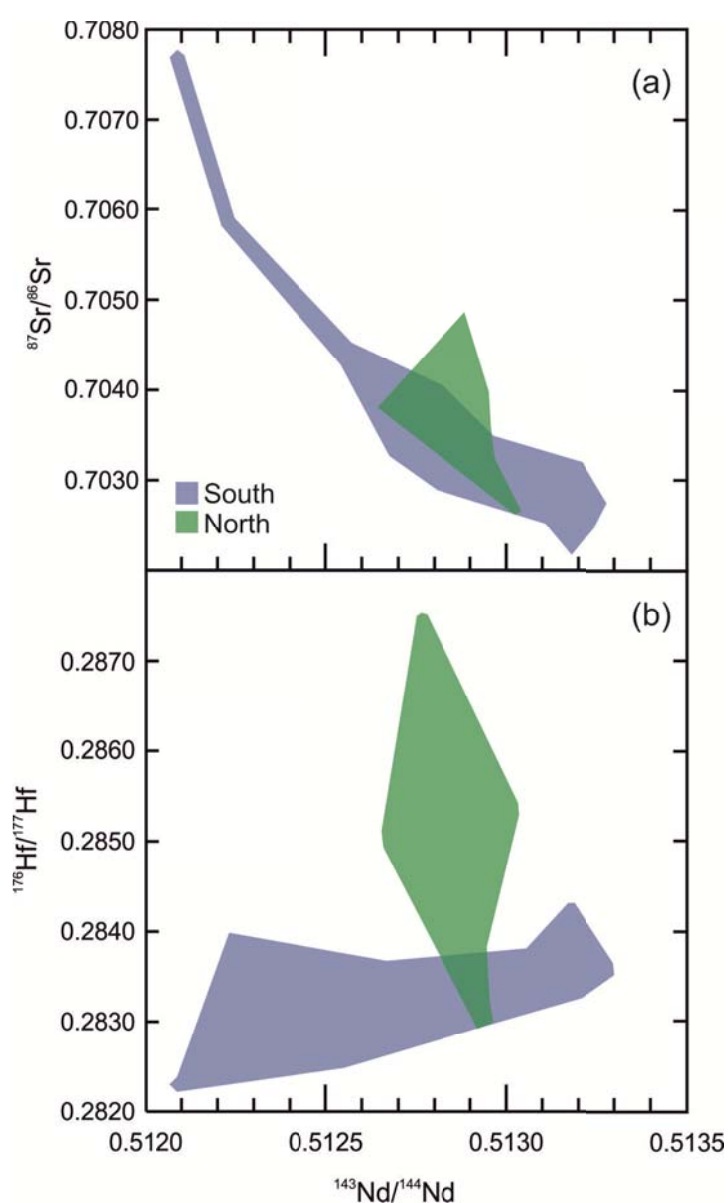


Fig. 9. Clinopyroxene Sr (a) and Hf (b) isotopic compositions plotted against Nd isotopic ratios of south (Chapter I) and north (Chapter II) Patagonian mantle xenoliths.

north Patagonia display a wide range in radiogenic hafnium ratios and show a strong decoupling from Nd (and Sr) isotopic compositions (Fig. 9, b). $^{176}\text{Hf}/^{177}\text{Hf}$ ratios vary between 0.2823 and 0.2874 in mantle peridotites from northern and between 0.2823 and 0.2843 in samples from the southern part of Patagonia (Fig. 9, b).

With the exception of one sample from Don Camilo (DC08), all Patagonian mantle xenoliths yield subchondritic osmium isotopic ratios (Table 1 Chapter I and Table 11 Chapter II). Southern Patagonian mantle xenoliths display a larger range in bulk rock radiogenic Osmium compositions (0.1115 to 0.1327) compared to samples from the North (0.1171 to 0.1257). The lowest $^{187}\text{Os}/^{188}\text{Os}$ ratios were analyzed in

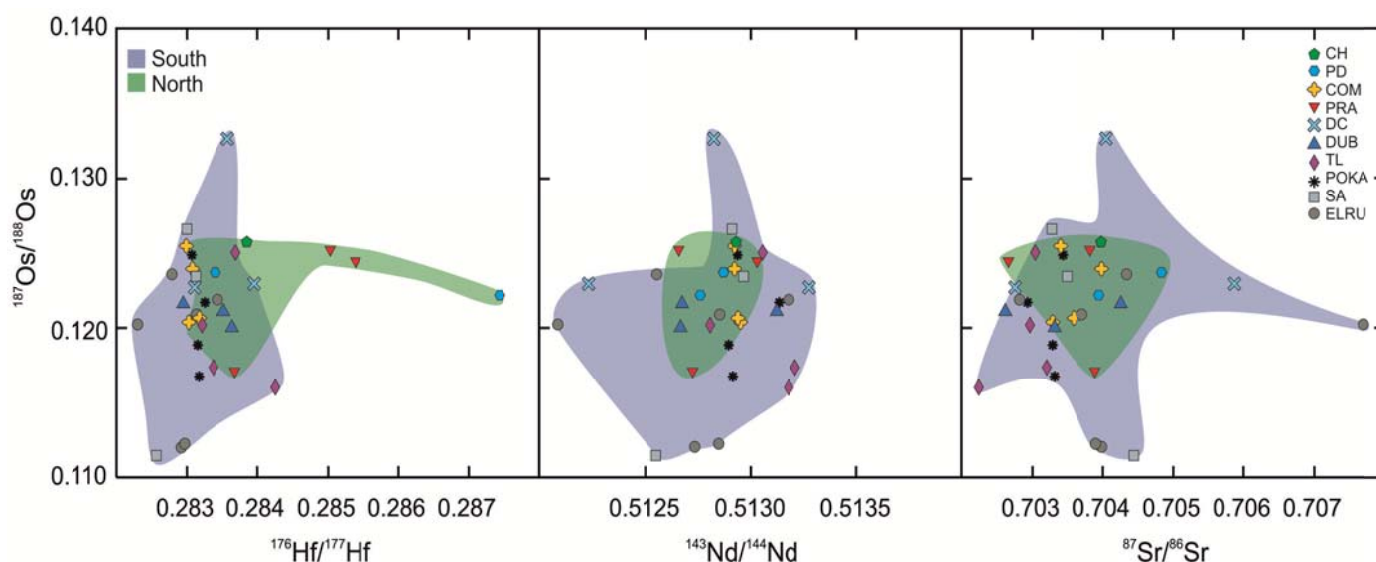


Fig. 10. Bulk rock osmium isotopic ratios plotted against Hf, Nd and Sr isotopic results from clinopyroxene separates for all studied Patagonian mantle xenoliths. Blue and green areas represent fields for southern and northern Patagonian mantle samples,

samples from the Pali Aike region (POKA, SA, ELRU) located in the southernmost part of Patagonia (Fig. 10). Generally, it must be noted that osmium isotopic results do not correlate with any of the other isotopic systems used in this study (Fig. 10). This is expected as rhenium and osmium are highly siderophile elements and in mantle rocks are preferably hosted in sulphide phases. On the other hand, hafnium, neodymium and strontium are lithophile elements and therefore reside in silicates. Hence, a metasomatic overprinting of the lithophile radiogenic isotope systems does not have an or the same effect on the Re-Os isotopic system. Hence, Hf-, Nd- and Sr-isotopically “disturbed“ samples may still be useful for determining the stabilization age of the SCLM using Re-Os isotope compositions.

V. Patagonian SCLM formation ages

Re-Os isotopic analyzes of 42 Patagonian mantle xenoliths lead to various SCLM formation ages ranging from early Neoproterozoic to early Paleoproterozoic (Fig. 11). The oldest SCLM fragment in northern Patagonia is represented by mantle

xenoliths from the Prahuanियeu area which yield a late Paleoproterozoic (1.7 Ga) age. Osmium isotopic results from mantle xenoliths sampled west of Prahuanियeu, namely Cerro Chenque, Puesto Diaz and Comallo reveal late to mid Mesoproterozoic (1.0 – 1.3 Ga), and hence distinctly younger mantle stabilization ages (Fig. 9 and Table 11 Chapter II). It is however important to keep in mind that the SCLM beneath those areas was highly affected by melt-rock reactions (Chapter II), which in turn could have had a strong influence on the HSE compositions and hence, the

osmium isotopic ratios. Thus, the determined mantle formation ages must be considered minimum. Consequently, we cannot argue with certainty that the SCLM beneath the North Patagonian Massif is made up of more than one fragment.

The situation in the South of Patagonia seems to be much clearer in terms of determined Re-Os SCLM formation ages (Fig. 4 and Table 1 Chapter I). Sample suites from our southern Patagonian outcrops comprise multiple mantle xenoliths that have not experienced obvious overprinting in terms of their HSE compositions. Hence, our

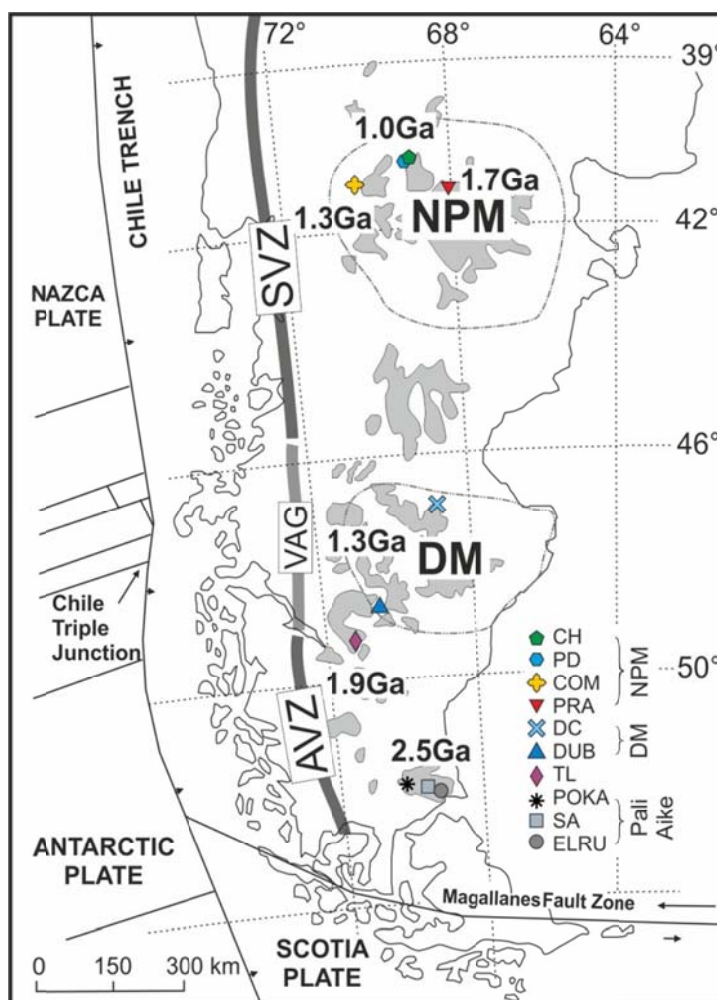


Fig. 11. Minimum Re-Os SCLM stabilization ages determined from north and south Patagonian mantle xenoliths. Legend as in Fig.I.

determined rhenium depletion ages are a reliable source to yield information on the actual formation of the SCLM beneath those areas. These osmium isotopic results lead to the conclusion that the southern part of Patagonia is made up of at least three continental fragments (Fig. 11) – the Deseado Massif with a Mesoproterozoic formation (1.3 Ga), the late Paleoproterozoic Tres Lagos area (1.9 Ga) and the early Paleoproterozoic Pali Aike fragment (2.5 Ga).

Due to the fact that the Patagonian terrane is at least of Proterozoic origin and pre-Gondwana supercontinent reconstructions are challenging, its exact evolution and ancient tectonic processes remain uncertain. However, our new osmium isotopic results prove previous assumptions on the evolution of the southernmost part of Patagonia wrong. Studies by e.g. Schilling et al. (2008), Stern et al. (1999) and Wang et al. (2008) led these authors to reason for a geologically young lithosphere beneath Pali Aike. Contrary to that, our study proves that the SCLM beneath southernmost Argentina stabilized as early as the early Paleoproterozoic and hence, represents the oldest part throughout Patagonia.

CONCLUSIONS

As previously mentioned in the Introduction part of this dissertation, the evolution, origin and age of the Patagonian continental terrane have been the topic of discussions for decades. In this study, we have added a substantial amount of new mantle xenolith data to the previously published information on the subcontinental lithospheric mantle (SCLM) from various outcrops within Patagonia. Among determining bulk rock and mineral major and trace element compositions we have conducted Os, Nd and Sr isotopic analyzes. In addition, we present the very first Hf isotopic results for Patagonian mantle xenoliths. Our newly obtained and recently published results may bring us one step closer to solving the “Patagonian puzzle“.

According to Re-Os isotopic results, southern Patagonia, the area south of the San Jorge basin (Fig. 1), is most likely made up of at least 3 different continental fragments (Chapter I). The oldest lithospheric fragment is represented by the subcontinental lithospheric mantle beneath the Pali Aike region, located in the very south of Argentina. The determined early Paleoproterozoic SCLM formation ages are particularly interesting as up until now, the southernmost part of Patagonia was thought to represent a Phanerozoic lithosphere, and hence, the youngest (Stern et al., 1999; Schilling et al., 2008; Wang et al., 2008) part of Patagonia. The data of this study supports the hypothesis of an evolutionary connection between the Deseado Massif of Patagonia and the Namaqua-Natal-Maud-Belt of South Africa (Chapter I; Fig. 12).

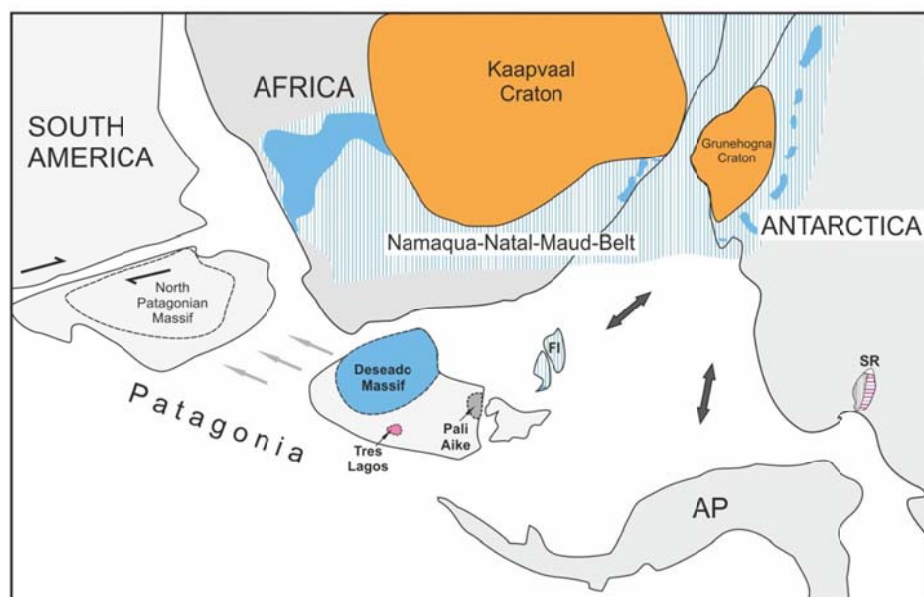


Fig. 12. Sketch map of the possible position of continental fragments during Gondwana breakup.

FI – Falkland Islands;
 SR – Shackleton Range;
 AP – Antarctic Peninsula.

North Patagonia, on the other hand, reveals slightly younger (late Paleoproterozoic) and more uniform Os isotopic ratios (Chapter II). Bulk rock and mineral trace element compositions reveal extensive melt extractions, followed by subsequent melt percolation processes. As these melt/rock reactions have – in some samples – had a considerable impact on the highly siderophile element systematics, Os isotopic compositions might have been affected by secondary processes and hence, are difficult to interpret. Nevertheless, the oldest determined rhenium depletion ages indicate a stabilization of the SCLM beneath the Prahuaniyeu area in North Patagonia at least 1.7 Ga ago (Chapter II). This is in good agreement with previously published Re-Os isotopic data from Schilling et al. (2008) and Sm-Nd model ages of metasedimentary North Patagonian Massif basement rocks (Martínez Dopico et al., 2011). Further osmium isotopic studies of North Patagonian mantle xenoliths are needed to get conclusive and reliable estimations on the timing of the stabilization of the subcontinental lithospheric mantle, and hence, the age of the North Patagonian continental terrane.

REFERENCES

- Alani, P., Ntaflos, T., and Bjerg, E.A., 2009, Origin of melt pockets in mantle xenoliths from southern Patagonia, Argentina: *Journal of South American Earth Sciences*, v. 28, p. 419-428.
- Anders, E., and Grevesse, N., 1989, Abundances of the elements: Meteoritic and solar: *Geochimica et Cosmochimica Acta*, v. 59, p. 197-214.
- Becker, H., Shirey, S.B., and Carlson, R.W., 2001, Effects of melt percolation on the Re-Os systematics of peridotite from a Paleozoic convergent plate margin: *Earth and Planetary Science Letters*, v. 188, p. 107-121.
- Bjerg, E.A., Ntaflos, T., Kurat, G., Dobosi, G., and Labudia, C.H., 2005, The upper mantle beneath Patagonia, Argentina, documented by xenoliths from alkali basalts: *Journal of South American Earth Sciences*, v. 189, p. 125-145.
- Bjerg, E.A., Ntaflos, T., Thöni, M., Aliani, P., and Labudia, C.H., 2009, Heterogeneous Lithospheric Mantle beneath Northern Patagonia: Evidence from Prahuaníyeu Garnet- and Spinel-Peridotites: *Journal of Petrology*, v. 50, p. 1267-1298.
- Bouvier, A., Vervoort, J.D. and Patchett, P.J., 2008, The Lu-Hf and Sm-Nd isotopic composition of CHUR: constraints from unequilibrated chondrites and implications for the bulk composition of terrestrial planets: *Earth and Planetary Science Letters*, v. 273, p. 48-57.
- Dantas, C., Gregoire, M., Koester, E., Conceição, and Rieck Jr., N., 2009, The lherzolite-websterite xenolith suite from Northern Patagonia (Argentina): Evidence of mantle-melt reaction processes: *Lithos*, v. 107, p. 107-120.
- Faccini, B., Bonadiman, C., Coltorti, M., Grégoire, M., and Siena, F., 2013, Oceanic Material Recycled within the Sub-Patagonian Lithospheric Mantle (Cerroo del Fraile, Argentina): *Journal of Petrology*, v. 54, p. 1211-1258.

- Giacosa, R., Márquez, M., and Panza, J., 2002, Basamento Paleozoico inferior del Macizo del Deseado. In: Haller, M., (Ed.), *Geología y Recursos Naturales de la provincial de Santa Cruz: Relatorio del Quince Congreso Geológico Argentino*, v. I-2, p. 33-44.
- Gorring, M.L., Kay, S.M., Zeitler, P.K., Ramos, V.A., Rubiolo, D., and Fernandez, M.I., 1997, Neogene Patagonian plateau lavas: continental magmas associated with ridge collision at the Chile Triple Junction: *Tectonics*, v. 16, p 1-17.
- Gorring, M.L., and Kay, S.M., 2001, Mantle Processes and Sources of Neogene Slab Window Magmas from Southern Patagonia, Argentina: *Journal of Petrology*, v. 42, p. 1067-1094.
- Griffin, W.L., O' Reilly, S.Y., and Ryan, C.G., 1999a, The composition and origin of subcontinental lithospheric mantle: In: Fei, Y., Bertka, C.M., and Mysen, B.O. (eds), *Mantle petrology: field observations and high pressure experimentation: a tribute to Francis F. (Joe) Boyd*. The Geochemical Society, p. 13-45.
- Guido, D.M., Escayola, M.P., and Schalamuk, I.B., 2004, the basement of the Deseado Massif at Bahia Laura, Patagonia, Argentina: a proposal for its evolution: *Journal of South American Earth Sciences*, v. 16, p. 567-577.
- Kay, S.M., Ardolino, A.A., Gorring, M.L., and Ramos, V.A., 2007, The Somuncura Large Igneous Province in Patagonia: Interaction of a Transient Mantle Thermal Anomaly with a Subducting Slab: *Journal of Petrology*, v. 48, p 43-77.
- Laurora, A., Mazzucchelli, M., Rivalenti, G., Vannucci, R., Zanetti, A., Barbieri, M.A., and Cingolani, C.A., 2001, Metasomatism and Melting in Carbonated Peridotite Xenoliths from the Mantle Wedge: The Gobernador Gregores Case (Southern Patagonia): *Journal of Petrology*, v. 42(1), p. 69-87.
- Lugmair, G.W. and Marti, K., 1978, Lunar initial $^{143}\text{Nd}/^{144}\text{Nd}$: differential evolution of the lunar crust and mantle: *Earth and Planetary Science Letters*, v. 39, p. 349-357.

- McDonough, W.F. and Sun, S., 1995, The composition of the Earth: *Chemical Geology* v. 120, p. 223-253.
- Martinez Dopico, C.I., Lopez de Luchi, M.G., Rapalini, A.E., and Kleinhanns, I.C., 2011, Crustal segments in the North Patagonian Massif, Patagonia: An integrated perspective based on Sm-Nd isotope systematics: *Journal of South American Earth Sciences*, v. 31, p. 324-341.
- Meisel, T., Walker, R.J., Irving, A.J., and Lorand, J.-P., 2001, Osmium isotopic compositions of mantle xenoliths: A global perspective: *Geochimica et Cosmochimica Acta*, v. 65, p. 1311-1323.
- Ntaflos, Th., Bjerg, E. A., Labudia, C. H., and Kurat, G., 2007, Depleted lithosphere from the mantle wedge beneath Tres Lagos, southern Patagonia, Argentina: *Lithos*, v. 94 (1-4), p. 46-65.
- Pankhurst, R.J., Rapela, C.W., Loske, W.P., M á rquez, M., and Fanning, C.M., 2003, Chronological study of the pre-Permian basement rocks of southern Patagonia: *Journal of South American Earth Sciences*, v. 16, p. 27-44.
- Pankhurst, R.J., Rapela, C.W., Fanning, C.M., and Marquez, M., 2006, Gondwanide continental collision and the origin of Patagonia: *Earth-Science Reviews*, v. 76, p. 235-257.
- Pearson, D.G., 1999, The age of continental roots: *Lithos*, v. 48, p. 171-194.
- Ramos, V.A., and Kay S.M., 1992, southern Patagonian plateau basalts and deformation: back-arc testimony of a ridge collision: *Tectonophysics*, v. 2015, p. 261-282.
- Ramos, V.A., 2008, Patagonia: A continental adrift?: *Journal of South American Earth Sciences*, v. 26, p. 235-251.
- Rivalenti, G., Zanetti, A., Mazzucchelli, M., Vannucci, R., and Cingolani, C.A., 2004, Equivocal carbonatite markers in the mantle xenoliths of the Patagonia backarc: the

- Gobernador Gregores Case (Santa Cruz Province, Argentina): Contributions to Mineralogy and Petrology, v. 147, p. 647-670.
- Scherer, E., Münker, C. and Metzger, K., 2001, Calibration of the Lutetium-Hafnium Clock: Science, v. 293, p. 683-686.
- Schilling, M.S., Carlson, R.W., Conceição, R.V., Dantas, C., Bertotto, G.W., and Koester, E., 2008, Re-Os isotope constraints on subcontinental lithospheric mantle evolution of southern South America: Earth and Planetary Science Letters, v. 268, p. 89-101.
- Shirey S.B., and Walker, R.J., 1998, The Re-Os isotope system in cosmochemistry and high-temperature geochemistry: Annual Review of Earth and Planetary Sciences, v. 26, p. 423-500.
- Smoliar, M.I., Walker, R.J., and Morgan, J.W., 1996, Re-Os ages of Group IIA, IIIA, IVA and IVB iron meteorites: Science 271, 1099-1102.
- Steiger, R.H. and Jäger, E., 1977, Subcommittee on geochronology: Convention on the use of decay constants in geo- and cosmochemistry: Earth and Planetary Science Letters, v. 36(3), p. 359-362.
- Stern, C.R., and Kilian, R., 1996, Role of the subducted slab, mantle wedge and continental crust in the generation of adakites from the Andean Austral Volcanic Zone: Contributions to Mineralogy and Petrology, v. 123, p. 263-281.
- Stern, C.R., Kilian, R., Oker, B., Hauri, E.H., and Dyser, T.K., 1999, Evidence from mantle evolution for relatively thin (<100 km) continental lithosphere below the Phanerozoic crust of southernmost South America: Lithos, v. 48, p. 217-235.
- Wang, J., Hattori, K.H., Li, J., and Stern C.R., 2008, Oxidation state of Paleozoic subcontinental lithospheric mantle below the Pali Aike volcanic field in southernmost Patagonia: Lithos, v. 105, p. 98-110.

CHAPTER I — South Patagonia

Mundl, A., Ntaflos, T., Ackerman, L., Bizimis, M., Bjerg, E.A. & Hauzenberger, C.A., (2015). Mesoproterozoic and Paleoproterozoic subcontinental lithospheric mantle domains beneath southern Patagonia: Isotopic evidence for its connection to Africa and Antarctica. *Geology*, v. 43, p. 39-42.

Mesoproterozoic and Paleoproterozoic subcontinental lithospheric mantle domains beneath southern Patagonia: Isotopic evidence for its connection to Africa and Antarctica

Andrea Mundl¹, Theodoros Ntaflou¹, Lukas Ackerman^{2,3}, Michael Bizimis⁴, Ernesto A. Bjerg⁵, and Christoph A. Hauzenberger⁶

¹Department of Lithospheric Research, University of Vienna, Althanstrasse 14, 1090 Vienna, Austria

²Institute of Geology v.v.i., Academy of Sciences of the Czech Republic, Rozvojová 269, 165 00 Prague 6 – Lysolaje, Czech Republic

³Czech Geological Survey, Geologická, 152 00 Prague 5, Czech Republic

⁴Department of Earth and Ocean Sciences, University of South Carolina, 701 Sumter Street, Columbia, South Carolina 29208, USA

⁵INGEOSUR (CONICET-UNS) and Departamento de Geología, Universidad Nacional del Sur, San Juan 670, B8000ICN Bahía Blanca, Argentina

⁶Institute for Earth Sciences, University of Graz, Heinrichstrasse 26, 8010 Graz, Austria

ABSTRACT

New isotopic studies on mantle xenoliths from Santa Cruz Province, southern Patagonia, Argentina, reveal that at least three discrete subcontinental lithospheric mantle (SCLM) domains—the Deseado Massif, Tres Lagos, and Pali Aike—form the southernmost part of South America. Re-Os systematics yield early Paleoproterozoic (up to 2.5 Ga) SCLM formation ages (rhenium depletion ages, T_{RD}) for Pali Aike spinel peridotites, while samples from the Deseado Massif and Tres Lagos indicate a younger SCLM origin with Neoproterozoic to Mesoproterozoic (0.9–1.3 Ga) and Mesoproterozoic to late Paleoproterozoic (1.3–1.9 Ga) T_{RD} ages, respectively. Hf-Sr-Nd isotopic compositions indicate metasomatic overprinting of the majority of the samples, which, however, has not affected the Os isotopic system. Based on similar formation ages, the geological evolution of the Deseado Massif is most likely connected to the evolution of the Namaqua-Natal belt of South Africa. T_{RD} ages from SCLM domains underneath Tres Lagos and Pali Aike indicate a common origin with crustal sections from Shackleton Range, Antarctica, positioning the southern tip of South America closer to west Antarctica in the reconstructed Rodinia supercontinent than previously assumed.

INTRODUCTION

The origin of the Patagonian continental terrane is highly debated. Whether Patagonia is a uniform part of the southernmost South American continental plate or an assemblage of fragments with different mantle roots is a matter of controversy (Stern et al., 1999; Pankhurst et al., 2006; Ramos, 2008; Schilling et al., 2008; Wang et al., 2008). As a result of the rarity of southern Patagonian crustal basement outcrops, which could provide precise evidence on the timing of crustal formation, Patagonia's geological evolution has remained enigmatic.

The formation of ancient continental terranes is related to the formation of their underlying subcontinental lithospheric mantle (SCLM) roots, as continental crust is formed by the extraction of melt of a mantle section that has experienced variable degrees of partial melting. This residual depleted lithospheric mantle coevally forms the root of the overlying continental crust (e.g., Griffin et al., 1999a, and references therein; Pearson, 1999). This relationship permits us to use the determined timing of lithospheric mantle formation as a proxy for the timing of the genesis of continental terranes. Hence, mantle xenoliths brought to the surface by magmas can provide detailed information on SCLM sections. The Re-Os isotopic system is, compared to other isotopic systems, less sensi-

tive to mantle metasomatism, providing reliable information on the timing of melt extraction events leading to the formation of the SCLM and its overlying crust (Walker et al., 1989; Carlson, 2005). We have used the Re-Os isotopic system on carefully selected mantle xenoliths to determine the timing of the stabilization of SCLM domains beneath southern Patagonia. In addition, Hf-Nd-Sr isotopic data obtained from leached clinopyroxene (cpx) separates of those samples analyzed for Os isotopic composition are presented to provide better insight into the origin and complex history of South Patagonia.

GEOLOGICAL SETTING

Patagonia, in southern South America, is geographically defined as the region south of Río Colorado and east of the Andean Cordillera. The only basement outcrop in southern Patagonia is the Deseado Massif which covers 60,000 km² (Fig. 1). Pankhurst et al. (2003) presented Mesoproterozoic (1.3–1.6 Ga) Sm-Nd mantle separation ages from Deseado Massif granites, amphibolites, and schists. The basement south of the Deseado Massif is covered by sedimentary sequences >7 km thick, reflecting several episodes of basin formation of Triassic to Cretaceous age. The Late Jurassic breakup of Gondwana resulted in voluminous rhyolitic volcanism in southern Patagonia (Bruhn et al., 1978; Kay et

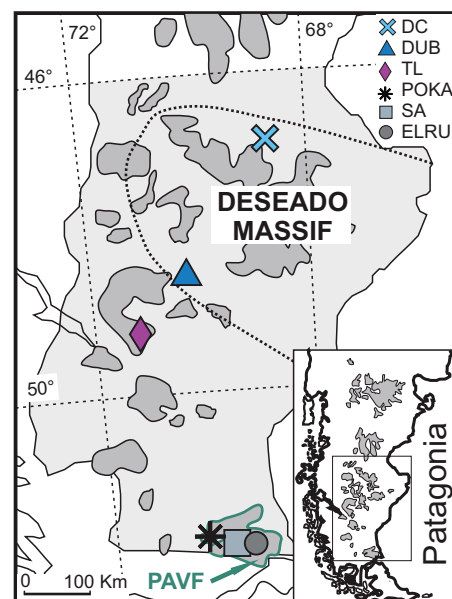


Figure 1. Simplified geological map of southern Patagonia. Light gray area is Santa Cruz Province. Dark gray fields are Tertiary/Quaternary flood basalts. Green outlined field is Pali Aike volcanic field (PAVF). DC—Don Camilo; DUB—Gobernador Gregores; TL—Tres Lagos; POKA—Potrok Aike; SA—Salsa; ELRU—El Ruido.

al., 1989). Since then, subsidence and sedimentation have dominated the area, forming the Magellanic Basin (Wang et al., 2008). Phanerozoic rhenium depletion ages (T_{RD}) obtained by Wang et al. (2008) have led them to interpret the basement beneath Pali Aike (Fig. 1) to be a young accretionary lithosphere that was either part of the Deseado Massif or a separate part that accreted to the Deseado Massif during the Paleozoic.

SAMPLES AND RESULTS

Sample Description

From a large number (>200) of mantle xenoliths collected at six different sites throughout Santa Cruz Province, 11 anhydrous spinel

lherzolites and 13 anhydrous spinel harzburgites were chosen and studied in detail (see the GSA Data Repository¹ for selection criteria). Host rocks are Pliocene and Quaternary alkali basalts, basanites, and pyroclastics (D'Orazio et al., 2000) that erupted in the back-arc region of the Andean subduction zone (Stern et al., 1990).

Sample localities are Don Camilo (DC) and Gobernador Gregores (DUB) within the Deseado Massif; Tres Lagos (TL); and Potrok Aike (POKA), El Ruido (ELRU), and Salsa (SA) from within the Pali Aike volcanic field (Fig. 1).

Bulk-rock major element analyses show that samples from Pali Aike (POKA, SA, ELRU) and Tres Lagos have mean Al_2O_3 contents and $\text{Mg}\#$ [$\text{Mg}/(\text{Mg} + \text{Fe}_{\text{tot}})$] of 1.46 wt% and 0.91, respectively, and are generally more depleted than mantle xenoliths found in the Deseado Massif with mean Al_2O_3 contents and $\text{Mg}\#$ of 2.08 wt% and 0.90, respectively. Bulk-rock rare earth element (REE) compositions reveal elevated light REE (LREE) in the majority of Pali Aike samples (ELRU and SA). All POKA samples exhibit a hump in middle REE (MREE) suggesting melt percolation processes. Except for sample TL143, Tres Lagos samples have slightly elevated LREE compositions. Deseado Massif samples exhibit roughly flat REE patterns with a minor increase in LREE in DC and a minor MREE and stronger LREE enrichment in DUB samples (Table DR2 and Fig. DR2 in the Data Repository).

Sulfide Petrography

The modal abundances of sulfides in the studied mantle xenoliths are generally low and do not correlate with fertility indices (e.g., bulk rock Al_2O_3). Sulfides occur either interstitially or as spherical inclusions and trails preferentially in olivine and orthopyroxene (Table DR4). Primary enclosed sulfides with diameters ranging from 30 to 150 μm are multiphase grains formed mainly of monosulfide solid solution, pentlandite, and chalcopyrite, with rare Pt- and/or Ir-rich microphases (Figs. DR3a–DR3f). Interstitial sulfides are commonly irregularly shaped and can be found in melt pockets, around spongy cpx, and as up to 10 μm elongated or round sulfide droplets in intergranular propagating fresh host basalt glass consisting mainly of Ni monosulfide solid solution, pyrrhotite, or pentland-

ite, as well as sulfide alteration products (Figs. DR3g–DR3l).

Re-Os Concentrations and Os-Hf-Nd-Sr Isotopic Systematics

Bulk-rock osmium concentrations vary from 0.5 to 3.3 ppb while rhenium contents are generally low, between 0.002 ppb and 0.105 ppb. Initial $^{187}\text{Os}/^{188}\text{Os}$ ratios, calculated back to time of eruption (4 Ma), are subchondritic, ranging from 0.1114 to 0.1266, except in one sample from the Deseado Massif (DC08) exhibiting a suprachondritic Os isotopic ratio of 0.1327 (Fig. 2). Osmium isotopic ratios do not correlate with either $^{187}\text{Re}/^{188}\text{Os}$ or bulk-rock Al_2O_3 (Figs. 2A and 2B). In samples from the Deseado Massif (DUB and DC), $^{187}\text{Os}/^{188}\text{Os}$ ratios lead to T_{RD} ages between 0.5 and 1.3 Ga. Except for sample TL142 (0.6 Ga), samples from Tres Lagos yield older T_{RD} ages ranging from 1.3 to 1.9 Ga. The largest variation in calculated T_{RD} ages can be found in the Pali Aike sample suite, with Neot to early Paleoproterozoic T_{RD} ages (0.7–2.5 Ga).

Hf isotopic analyses from Deseado Massif cpx separates yield ϵ_{Hf} ranging from +5.8 to +41.5. One sample (DC18) yields a model age (T_{MA}) of 1.2 Ga, consistent with Mesoproterozoic T_{RD} ages determined from Os isotopic analyses for Deseado Massif samples. ϵ_{Hf} values from Tres Lagos samples lie between +15.2 and +52.0. Sample TL142 yields a calculated T_{MA} age of 1.8 Ga. Samples from Pali Aike show a broad range in ϵ_{Hf} values from –17.1 to +23.0. Sample ELRU3, with ϵ_{Hf} of +23.0, yields a T_{MA} age of 2.7 Ga, slightly older than the oldest Pali Aike T_{RD} ages (2.4–2.5 Ga). Laser ablation analyses of cpx reveal no metasomatic addition of Hf or Lu to samples DC18, TL142, or ELRU3

(Table DR3). Hence, calculated T_{MA} ages can be considered reliable. Hf isotopic ratios from the remaining South Patagonian peridotites yield unrealistic future or impossibly old T_{MA} ages and suggest a resetting of the Lu-Hf system, also evidenced by enriched cpx trace element concentrations (Table DR3).

Sr and Nd isotopic compositions in the Deseado Massif mantle xenoliths yield variable $^{87}\text{Sr}/^{86}\text{Sr}$ ratios ranging from 0.70278 to 0.70588 and $^{143}\text{Nd}/^{144}\text{Nd}$ ratios between 0.51223 and 0.51328 (present-day ϵ_{Nd} of –7.9 to +11.2). Samples from Tres Lagos show Sr and Nd isotopic ratios between 0.70225 and 0.70320 and 0.51283 and 0.51321 (ϵ_{Nd} +3.32 to +11.2), respectively. Sr and Nd isotopic compositions in Pali Aike cpx range from 0.70282 to 0.70769 and 0.51209 to 0.51318 (ϵ_{Nd} –10.7 to +10.6), respectively, and correlate well with each other as well as with Hf isotopes (Figs. 3A–3C). Sr and Nd isotopic results combined with cpx trace element analyses reveal a cryptic metasomatic overprint of the majority of our studied samples.

DISCUSSION

SCLM Formation Ages

A scatter in Os isotopic ratios and the absence of a correlation thereof with melt depletion indices (e.g., bulk rock Al_2O_3) within a sample suite is often interpreted to indicate metasomatic overprint (i.e., Pearson et al., 1995; Brandon et al., 1996; Handler et al., 2005). However, our samples do not show significant variations in their highly siderophile element abundances (i.e., enrichment in the palladium group of the platinum-group elements, Ir-Ru fractionation; Fig. DR1) as is typical for many metasomatized

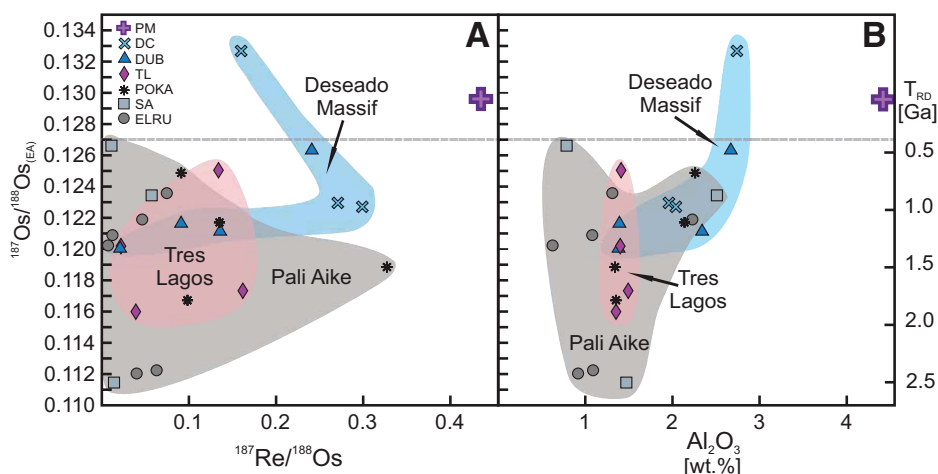
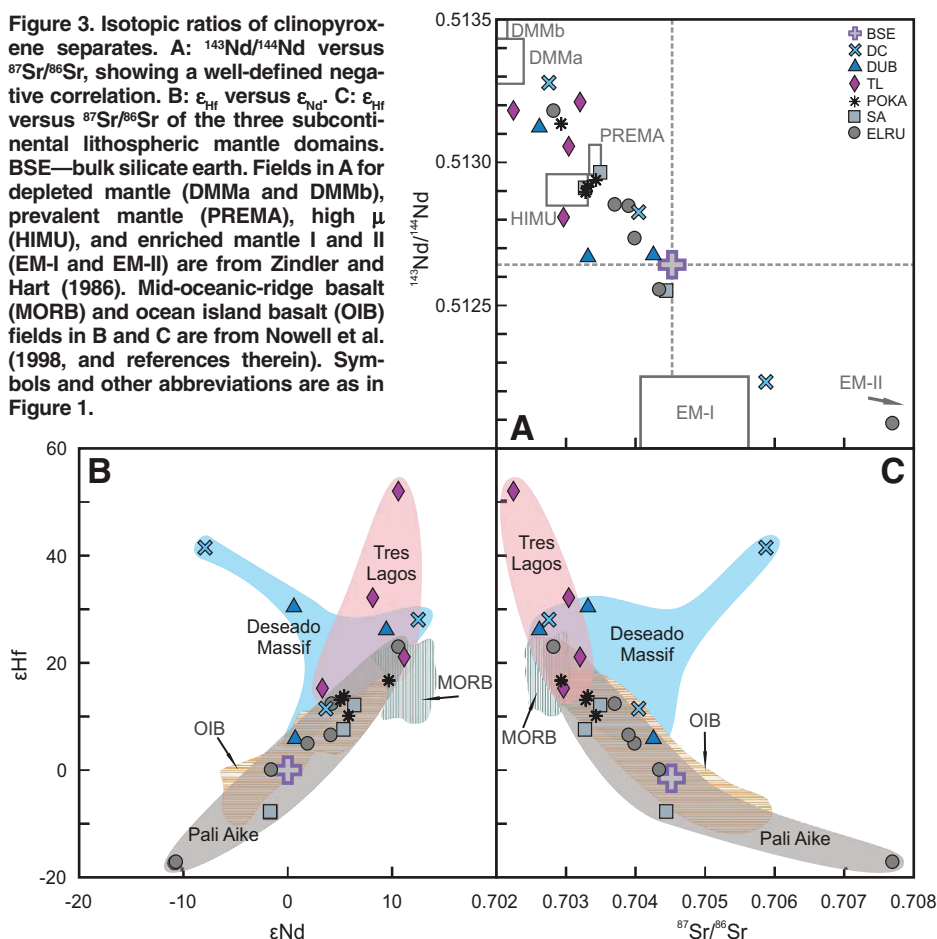


Figure 2. Bulk-rock $^{187}\text{Os}/^{188}\text{Os}$ versus $^{187}\text{Re}/^{188}\text{Os}$ (A) and bulk-rock Al_2O_3 [wt.%] (B), respectively, of 24 spinel peridotites with reference to primitive mantle (PM) values from Meisel et al. (1996) ($^{187}\text{Os}/^{188}\text{Os} = 0.1296$ and $^{187}\text{Re}/^{188}\text{Os} = 0.4353$) and McDonough and Sun (1995) ($\text{Al}_2\text{O}_3 = 4.45$ wt%). Rhenium depletion ages (T_{RD}) on right are mantle formation ages calculated using PM values from Meisel et al. (1996) at time of eruption (4 Ma). Gray dashed line is $^{187}\text{Os}/^{188}\text{Os}$ chondrite value (0.127; Walker and Morgan, 1989). Fields for subcontinental lithospheric mantle domains: Deseado Massif (DC and DUB), Tres Lagos (TL), and Pali Aike (POKA, SA, ELRU). Symbols and abbreviations are as in Figure 1.

¹GSA Data Repository item 2015029, detailed information on sample localities; analytical methods; isotopic results and HSE abundances (Table DR1 and Figure DR1); bulk rock major and trace element compositions (Table DR2) and bulk rock primitive mantle normalized REE patterns (Figure DR2); clinopyroxene major and trace element concentrations (Table DR3); sulfide occurrences (Table DR4); backscattered electron images and photomicrographs of primary and secondary sulfides (Figures DR3 and DR4), is available online at www.geosociety.org/pubs/ft2015.htm, or on request from editing@geosociety.org or Documents Secretary, GSA, P.O. Box 9140, Boulder, CO 80301, USA.

Figure 3. Isotopic ratios of clinopyroxene separates. A: $^{143}\text{Nd}/^{144}\text{Nd}$ versus $^{87}\text{Sr}/^{86}\text{Sr}$, showing a well-defined negative correlation. **B:** ϵ_{Hf} versus ϵ_{Nd} . **C:** ϵ_{Hf} versus $^{87}\text{Sr}/^{86}\text{Sr}$ of the three subcontinental lithospheric mantle domains. BSE—bulk silicate earth. Fields in A for depleted mantle (DMMa and DMMb), prevalent mantle (PREMA), high μ (HIMU), and enriched mantle I and II (EM-I and EM-II) are from Zindler and Hart (1986). Mid-oceanic-ridge basalt (MORB) and ocean island basalt (OIB) fields in B and C are from Nowell et al. (1998, and references therein). Symbols and other abbreviations are as in Figure 1.



peridotites (e.g., Lorand et al., 2013, and references therein).

Two populations of sulfides have been petrographically identified in our South Patagonian samples (Table DR4). While the Os isotopic composition in the majority of the samples is most likely controlled by primary sulfide inclusions in silicates (Alard et al., 2000), some samples also exhibit an abundance of secondary sulfides, which may lead to mixed whole-rock Os isotopic compositions. Clinopyroxene and bulk-rock primitive mantle-normalized REE patterns suggest that percolating melts have affected the bulk compositions of all POKA samples (Tables DR2 and DR3; Fig. DR2). This may have led to an addition of secondary sulfides prior to host basalt entrainment, and hence, resulted in a refertilization of the samples leading to T_{RD} ages younger than their actual melt depletion ages. Secondary sulfides in most other samples are found in fresh intergranular propagating glass and have likely been added to the xenoliths by host basalt infiltration. It is important to point out that the samples with the oldest calculated T_{RD} ages from each studied sample suite also exhibit the highest primary to secondary sulfide ratio, where secondary sulfides can only rarely be found within a thin section (Table DR4). Thus, we infer that the Os isotopic composition in those samples is

likely controlled by primary sulfides and yields minimum but reasonable T_{RD} ages.

Calculated T_{RD} ages (Fig. 4) from DUB and DC group at ca. 1 Ga, with the oldest T_{RD} age at 1.3 Ga. The Tres Lagos samples yield T_{RD} ages of up to 1.9 Ga. Samples from Pali Aike exhibit the broadest range in T_{RD} ages with three samples displaying a peak at ca. 2.4 Ga. Even though samples from within one sample suite yield variable T_{RD} ages, Figure 4 clearly shows that the oldest samples come from Pali Aike with an age of up to 2.5 Ga, followed by the Tres Lagos sample suite with the oldest determined T_{RD} ages of 1.9 Ga, and the “youngest” sample suite from Santa Cruz Province, the Deseado Massif, with T_{RD} ages of up to 1.3 Ga.

SCLM Domains

Deseado Massif

The determined SCLM formation ages for DC and DUB mantle xenoliths match that of the Mesoproterozoic basement interpreted by Pankhurst et al. (2003), as well as Meso- to Paleoproterozoic T_{RD} ages from Cerro Redondo and Estancia Lote 17 (Schilling et al., 2008). Rodinia and Gondwana reconstructions have placed the Deseado Massif close to South Africa and West Antarctica (e.g., Dalziel et al., 2000; König and

Jokat, 2006). U-Pb zircon data from exposed basement rocks of the Natal belt and Mesoproterozoic ages from Dronning Maud Land in East Antarctica suggest a continental crust formation between 1.2 and 1.0 Ga (McCourt et al., 2006; Jacobs et al., 1996). These ages are similar to our determined T_{RD} ages of up to 1.3 Ga for the Deseado Massif mantle xenoliths, as well as to Mesoproterozoic ages (1.1–1.0 Ga) obtained for basement rocks from Cape Meredith Complex, West Falkland–Malvinas (Thomas et al., 2000, and references therein). We suggest that the Patagonian SCLM fragment represented by Deseado Massif mantle xenoliths was accreted together with other microcontinents during the formation of Rodinia and stayed contiguous to South Africa and West Antarctica until the Mesozoic breakup of Gondwana.

Tres Lagos and Pali Aike

T_{RD} ages of the Tres Lagos samples are distinctly older than Deseado Massif ages, indicating a different origin. Ntaflos et al. (2007) proposed that the SCLM beneath Tres Lagos represents an isolated old Proterozoic lithospheric mantle fragment, based on the depleted nature and low pressure-temperature conditions of the mantle xenoliths. Our data support this model and further reveal distinct isotopic and trace element compositional differences between Tres Lagos and other Patagonian mantle xenoliths.

Previous studies suggest a Mesoproterozoic to early Paleozoic (Stern et al., 1999; Schilling et al., 2008) or even younger (Wang et al., 2008) formation of the SCLM beneath Pali Aike. However, our Re-Os data clearly show that the SCLM beneath Pali Aike was formed at least as long ago as early Paleoproterozoic times.

Crustal rocks of similar age close to the position of southernmost Patagonia in Gondwana occur only at Shackleton Range, a composite terrane located at the northwestern edge of the East

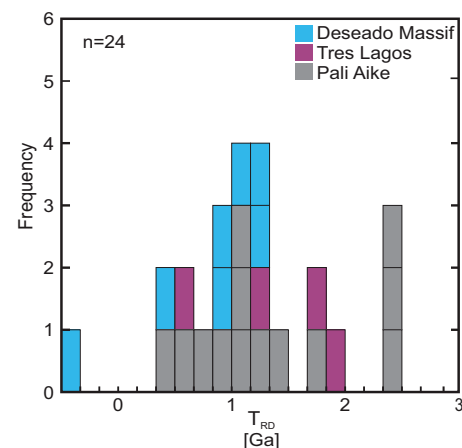


Figure 4. Histogram of calculated rhenium depletion ages (T_{RD}), comprising all 24 Patagonian spinel peridotites, using primitive mantle values from Meisel et al. (1996) ($^{187}\text{Os}/^{188}\text{Os} = 0.1296$).

Antarctic craton. U-Pb data from orthogneisses from the northern belt of Shackleton Range suggest granite emplacement at 2.3 Ga (Brommer et al., 1999), indicating the existence of early Paleoproterozoic crust. U-Pb data from magmatic zircons in gneisses from the Shackleton Range's Southern Terrane document an additional slightly younger Paleoproterozoic (1.9 Ga) magmatic period in this region (Will et al., 2009). These ages match our determined T_{RD} ages from Pali Aike (2.5 Ga) and Tres Lagos (1.9 Ga) and hence suggest a common geological origin.

CONCLUSIONS

The Mesoproterozoic evolution of the SCLM beneath the Deseado Massif, southern Patagonia, is most likely connected to the formation of the Namaqua-Natal belt and hence was formed during the assembly of Rodinia. Osmium isotopic results show that, contrary to previous studies suggesting Mesoproterozoic to Paleozoic formation (Stern et al., 1999; Wang et al., 2008; Schilling et al., 2008), the SCLM beneath Pali Aike in southernmost South Patagonia was formed as early as the early Paleoproterozoic. We suggest that the SCLM underneath the southernmost part of Patagonia and southwest of the Deseado Massif is represented by late Archean to early Paleoproterozoic and mid-Paleoproterozoic fragments whose origin is connected to the geological evolution of Shackleton Range, Antarctica. These SCLM fragments accreted to the Deseado Massif probably during the formation of supercontinent Rodinia before drifting off together with the rest of South Patagonia during Gondwana breakup.

ACKNOWLEDGMENTS

This work was financed by Austrian Science Fund grant P 23557-N19 (Principal Investigator: Th. Ntaflos). We gratefully acknowledge W. Wegner (University of Vienna) for Sr and Nd isotope analyses; V. Erban (Czech Geological Survey) for Os isotope analyses; and J. Ďurišová (Czech Academy of Sciences) for inductively coupled plasma-mass spectrometry analyses of highly siderophile elements. We thank W.L. Griffin, J. Bédard, and two anonymous reviewers for their constructive comments to improve this manuscript. The editorial handling and suggestions by J.B. Murphy are greatly appreciated.

REFERENCES CITED

- Alard, O., Griffin, W.L., Lorand, J.-P., Jackson, S.E., and O'Reilly, S.Y., 2000, Non-chondritic distribution of the highly siderophile elements in mantle sulphides: *Nature*, v. 407, p. 891–894, doi:10.1038/35038049.
- Brandon, A.D., Creaser, R.A., Shirey, S.B., and Carlson, R.W., 1996, Osmium recycling in subduction zones: *Science*, v. 272, p. 861–863, doi:10.1126/science.272.5263.861.
- Brommer, A., Millar, I.L., and Zeh, A., 1999, Geochronology, structural geology and petrology of the northwestern Lagrange Nunataks, Shackleton Range, Antarctica: *Terra Antarctica*, v. 6, p. 269–278.
- Bruhn, R.L., Stern, C.R., and De Wit, M.J., 1978, Field and geochemical data bearing on the development of a Mesozoic volcanotectonic rift zone and back-arc basin in southernmost South America: *Earth and Planetary Science Letters*, v. 41, p. 32–46, doi:10.1016/0012-821X(78)90039-0.
- Carlson, R.W., 2005, Application of the Pt-Re-Os isotopic systems to mantle geochemistry and geochronology: *Lithos*, v. 82, p. 249–272, doi:10.1016/j.lithos.2004.08.003.
- Dalziel, I.W.D., Mosher, S., and Gahagan, L.M., 2000, Laurentia-Kalahari collision and the assembly of Rodinia: *The Journal of Geology*, v. 108, p. 499–513, doi:10.1086/314418.
- D'Orazio, M., Agostini, S., Mazzarini, F., Innocenti, F., Manetti, P., Haller, M.J., and Lahsen, A., 2000, The Pali Aike Volcanic Field, Patagonia: Slab-window magmatism near the tip of South America: *Tectonophysics*, v. 321, p. 407–427, doi:10.1016/S0040-1951(00)00082-2.
- Griffin, W.L., O'Reilly, S.Y., and Ryan, C.G., 1999a, The composition and origin of subcontinental lithospheric mantle, *in* Fei, Y., et al., eds., *Mantle Petrology: Field Observations and High Pressure Experimentation: A Tribute to Francis F. (Joe) Boyd*: Houston, Texas, The Geochemical Society, v. 6, p. 13–45.
- Handler, R.M., Bennet, V.C., and Carlson, R.W., 2005, Nd, Sr and Os isotope systematics in young, fertile spinel peridotite xenoliths from northern Queensland, Australia: A unique view of depleted MORB mantle?: *Geochimica et Cosmochimica Acta*, v. 69, p. 5747–5763, doi:10.1016/j.gca.2005.08.003.
- Jacobs, J., Bauer, W., Spaeth, G., Thomas, R.J., and Weber, K., 1996, Lithology and structure of the Grenville-aged (~1.1 Ga) basement of Heimefrontfjella (East Antarctica): *Geologische Rundschau*, v. 85, p. 800–822.
- Kay, S.M., Ramos, V.A., Mpodozis, C., and Sruoga, P., 1989, Late Paleozoic to Jurassic silicic magmatism at the Gondwana margin: Analogy to the Middle Proterozoic in North America?: *Geology*, v. 17, p. 324–328, doi:10.1130/0091-7613(1989)017<0324:LPTJSM>2.3.CO;2.
- König, M., and Jokat, W., 2006, The Mesozoic breakup of the Weddell Sea: *Journal of Geophysical Research*, v. 111, B12102, doi:10.1029/2005JB004035.
- Lorand, J.-P., Lugué, A., and Alard, O., 2013, Platinum-group element systematics and petrogenetic processing of the continental upper mantle: A review: *Lithos*, v. 164–167, p. 2–21, doi:10.1016/j.lithos.2012.08.017.
- McCourt, S., Armstrong, R.A., Grantham, G.H., and Thomas, R.J., 2006, Geology and evolution of the Natal belt, South Africa: *Journal of African Earth Sciences*, v. 46, p. 71–92, doi:10.1016/j.jafrearsci.2006.01.013.
- McDonough, W.F., and Sun, S., 1995, The composition of the Earth: *Chemical Geology*, v. 120, p. 223–253, doi:10.1016/0009-2541(94)00140-4.
- Meisel, T., Walker, R.J., and Morgan, J.W., 1996, The osmium isotopic composition of the Earth's primitive upper mantle: *Nature*, v. 383, p. 517–520, doi:10.1038/383517a0.
- Nowell, G.M., Kempton, P.D., Noble, S.R., Fitton, J.G., Saunders, A.D., Mahoney, J.J., and Taylor, R.N., 1998, High-precision Hf isotope measurements of MORB and OIB by thermal ionization mass spectrometry: Insights into the depleted mantle: *Chemical Geology*, v. 149, p. 211–233, doi:10.1016/S0009-2541(98)00036-9.
- Ntaflos, Th., Bjerg, E.A., Labudia, C.H., and Kurat, G., 2007, Depleted lithosphere from the mantle wedge beneath Tres Lagos, southern Patagonia, Argentina: *Lithos*, v. 94, p. 46–65, doi:10.1016/j.lithos.2006.06.011.
- Pankhurst, R.J., Rapela, C.W., Loske, W.P., Márquez, M., and Fanning, C.M., 2003, Chronological study of the pre-Permian basement rocks of southern Patagonia: *Journal of South American Earth Sciences*, v. 16, p. 27–44, doi:10.1016/S0895-9811(03)00017-8.
- Pankhurst, R.J., Rapela, C.W., Loske, W.P., Fanning, C.M., and Márquez, M., 2006, Gondwanide continental collision and the origin of Patagonia: *Earth-Science Reviews*, v. 76, p. 235–257, doi:10.1016/j.earscirev.2006.02.001.
- Pearson, D.G., 1999, The age of continental roots: *Lithos*, v. 48, p. 171–194, doi:10.1016/S0024-4937(99)00026-2.
- Pearson, D.G., Shirey, S.B., Carlson, R.W., Boyd, F.R., Pokhilenko, N.P., and Shimizu, N., 1995, Re-Os, Sm-Nd, and Rb-Sr isotope evidence for thick Archean lithospheric mantle beneath the Siberian craton modified by multistage metamorphism: *Geochimica et Cosmochimica Acta*, v. 59, p. 959–977.
- Ramos, V.A., 2008, Patagonia: A Paleozoic continent adrift?: *Journal of South American Earth Sciences*, v. 26, p. 235–251, doi:10.1016/j.jsames.2008.06.002.
- Schilling, M.S., Carlson, R.W., Conceição, R.V., Dantas, C., Bertotto, G.W., and Koester, E., 2008, Re-Os isotope constraints on subcontinental lithospheric mantle evolution of southern South America: *Earth and Planetary Science Letters*, v. 268, p. 89–101, doi:10.1016/j.epsl.2008.01.005.
- Stern, C.R., Frey, F.A., Futa, K., Zartman, R.E., Peng, Z., and Kyser, T.K., 1990, Trace-element and Sr, Nd, Pb, and O isotopic composition of Pliocene and Quaternary alkali basalts of the Patagonian Plateau lavas of southernmost South America: Contributions to Mineralogy and Petrology, v. 104, p. 294–308, doi:10.1007/BF00321486.
- Stern, C.R., Kilian, R., Oker, B., Hauri, E.H., and Dysler, T.K., 1999, Evidence from mantle evolution for relatively thin (<100 km) continental lithosphere below the Phanerozoic crust of southernmost South America: *Lithos*, v. 40, p. 217–235, doi:10.1016/S0024-4937(99)00030-4.
- Thomas, R.J., Jacobs, J., and Eglinton, B.M., 2000, Geochemistry and isotopic evolution of the Mesoproterozoic Cape Meredith Complex, West Falkland: *Geological Magazine*, v. 137, p. 537–553, doi:10.1017/S0016756800004519.
- Walker, R.J., and Morgan, J.W., 1989, Rhenium-osmium isotope systematics of carbonaceous chondrites: *Science*, v. 243, p. 519–522, doi:10.1126/science.243.4890.519.
- Walker, R.J., Carlson, R.W., and Shirey, S.B., 1989, Os, Sr, Nd, and Pb isotope systematics of southern African peridotite xenoliths: Implications for the chemical evolution of the subcontinental mantle: *Geochimica et Cosmochimica Acta*, v. 53, p. 1583–1595, doi:10.1016/0016-7037(89)90240-8.
- Wang, J., Hattori, K.H., Li, J., and Stern, C.R., 2008, Oxidation state of Paleozoic subcontinental lithospheric mantle below the Pali Aike volcanic field in southernmost Patagonia: *Lithos*, v. 105, p. 98–110, doi:10.1016/j.lithos.2008.02.009.
- Will, T.M., Zeh, A., Gerdes, A., Frimmel, H.E., Millar, I.L., and Schmädicke, E., 2009, Palaeoproterozoic to Palaeozoic magmatic and metamorphic events in the Shackleton Range, East Antarctica: Constraints from zircon and monazite dating, and implications from the amalgamation of Gondwana: *Precambrian Research*, v. 172, p. 25–45, doi:10.1016/j.precamres.2009.03.008.
- Zindler, A., and Hart, S., 1986, Chemical geodynamics: *Annual Review of Earth and Planetary Sciences*, v. 14, p. 493–571, doi:10.1146/annurev.earth.14.050186.002425.

Manuscript received 9 October 2014
 Revised manuscript received 21 October 2014
 Manuscript accepted 21 October 2014
 Printed in USA

CHAPTER I — South Patagonia

Data Repository

GSA DATA REPOSITORY 2015029

SAMPLE LOCALITIES

Don Camilo: S46°59'13.6'' W69°32'01.8''

Gobernador Gregores: S48°34'23.5'' W70°10'55.5''

Tres Lagos: S49°11'06.5'' W71°20'23.2''

Potrok Aike: S51°57'45.6'' W70°22'24.6''

Salsa: S51°59'38.3'' W70°10'06.8''

El Ruido: S51°59'24.0'' W70°08'36.0''

ANALYTICAL METHODS

Samples were chosen from a pool of >200 fertile lherzolites, depleted lherzolites and harzburgites according to the following criteria:

- Fresh, unweathered mantle xenoliths.
- Representative sample size (7 to 15 cm in diameter) to obtain reasonable whole rock data as well as to provide enough material for mineral separation.
- Polished thin sections were made for all available samples and analyzed by EPMA in order to characterize them.
- Samples were studied under the microscope as well as with microprobe and modally metasomatized samples were excluded (samples containing hydrous phases).
- LA-ICP-MS results of clinopyroxene (cpx), as well as bulk rock major and trace element compositions were determined and samples showing the least cryptic metasomatic overprint were selected.
- Out of the remaining samples, the most depleted ones were chosen (leading to the assumption that most of Re was extracted) in order to minimize continuing ^{187}Os production from ^{187}Re decay after the initial melting event. The degree of depletion was inferred from modal compositions and from bulk rock and mineral compositions (i.e. bulk rock Al_2O_3 contents, bulk rock and olivine Mg#).

Host basalt rims were completely removed from mantle xenoliths and the inner parts of the samples were then crushed and processed to rock powders in an agate mill.

Bulk rock major and some trace elements were analyzed with the sequential X-ray spectrometer Phillips PW 2400, equipped with a Rh-excitation source at the University of Vienna, Department of Lithospheric Research. Fused disks for major element analyses were produced at 950°C from a mixture of specimen and $\text{Li}_2\text{B}_4\text{O}_7$ flux, diluted 1:5 to gain accurate and precise results. Trace elements were analyzed on pressed pellets. Replicate analyses of geo-standard GSR-3 gave an overall procedural uncertainty better than 2% for major elements and 5% (Cu = 8.5%) for trace elements.

~100 mg of whole rock powder per sample were dissolved in a mixture of HNO_3 and HF and trace elements were analyzed as solutions on an ICP-MS system (Agilent 7500) at the Central Lab for Water, Minerals and Rocks, NAWI Graz, Karl-Franzens-University of Graz and Graz University of Technology. (See Repository Data, Table 2 for element list)

Bulk rock osmium isotopes and Re-Os concentrations were obtained at the Academy of Sciences of the Czech Republic (chemistry and ICP-MS) and at the Czech Geological Survey in Prague (N-TIMS). The samples were dissolved and equilibrated with a mixed ^{185}Re - ^{190}Os spike using Carius Tube technique (Shirey and Walker, 1995), followed by Os separation through solvent extraction by CCl_4 (Cohen and Waters, 1996) and Os microdistillation (Birck et al., 1997). Rhenium was separated using anion exchange chromatography and then analyzed on sector field ICP-MS *Element 2* (Thermo) coupled with an Aridus IITM (CETAC) desolvating nebulizer. The Os isotopic compositions were determined by N-TIMS technique (Creaser et al., 1991; Völkening et al., 1991) on Finnigan MAT 262 thermal ionization spectrometer. Rhenium depletions ages (T_{RD}) were calculated using primitive upper mantle values from Meisel et al. (2001): $^{187}\text{Re}/^{188}\text{Os} = 0.4353$ and $^{187}\text{Os}/^{188}\text{Os} = 0.1296$; $\lambda^{187}\text{Re} = 1.666 \cdot 10^{-11}$ from Smoliar et al. (1996). Rhenium measurements were corrected for isotopic fractionation using a linear law and standard Re (NIST 3143) solutions. In-run precision of

measured isotopic ratios was always better than $\pm 0.4\%$ (2σ). After analysis, raw Os isotopic ratios were corrected offline for oxygen isobaric interferences, spike contribution, instrumental mass fractionation using $^{192}\text{Os}/^{188}\text{Os} = 3.08271$ (Shirey and Walker, 1998) and blank contribution. Total procedural blanks were 2.3 ± 1.7 pg and 0.5 ± 0.1 pg for Re and Os, respectively.

For Hf-Nd-Sr analyses, ~ 100 mg of cpx per sample was separated at the University of Vienna, Department of Lithospheric Sciences. Spongy rims and inclusions were completely removed. The separates were then leached in hot 6N HCl overnight and dissolved in 4 ml of mixture conc. HF:HNO₃ (1:3) for 3 days before being dried down.

The Hf isotope ratios were determined at the Center for Elemental Mass, University of South Carolina on a NEPTUNE MC-ICP-MS, with the Plus option installed (Bizimis et al., 2013). Hf was separated from the matrix on the Ln resin (Eichrom, USA), following Munker et al., 2001. Sample introduction was through a 100 μ l Teflon nebulizer coupled to an APEX system (ESI, USA). The measured ratios were corrected for mass fractionation using $^{179}\text{Hf}/^{177}\text{Hf} = 0.7325$. The JMC-475 standard was determined with $^{176}\text{Hf}/^{177}\text{Hf} = 0.282134 \pm 5$ ($n=13$, ~ 35 ng Hf runs). All data are reported relative to the accepted JMC value of $^{176}\text{Hf}/^{177}\text{Hf} = 0.282160$. Hf blanks are typically < 50 pg.

Sr and Nd isotopic compositions were obtained at the University of Vienna, Department of Lithospheric Research. About 50 mg of separated cpx fractions were dissolved using the same protocol as for Hf. Element extraction (Sr, REE) was performed using AG 50W-X8 (200-400 mesh, Bio-Rad) resin and 2.5 N and 4.0 N HCl as eluents. Nd was separated from the REE group using teflon-coated HfEHP and 0.24 N HCl as eluent. Maximum total procedural blanks were < 1 ng for Sr and 50 pg for Nd, and were taken as negligible. The pure element fractions were evaporated using a Re double filament assembly and run in static mode on a Thermo-Finnigan Triton TIMS machine. A mean $^{87}\text{Sr}/^{86}\text{Sr}$ ratio of 0.710284 ± 0.000003 ($n=2$) was determined for NBS987 (Sr) and a mean $^{143}\text{Nd}/^{144}\text{Nd}$ ratio of 0.511851 ± 0.000004

(n = 2) for La Jolla (Nd) international standards during the period of investigation. Within-run mass fractionation was corrected using $^{88}\text{Sr}/^{86}\text{Sr} = 8.3752$, and $^{146}\text{Nd}/^{144}\text{Nd} = 0.7219$, respectively.

Cpx trace elements were analyzed with a LA-ICP-MS system (Laser ablation unit: ESI NWR 193; ICP-MS: Agilent 7500) at the Central Lab for Water, Minerals and Rocks, NAWI Graz, Karl-Franzens-University of Graz and Graz University of Technology. The material was ablated by using a 193 nm laser pulsed at 10 Hz, 50 to 75 μm spot size with an energy of ~ 7 J/cm². Helium was used as carrier gas at ~ 0.7 l/min flow and data were acquired in time resolved mode. For each analysis a 30 second gas blank was obtained for background correction. A laser warmup for 30 seconds was done prior to ablation, then it was active for 60 seconds followed by 60 seconds washout time. The standard glasses NIST610 or NIST612 were routinely analyzed for standardization and drift correction while standards NIST614 and BCR-2 were analyzed as unknowns to monitor the accuracy of the measurements. Both standards could be reproduced within $\pm 10\%$ of the certified values. Silicon or calcium was used as internal standard.

Table 1
Isotopic analyses

Sample	rock type [†]	Ol	Opx	Cpx	Sp	Al ₂ O ₃ [§] [wt%]	Fo ^{††}	Cr# ^{§§}	Re [ppb]	Os [ppb]	Ir [ppb]	Ru [ppb]	Pt [ppb]	Pd [ppb]
<u>Pali Aike</u>														
SA 02	L	64.7	23.7	9.4	2.3	2.51	90.3	25.7	0.015	1.24	2.20	4.36	6.35	2.29
SA 03	H	78.6	19.9	1.2	0.4	0.79	91.6	56.1	0.002	0.87	0.98	2.40	2.16	0.68
SA 11	H	70.5	25.6	2.9	1.0	1.47	92.0	33.2	0.010	3.28	3.12	5.98	3.46	0.66
ELRU 01	H	78.8	18.5	2.3	0.4	1.09	91.5	35.9	0.022	1.68	3.24	5.38	6.28	1.67
ELRU 03	L	68.1	21.1	9.1	1.7	2.23	90.6	16.0	0.014	1.44	2.62	5.72	4.35	2.91
ELRU 04	H	80.6	17.2	2.1	0.1	0.63	91.1	54.4	0.005	3.31	3.35	8.85	8.51	1.03
ELRU 15	H	70.0	27.1	2.0	0.9	1.31	92.1	34.0	0.011	0.71	1.41	3.52	2.20	0.80
ELRU 16	H	71.2	25.5	2.5	0.8	1.08	90.6	54.4	0.004	1.57	2.34	3.31	7.65	0.44
ELRU 19	H	86.5	11.0	1.4	1.1	0.92	92.2	26.4	0.016	1.92	3.17	6.06	3.69	1.28
ELRU 19 ^{###}	H								n.d.	n.d.	2.89	5.68	3.51	1.18
POKA 42	L	67.3	22.5	9.1	1.1	2.14	90.4	20.2	0.050	1.77	2.64	5.24	4.06	2.79
POKA 48	L	64.8	27.1	6.2	1.9	2.26	91.1	15.7	0.031	1.63	1.64	4.74	2.89	1.70
POKA 50	H	75.8	19.0	4.1	1.0	1.34	91.2	33.3	0.034	0.50	1.31	5.26	3.42	1.72
POKA 51	H	75.2	19.9	3.8	1.1	1.35	91.1	25.7	0.037	1.81	2.06	5.93	4.06	2.20
<u>Tres Lagos</u>														
TL 141	H	75.3	19.3	4.7	0.7	1.35	90.8	29.1	0.010	1.28	1.68	3.16	2.85	0.58
TL 142	H	65.8	29.3	3.8	1.1	1.41	90.5	30.0	0.015	0.54	2.41	2.39	2.05	0.37
TL 143	H	73.9	20.8	4.7	0.6	1.40	90.9	21.7	0.006	1.40	n.d.	n.d.	n.d.	n.d.
TL 143 ^{###}	H								0.014	1.83	1.97	2.94	6.01	0.88
TL 145	H	70.4	25.2	3.3	1.1	1.49	90.6	22.4	0.043	1.28	1.91	3.30	3.14	1.15
<u>Gobernador</u>														
<u>Gregores</u>														
DUB 170	L	61.6	24.5	12.3	1.6	2.67	90.3	13.1	0.054	1.08	2.12	4.26	4.66	3.20
DUB 300	L	69.4	24.1	5.7	0.8	1.38	90.9	30.9	0.005	1.28	2.61	4.81	4.90	2.30
DUB 312	L	74.8	17.6	6.7	0.9	1.39	91.1	33.5	0.019	1.00	2.57	5.43	3.14	1.43
DUB 317	L	63.1	26.8	8.7	1.3	2.34	90.8	16.6	0.047	1.67	3.05	5.97	5.16	3.54
<u>Don Camilo</u>														
DC 08	L	58.9	23.9	15.4	1.8	2.74	90.4	14.9	0.054	1.62	2.73	5.42	4.45	2.90
DC 09	L	64.3	26.3	7.6	1.8	2.04	90.6	16.7	0.105	1.69	2.26	5.66	5.65	3.20
DC 18	L	63.8	27.3	7.3	1.5	1.96	90.7	19.4	0.085	1.51	2.14	5.98	5.03	3.28

[†]rock type: L, lherzolite, H, harzburgite; Ol, olivine, Opx, orthopyroxene, Cpx, clinopyroxene, Sp, spinel. ^{**}Re-Os Model ages (T_{MA} and T_{RD}) were calculated using primitive upper mantle values from Meisel et al. (2001): $^{187}\text{Re}/^{188}\text{Os} = 0.4353$ and $^{187}\text{Os}/^{188}\text{Os} = 0.1296$, $\lambda^{187}\text{Re} = 1.666 \cdot 10^{-11}$ from Smoliar et al. (1996); $^{187}\text{Os}/^{188}\text{Os}_{(m)}$ = measured value, $^{187}\text{Os}/^{188}\text{Os}_{(EA)}$ = calculated value at time of eruption (4 Ma); $^{187}\text{Re}/^{188}\text{Os}$ determined using Re and Os concentrations; $T_{RD(EA)}$ = Rhenium depletion age at time of eruption assuming Re = 0; $^{176}\text{Lu}/^{177}\text{Hf}$ and $^{147}\text{Sm}/^{144}\text{Nd}$ determined using Lu and Hf and Sm and Nd concentrations in Cpx from LA-ICP-MS analyses; ϵHf and ϵNd calculated with reference to CHUR values $^{176}\text{Hf}/^{177}\text{Hf} = 0.282785$ and $^{143}\text{Nd}/^{144}\text{Nd} = 0.512638$ (Bouvier et al., 2008); [§]whole rock composition determined by XRF, ^{††}Olivine forsterite content (Fo = Mg/(Mg + Fe²⁺)*100), ^{§§}Cr number in spinel (Cr# = Cr/(Cr + Al)*100), ^{###}duplicate TIMS analyses of sample.

Table 1 cont.

Sample	$^{187}\text{Re}/^{188}\text{Os}$	$^{187}\text{Os}/^{188}\text{Os}_{(m)}$	$^{187}\text{Os}/^{188}\text{Os}_{(EA)}$	$2\sigma \cdot 10^{-6}$	γOs	T_{MA} [Ga]**	$T_{RD(EA)}$ [Ga]**
<i><u>Pali Aike</u></i>							
SA 02	0.057	0.12344	0.12344	6	-4.8	1.0	0.8
SA 03	0.011	0.12661	0.12661	12	-2.3	0.4	0.4
SA 11	0.014	0.11145	0.11145	12	-14.0	2.5	2.5
ELRU 01	0.063	0.11224	0.11224	4	-13.4	2.7	2.3
ELRU 03	0.046	0.12189	0.12189	10	-6.0	1.2	1.1
ELRU 04	0.007	0.12023	0.12023	6	-7.2	1.3	1.3
ELRU 15	0.075	0.12358	0.12358	6	-4.7	1.0	0.8
ELRU 16	0.012	0.12089	0.12089	6	-6.7	1.2	1.2
ELRU 19	0.040	0.11203	0.11203	6	-13.6	n.d.	n.d.
ELRU 19 *)	n.d.	n.d.	n.d.		n.d.	2.6	2.4
POKA 42	0.135	0.12171	0.12170	8	-6.1	1.6	1.1
POKA 48	0.091	0.12487	0.12487	18	-3.7	0.8	0.6
POKA 50	0.327	0.11887	0.11885	10	-8.3	5.7	1.5
POKA 51	0.098	0.11673	0.11672	4	-9.9	2.3	1.7
<i><u>Tres Lagos</u></i>							
TL 141	0.039	0.11599	0.11599	10	-10.5	2.0	1.8
TL 142	0.134	0.12505	0.12504	16	-3.5	0.9	0.6
TL 143	0.022	0.12018	0.12018	16	-7.3	1.4	1.3
TL 143 *)	0.037	0.12014	0.12014	6	-7.3	1.4	1.3
TL 145	0.162	0.11734	0.11733	8	-9.5	2.6	1.7
<i><u>Gobernador Gregores</u></i>							
DUB 170	0.241	0.12632	0.12631	10	-2.5	1.0	0.5
DUB 300	0.021	0.12002	0.12002	4	-7.4	1.4	1.3
DUB 312	0.091	0.12163	0.12162	6	-6.2	1.4	1.1
DUB 317	0.136	0.12112	0.12111	10	-6.6	1.7	1.2
<i><u>Don Camilo</u></i>							
DC 08	0.160	0.13268	0.13267	4	2.4	-0.7	-0.4
DC 09	0.299	0.12272	0.12270	10	-5.3	3.0	0.9
DC 18	0.271	0.12297	0.12295	6	-5.1	2.4	0.9

Table 1 cont.

Sample	$^{176}\text{Lu}/^{177}\text{Hf}$	$^{176}\text{Hf}/^{177}\text{Hf}$	$2\sigma \cdot 10^{-6}$	ϵHf	$^{87}\text{Sr}/^{86}\text{Sr}$	$2\sigma \cdot 10^{-6}$	$^{143}\text{Nd}/^{144}\text{Nd}$	$2\sigma \cdot 10^{-6}$	ϵNd
<i><u>Pali Aike</u></i>									
SA 02	0.0214	0.283128	4	12.14	0.703493	6	0.512965	4	6.38
SA 03	0.0224	0.282999	5	7.58	0.703275	7	0.512911	4	5.33
SA 11	0.0131	0.282566	5	-7.74	0.704442	8	0.512551	4	-1.69
ELRU 01	0.0101	0.282970	16	6.55	0.703900	8	0.512848	4	4.10
ELRU 03	0.0462	0.283436	3	23.01	0.702820	7	0.513181	4	10.59
ELRU 04	0.0057	0.282301	5	-17.10	0.707693	6	0.512088	4	-10.72
ELRU 15	0.0220	0.282788	3	0.10	0.704339	6	0.512556	3	-1.61
ELRU 16	0.0106	0.283136	5	12.40	0.703699	7	0.512853	4	4.20
ELRU 19	0.0265	0.282926	4	5.00	0.703986	7	0.512735	5	1.89
ELRU 19 *)	n.d.	n.d.		n.d.	n.d.		n.d.		n.d.
POKA 42	0.0273	0.283257	4	16.70	0.702931	6	0.513135	4	9.69
POKA 48	0.0136	0.283070	5	10.09	0.703432	7	0.512938	4	5.84
POKA 50	0.0137	0.283154	4	13.06	0.703285	7	0.512896	5	5.03
POKA 51	0.0135	0.283175	4	13.80	0.703314	6	0.512915	4	5.41
<i><u>Tres Lagos</u></i>									
TL 141	0.0470	0.284256	3	52.02	0.702246	4	0.513181	4	10.60
TL 142	0.0600	0.283694	4	32.16	0.703041	5	0.513056	5	8.15
TL 143	0.0309	0.283216	4	15.23	0.702966	4	0.512808	4	3.32
TL 143 *)	n.d.	n.d.		n.d.	n.d.		n.d.		n.d.
TL 145	0.0723	0.283381	5	21.09	0.703204	4	0.513211	4	11.17
<i><u>Gobernador Gregores</u></i>									
DUB 170	n.d.	n.d.		n.d.	n.d.		n.d.		n.d.
DUB 300	0.0361	0.283644	4	30.37	0.703318	4	0.512668	4	0.59
DUB 312	0.0181	0.282948	4	5.78	0.704258	3	0.512675	4	0.72
DUB 317	0.0382	0.283522	4	26.07	0.702617	4	0.513122	4	9.45
<i><u>Don Camilo</u></i>									
DC 08	0.0393	0.283109	4	11.45	0.704045	2	0.512826	4	3.66
DC 09	0.0447	0.283578	4	28.04	0.702777	4	0.513279	4	12.50
DC 18	0.0876	0.283958	4	41.48	0.705876	2	0.512232	4	-7.92

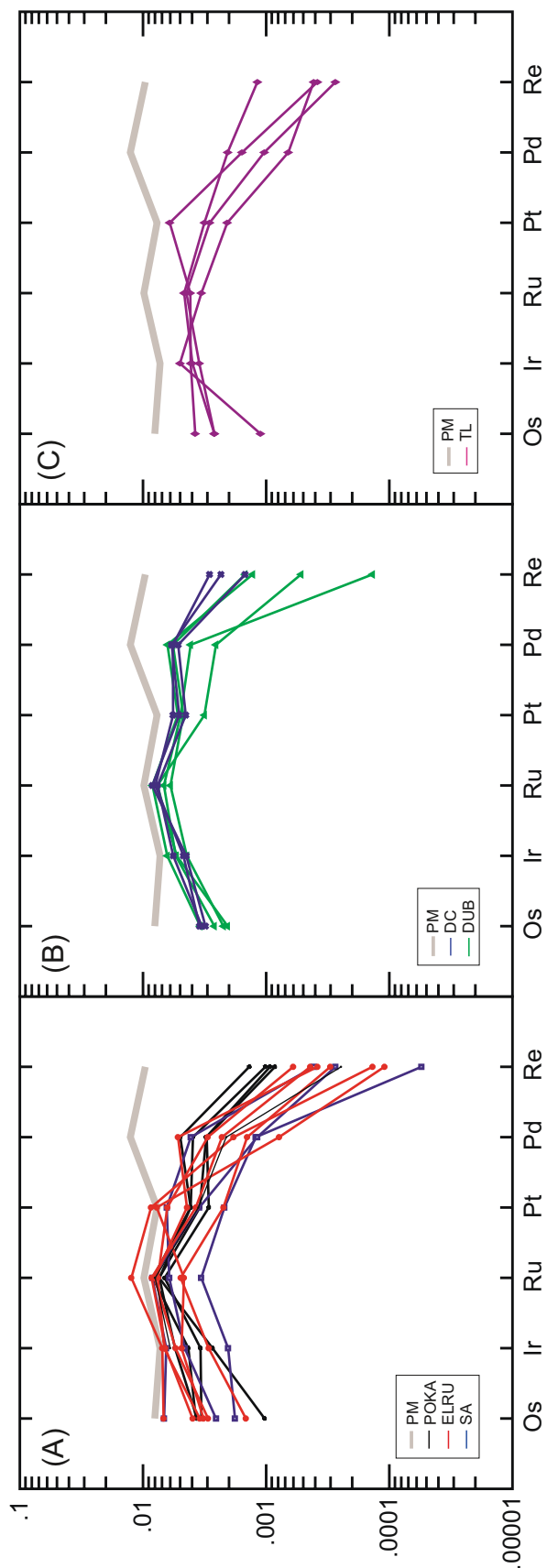


Fig. 1: PGE abundances of Pali Aike (A), Deseado Massif (B) and Tres Lagos (C) sample suits, normalized to CI chondrite after Anders and Grevesse (1989), compared to PM values from Becker et al. (2006)

Table 2

Bulk rock analyzes, major elements from XRF (wt.%), trace elements from XRF (ppm) and ICP-MS (ppm)

	SA 02	SA 03	SA 11	ELRU 01	ELRU 03	ELRU 04	ELRU 15	ELRU 16	ELRU 19	POKA 42	POKA 48	POKA 50
SiO ₂	45.31	44.84	45.06	44.36	44.17	44.34	45.04	44.82	42.50	44.70	45.01	43.86
TiO ₂	0.14	0.05	0.08	0.07	0.08	0.06	0.10	0.05	0.04	0.10	0.10	0.05
Al ₂ O ₃	2.51	0.79	1.47	1.09	2.23	0.63	1.31	1.08	0.92	2.14	2.26	1.34
FeO	7.70	7.41	6.93	7.56	7.88	8.00	7.26	7.85	7.38	8.06	8.46	7.67
MnO	0.12	0.12	0.11	0.12	0.13	0.12	0.11	0.13	0.11	0.13	0.12	0.12
MgO	42.27	47.05	44.81	47.02	42.09	47.39	44.96	44.54	47.78	42.61	42.35	45.08
CaO	2.17	0.53	0.83	0.66	2.09	0.65	0.66	0.86	0.42	2.05	1.47	1.02
Na ₂ O	0.26	0.00	0.06	0.01	0.51	0.00	0.01	-0.01	-0.07	0.12	0.06	0.03
K ₂ O	0.09	0.02	0.04	0.04	0.01	0.03	0.02	0.03	0.00	0.02	0.02	0.02
P ₂ O ₅	0.04	0.01	0.02	0.02	0.03	0.03	0.01	0.02	0.01	0.02	0.01	0.02
Total	100.61	100.83	100.09	100.93	99.88	101.24	100.13	100.11	99.77	100.59	100.49	99.86
Mg#	0.91	0.92	0.92	0.92	0.90	0.91	0.92	0.91	0.92	0.90	0.90	0.91
Cr#	0.10	0.22	0.15	0.16	0.10	0.18	0.15	0.20	0.19	0.10	0.09	0.14
LOI%	-0.38	0.24	-0.30	-0.38	-0.41	-0.43	-0.34	-0.38	-0.40	-0.36	-0.44	-0.42
Zr	16.41	3.63	5.79	6.22	5.04	5.04	4.31	4.05	0.76	9.52	4.19	8.21
Sr	39.81	6.58	20.19	12.47	19.45	18.62	6.57	17.29	n.a.	8.98	4.06	5.66
Rb	1.18	0.21	0.56	0.42	0.24	0.40	0.14	0.38	0.02	0.05	0.29	0.07
Ga	2.40	0.50	1.10	1.00	1.70	0.20	1.40	1.00	1.00	1.80	2.40	1.10
Zn	55	49	44	47	49	45	48	48	43	52	66	50
Ni	2142	2403	2222	2431	2152	2477	2236	2277	2523	2178	2147	2310
Co	110	114	109	116	112	121	112	114	119	113	116	115
Cr	2828	2232	2492	2052	2532	1371	2242	2573	2082	2343	2099	2207
Sc	9.5	6.0	5.4	4.0	10.3	5.9	5.3	6.9	4.5	8.3	7.7	7.2
V	48.4	19.8	27.3	22.5	46.0	17.2	24.0	33.6	18.9	45.3	45.6	28.0
Y	2.04	0.26	0.85	0.66	1.96	0.46	0.41	0.39	0.28	0.88	0.74	0.70
Nb	3.76	0.69	1.76	1.31	0.94	1.45	4.17	1.30	0.16	0.79	0.26	1.04
Mo	0.43	0.29	0.36	0.31	0.40	0.32	0.26	0.31	0.27	0.26	0.26	0.27
Ba	28.66	8.79	15.28	22.80	6.07	8.20	3.83	8.50	7.09	8.80	3.44	4.98
La	1.80	0.45	1.05	0.86	1.29	1.23	0.40	1.28	0.14	0.50	0.24	0.23
Ce	3.67	0.93	2.04	1.59	2.56	2.52	0.88	2.29	0.28	1.17	0.58	0.66
Pr	0.45	0.14	0.26	0.22	0.32	0.34	0.14	0.27	0.07	0.20	0.12	0.15
Nd	1.90	0.60	1.10	0.91	1.38	1.44	0.58	1.09	0.29	0.96	0.59	0.78
Sm	0.43	0.13	0.25	0.20	0.32	0.27	0.14	0.20	0.08	0.26	0.17	0.23
Eu	0.14	0.04	0.08	0.07	0.10	0.07	0.04	0.06	0.03	0.08	0.06	0.07
Gd	0.46	0.14	0.23	0.20	0.36	0.23	0.14	0.20	0.08	0.26	0.19	0.23
Tb	0.07	0.02	0.04	0.03	0.06	0.03	0.02	0.03	0.01	0.04	0.03	0.04
Dy	0.41	0.10	0.20	0.16	0.37	0.14	0.12	0.13	0.09	0.23	0.19	0.20
Ho	0.08	0.02	0.04	0.03	0.08	0.03	0.02	0.02	0.02	0.04	0.04	0.04
Er	0.23	0.05	0.10	0.09	0.23	0.07	0.07	0.06	0.06	0.11	0.10	0.09
Tm	0.03	0.01	0.02	0.01	0.04	0.01	0.01	0.01	0.01	0.02	0.02	0.01
Yb	0.21	0.04	0.10	0.08	0.22	0.06	0.06	0.06	0.06	0.10	0.10	0.08
Lu	0.03	0.00	0.01	0.01	0.03	0.01	0.01	0.01	0.01	0.01	0.01	0.01
Hf	0.44	0.12	0.16	0.19	0.16	0.14	0.17	0.11	0.05	0.27	0.17	0.15
Ta	0.25	0.04	0.23	0.06	0.03	0.07	0.48	0.08	0.04	0.06	0.03	0.09
W	24.52	4.91	64.53	13.93	3.08	23.04	421.85	74.02	37.93	25.85	1.26	57.94
Pb	0.24	0.35	0.68	0.86	0.75	0.38	0.25	0.28	0.16	0.21	0.10	0.10
Th	0.25	0.08	0.14	0.12	0.17	0.14	0.06	0.13	0.04	0.07	0.04	0.04
U	0.07	0.02	0.04	0.04	0.06	0.04	0.02	0.04	0.01	0.02	0.01	0.02

n.a. - not analysed; bdl - blow detection limit

Table 2 cont.

	POKA 51	TL 141	TL 142	TL 143	TL 145	DUB 170	DUB 300	DUB 312	DUB 317	DC 08	DC 09	DC 18
SiO ₂	43.97	44.44	45.37	44.43	44.71	45.13	45.85	43.88	45.55	45.02	44.65	44.73
TiO ₂	0.07	0.05	0.05	0.04	0.04	0.09	0.03	0.08	0.08	0.08	0.08	0.04
Al ₂ O ₃	1.35	1.35	1.41	1.40	1.49	2.67	1.38	1.39	2.34	2.74	2.04	1.96
FeO	8.14	8.05	8.11	7.96	8.18	7.81	7.64	7.85	7.58	7.44	7.99	7.75
MnO	0.12	0.13	0.13	0.12	0.13	0.13	0.12	0.13	0.12	0.12	0.13	0.12
MgO	44.85	45.48	43.71	44.80	44.38	41.27	44.54	44.22	42.00	39.66	41.97	42.16
CaO	0.97	1.17	1.11	1.15	0.88	2.81	1.50	1.48	2.10	3.44	1.76	1.76
Na ₂ O	0.02	0.00	0.00	0.00	0.00	0.04	0.00	0.06	0.05	0.11	0.03	0.01
K ₂ O	0.02	0.00	0.01	0.00	0.00	0.02	0.01	0.01	0.00	0.07	0.01	0.01
P ₂ O ₅	0.01	0.01	0.01	0.01	0.01	0.02	0.02	0.03	0.01	0.02	0.03	0.07
Total	100.17	100.69	100.56	100.56	100.43	99.99	101.09	99.87	100.48	99.54	99.57	99.49
Mg#	0.91	0.91	0.91	0.91	0.91	0.90	0.91	0.91	0.91	0.90	0.90	0.91
Cr#	0.14	0.17	0.15	0.14	0.13	0.12	0.14	0.17	0.10	0.08	0.14	14.17
LOI%	-0.45	-0.36	-0.36	-0.40	-0.42	-0.18	-0.08	-0.17	-0.23	0.02	0.91	-0.18
Zr	8.17	1.64	3.15	2.44	1.29	4.96	1.81	4.14	2.58	7	8	7
Sr	7.32	0.98	0.16	0.14	<i>n.a.</i>	9.42	7.57	29.08	3.24	6	19	17
Rb	0.08	<i>bdl</i>	0.10	<i>bdl</i>	<i>bdl</i>	0.28	0.07	0.06	<i>bdl</i>	<2	2	<2
Ga	0.80	1.40	1.20	1.30	1.60	4.8	0.90	1.20	1.80	6.90	<2	3.70
Zn	60	48	45	47	48	71.7	45	51	45	46	54	52
Ni	2326	2185	2160	2311	2177	2583.3	2233	2250	2071	2334	2022	2133
Co	115	116	113	117	114	189.2	112	116	110	125	111	119
Cr	2169	2792	2394	2194	2234	3424.1	2173	2794	2560	2440	3259	3173
Sc	5.9	8.2	8.2	7.0	8.5	11.6	7.6	6.6	8.4	8.4	10.6	10.2
V	27.0	32.3	28.9	26.5	35.7	75.6	31.8	31.5	45.7	58.4	50.4	41.7
Y	0.68	0.57	0.60	0.49	0.45	2.08	0.29	1.05	1.55	1.45	2.02	1.06
Nb	0.61	0.02	0.27	0.02	0.11	1.90	0.25	0.54	0.17	3	3	2
Mo	0.26	0.26	0.27	0.26	0.28	0.26	0.28	0.32	0.25	<i>n.a.</i>	<i>n.a.</i>	<i>n.a.</i>
Ba	2.20	<i>b. dl</i>	2.31	0.49	5.20	4.86	0.73	4.20	10.80	38	2	14
La	0.34	0.08	0.18	0.04	0.16	0.61	0.38	1.42	0.07	0.29	0.39	0.24
Ce	0.82	0.19	0.38	0.17	0.26	1.36	0.56	3.36	0.30	0.67	0.87	0.56
Pr	0.15	0.06	0.08	0.06	0.06	0.20	0.09	0.40	0.08	0.09	0.12	0.07
Nd	0.69	0.31	0.34	0.34	0.26	0.92	0.39	1.62	0.45	0.53	0.69	0.42
Sm	0.19	0.09	0.09	0.10	0.06	0.26	0.08	0.29	0.16	0.15	0.21	0.10
Eu	0.06	0.03	0.03	0.03	0.02	0.09	0.03	0.09	0.06	0.06	0.08	0.04
Gd	0.20	0.11	0.11	0.11	0.08	0.31	0.10	0.29	0.20	0.22	0.30	0.14
Tb	0.03	0.02	0.02	0.02	0.02	0.06	0.01	0.04	0.04	0.04	0.05	0.02
Dy	0.18	0.12	0.12	0.12	0.10	0.40	0.08	0.23	0.28	0.26	0.37	0.17
Ho	0.03	0.03	0.03	0.03	0.02	0.09	0.02	0.04	0.06	0.06	0.08	0.04
Er	0.09	0.09	0.09	0.08	0.08	0.26	0.06	0.13	0.19	0.19	0.26	0.15
Tm	0.01	0.01	0.02	0.01	0.01	0.04	0.01	0.02	0.03	0.03	0.04	0.02
Yb	0.09	0.10	0.11	0.09	0.10	0.26	0.07	0.11	0.20	0.22	0.29	0.18
Lu	0.01	0.02	0.02	0.01	0.02	0.04	0.01	0.02	0.03	0.04	0.05	0.03
Hf	0.21	0.07	0.09	0.10	0.06	0.42	0.07	0.13	0.11	<i>n.a.</i>	<i>n.a.</i>	<i>n.a.</i>
Ta	0.04	0.00	0.06	0.05	0.10	0.57	0.02	0.03	0.41	<i>n.a.</i>	<i>n.a.</i>	<i>n.a.</i>
W	65.45	14.06	0.91	0.97	5.51	9.90	53.78	72.56	618.10	<i>n.a.</i>	<i>n.a.</i>	<i>n.a.</i>
Pb	0.08	0.83	0.58	0.14	0.57	0.77	0.29	0.61	0.42	<i>n.a.</i>	<i>n.a.</i>	<i>n.a.</i>
Th	0.05	0.04	0.08	0.03	0.05	0.13	0.09	0.09	0.03	0.04	0.07	0.07
U	0.01	0.01	0.02	0.01	0.02	0.05	0.04	0.05	0.02	<i>n.a.</i>	<i>n.a.</i>	<i>n.a.</i>

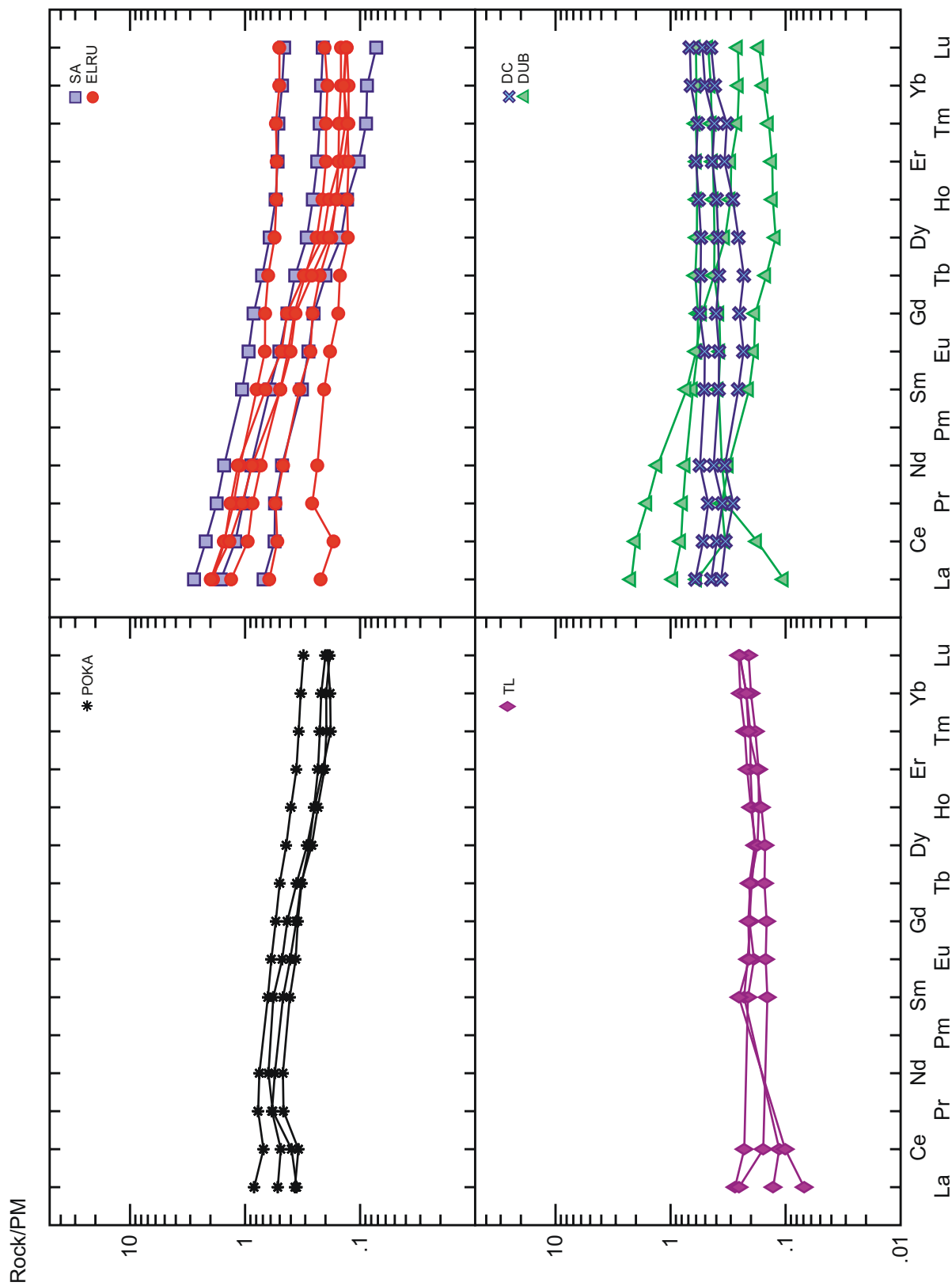


Fig.2: Bulk rock rare earth element patterns normalized to primitive mantle (PM) values from McDonough and Sun, 1995. Legend: POKA, Potrok Aike; SA, Salsa; ELRU, El Ruido; TL, Tres Lagos; DC, Don Camilo; DUB, Gobernador Gregores

Table 3

Clinopyroxene major element microprobe analyzes (wt.%) and LA-ICP-MS trace elements (ppm)

	SA 02	SA 03	SA 11	ELRU 01	ELRU 03	ELRU 04	ELRU 15	ELRU 16	ELRU 19
SiO ₂	52.26	53.43	53.28	52.98	52.35	53.52	52.84	53.30	52.14
TiO ₂	0.52	0.49	0.18	0.21	0.42	0.12	0.16	0.04	0.43
Al ₂ O ₃	5.41	2.62	4.81	4.33	6.11	2.25	4.60	2.71	4.25
Cr ₂ O ₃	1.12	1.62	1.48	1.39	1.11	0.89	1.39	1.04	1.09
FeO [†]	2.78	2.80	2.29	2.43	2.16	2.41	2.31	2.55	1.77
MnO	0.09	0.09	0.08	0.09	0.08	0.09	0.09	0.09	0.05
MgO	15.65	17.93	16.18	16.38	14.87	17.74	16.37	17.27	15.76
CaO	20.55	20.14	20.30	20.72	21.32	22.39	20.39	21.91	23.62
NiO	0.05	0.06	n.a.	0.05	0.04	0.07	0.06	0.05	0.03
Na ₂ O	1.56	0.94	1.51	1.32	1.65	0.56	1.55	0.70	0.89
Total	99.99	100.11	100.12	99.90	100.10	100.04	99.76	99.67	100.06
Mg#*100	90.95	91.95	92.65	92.31	92.48	92.91	92.67	92.36	94.07
En	48.86	52.69	50.40	50.12	47.29	50.35	50.57	50.06	46.68
Fs	5.02	4.77	4.15	4.33	3.99	3.99	4.16	4.28	3.03
Wo	46.12	42.55	45.45	45.55	48.72	45.67	45.27	45.66	50.29
Cr	7325	9347	9020	8861	7896	4986	8776	6808	8856
Co	20.5	23.5	20.4	22.7	20.3	24.8	21.6	23.9	18.9
Ni	372	402	384	420	331	441	400	430	325
Zn	10.3	11.6	8.7	10.0	15.9	10.5	9.4	10.1	10.0
Cu	1.51	1.46	1.73	2.00	1.18	2.33	1.61	1.81	0.57
V	235	155	209	232	254	169	207	197	283
Sr	80.9	45.7	76.2	76.8	55.7	177.3	90.7	124.0	16.4
Y	10.95	1.95	9.59	9.42	15.20	4.20	8.22	2.94	12.61
Zr	67.2	11.0	32.0	65.8	19.2	44.5	24.3	32.7	18.3
La	2.146	0.674	0.815	2.665	1.658	4.508	1.467	7.163	0.485
Ce	7.450	2.740	4.545	6.070	4.078	16.475	6.803	17.885	1.906
Pr	1.195	0.485	0.942	0.897	0.606	3.213	1.245	2.186	0.428
Nd	5.958	2.503	5.498	4.760	3.258	17.653	6.288	8.800	3.555
Sm	1.803	0.679	1.924	1.558	1.321	3.305	1.751	1.649	2.014
Eu	0.681	0.251	0.692	0.583	0.574	0.916	0.627	0.486	0.732
Gd	2.064	0.650	2.201	1.838	2.033	2.045	1.905	1.318	2.545
Tb	0.343	0.086	0.339	0.310	0.392	0.251	0.288	0.156	0.409
Dy	2.246	0.480	2.096	1.916	2.760	1.131	1.697	0.744	2.618
Ho	0.450	0.081	0.401	0.397	0.617	0.189	0.344	0.123	0.523
Er	1.305	0.180	1.081	1.102	1.727	0.422	0.927	0.343	1.450
Tm	0.168	0.020	0.135	0.145	0.251	0.050	0.117	0.042	0.179
Yb	1.112	0.131	0.842	0.886	1.611	0.354	0.707	0.301	1.116
Lu	0.150	0.019	0.109	0.123	0.229	0.053	0.107	0.050	0.157
Hf	1.111	0.128	1.178	1.921	0.701	1.338	0.692	0.668	0.841

[†]Fe total as FeO; n.a. - not analysed

Table 3 cont.

	POKA 42	POKA 48	POKA 50	POKA 51	TL 141		TL 142		TL 143		TL 145	
					core	rim	core	rim	core	rim	core	rim
SiO ₂	52.35	52.48	53.10	52.60	52.20	52.50	52.54	52.94	52.51	53.03	52.51	52.96
TiO ₂	0.38	0.40	0.19	0.27	0.36	0.35	0.26	0.24	0.20	0.19	0.28	0.22
Al ₂ O ₃	5.78	6.25	4.80	5.17	4.86	4.24	4.52	3.73	4.96	4.01	4.21	3.41
Cr ₂ O ₃	1.01	0.99	1.29	1.26	1.43	1.28	1.38	1.04	1.34	1.01	0.94	0.80
FeO*	2.83	2.73	2.54	2.55	2.12	2.20	2.14	2.29	2.02	2.10	2.11	2.23
MnO	0.09	0.09	0.08	0.08	0.07	0.07	0.06	0.06	0.06	0.07	0.08	0.07
MgO	15.54	15.48	15.85	15.72	15.44	15.78	15.45	16.08	15.25	15.99	15.95	16.49
CaO	20.40	19.80	20.33	20.35	22.25	22.63	22.30	22.55	22.25	22.56	22.94	23.15
NiO	0.09	n.a.	0.05	0.04	0.04	0.05	0.04	0.05	0.05	0.05	0.03	0.05
Na ₂ O	1.66	1.73	1.74	1.65	1.29	1.07	1.22	0.92	1.39	1.15	0.96	0.76
Total	100.14	99.95	99.97	99.71	100.05	100.18	99.92	99.89	100.01	100.16	100.02	100.16
Mg#*100	90.74	90.99	91.76	91.67	92.86	92.73	92.77	92.62	93.09	93.13	93.08	92.95
En	48.81	49.46	49.63	49.39	47.28	47.35	47.22	47.85	47.05	47.83	47.38	47.91
Fs	5.13	5.05	4.61	4.64	3.76	3.83	3.79	3.92	3.60	3.65	3.65	3.75
Wo	46.05	45.48	45.76	45.97	48.96	48.82	49.00	48.23	49.35	48.52	48.97	48.34
Cr	6475	6194	8014	8012	10107		9499		9192		7941	
Co	22.6	22.6	20.7	21.8	20.1		20.1		20.6		22.4	
Ni	390	382	363	380	313		325		335		347	
Zn	10.9	12.0	10.0	12.0	13.3		13.0		16.6		22.5	
Cu	2.07	1.91	0.97	2.14	3.04		1.19		0.94		1.05	
V	257	278	240	241	280		224		253		275	
Sr	61.1	42.6	86.0	84.9	64.9		20.5		46.4		10.5	
Y	12.49	8.25	9.54	9.46	10.30		10.01		9.02		10.31	
Zr	36.5	46.9	94.2	75.4	16.3		10.4		22.9		7.1	
La	1.791	0.665	1.066	2.272	0.865		0.486		0.543		0.141	
Ce	4.695	2.976	5.835	8.080	3.498		1.707		2.666		0.583	
Pr	0.763	0.619	1.356	1.408	0.698		0.331		0.632		0.132	
Nd	4.290	3.810	8.670	7.793	4.085		1.976		4.325		0.982	
Sm	1.524	1.498	3.038	2.508	1.425		0.759		1.547		0.610	
Eu	0.581	0.551	1.053	0.850	0.530		0.319		0.512		0.264	
Gd	2.140	1.870	2.995	2.558	1.823		1.230		1.680		1.053	
Tb	0.377	0.304	0.435	0.394	0.295		0.240		0.270		0.224	
Dy	2.518	1.857	2.410	2.231	1.952		1.722		1.706		1.803	
Ho	0.519	0.359	0.426	0.396	0.416		0.405		0.352		0.403	
Er	1.501	1.003	1.106	1.085	1.227		1.222		1.045		1.335	
Tm	0.196	0.124	0.129	0.136	0.164		0.177		0.145		0.190	
Yb	1.239	0.764	0.851	0.868	1.166		1.143		0.982		1.241	
Lu	0.176	0.108	0.114	0.112	0.177		0.168		0.143		0.180	
Hf	0.978	1.295	1.327	1.494	0.579		0.394		0.678		0.346	

Table 3 cont.

	DUB 170		DUB 300	DUB 312	DUB 317		DC 08		DC 09		DC 18
	core	rim			core	rim	core	rim	core	rim	
SiO ₂	51.27	51.50	53.00	52.83	52.19	52.29	51.90	52.30	52.52	52.43	52.92
TiO ₂	0.46	0.46	0.09	0.41	0.39	0.44	0.49	0.52	0.43	0.40	0.23
Al ₂ O ₃	5.94	5.08	4.07	5.21	5.35	4.79	5.93	5.33	5.25	5.65	4.24
Cr ₂ O ₃	0.87	0.71	1.15	1.56	1.11	1.10	0.96	0.89	0.84	1.10	0.82
FeO*	2.15	2.20	2.47	2.18	2.11	2.38	2.35	2.35	2.45	2.40	2.30
MnO	0.09	0.08	0.08	0.09	0.07	0.07	0.08	0.08	0.07	0.07	0.06
MgO	15.06	15.51	16.55	15.04	15.29	16.33	15.25	15.64	16.19	15.41	16.12
CaO	21.45	21.68	21.68	20.32	22.53	21.68	21.67	21.82	20.99	21.23	22.07
NiO	0.02	0.06	0.05	0.04	n.a.	n.a.	0.03	0.04	0.04	0.04	0.05
Na ₂ O	1.79	1.60	1.07	2.05	1.01	0.89	1.30	1.28	1.25	1.43	1.17
Total	99.14	98.91	100.20	99.74	100.03	99.97	99.97	100.26	100.03	100.16	99.99
Mg#*100	92.57	92.61	92.28	92.50	92.82	92.46	92.04	92.22	92.18	91.96	92.59
En	47.44	47.89	49.32	48.64	46.76	49.07	47.38	47.84	49.53	48.08	48.39
Fs	3.99	3.99	4.26	4.12	3.73	4.14	4.24	4.17	4.33	4.32	3.98
Wo	48.57	48.12	46.42	47.24	49.51	46.80	48.38	47.99	46.14	47.60	47.63
Cr	n.a.		7563	9957	7281		n.a.		8422		n.a.
Co	n.a.		22.5	19.1	21.7		n.a.		18.9		n.a.
Ni	n.a.		392	325	350		n.a.		326		n.a.
Zn	n.a.		9.9	8.7	19.4		n.a.		8.0		n.a.
Cu	n.a.		1.64	4.06	1.25		n.a.		1.09		n.a.
V	n.a.		224	260	247		n.a.		260		n.a.
Sr	n.a.		84.5	101.8	40.9		49.6		49.2		52.0
Y	n.a.		4.07	10.47	13.77		16.95		14.38		12.45
Zr	n.a.		11.5	30.1	20.1		20.2		22.0		11.7
La	n.a.		5.730	3.990	0.639		1.162		0.672		1.062
Ce	n.a.		6.610	7.005	2.980		3.354		2.519		3.176
Pr	n.a.		0.679	0.921	0.579		0.663		0.501		0.589
Nd	n.a.		2.795	4.985	3.313		4.190		3.153		3.503
Sm	n.a.		0.628	1.634	1.348		1.608		1.277		1.065
Eu	n.a.		0.250	0.668	0.545		0.648		0.543		0.368
Gd	n.a.		0.647	1.959	1.973		2.233		1.936		1.346
Tb	n.a.		0.116	0.356	0.364		0.416		0.375		0.250
Dy	n.a.		0.750	2.144	2.583		3.006		2.638		2.048
Ho	n.a.		0.160	0.464	0.560		0.671		0.569		0.477
Er	n.a.		0.483	1.148	1.664		1.897		1.661		1.409
Tm	n.a.		0.070	0.156	0.231		0.264		0.237		0.216
Yb	n.a.		0.515	1.024	1.485		1.871		1.560		1.516
Lu	n.a.		0.077	0.139	0.214		0.231		0.212		0.226
Hf	n.a.		0.332	1.064	0.749		0.835		0.673		0.367

Table 4
Sulfide occurrences in analyzed mantle xenoliths

Sample	enclosed	comment	interstitial	comment
<i>Pali Aike</i>				
SA 02	✓	inclusion in ol, trails in ol	✓✓	around spongy cpx, in glass
SA 03	n.f.		✓	intergranular altered
SA 11	✓✓	inclusions in ol, trails in ol	✓	in HB MI
ELRU 01	✓	inclusion in ol	✓	in HB MI
ELRU 03	✓	inclusion in ol	✓✓	in HB MI, in MP
ELRU 04	✓	around ol inclusion in opx	n.f.	
ELRU 15	✓	inclusion in ol	✓	in HB MI
ELRU 16	n.f.		n.f.	
ELRU 19	✓	inclusion in ol	n.f.	
POKA 42	✓✓	inclusions in ol, trails in ol	✓✓	intergranular and in MP
POKA 48	✓✓	inclusions in ol	✓✓	intergranular and with spongy cpx
POKA 50	n.i.		n.i.	
POKA 51	✓	inclusion in ol	✓✓	intergranular and with spongy cpx
<i>Tres Lagos</i>				
TL 141	✓✓	inclusions ol, trails in opx	✓	intergranular, altered
TL 142	✓	inclusions in ol and opx, trails	✓✓	intergranular, altered
TL 143	n.f.		n.f.	
TL 145	✓✓	inclusion in ol, trails in ol	n.f.	
<i>Gobernador Gregores</i>				
DUB 170	n.i.		n.i.	
DUB 300	✓✓	large inclusions in opx, trails	✓	in HB MI
DUB 312	n.i.		n.i.	
DUB 317	✓✓	inclusion in ol, trails in cpx	✓	in HB MI
<i>Don Camilo</i>				
DC 08	✓	inclusion in ol, trails in ol and opx	✓✓✓	intergranular with serpentized glass
DC 09	n.i.		n.i.	
DC 18	✓✓	inclusion in ol and sp	✓	elongated intergranular, partially altered

✓, rare (≤ 2 per thin section); ✓✓, common (> 2 per thin section); ✓✓✓, very common; n.f., none found; n.i., not investigated; HB, host basalt; MP, melt pocket; MI, melt infiltration.

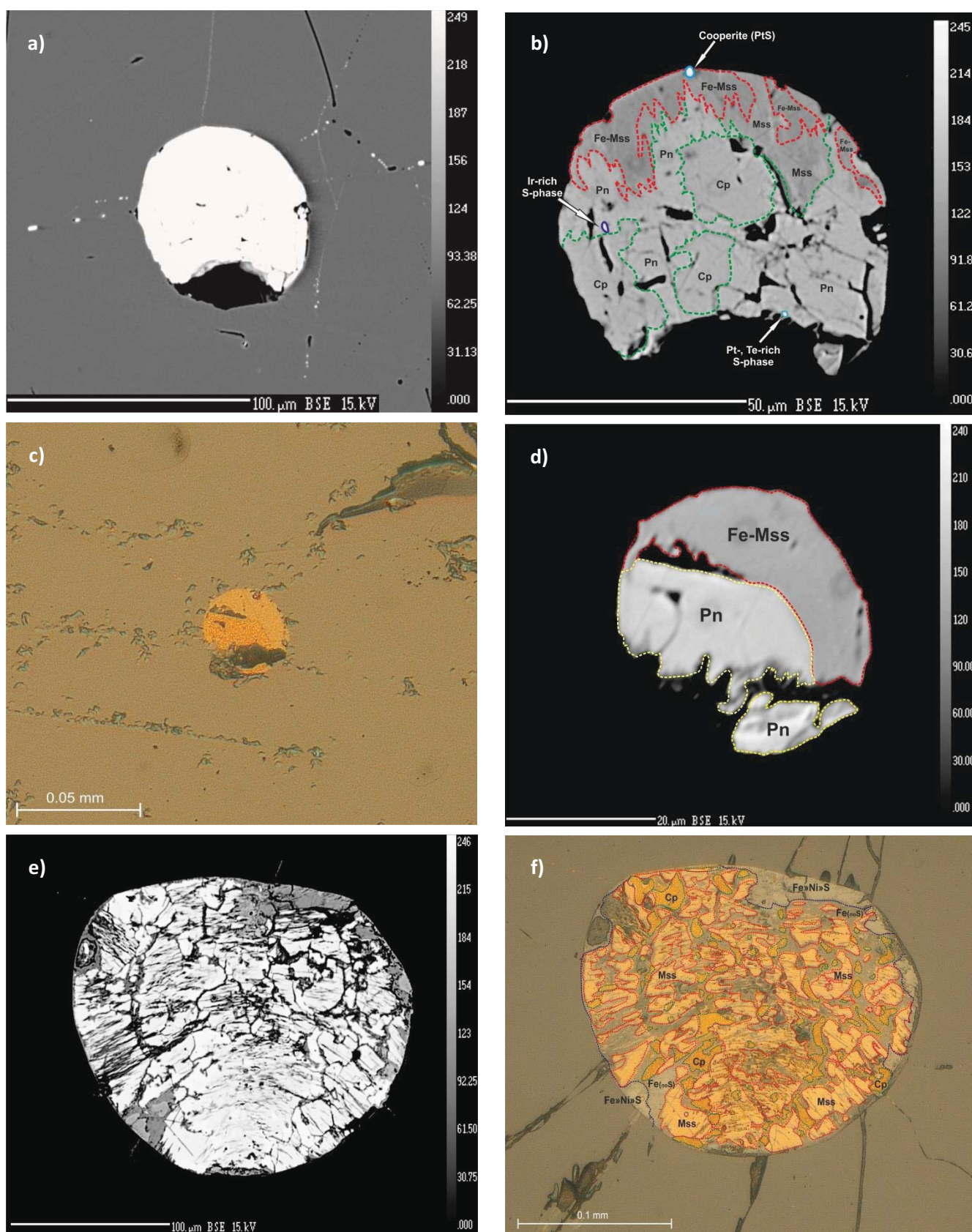


Fig.3: Backscattered-electron images (BSE) and photomicrographs of southern Patagonian mantle xenoliths displaying sulphide occurrence and mineralogy. a-f primary sulphides; a) and b) sample SA11, BSE of primary spherical sulphide inclusion and trails in ol. c) photomicrograph in reflected light and d) BSE of 2-phase round sulphide inclusion in Ol of sample TL145. e) and d) sample DUB300: BSE and photomicrograph in reflected light, respectively, of multi-phase round sulphide inclusion in opx. Note sulphide alteration around the edges.

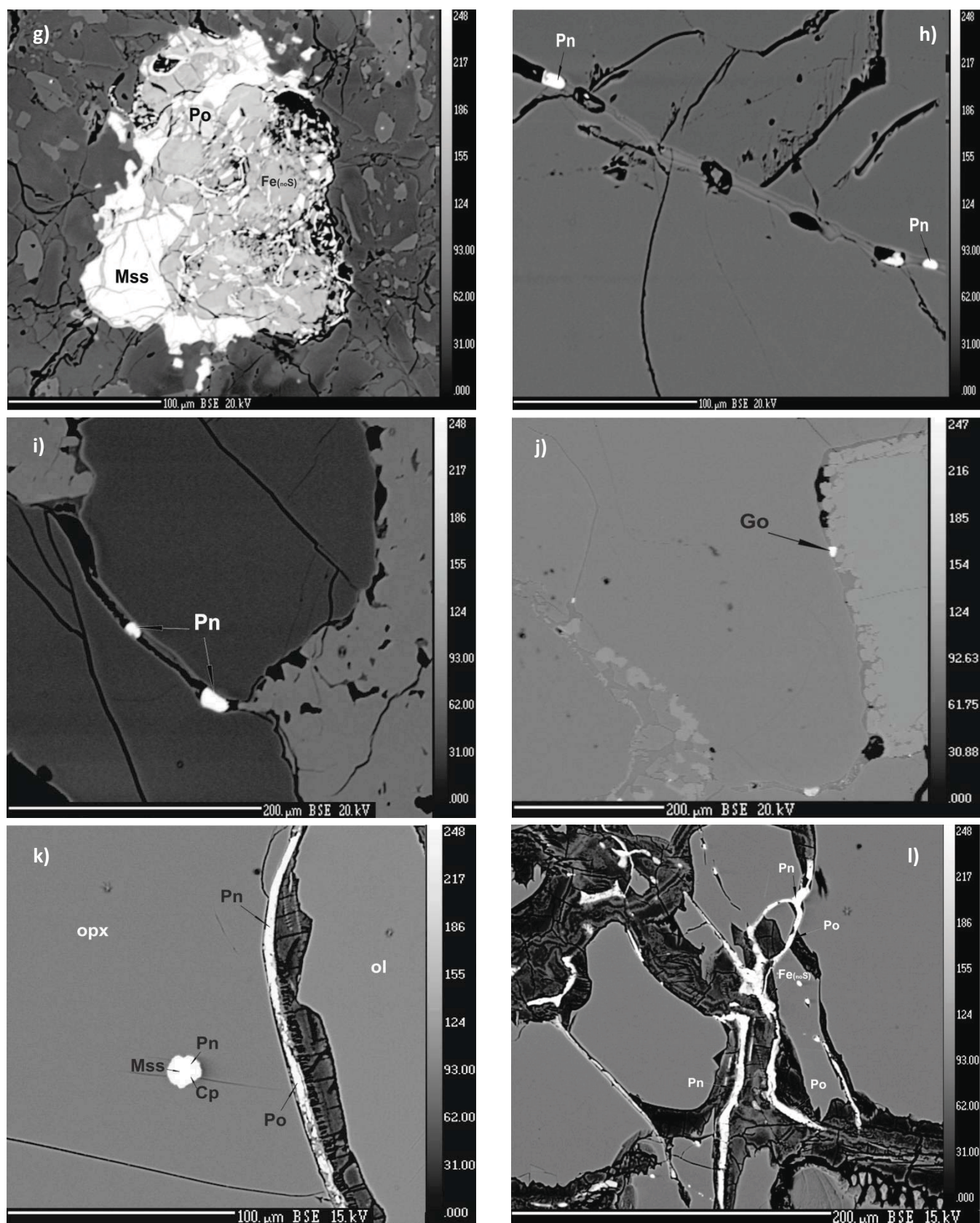


Fig.3. cont.: g-l BSE images of secondary sulphides. g) and h) sample POKA42; g) irregular shaped, strongly altered sulphide in melt pocket. h) secondary sulphides (Pn) in melt infiltration along cracks in ol . i) elongated round intergranular sulphides formed of Pn (POKA48). j) sample SA02: round godlevskite in spongy rim of cpx. k) (primary) 3-phase round sulphide inclusion in opx (left). k) (right) and l) elongated intergranular Pn, Po and alteration product of sulphide together with serpentinized glass in sample DC08. Mss, monosulfide solid solution; Fe-Mss, iron rich Mss; Pn, pentlandite; Cp, chalcopyrite; Po, pyrrhotite; Go, godlevskite.

REFERENCES CITED

- Anders, E., and Grevesse, N., 1989, Abundances of the elements: Meteoritic and solar: *Geochimica et Cosmochimica Acta*, v. 59, p. 197-214.
- Becker, H., Horan, M.F., Walker, R.J., Gao, S., Lorand, J.-P., and Rudnick, R.L., 2006, Highly siderophile element composition of the Earth's primitive upper mantle: Constraints from new data on peridotite massifs and xenoliths: *Geochimica et Cosmochimica Acta*, v. 70, p. 4528-4550.
- Birck, J.L., Roy Barman, M., and Capmas, F., 1997, Re-Os isotopic measurements at the femtomole level in natural samples: *Journal of Geostandards and Geoanalysis*, v. 20, p. 19-27.
- Bizimis, M., Salters, V.J.M., Garcia, M.O., and Norman, M.D., 2013, The composition and distribution of rejuvenated component across the Hawaiian plume: Hf-Nd-Sr-Pb isotope systematics of Kula lavas and pyroxenite xenoliths: *Geochemistry, Geophysics, Geosystems*, v. 14, p. 4458-4478.
- Bouvier, A., Vervoort, J.D., and Patchett, P.J., 2008, The Lu-Hf and Sm-Nd isotopic composition of CHUR: constraints from unequilibrated chondrites and implications for the bulk composition of terrestrial planets: *Earth and Planetary Science Letters*, v. 273, p. 48-57.
- Cohen, A.S., and Waters, F.G., 1996, Separation of osmium from geological materials by solvent extraction for analysis by thermal ionization mass spectrometry: *Analytica Chimica Acta*, v. 332, p. 269-275.
- Creaser, R.A., Papanastassiou, D.A., and Wasserburg, G.J., 1991, Negative thermal ion mass spectrometry of osmium, rhenium, and iridium: *Geochimica et Cosmochimica Acta*, v. 55, p. 397-401.
- McDonough, W.F., and Sun, S., 1995, The composition of the Earth: *Chemical Geology*, v. 120, p. 223-253.

- Meisel, T., Walker, R.J., Irving, A.J., and Lorand, J.-P., 2001, Osmium isotopic compositions of mantle xenoliths: A global perspective: *Geochimica et Cosmochimica Acta*, v. 65, p. 1311-1323.
- Munker, C., Weyer, S., Scherer, E., and Mezger, K., 2001, Separation of high field strength elements (Nb, Ta, Zr, Hf) and Lu from rock samples for MC-ICPMS measurements: *Geochemistry, Geophysics, Geosystems*, v. 2.
- Shirey S.B., and Walker, R.J., 1995, Carius tube digestion for low blank rhenium-osmium analysis: *Analytical Chemistry*, v. 67 (34), p. 2136-2141.
- Shirey S.B., and Walker, R.J., 1998, The Re-Os isotope system in cosmochemistry and high-temperature geochemistry: *Annual Review of Earth and Planetary Sciences*, v. 26, p. 423-500.
- Smoliar, M.I., Walker, R.J., and Morgan, J.W., 1996, Re-Os ages of Group IIA, IIIA, IVA and IVB iron meteorites: *Science*, v. 271, p. 1099-1102.
- Völkening, J., Walczyk, T., and Heumann, K.G., 1991, Osmium isotope ratio determinations by negative thermal ionization mass spectrometry: *International Journal of Mass Spectrometry and Ion Processes*, v. 105, p. 147-159.

CHAPTER I — South Patagonia

Additional Data

Table AD1
Modal compositions calculated using bulk rock and mineral data

	SA01	SA02	SA03	SA04	SA09	SA10	SA11	ELRU1	ELRU2	ELRU3	ELRU4	ELRU5	ELRU6	ELRU7	ELRU9
Ol	64.9	64.7	78.6	61.6	63.9	65.7	70.5	78.8	65.1	68.1	80.6	55.8	64.2	58.9	50.8
Opx	19.5	23.7	19.9	18.3	16.0	22.0	25.6	18.5	10.9	21.1	17.2	31.6	17.9	27.7	45.2
Cpx	10.7	9.4	1.2	11.0	12.1	10.2	2.9	2.3	14.3	9.1	2.1	4.4	10.5	0.8	1.1
Sp	-0.1	2.3	0.4	0.4	0.2	2.0	1.0	0.4	0.1	1.7	0.1	1.7	0.2	0.8	0.1
Gt/Gt-Rikt	5.0	-	-	8.7	7.8	-	-	-	9.6	-	-	6.0	7.2	11.4	2.8
Total	100	100	100	100	100	100	100	100	100	100	100	100	100	100	100
rock type	L	L	H	L	L	L	H	H	L	L	H	H	L	H	H
ELRU10 ELRU11 ELRU13 ELRU15 ELRU16 ELRU19 POKA40 POKA41 POKA42 POKA44 POKA45 POKA48 POKA50 POKA51 DUB170															
Ol	51.1	59.7	96.1	70.0	71.2	86.5	65.6	72.0	67.3	66.3	67.4	64.8	75.8	75.2	61.6
Opx	46.6	35.2	-	27.1	25.5	11.0	25.0	21.8	22.5	23.2	22.3	27.1	19.0	19.9	24.5
Cpx	0.7	2.3	1.5	2.0	2.5	1.4	8.5	5.7	9.1	8.9	9.1	6.2	4.1	3.8	12.3
Sp	1.6	2.8	2.4	0.9	0.8	1.1	0.9	0.4	1.1	1.6	1.3	1.9	1.0	1.1	1.6
Gt/Gt-Rikt	-	-	-	-	-	-	-	-	-	-	-	-	-	-	-
Total	100	100	100	100	100	100	100	100	100	100	100	100	100	100	100
rock type	H	H	D	H	H	H	L	L	L	L	L	L	H	H	L
DUB300 DUB301 DUB311 DUB312 DUB317 DC08 DC09 DC18 TL141 TL142 TL143 TL145															
Ol	69.4	64.6	72.0	74.8	63.1	58.9	64.3	63.8	75.3	65.8	73.9	70.4			
Opx	24.1	26.0	15.7	17.6	26.8	23.9	26.3	27.3	19.3	29.3	20.8	25.2			
Cpx	5.7	8.7	10.9	6.7	8.7	15.4	7.6	7.3	4.7	3.8	4.7	3.3			
Sp	0.8	0.7	1.3	0.9	1.3	1.8	1.8	1.5	0.7	1.1	0.6	1.1			
Gt/Gt-Rikt	-	-	-	-	-	-	-	-	-	-	-	-			
Total	100	100	100	100	100	100	100	100	100	100	100	100			
rock type	L	L	L	L	L	L	L	L	H	H	H	H			

Ol - olivine; Opx - orthopyroxene; Cpx - clinopyroxene;
Sp - spinel; Gt - garnet; Gt-Rikt - relicts of garnet;
L - lherzolitite; H - harzburgite; D - dunite

Table AD2

Bulk rock analyzes, major elements from XRF (wt.%), trace elements from XRF (ppm) and ICP-MS (ppm)

	SA01	SA04	SA08	SA09	SA10	ELRU2	ELRU6	ELRU9	ELRU10	ELRU11	ELRU12	ELRU13
SiO ₂	45.45	44.92	45.52	44.47	44.40	44.81	44.91	47.64	47.87	45.24	45.05	40.34
TiO ₂	0.10	0.15	0.22	0.14	0.10	0.13	0.11	0.19	0.24	0.14	0.13	0.04
Al ₂ O ₃	2.44	3.54	3.28	3.14	2.36	3.40	3.07	2.49	2.03	2.74	2.24	0.75
FeO*	7.92	8.36	9.47	8.40	8.31	8.45	8.14	8.16	8.48	9.11	8.50	8.52
MnO	0.12	0.14	0.13	0.13	0.13	0.14	0.13	0.12	0.11	0.13	0.13	0.14
MgO	41.55	39.90	39.58	40.09	41.56	40.19	40.89	40.64	40.54	41.61	42.35	49.01
CaO	2.62	2.79	1.15	2.90	2.28	3.53	2.65	0.77	0.54	0.76	1.36	0.24
Na ₂ O	0.21	0.25	0.13	0.22	0.18	0.23	0.18	0.03	0.09	0.05	0.18	0.00
K ₂ O	0.02	0.04	0.05	0.01	0.05	0.02	0.01	0.06	0.08	0.02	0.09	0.01
P ₂ O ₅	0.01	0.03	0.03	0.01	0.03	0.02	0.02	0.01	0.02	0.04	0.03	0.01
Total	100.44	100.73	100.21	100.18	100.04	100.93	100.73	100.72	100.54	100.51	100.75	100.33
Mg#	0.90	0.89	0.88	0.89	0.90	0.89	0.90	0.90	0.89	0.89	0.90	0.91
Cr#	7.13	6.48	6.94	8.06	8.92	6.91	6.84	9.01	8.85	9.57	10.55	40.47
LOI%	-0.44	-0.39	-0.46	-0.39	-0.41	-0.41	-0.42	-0.35	-0.48	-0.47	-0.38	-0.53
Zr	4.01	7.29	9.93	14.57	5.47	12.74	3.67	4.31	6.95	7.83	11.62	1.23
Sr	12.80	18.31	21.62	11.13	24.07	17.95	14.34	6.97	11.83	24.70	26.91	2.83
Rb	0.20	0.37	0.63	0.15	0.68	0.21	0.12	0.98	1.10	0.27	0.79	0.18
Ga	2.20	2.90	4.20	2.70	2.40	2.80	2.10	3.60	4.20	3.10	2.80	1.20
Zn	53	52	73	58	57	61	51	57	64	71	62	38
Ni	2087	1974	2084	2029	2140	2019	2049	1982	2119	2041	2133	2864
Co	111	110	115	110	113	110	112	106	112	118	111	130
Cr	1837	2407	2401	2699	2267	2475	2209	2421	1931	2842	2591	4978
Sc	10.8	14.2	11.5	12.3	10.0	15.9	12.6	7.2	3.7	10.3	9.1	4.2
V	51.1	59.6	53.5	57.3	52.7	64.3	60.4	60.2	75.7	49.0	42.6	15.6
Y	1.48	3.08	2.28	2.06	1.47	3.12	2.01	1.14	0.35	1.51	1.25	0.16
Nb	0.68	0.95	1.82	0.64	1.81	0.89	0.58	0.56	1.19	1.64	3.06	0.45
Mo	0.27	0.52	0.34	0.28	0.35	0.27	0.29	0.28	0.29	0.37	0.32	0.25
Ba	3.59	5.11	23.07	5.01	17.82	2.60	5.84	5.28	10.22	7.51	12.53	2.63
La	0.57	0.95	1.21	0.43	1.27	0.76	0.52	0.39	0.77	1.84	1.17	0.34
Ce	1.14	1.88	2.41	1.16	2.67	2.15	1.66	0.72	1.50	3.40	2.57	0.65
Pr	0.18	0.28	0.31	0.19	0.36	0.33	0.28	0.11	0.20	0.42	0.33	0.11
Nd	0.84	1.29	1.33	0.96	1.55	1.52	1.32	0.47	0.81	1.66	1.42	0.44
Sm	0.24	0.38	0.32	0.28	0.36	0.42	0.32	0.13	0.17	0.33	0.34	0.09
Eu	0.09	0.13	0.11	0.10	0.11	0.14	0.10	0.04	0.05	0.10	0.11	0.03
Gd	0.29	0.45	0.37	0.36	0.36	0.49	0.34	0.15	0.16	0.35	0.34	0.09
Tb	0.05	0.08	0.07	0.07	0.06	0.09	0.06	0.03	0.02	0.05	0.05	0.01
Dy	0.31	0.56	0.43	0.43	0.33	0.60	0.38	0.21	0.12	0.33	0.30	0.07
Ho	0.06	0.12	0.09	0.09	0.06	0.12	0.08	0.05	0.02	0.07	0.06	0.02
Er	0.18	0.36	0.27	0.24	0.17	0.37	0.24	0.16	0.06	0.18	0.16	0.04
Tm	0.03	0.06	0.04	0.03	0.02	0.06	0.04	0.03	0.01	0.03	0.02	0.01
Yb	0.18	0.35	0.26	0.21	0.15	0.36	0.24	0.17	0.05	0.16	0.14	0.04
Lu	0.03	0.06	0.04	0.03	0.02	0.06	0.04	0.03	0.01	0.02	0.02	0.01
Hf	0.15	0.22	0.31	0.50	0.15	0.35	0.15	0.25	0.34	0.25	0.43	0.18
Ta	0.05	0.06	0.26	0.06	0.10	0.06	0.02	0.03	0.06	0.06	0.47	0.12
W	30.28	1.37	1.56	0.82	1.28	25.88	1.52	1.31	1.04	1.37	1.50	10.66
Pb	0.31	0.28	0.29	0.27	0.39	0.21	0.45	0.38	0.42	0.40	0.21	0.53
Th	0.09	0.13	0.15	0.07	0.15	0.07	0.07	0.09	0.11	0.20	0.13	0.06
U	0.03	0.04	0.05	0.02	0.05	0.02	0.02	0.02	0.03	0.06	0.04	0.02

Mg# = Mg/(Mg+Fe); Cr# = Cr/(Cr+Al); LOI - loss on ignition; Fe* - total Fe as FeO; bdl - below detection limit

Table AD2 cont.

	POKA40	POKA43	POKA44	POKA45	POKA54	DUB301	DUB303	DUB304	DUB311	DUB313	DUB314	DC41
SiO ₂	45.77	45.15	44.66	44.73	45.35	46.22	46.15	42.61	43.71	45.10	44.28	46.01
TiO ₂	0.05	0.08	0.06	0.06	0.14	0.19	0.11	0.11	0.09	0.03	0.06	0.12
Al ₂ O ₃	2.23	1.51	2.30	2.11	3.64	1.49	1.82	1.12	1.98	1.36	1.77	2.89
FeO	7.91	7.80	8.01	8.12	9.74	8.18	8.26	10.69	7.88	7.56	7.65	8.04
MnO	0.13	0.12	0.13	0.13	0.14	0.13	0.13	0.18	0.13	0.12	0.12	0.13
MgO	43.01	44.94	42.34	42.56	39.89	42.34	43.14	41.80	43.25	43.56	43.35	39.31
CaO	2.05	1.35	2.09	2.09	0.84	2.06	2.24	3.03	2.31	1.62	2.29	4.03
Na ₂ O	0.05	0.06	0.07	0.07	-0.01	0.10	0.10	0.24	0.14	-0.02	0.12	0.19
K ₂ O	0.01	0.01	0.01	0.01	0.01	0.01	0.01	0.06	0.03	0.01	0.01	0.00
P ₂ O ₅	0.01	0.02	0.01	0.01	0.02	0.08	0.08	0.05	0.12	0.03	0.04	0.02
Total	101.21	101.05	100.36	100.54	100.36	100.80	102.79	100.48	100.31	100.04	100.32	101.37
Mg#	0.91	0.91	0.90	0.90	0.88	0.90	0.90	0.87	0.91	0.91	0.91	0.90
Cr#	9.73	14.31	10.48	10.17	5.84	15.34	14.24	16.52	10.91	15.09	11.07	8.29
LOI%	-0.37	-0.40	-0.41	-0.37	-0.50	-0.12	0.10	0.51	0.20	0.14	0.48	-0.1
Zr	2.91	5.64	3.99	5.82	7.25	4.00	10.05	26.51	7.57	1.82	2.27	9.1
Sr	6.57	9.61	7.24	6.83	10.27	38.01	34.26	49.85	68.10	13.17	40.82	13.0
Rb	0.05	0.10	0.08	0.03	<i>n.a.</i>	0.13	0.13	0.33	0.44	0.07	0.03	<i>bdl</i>
Ga	1.50	1.10	1.20	1.90	3.90	1.60	1.50	2.20	1.40	1.00	1.10	6.80
Zn	50	56	53	53	78	54	60	106	55	44	46	45
Ni	2120	2249	2152	2174	2104	1879	2108	2113	2221	2148	2141	1936
Co	111	111	113	112	118	107	110	108	112	109	112	107
Cr	2355	2479	2640	2342	2216	2653	2956	2180	2374	2373	2167	2660
Sc	11.7	7.1	10.4	9.6	11.4	8.3	8.7	8.1	7.8	7.8	9.1	16.1
V	45.7	31.1	47.0	42.1	44.6	47.9	37.6	24.0	37.3	33.3	36.5	62.9
Y	0.97	1.34	0.92	0.97	2.61	1.49	1.18	1.92	1.79	0.35	1.19	2.88
Nb	0.30	0.71	0.54	0.57	1.41	0.70	0.59	3.16	1.74	0.37	0.53	0.22
Mo	0.28	0.26	0.25	0.25	0.30	0.57	0.27	0.27	0.46	0.30	0.36	0.27
Ba	2.99	1.99	1.81	0.83	<i>< b. dl.</i>	22.23	5.20	19.77	21.57	15.47	8.28	1.52
La	0.44	0.54	0.47	0.44	0.28	7.74	1.77	1.32	7.54	0.46	2.87	0.27
Ce	1.03	1.16	1.10	1.03	0.87	5.82	3.11	3.86	12.67	0.80	5.44	0.53
Pr	0.16	0.20	0.17	0.16	0.18	0.51	0.46	0.63	1.05	0.12	0.56	0.10
Nd	0.71	0.94	0.76	0.74	0.91	1.95	1.95	3.22	3.51	0.53	1.95	0.43
Sm	0.16	0.26	0.17	0.19	0.31	0.41	0.42	0.83	0.57	0.11	0.27	0.14
Eu	0.05	0.09	0.06	0.06	0.11	0.14	0.13	0.26	0.17	0.04	0.08	0.06
Gd	0.18	0.29	0.20	0.20	0.39	0.46	0.39	0.74	0.59	0.11	0.28	0.25
Tb	0.03	0.05	0.03	0.03	0.07	0.07	0.05	0.11	0.07	0.02	0.04	0.06
Dy	0.20	0.30	0.20	0.21	0.51	0.34	0.27	0.51	0.37	0.09	0.22	0.48
Ho	0.04	0.06	0.04	0.05	0.11	0.06	0.05	0.08	0.07	0.02	0.05	0.12
Er	0.14	0.16	0.13	0.13	0.32	0.15	0.13	0.19	0.20	0.06	0.15	0.37
Tm	0.02	0.02	0.02	0.02	0.05	0.02	0.02	0.02	0.03	0.01	0.02	0.06
Yb	0.14	0.14	0.13	0.13	0.33	0.12	0.11	0.13	0.18	0.07	0.15	0.39
Lu	0.02	0.02	0.02	0.02	0.05	0.02	0.02	0.02	0.03	0.01	0.02	0.06
Hf	0.08	0.19	0.12	0.15	0.18	0.19	0.27	0.58	0.19	0.07	0.10	0.26
Ta	0.14	0.05	0.05	0.04	0.01	0.02	0.05	0.18	0.07	0.03	0.02	0.02
W	21.86	0.40	0.24	3.40	0.44	34.70	0.96	39.70	136.96	47.61	58.00	520.34
Pb	0.16	0.09	0.10	0.08	0.15	0.61	0.24	0.30	0.44	2.47	0.33	0.15
Th	0.06	0.07	0.06	0.06	0.04	0.95	0.14	0.08	0.84	0.09	0.34	0.05
U	0.02	0.02	0.02	0.02	0.08	0.27	0.10	0.09	0.28	0.06	0.11	0.02

Table AD3

Average olivine microprobe core analyses of south Patagonian mantle xenoliths

	SA01	SA02	SA03	SA04	SA09	SA10	SA11	ELRU1	ELRU2	ELRU3	ELRU4	ELRU5	ELRU6	ELRU7	ELRU8
SiO ₂	40.78	40.71	41.21	40.78	40.69	40.87	41.40	41.05	40.79	40.82	40.89	40.69	40.70	40.43	40.23
TiO ₂	0.01	0.01	0.01	0.01	0.01	0.01	0.02	0.01	0.01	0.01	0.01	0.01	0.01	0.01	0.00
Al ₂ O ₃	0.02	0.00	0.02	0.02	0.00	0.01	0.02	0.01	0.01	0.01	0.01	0.01	0.00	0.02	0.02
Cr ₂ O ₃	0.02	0.03	0.07	0.02	0.02	0.03	0.03	0.03	0.02	0.01	0.02	0.04	0.01	0.03	0.01
FeO†	9.53	9.41	8.16	10.12	10.27	9.83	7.77	8.33	9.98	9.17	8.65	10.16	9.62	10.65	11.38
MnO	0.12	0.14	0.12	0.13	0.14	0.14	0.11	0.13	0.13	0.13	0.13	0.12	0.12	0.12	0.18
NiO	0.42	0.41	0.40	0.41	0.39	0.40	0.40	0.43	0.42	0.42	0.41	0.44	0.39	0.45	0.27
MgO	49.13	49.23	50.11	48.59	48.72	48.83	50.39	50.25	48.88	49.60	49.83	48.59	48.99	48.25	47.52
CaO	0.06	0.05	0.11	0.07	0.08	0.09	0.08	0.05	0.06	0.02	0.06	0.06	0.06	0.07	0.03
Total	100.09	100.00	100.23	100.14	100.32	100.20	100.21	100.31	100.33	100.19	100.01	100.13	99.90	99.94	99.63
Mg#*100	90.2	90.3	91.6	89.5	89.4	89.9	92.0	91.5	89.7	90.6	91.1	89.5	90.1	89.0	88.2
	ELRU9	ELRU10	ELRU11	ELRU13	ELRU15	ELRU16	ELRU19	POKA42	POKA43	POKA44	POKA45	POKA48	POKA50	POKA51	DUB170
SiO ₂	40.54	40.57	40.56	41.03	40.98	40.83	41.18	40.68	40.91	40.60	40.61	41.33	40.96	40.80	40.16
TiO ₂	0.02	0.02	0.01	0.01	0.00	0.00	0.01	0.00	0.01	0.00	0.01	0.01	0.00	0.01	0.01
Al ₂ O ₃	0.05	0.01	0.02	0.01	0.02	0.01	0.00	0.01	0.01	0.01	0.05	0.06	0.02	0.02	0.01
Cr ₂ O ₃	0.03	0.02	0.02	0.01	0.04	0.04	0.01	0.04	0.02	0.02	0.04	0.01	0.03	0.02	9.35
FeO†	9.84	10.66	10.78	8.42	7.74	9.10	7.60	9.35	8.70	9.40	9.39	8.71	8.52	8.66	0.13
MnO	0.13	0.11	0.15	0.14	0.11	0.15	0.11	0.14	0.13	0.13	0.14	0.11	0.13	0.14	0.43
NiO	0.42	0.46	0.40	0.41	0.39	0.41	0.40	0.40	0.40	0.38	0.40	0.39	0.40	0.42	49.08
MgO	48.72	48.25	47.98	49.94	50.37	49.37	50.49	49.31	49.92	48.98	49.14	49.76	49.76	49.62	0.04
CaO	0.07	0.07	0.09	0.07	0.08	0.13	0.04	0.08	0.07	0.09	0.07	0.07	0.12	0.06	0.02
Total	99.81	100.21	100.02	100.04	99.73	100.04	99.84	100.01	100.18	99.62	99.84	100.45	99.94	99.74	99.26
Mg#*100	89.8	89.0	88.8	91.4	92.1	90.6	92.2	90.4	91.1	90.3	90.3	91.1	91.2	91.1	90.3

Table AD3 cont.

	DUB300	DUB301	DUB311	DUB312	DUB313	DUB316	DUB317	DC08	DC09	DC18	DC41	TL141	TL142	TL143	TL145
SiO2	40.82	40.84	40.60	40.85	40.90	41.15	41.24	40.97	40.83	40.77	40.68	40.83	40.63	41.00	40.89
TiO2	0.01	0.01	0.01	0.01	0.01	0.01	0.01	0.01	0.00	0.01	0.01	0.01	0.00	0.01	0.00
Al2O3	0.02	0.01	0.02	0.00	0.03	0.01	0.03	0.01	0.01	0.01	0.00	0.01	0.01	0.01	0.01
Cr2O3	0.03	0.04	0.02	0.02	0.12	0.02	0.01	0.01	0.01	0.02	0.01	0.01	0.01	0.02	0.00
FeO†	8.92	9.84	8.81	8.64	8.71	8.81	8.91	9.44	9.15	9.09	9.82	9.01	9.27	8.93	9.16
MnO	0.13	0.14	0.13	0.13	0.13	0.13	0.11	0.14	0.14	0.14	0.15	0.13	0.14	0.13	0.14
NiO	0.41	0.38	0.39	0.39	0.40	0.39	0.39	0.38	0.41	0.38	0.37	0.40	0.43	0.42	0.41
MgO	49.75	48.75	49.37	49.52	49.63	49.58	49.62	49.63	49.76	49.77	48.79	49.74	49.37	49.74	49.55
CaO	0.06	0.07	0.12	0.04	0.09	0.09	0.04	0.03	0.06	0.04	0.05	0.03	0.05	0.03	0.04
Total	100.16	100.08	99.46	99.59	100.01	100.19	100.38	100.62	100.38	100.23	99.89	100.18	99.91	100.28	100.20
Mg#*100	90.9	89.8	90.9	91.1	91.0	90.9	90.8	90.4	90.6	90.7	89.9	90.8	90.5	90.9	90.6

Mg# = Mg/(Mg+Fe); Fe† - total Fe as FeO

Table AD4
Average orthopyroxene microprobe core analyses of south Patagonian mantle xenoliths

	SA01	SA02	SA03	SA04	SA09	SA10	SA11	ELRU1	ELRU2	ELRU3	ELRU4	ELRU5	ELRU6	ELRU7	ELRU8
SiO ₂	55.72	55.40	56.13	55.66	55.47	55.53	56.23	55.94	55.64	55.50	56.42	55.18	55.04	54.54	55.31
TiO ₂	0.10	0.14	0.12	0.16	0.16	0.07	0.07	0.08	0.12	0.10	0.06	0.25	0.23	0.38	0.08
Al ₂ O ₃	3.43	3.74	2.62	3.57	3.64	3.53	3.43	3.30	3.46	3.88	2.20	3.80	3.81	4.08	2.72
FeO†	5.95	6.01	5.14	6.29	6.32	6.17	4.86	5.25	6.30	6.01	5.44	6.45	6.38	6.80	7.69
MnO	0.12	0.14	0.11	0.13	0.12	0.14	0.11	0.13	0.12	0.15	0.14	0.13	0.12	0.12	0.21
MgO	33.37	33.27	33.55	33.03	32.94	33.17	33.88	34.09	33.19	33.71	34.29	32.77	32.85	32.30	32.67
CaO	0.68	0.63	1.21	0.69	0.75	0.77	0.73	0.71	0.68	0.37	0.79	0.78	0.74	0.82	0.54
Na ₂ O	0.13	0.09	0.14	0.12	0.14	0.10	0.07	0.08	0.09	0.02	0.02	0.15	0.12	0.11	0.00
NiO	0.11	0.11	0.13	0.11	0.11	0.10	n.a.	0.12	0.12	0.09	0.11	0.12	0.10	0.12	0.05
Cr ₂ O ₃	0.49	0.51	0.85	0.39	0.61	0.54	0.64	0.66	0.49	0.43	0.57	0.59	0.50	0.62	0.47
Total	100.11	100.04	100.01	100.16	100.27	100.15	100.03	100.36	100.19	100.25	100.04	100.22	99.89	99.89	99.73
Mg#*100	90.9	90.8	92.1	90.4	90.3	90.6	92.6	92.1	90.4	90.9	91.8	90.0	90.2	89.4	88.3
en	89.5	89.5	89.8	89.0	88.8	89.0	91.1	90.6	89.0	90.0	90.3	88.5	88.7	87.8	87.1
fs	9.1	9.3	7.9	9.7	9.7	9.5	7.5	8.0	9.7	9.2	8.2	10.0	9.9	10.6	11.8
wo	1.3	1.2	2.3	1.3	1.5	1.5	1.4	1.4	1.3	0.7	1.5	1.5	1.4	1.6	1.0
	ELRU9	ELRU10	ELRU11	ELRU13	ELRU15	ELRU16	ELRU19	POKA42	POKA43	POKA44	POKA45	POKA48	POKA50	POKA51	DUB170
SiO ₂	54.94	54.82	54.67	55.96	56.26	56.19	55.28	55.28	55.67	55.25	54.86	55.48	55.84	55.43	54.07
TiO ₂	0.28	0.36	0.30	0.06	0.01	0.11	0.06	0.11	0.14	0.05	0.07	0.10	0.07	0.08	0.09
Al ₂ O ₃	3.86	3.72	4.08	3.36	2.51	2.70	4.07	3.95	3.44	4.20	4.17	4.43	3.34	3.66	4.22
FeO†	6.23	6.70	6.63	4.90	5.53	5.28	6.02	5.96	5.56	5.92	6.03	5.56	5.44	5.50	5.94
MnO	0.12	0.11	0.13	0.13	0.14	0.13	0.14	0.13	0.14	0.13	0.13	0.12	0.13	0.13	0.14
MgO	32.79	32.63	32.03	34.00	33.99	34.58	33.37	33.37	33.72	33.35	33.18	33.25	33.87	33.61	33.08
CaO	0.79	0.79	1.12	0.77	0.71	0.37	0.66	0.65	0.68	0.62	0.65	0.68	0.58	0.65	0.43
Na ₂ O	0.14	0.11	0.14	0.09	0.03	n.a.	0.06	0.09	0.11	0.08	0.06	0.10	0.06	0.05	0.08
NiO	0.12	0.13	0.11	0.11	0.11	0.08	0.11	0.10	0.11	0.11	0.10	n.a.	0.10	0.10	0.10
Cr ₂ O ₃	0.65	0.59	0.70	0.65	0.57	0.41	0.44	0.46	0.58	0.42	0.47	0.45	0.52	0.57	0.44
Total	99.93	99.97	99.90	100.02	99.85	99.85	100.22	100.10	100.15	100.15	99.73	100.18	99.96	99.78	98.60
Mg#*100	90.4	89.7	89.6	92.5	91.6	92.1	90.8	90.9	91.5	90.9	90.8	91.4	91.7	91.6	90.8
en	88.8	88.1	87.5	91.0	90.2	91.3	89.5	89.6	90.1	89.7	89.4	90.0	90.5	90.3	89.9
fs	9.6	10.3	10.3	7.5	8.4	8.0	9.3	9.2	8.5	9.1	9.3	8.6	8.4	8.5	9.3
wo	1.5	1.5	2.2	1.5	1.4	0.7	1.3	1.2	1.3	1.2	1.3	1.3	1.1	1.3	0.8

Table AD4 cont.

	DUB 300	DUB 301	DUB 311	DUB 312	DUB 313	DUB 316	DUB 317	DC08	DC09	DC18	DC41	TL141	TL142	TL143	TL145
SiO ₂	55.89	53.82	54.74	55.96	55.58	55.67	56.07	55.99	56.00	55.78	55.44	55.98	55.79	56.17	55.96
TiO ₂	0.02	0.24	0.10	0.11	0.03	0.12	0.10	0.07	0.06	0.08	0.10	0.09	0.05	0.04	0.06
Al ₂ O ₃	3.23	2.42	4.26	2.81	3.42	4.26	3.23	3.33	3.23	3.25	4.25	2.88	2.83	3.05	3.09
FeO†	5.65	6.74	5.63	5.53	5.50	5.66	6.05	5.89	5.85	6.36	5.87	5.90	5.97	5.72	6.00
MnO	0.13	0.14	0.14	0.14	0.12	0.15	0.14	0.14	0.14	0.16	0.14	0.15	0.15	0.14	0.15
MgO	33.78	35.39	33.07	33.96	33.58	33.10	34.05	33.96	34.17	33.60	33.45	34.07	33.91	34.24	34.00
CaO	0.76	0.67	0.78	0.54	0.84	0.73	0.46	0.51	0.48	0.48	0.38	0.40	0.45	0.46	0.41
Na ₂ O	0.05	0.08	0.14	n.a.	0.05	0.08	0.04	0.05	0.05	0.04	0.00	0.05	0.01	0.04	0.02
NiO	0.11	0.15	0.12	0.09	0.12	n.a.	0.08	0.10	0.09	0.08	n.a.	0.08	0.10	0.09	0.09
Cr ₂ O ₃	0.58	0.51	0.56	0.49	0.65	0.50	0.30	0.34	0.43	0.27	0.55	0.52	0.52	0.39	0.46
Total	100.20	100.18	99.54	99.68	99.88	100.25	100.51	100.38	100.50	100.10	100.19	100.11	99.78	100.35	100.23
Mg#*100	91.4	90.4	90.9	91.6	91.6	91.2	90.9	91.1	91.2	90.4	91.0	91.1	91.0	91.4	91.0
en	89.9	89.0	89.7	90.5	89.9	89.7	90.0	90.1	90.2	89.4	90.2	90.2	90.0	90.4	90.1
fs	8.6	9.8	8.8	8.5	8.5	8.8	9.2	9.0	8.9	9.7	9.1	9.0	9.1	8.7	9.2
wo	1.4	1.2	1.5	1.0	1.6	1.4	0.9	1.0	0.9	0.9	0.7	0.8	0.8	0.9	0.8

Mg# = Mg/(Mg+Fe); Fe† - total Fe as FeO; n.a. - not analyzed

Table AD5

Average clinopyroxene microprobe core analyses of south Patagonian mantle xenoliths

	SA01	SA04	SA09	SA10	ELRU2	ELRU5	ELRU6	ELRU7	ELRU8	ELRU9	ELRU10
SiO ₂	52.73	52.37	52.36	52.89	52.65	52.35	52.34	51.39	51.95	51.57	51.45
TiO ₂	0.36	0.61	0.53	0.20	0.44	0.63	0.48	1.06	0.24	1.03	1.07
Al ₂ O ₃	5.65	6.13	5.54	5.14	5.30	5.56	5.73	5.84	3.38	6.06	4.85
FeO ⁺	2.90	3.01	3.16	2.94	2.99	3.17	2.98	3.62	2.61	3.27	3.66
MnO	0.07	0.09	0.09	0.08	0.08	0.09	0.08	0.09	0.11	0.09	0.09
MgO	15.56	15.23	15.46	15.98	15.61	15.65	15.40	15.59	16.08	15.32	16.50
CaO	19.39	19.69	19.27	20.10	20.13	19.46	19.89	19.08	23.72	19.02	19.49
Na ₂ O	1.99	1.99	1.94	1.59	1.75	1.79	1.85	1.72	0.46	1.92	1.27
NiO	0.06	0.05	0.06	0.05	0.05	0.06	0.06	0.07	0.02	0.06	0.06
Cr ₂ O ₃	1.16	0.83	1.37	1.15	1.12	1.18	1.00	1.22	1.01	1.43	1.43
Total	99.89	99.98	99.79	100.12	100.13	99.94	99.80	99.66	99.60	99.75	99.86
Mg#*100	90.5	90.0	89.7	90.7	90.3	89.8	90.2	88.5	91.6	89.3	88.9
en	49.9	48.9	49.6	49.7	49.1	49.7	49.0	49.7	46.4	49.6	50.6
fs	5.4	5.6	5.9	5.3	5.4	5.8	5.5	6.6	4.4	6.1	6.4
wo	44.7	45.5	44.5	45.0	45.5	44.5	45.5	43.7	49.2	44.3	43.0

	ELRU11	ELRU13	POKA40	POKA43	POKA44	POKA45	DUB301	DUB311	DUB313	DC41
SiO ₂	51.62	53.27	52.36	52.53	52.58	52.18	52.09	51.58	52.79	51.73
TiO ₂	0.95	0.23	0.22	0.43	0.19	0.25	0.88	0.34	0.08	0.51
Al ₂ O ₃	5.67	2.22	5.08	5.13	5.10	5.10	4.70	6.28	3.99	5.88
FeO ⁺	3.34	1.79	2.81	2.65	2.77	2.80	3.02	2.87	2.53	2.56
MnO	0.09	0.06	0.10	0.08	0.09	0.09	0.09	0.10	0.09	0.08
MgO	15.44	16.86	16.05	15.76	16.00	16.03	15.70	15.48	16.87	14.89
CaO	19.64	24.60	21.18	20.35	21.17	21.09	20.37	19.38	21.51	21.68
Na ₂ O	1.72	0.39	1.26	1.75	1.28	1.27	1.51	1.92	0.84	1.38
NiO	0.05	0.05	0.05	0.05	0.06	0.05	0.05	0.04	0.05	0.03
Cr ₂ O ₃	1.35	0.89	0.86	1.30	0.86	0.89	1.48	1.22	1.10	1.06
Total	99.86	100.37	99.98	100.05	100.10	99.75	99.89	99.21	99.85	99.80
Mg#*100	89.2	94.4	91.1	91.4	91.1	91.1	90.3	90.6	92.2	91.2
en	49.0	47.4	48.8	49.4	48.7	48.9	48.9	49.8	49.9	46.6
fs	6.1	2.9	4.9	4.8	4.9	4.9	5.4	5.4	4.3	4.6
wo	44.9	49.7	46.3	45.8	46.4	46.2	45.6	44.8	45.7	48.8

Mg# = Mg/(Mg+Fe); Fe⁺ - total Fe as FeO

Table AD6

Average garnet microprobe core analyses of south Patagonian mantle xenoliths

	SA01	SA04	ELRU2	ELRU5	ELRU6	ELRU7	ELRU9
SiO ₂	41.60	42.59	41.86	42.03	42.46	42.17	42.21
Al ₂ O ₃	23.19	23.09	22.80	22.79	23.09	22.66	23.16
Cr ₂ O ₃	1.64	1.18	1.49	1.47	1.22	1.34	1.27
FeO ⁺	7.51	7.90	7.88	7.73	7.71	8.12	7.54
MnO	0.33	0.35	0.35	0.33	0.36	0.31	0.34
MgO	21.21	23.09	20.54	20.86	21.12	20.71	21.05
CaO	4.46	4.99	5.01	4.99	4.97	4.79	5.03
Na ₂ O	0.11	0.17	0.10	0.04	0.03	0.05	0.01
TiO	0.13	0.17	0.16	0.23	0.14	0.32	0.15
Total	100.17	100.75	100.19	100.47	101.10	100.49	100.75
Mg#*100	83.4	83.9	82.3	82.8	83.0	82.0	83.3
alm	14.6	14.2	15.4	15.0	14.8	15.8	14.5
pyr	73.6	73.8	71.4	72.0	72.3	71.7	72.4
gro	11.1	11.4	12.5	12.4	12.2	11.9	12.4
spess	0.6	0.6	0.7	0.6	0.7	0.6	0.7

Mg# = Mg/(Mg+Fe); Fe⁺ - total Fe as FeO

Table AD7
Clinopyroxene and garnet LA-ICP-MS trace element (ppm) analyses

	clinopyroxene													
	SA01	SA04	SA08	SA09	SA10	ELRU02	ELRU5	ELRU12	POKA40	POKA41	POKA44	DUB301	DUB304	DUB311
Cr	6140	5254	8008	8142	5883	5378	7004	7185	5957	7933	5669	12995	7649	10587
Co	22.8	20.9	25.0	22.5	21.6	23.6	24.1	22.2	22.1	20.9	22.0	19.5	21.5	20.4
Ni	400	324	398	345	346	398	403	381	385	374	385	321	394	341
Zn	13.4	11.7	16.3	15.0	12.7	15.2	15.0	11.5	9.5	10.8	9.9	22.3	11.0	16.8
Cu	2.69	1.91	1.83	2.19	2.79	2.54	2.47	2.46	1.82	1.42	1.76	0.81	6.60	1.37
V	296	293	302	331	270	324	349	240	233	241	233	191	256	220
Sr	58.5	84.3	63.0	86.1	62.7	74.0	75.0	93.5	60.5	90.0	60.5	293.7	395.3	315.8
Y	2.49	5.14	3.16	2.70	3.43	3.48	3.81	11.15	9.05	11.87	8.61	14.38	13.59	13.77
Zr	12.9	30.3	20.3	60.0	11.3	49.4	25.8	50.6	12.1	83.7	13.5	203.3	35.0	112.0
La	1.609	2.475	0.990	2.241	1.315	1.516	1.001	2.845	2.398	2.030	2.289	13.028	34.790	20.750
Ce	3.790	6.205	5.315	7.015	4.988	7.123	4.190	10.633	6.535	7.383	6.410	40.240	74.150	53.573
Pr	0.517	0.999	1.005	1.100	0.875	1.185	0.839	1.608	0.907	1.346	0.902	5.905	7.533	6.478
Nd	2.748	5.218	5.033	5.373	4.280	5.730	4.778	7.303	3.918	7.730	4.113	29.130	26.848	27.415
Sm	1.038	1.696	1.394	1.533	1.129	1.656	1.594	1.858	0.900	2.480	0.983	7.578	4.653	6.008
Eu	0.371	0.642	0.488	0.533	0.377	0.606	0.576	0.684	0.315	0.911	0.351	2.586	1.563	2.026
Gd	1.091	1.811	1.338	1.443	1.061	1.648	1.598	2.163	1.183	2.890	1.195	6.173	3.695	4.845
Tb	0.146	0.249	0.165	0.177	0.139	0.229	0.222	0.347	0.211	0.424	0.210	0.901	0.551	0.719
Dy	0.729	1.327	0.862	0.833	0.809	1.047	1.090	2.275	1.633	2.618	1.521	4.145	2.890	3.475
Ho	0.110	0.221	0.130	0.119	0.144	0.149	0.162	0.468	0.365	0.499	0.343	0.648	0.572	0.605
Er	0.245	0.441	0.257	0.213	0.342	0.300	0.315	1.325	1.131	1.331	1.082	1.311	1.439	1.369
Tm	0.029	0.048	0.029	0.020	0.039	0.031	0.032	0.183	0.154	0.176	0.155	0.147	0.200	0.168
Yb	0.159	0.252	0.131	0.100	0.205	0.146	0.162	1.193	1.087	1.069	1.015	0.842	1.384	1.077
Lu	0.017	0.032	0.015	0.011	0.027	0.019	0.018	0.167	0.166	0.147	0.157	0.100	0.192	0.140
Hf	0.607	1.023	0.759	1.723	0.308	1.149	1.075	1.023	0.225	1.598	0.231	3.775	0.740	2.259

n.a. - not analyzed; bdl - below detection limit

Table AD7 cont.

	clinopyroxene		garnet				
	DUB313	DUB314	ELRU5	ELRU6	ELRU7 (1)	ELRU7 (2)	
Cr	6962	8257	9464	8513	7585	6421	
Co	23.2	20.6	41.2	48.0	50.9	49.0	
Ni	405	351	52.6	87.0	70.7	64.8	
Zn	9.5	9.5	13.7	13.8	17.7	16.7	
Cu	1.48	1.30	0.304	0.379	0.295	0.289	
V	219	265	88.4	99.7	105.4	94.9	
Sr	91.5	421.2	0.068	0.119	0.108	0.100	
Y	4.79	12.30	29.3	25.8	25.1	37.8	
Zr	6.2	20.7	22.2	14.4	20.3	24.5	
La	5.838	49.833	bdl	0.009	bdl	bdl	
Ce	10.230	85.873	0.042	0.110	0.082	0.121	
Pr	1.216	7.465	0.023	0.051	0.052	0.047	
Nd	5.238	23.760	0.344	0.621	0.572	0.572	
Sm	1.076	2.810	0.459	0.661	0.561	0.636	
Eu	0.340	0.929	0.326	0.393	0.359	0.363	
Gd	0.898	2.205	1.684	1.767	1.808	1.868	
Tb	0.150	0.378	0.447	0.443	0.439	0.518	
Dy	0.883	2.280	4.242	4.097	4.060	5.485	
Ho	0.196	0.496	1.095	1.008	0.985	1.558	
Er	0.531	1.367	3.557	3.250	3.215	5.970	
Tm	0.084	0.193	0.551	0.508	0.515	1.047	
Yb	0.555	1.334	3.892	3.812	4.170	8.540	
Lu	0.088	0.193	0.603	0.586	0.702	1.502	
Hf	0.111	0.707	0.330	0.224	0.272	0.390	

Table AD8

Average spinel microprobe core analyses of south Patagonian mantle xenoliths

	SA01	SA02	SA03	SA04	SA09	SA10	SA11	ELRU1	ELRU2	ELRU3	ELRU4
Cr ₂ O ₃	26.17	22.71	43.63	23.99	26.54	23.69	29.28	31.09	25.59	15.03	43.07
Al ₂ O ₃	41.00	44.07	22.88	42.19	39.43	42.81	39.58	37.22	40.43	52.83	24.21
TiO ₂	0.34	0.43	0.86	0.51	0.58	0.20	0.19	0.31	0.45	0.11	0.43
FeO [†]	14.12	13.79	15.97	15.24	15.25	14.18	11.64	12.44	15.33	11.43	15.48
MgO	17.24	18.22	15.49	17.22	17.10	18.28	19.16	18.06	17.07	19.63	15.94
MnO	0.17	0.13	0.16	0.20	0.13	0.13	0.09	0.13	0.15	0.13	0.16
NiO	0.28	0.31	0.21	0.28	0.30	0.28	0.25	0.25	0.29	0.33	0.19
SiO ₂	0.08	n.a.	0.07	0.06	0.06	0.08	0.04	0.06	0.07	0.01	0.05
CaO	n.a.	0.02	0.01	0.01	0.02	0.11	0.05	0.01	0.03	0.00	0.02
ZnO	0.12	0.11	0.04	0.10	0.09	0.12	0.12	0.07	0.12	0.16	0.10
Total	99.54	99.84	99.32	99.79	99.48	99.87	100.41	99.63	99.53	99.66	99.65
Cr [#] *100	30.0	25.7	56.1	27.6	31.1	27.1	33.2	35.9	29.8	16.0	54.4
Mg [#] *100	68.5	70.2	63.4	66.8	66.7	69.7	74.6	72.1	66.5	75.4	64.7

	ELRU5	ELRU6	ELRU7	ELRU8	ELRU9	ELRU11	ELRU13	ELRU15	ELRU16	ELRU19	POKA40
Cr ₂ O ₃	25.66	24.78	24.77	27.30	26.56	26.87	40.64	29.81	38.51	23.56	17.04
Al ₂ O ₃	39.10	41.57	38.26	35.37	38.32	37.37	26.72	38.85	28.68	44.17	49.65
TiO ₂	0.97	0.41	1.54	0.15	0.92	1.21	0.36	0.16	0.10	0.13	0.17
FeO [†]	15.85	14.60	17.29	22.44	15.48	16.53	18.07	11.83	15.78	12.56	12.30
MgO	17.43	17.71	17.06	13.30	18.08	17.60	13.54	18.36	15.74	18.82	19.64
MnO	0.12	0.13	0.12	0.23	0.10	0.08	0.21	0.10	0.18	0.12	0.11
NiO	0.31	0.30	0.36	0.14	0.34	0.31	0.13	0.24	0.20	0.23	0.36
SiO ₂	0.07	0.06	0.10	0.04	0.09	0.11	0.02	0.10	0.06	0.03	0.06
CaO	0.01	0.05	0.01	0.12	0.02	0.02	n.a.	n.a.	0.01	0.01	0.01
ZnO	0.11	0.14	0.14	0.15	0.11	0.11	0.16	0.08	0.11	n.a.	0.13
Total	99.61	99.76	99.66	99.24	100.00	100.21	99.85	99.53	99.37	99.62	99.46
Cr [#] *100	30.6	28.6	30.3	34.1	31.7	32.5	50.5	34.0	47.4	26.4	18.7
Mg [#] *100	66.2	68.4	63.7	51.4	67.5	65.5	57.2	73.5	64.0	72.8	74.0

	POKA42	POKA44	POKA45	POKA48	POKA50	POKA51	DUB 170	DUB 300	DUB 301	DUB 311	DUB 312
Cr ₂ O ₃	18.26	16.36	15.83	14.61	28.88	23.12	12.40	27.14	0.06	19.10	29.35
Al ₂ O ₃	48.44	50.60	51.19	52.49	38.76	44.73	55.09	40.77	33.06	47.71	39.02
TiO ₂	0.26	0.12	0.17	0.21	0.20	0.25	0.10	0.09	29.90	0.17	0.18
FeO [†]	12.42	12.26	11.99	11.04	13.39	12.00	10.84	12.70	1.54	11.94	11.70
MgO	19.50	20.29	20.41	21.32	18.49	19.97	19.59	18.15	17.97	20.25	18.86
MnO	0.09	0.09	0.10	0.10	0.13	0.10	0.07	0.12	15.81	0.10	0.12
NiO	0.34	0.37	0.38	0.35	0.25	0.30	0.36	0.28	0.16	0.35	0.23
SiO ₂	0.09	0.06	0.08	0.18	0.05	0.05	0.02	0.06	0.24	0.08	0.04
CaO	0.01	0.01	0.00	0.02	0.04	0.01	0.01	n.a.	0.05	0.02	0.09
ZnO	0.08	n.a.	0.09	0.09	0.10	0.13	0.00	0.11	0.12	n.a.	n.a.
Total	99.49	100.17	100.24	100.40	100.29	100.65	98.50	99.44	98.90	99.72	99.58
Cr [#] *100	20.2	17.8	17.2	15.7	33.3	25.7	13.1	30.9	37.7	21.2	33.5
Mg [#] *100	73.7	74.7	75.2	77.5	71.1	74.8	76.3	71.8	95.4	75.1	74.2

Table AD8 cont.

	DUB 313	DUB 316	DUB 317	DC 08	DC 09	DC 18	DC 41	TL141	TL142	TL 143	TL145
Cr ₂ O ₃	28.15	16.42	15.60	14.06	15.70	17.56	13.09	25.83	26.57	20.11	20.47
Al ₂ O ₃	39.29	51.05	52.76	53.83	52.48	48.88	54.23	42.29	41.66	48.57	47.67
TiO ₂	0.06	0.18	0.04	0.07	0.08	0.06	0.11	0.09	0.10	0.06	0.07
FeO ⁺	12.87	11.02	10.97	11.30	10.80	11.21	11.63	13.19	13.57	11.17	12.17
MgO	18.75	20.92	20.71	20.16	20.02	19.61	20.29	17.68	17.44	19.29	18.77
MnO	0.11	0.11	0.09	0.06	0.11	0.10	0.10	0.11	0.09	0.09	0.11
NiO	0.27	0.35	0.35	0.37	0.38	0.32	0.36	0.27	0.25	0.30	0.29
SiO ₂	0.07	0.06	0.02	0.02	0.02	0.02	0.05	0.02	0.04	0.04	0.04
CaO	0.05	0.04	0.02	n.a.	n.a.	n.a.	0.01	n.a.	n.a.	0.01	0.03
ZnO	0.08	0.11	0.17	n.a.	n.a.	n.a.	0.12	0.11	0.19	0.13	0.14
Total	99.69	100.25	100.73	99.89	99.58	97.76	99.98	99.59	99.91	99.78	99.76
Cr#*100	32.5	17.7	16.6	14.9	16.7	19.4	13.9	29.1	30.0	21.7	22.4
Mg#*100	72.2	77.2	77.1	76.1	76.8	75.7	75.7	70.5	69.6	75.5	73.3

Mg# = Mg/(Mg+Fe); Cr# = Cr/(Cr+Al); Fe⁺ - total Fe as FeO

Table AD9
Sulfide microprobe analyses of south Patagonian mantle xenoliths

	SA02				SA11				ELRU 1				
S	39.02	33.33	34.51	36.51	38.52	36.55	32.42	33.80	35.13	35.02	33.34	34.56	25.83
Fe	49.02	29.49	30.44	2.81	49.04	12.12	27.12	30.50	0.80	53.00	32.17	30.26	13.00
Co	0.07	0.27	0.04	0.04	0.08	0.09	0.83	0.01	0.31	0.11	0.33	0.01	0.03
Ni	11.27	36.70	0.19	60.32	10.49	46.62	37.30	0.63	61.66	7.27	33.88	0.44	0.53
Cr	0.02	0.01	0.00	0.02	0.00	0.03	0.00	0.01	0.00	0.02	0.00	0.01	0.01
Cu	0.02	0.01	32.72	0.04	0.00	0.00	0.10	31.84	0.02	2.61	0.09	33.88	60.19
Total	99.42	99.80	97.90	99.74	98.17	96.21	97.81	96.83	97.94	98.04	99.82	99.18	99.61
Sulf	e	i	e	i	e	i	e	e	i	i	e	e	i
	Mss	Pn	Cp	Go	Mss	Ni-Mss	Pn	Cp	Mi	Cu-Mss	Pn	Cp	Bo

	ELRU 3			ELRU 4			ELRU 15			POKA 42				
S	37.15	37.29	33.15	35.20	31.96	37.75	33.02	32.90	39.22	38.05	33.22	46.12	44.78	30.54
Fe	48.36	45.56	31.54	36.18	32.74	49.61	25.29	30.33	46.12	44.78	30.54	0.24	0.22	0.35
Co	0.27	0.24	0.41	0.05	0.28	0.13	0.33	0.30	0.24	0.22	0.35	14.95	16.59	34.74
Ni	13.69	14.70	33.41	2.89	28.59	8.75	39.33	34.10	14.95	16.59	34.74	0.01	0.01	0.01
Cr	0.03	0.00	0.01	0.02	0.00	0.03	0.01	0.00	0.01	0.01	0.01	0.24	0.10	0.80
Cu	0.79	2.05	1.42	25.54	0.91	0.18	0.12	0.03	0.24	0.10	0.80	100.78	99.75	99.67
Total	100.28	99.84	99.94	99.88	94.65	96.58	98.12	97.71	100.78	99.75	99.67	i	e	e
Sulf	i	i	i	i	i	i	i	e	i	e	e	Mss	Mss	Pn
	Mss	Cu-MSS	Pn	Cp	Pn	Mss	Pn	Pn	Mss	Mss	Pn			

Table AD9 cont.

	POKA 48				POKA51				DUB 300				DUB317			
	S	Fe	Co	Ni	S	Fe	Co	Ni	S	Fe	Co	Ni	S	Fe	Co	Ni
S	38.59	38.26	37.09	33.17	37.30	32.69	34.74		38.00	32.31	34.41		32.70	35.31	38.88	
Fe	49.04	49.74	48.51	32.69	37.99	29.70	40.18		39.51	24.20	38.98		32.22	36.45	57.46	
Co	0.24	0.22	0.16	0.44	0.30	0.36	0.10		0.37	0.34	0.10		0.40	0.04	0.02	
Ni	11.45	12.78	9.82	33.79	21.60	32.89	2.47		20.52	39.84	2.41		31.14	0.27	1.78	
Cr	0.03	0.01	0.03	0.03	0.33	0.00	0.55		0.08	0.03	0.01		0.05	0.02	0.02	
Cu	0.02	0.16	2.51	0.47	0.11	0.60	19.23		0.13	0.06	20.28		0.49	24.26	0.05	
Total	99.37	101.16	98.12	100.60	97.65	96.28	97.30		98.63	96.81	96.19		96.98	96.38	98.21	
Sulf	<i>i</i>	<i>e</i>	<i>i</i>	<i>e</i>	<i>i</i>	<i>i</i>	<i>i</i>		<i>e</i>	<i>e</i>	<i>e</i>		<i>i</i>	<i>i</i>	<i>e</i>	
	Mss	Mss	Cu-MSS	Pn	Mss	Pn	Cp		Mss	Pn	Cp		Pn	Cp	Po	
	DC 08				DC 18				TL 142				TL 145			
	S	Fe	Co	Ni	S	Fe	Co	Ni	S	Fe	Co	Ni	S	Fe	Co	Ni
S	38.75	33.93	33.75	33.97	32.78	39.04			34.13	38.37			32.93	39.05		
Fe	44.49	31.01	29.49	29.89	30.94	58.22			30.48	50.29			29.35	51.47		
Co	0.21	0.16	0.31	0.01	0.51	0.02			0.00	0.11			0.63	0.11		
Ni	14.42	31.75	32.84	0.42	33.22	0.51			0.40	8.30			36.61	9.21		
Cr	0.02	0.01	0.36	0.02	0.01	0.01			0.05	0.03			-0.01	0.00		
Cu	0.10	0.28	0.10	31.89	0.08	0.07			31.51	0.06			-0.04	-0.01		
Total	98.00	97.18	96.91	96.22	97.58	97.90			96.59	97.22			99.48	99.87		
Sulf	<i>e</i>	<i>e</i>	<i>i</i>	<i>e</i>	<i>i</i>	<i>e</i>			<i>e</i>	<i>e</i>			<i>e</i>	<i>e</i>		
	Mss	Pn	Pn	Cp	Pn	Po			Cp	Fe-Mss			Pn	Mss		

e - enclosed; *i* - interstitial

Mss - monosulfide solid solution; Ni-Mss - nickel rich Mss; Cu-Mss - Cu bearing Mss;

Pn - pentlandite; Cp - chalcopyrite; Po - pyrrhotite; Go - godlevskite; Bo - bornite;

Mi - millerite

Table AD10

Core temperatures and pressures determined using geothermobarometer by Brey&Köhler (1990)

sample	T [°C]	P [GPa]	sample	T [°C]
SA01	1032.0	1.8	DUB170	669.94
SA02	941.8		DUB300	931.34
SA03	1098.3		DUB301	951.98
SA04	993.8		DUB311	1198.47
SA09	1033.2		DUB312	1149.57
SA10	1018.0		DUB313	962.00
SA11	1020.3		DUB316	1023.25
ELRU1	988.6		DUB317	802.46
ELRU2	942.0	1.9	DC08	896.50
ELRU3	760.3		DC09	967.88
ELRU4	952.3		DC18	904.78
ELRU5	1028.4	1.9	DC41	846.67
ELRU6	979.8	1.9	TL141	807.66
ELRU7	1034.0	1.9	TL142	748.60
ELRU9	1020.5	2.0	TL143	680.25
ELRU10	1035.0		TL145	708.73
ELRU11	918.6			
ELRU15	918.6			
ELRU16	969.3			
ELRU19	708.7			
POKA40	968.9			
POKA42	971.7	2.0		
POKA43	963.9			
POKA44	1097.0			
POKA45	929.7			
POKA48	1017.6			
POKA50	951.9			
POKA51	985.1			

CHAPTER II — North Patagonia

Mundl, A., Ntaflos, T., Ackerman, L., Bizimis, M., Bjerg, E.A., Wegner, W. & Hauzenberger, C.A., (accepted). Geochemical and Os-Hf-Nd-Sr isotopic characterization of north Patagonian mantle xenoliths: Implications for extensive melt extraction and percolation processes. *Journal of Petrology*, Thematic issue – 6th Orogenic Lherzolite Conference 2014.

Geochemical and Os-Hf-Nd-Sr isotopic characterization of north Patagonian mantle xenoliths: Implications for extensive melt extraction and percolation processes

Mundl, A.¹; Ntaflos, T.¹; Ackerman, L.²; Bizimis, M.³; Bjerg, E.A.⁴; Wegner, W.¹; Hauzenberger, C.A.⁵

¹Department of Lithospheric Research, University of Vienna, Althanstrasse 14, 1090 Vienna, Austria.

²Institute of Geology v.v.i., Academy of Sciences of the Czech Republic, Rozvojová 269, 165 00 Prague 6 – Lysolaje, Czech Republic. Czech Geological Survey, Geologická 6, 152 00 Prague 5, Czech Republic.

³Department of Earth and Ocean Sciences, University of South Carolina, 701 Sumter Street, Columbia, SC 29208, USA.

⁴INGEOSUR (CONICET-UNS) and Departamento de Geología, Universidad Nacional del Sur, San Juan 670, B8000ICN Bahía Blanca, Argentina.

⁵Institute for Earth Sciences, University of Graz, Heinrichstraße 26, 8010 Graz, Austria
(Corresponding author; andrea.mundl@univie.ac.at; +43-1-4277-53318)

ABSTRACT

Alkali basalt hosted mantle xenoliths were sampled at 4 different locations within the North Patagonian Massif, Argentina. The subcontinental lithospheric mantle (SCLM) beneath Comallo, Puesto Diaz and Cerro Chenque is mostly represented by spinel-harzburgites, while at Prahuaniyeu, spinel-garnet- and garnet-peridotites occur next to spinel-peridotites. Partial melting estimates of north Patagonian mantle xenoliths determined from clinopyroxene trace elements reveal up to 25 % melt extraction. While the SCLM beneath Puesto Diaz, Cerro Chenque and Comallo is exclusively represented by highly depleted mantle xenoliths, the Prahuaniyeu sample suite comprises both fertile lherzolites and depleted harzburgites. Elevated trace element compositions in all studied north Patagonian mantle samples indicate melt-rock interaction taking place after the initial melt depletion event. Variable primitive mantle normalized REE patterns of clinopyroxenes from within one sample locality suggest compositional changes attributed to melt percolation, which has not significantly affected the bulk rock and mineral major element compositions. Melt percolation processes have also been detected in isotopic compositions, as well as in highly siderophile element (HSE) systematics. Hf isotopic compositions are decoupled from Nd and Sr and have been affected by variable degrees of enrichment processes. Platinum group element (PGE) abundances also reveal indications for melt-rock reactions. This is, in some samples, reflected in a fractionation of the iridium-group PGEs and/or enrichment in the palladium-group PGEs and/or rhenium, which cannot result merely from partial melting processes. Rhenium depletion ages (T_{RDs}) determined from Os isotopic analyses reveal an at least late Paleoproterozoic (1.7 Ga) stabilization of the Prahuaniyeu SCLM. Mantle xenoliths sampled from beneath Comallo and Puesto

Diaz – Cerro Chenque yield distinctly younger T_{RDs} of 1.3 Ga and 1.0 Ga, respectively. Distinct differences in the character of mantle xenoliths from Prahuanियeu and from Puesto Diaz and Cerro Chenque (i.e. SCLM stabilization age and range of fertility) suggest at least 2 SCLM domains underneath the North Patagonian Massif.

Metasomatism; Patagonia; radiogenic isotopes; Re-Os; SCLM

INTRODUCTION

Mantle xenoliths - fragments of the lithospheric mantle - brought to the surface by volcanic eruptions can provide detailed information on the evolution and geological history of lithospheric mantle domains. Several studies of alkali basalt hosted Patagonian mantle xenoliths have been conducted over the past few decades to provide insights into the origin and geological history of Patagonia (e.g. Skewes & Stern, 1979; Stern *et al.*, 1989, 1999; Kempton *et al.*, 1999a, 1999b; Gorrington & Kay, 2000; Rivalenti *et al.*, 2004; Bjerg *et al.*, 2005, 2009; Conceição *et al.*, 2005; Schilling *et al.*, 2005, 2008; Ntaflos *et al.*, 2007; Wang *et al.*, 2008; Mundl *et al.*, 2014). Bjerg *et al.* (2005) concluded that peridotites from northern Patagonia have generally experienced greater melt depletion than mantle xenoliths from southern Patagonia. These authors also point out intense cryptic and modal metasomatic events that affected the SCLM underneath Patagonia. Rivalenti *et al.* (2004) mention an eastward fading slab imprint in the metasomatic agent affecting the SCLM of Patagonia. They also suggest differences in the extent of mantle wedge – melt interaction in northern and southern Patagonia attributed to different properties of the subducting slab. Based on Re-Os

isotopic data of Patagonian mantle xenoliths, Schilling *et al.* (2008) interpreted a Paleoproterozoic formation of the subcontinental lithospheric mantle (SCLM) underneath Prahuanियeu in the North Patagonian Massif (NPM) (Fig.1) and proposed a connection to the Cuyania terrane, the Pampeia terrane or the Río de la Plata craton, all located north of the North Patagonian Massif. These authors also argued for a younger Neoproterozoic lithospheric mantle underneath the rest of the North Patagonian Massif. From Re-Os isotopic systematics of mantle xenoliths, Schilling *et al.* (2008) and Mundl *et al.* (2014) interpreted a Mesoproterozoic stabilization age of the Deseado Massif SCLM located south of the North Patagonian Massif. Mundl *et al.* (2014) suggest an even older (early to late Paleoproterozoic) stabilization of the SCLM located south of the Deseado Massif.

The evolution of Patagonia is a matter of ongoing discussions, some interpretations favoring an allochthonous and other an autochthonous origin (Pankhurst *et al.*, 2006; Ramos, 2008; Rapalini *et al.*, 2010; 2013 and references therein). In this context, the accretionary history of the North Patagonian Massif and the Deseado Massif remain uncertain. The combination of various radiogenic isotope systems (Os-Hf-Nd-Sr) offers

an important tool to characterize the SCLM and potentially yields information on its age of stabilization and hence, the timing of the formation of the SCLM beneath continental regions. In addition to lithophile major and trace element analyses, the study of highly siderophile elements (HSE) can be used to monitor melt-depletion events and provide better insights into metasomatic processes within the lithospheric mantle.

In this study, we have conducted extensive geochemical and isotopic studies on mantle xenoliths collected at 4 locations within the North Patagonian Massif in order to contribute towards deciphering the character and the evolution of the back-arc SCLM in northern Patagonia.

GEOLOGICAL SETTING

Patagonia consists of three

geographical provinces. Rio Negro, in north Patagonia extends from S39° to S42°, Chubut Province from S42° to S46° and the southernmost Santa Cruz from S46° to S54°. The evolution of the Andean Cordillera is related to the subduction of the Nazca plate in the North and the Antarctic plate in the South underneath the South American plate. The Cordillera is divided into the Southern Volcanic Zone (SVZ) that extends down to S46° and the Austral Volcanic Zone (AVZ) from S49° to S53° (Stern *et al.*, 1999). These 2 zones are separated by a gap in volcanic activity (VAG) that is likely due to the subduction of the Chile Ridge (Fig. 1; e.g. Ramos, 1999). The North Patagonian Massif (NPM) is located between 39° and 44°S (Fig. 1). Its northern border is represented by the Neuquén and Colorado basins. To the south, the North Patagonian Massif is separated from the Deseado Massif

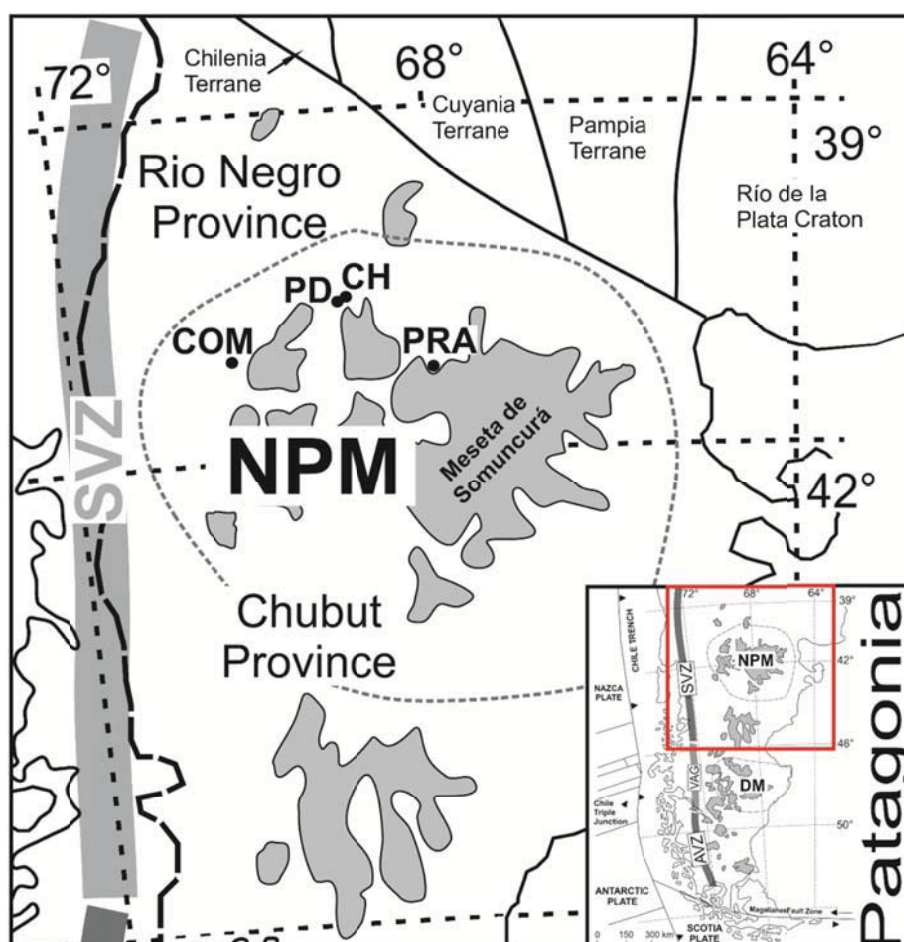


Fig. 1. Sample localities in simplified map of north Patagonia, modified from Bjerg *et al.* (2009). Area within dark grey dashed line: North Patagonian Massif (NPM). Light grey fields represent Tertiary and Quaternary flood basalts. DM – Deseado Massif; AVZ – Austral Volcanic Zone; VAG – Volcanic Activity Gap; SVZ – Southern Volcanic Zone. Mantle xenoliths were collected within the Rio Negro Province. Legend: CH – Cerro Chenque; PD – Puesto Diaz; COM – Comallo; PRA – Prahuaniqueu.

(Fig. 1) by the San Jorge basin. Martínez Dopico *et al.* (2011) suggested an initial basement formation of the North Patagonian Massif between 2.1 and 1.6 Ga inferred from Sm-Nd isotope characteristics of granites and orthogneisses. This Meso- to Paleoproterozoic basement is *inter alia* covered by voluminous products of various Phanerozoic magmatic events in northern Patagonia. The Meseta de Somuncura, a large volcanic province located between 40° and 43°S in the back arc tectonic area east of the Andean Cordillera (Fig. 1), consists of late Oligocene-Miocene to Pliocene volcanic rocks (Kay *et al.*, 2007; Labudia *et al.*, 2011). The basement comprises of late Precambrian to Paleozoic magmatic and metamorphic rocks that are covered by the extensive Jurassic silicic volcanics of the Chon Aike province (e.g. Kay *et al.*, 1989; Pankhurst & Rapela, 1995) and Cretaceous to Tertiary volcanic and sedimentary rocks (e.g. Rapela & Kay, 1988; Rapela *et al.*, 1988; Ardolino *et al.*, 1999). Munoz *et al.* (2002) and Kay *et al.* (2007) suggested a plume-like mantle upwelling responsible for the extensive plateau lavas in this region. Postdating the Meseta volcanic rocks are late Pliocene to early Pleistocene post-plateau alkali lava flows and cinder cones carrying mantle xenoliths.

ANALYTICAL METHODS

For bulk rock analyses, mantle xenolith samples were cut and host basalt rims and surface alterations were completely removed. After drying, samples were crushed and powdered in an agate mill. Bulk rock major and trace

elements were analyzed with the sequential X-ray spectrometer Phillips PW 2400, equipped with a Rh-excitation source at the University of Vienna, Department of Lithospheric Research. Fused disks for major element analyses were produced at 950°C from a mixture of specimen and Li₂B₄O₇ flux, diluted 1:5. The trace elements Sc, Ni, Cr, Co, Zn and Ga were analyzed on pressed pellets. Replicate analyses of geo-standard GSR-3 gave an overall procedural uncertainty better than 2% for major elements and 5% (Cu = 8.5%) for trace elements. Bulk rock powders were dissolved in HF:HNO₃ 1:3 mixture and trace elements (REE, HFSE, LILE, U and Th) were analyzed in solution on ICP-MS (Agilent 7500) at the Central Lab for Water, Minerals and Rocks, NAWI Graz, Karl-Franzens-University of Graz and Graz University of Technology.

Mineral major element analyses were carried out using a Cameca SX100 electron microprobe at the Department of Lithospheric Research, University of Vienna. The operating conditions were 15 kV acceleration voltage and 20 nA beam current. Natural and synthetic standards were used for calibration and standard correction procedures were applied.

Bulk rock osmium isotopic compositions and Re-Os concentrations were obtained at the Academy of Sciences of the Czech Republic (chemistry and ICP-MS) and at the Czech Geological Survey in Prague (N-TIMS). The chemical procedures followed that in Ackerman *et al.* (2013). In brief, the samples were dissolved and equilibrated with a mixed ¹⁸⁵Re-¹⁹⁰Os and ¹⁹¹Ir-⁹⁹Ru-¹⁰⁵Pd-¹⁹⁴Pt spikes

using Carius Tube technique (Shirey & Walker, 1995), followed by Os separation through solvent extraction by CCl_4 (Cohen & Waters, 1996) and Os microdistillation (Birck *et al.*, 1997). Iridium, ruthenium, platinum, palladium and rhenium were separated using anion exchange chromatography and then analyzed on sector field ICP-MS *Element 2* (Thermo) coupled with an Aridus IITM (CETAC) desolvating nebulizer. The Os isotopic compositions were determined by N-TIMS technique (Creaser *et al.*, 1991; Völkening *et al.*, 1991) on Finnigan MAT 262 thermal ionization spectrometer. Rhenium depletions ages (T_{RD} ; Walker *et al.*, 1989) were calculated using primitive upper mantle values of Meisel *et al.* (2001): $^{187}\text{Re}/^{188}\text{Os} = 0.4353$ and $^{187}\text{Os}/^{188}\text{Os} = 0.1296$; $\lambda^{187}\text{Re} = 1.666 \cdot 10^{-11}$ from Smoliar *et al.* (1996). Total procedural blanks were 0.1 pg for Os, 28 ± 32 pg for Ir, 28 ± 12 pg for Ru, 159 ± 82 pg for Pt, 110 ± 16 pg for Pd and 8 ± 6 pg for Re.

For Hf-Nd-Sr analyses, ~100 mg of optically pure clinopyroxenes per sample were handpicked under a binocular microscope from the crushed peridotite samples at the University of Vienna, Department of Lithospheric Sciences. Spongy rims and inclusions were completely removed. The separates were then leached in hot 6N HCl overnight and dissolved in 4 ml of mixture concentrated HF:HNO₃ (1:3) for 3 days before being dried down. The Hf isotope ratios were determined at the Center for Elemental Mass Spectrometry, University of South Carolina on a NEPTUNE MC-ICP-MS, with the Plus option installed (Bizimis *et al.*, 2013; Mallic *et al.*, in press). Hf was

separated from the matrix on the Ln resin (Eichrom, USA), following Munker *et al.* (2001). Sample introduction was through a 100 μl Teflon nebulizer coupled to an APEX system (ESI, USA). The measured ratios were corrected for mass fractionation using $^{179}\text{Hf}/^{177}\text{Hf} = 0.7325$. The JMC-475 standard was determined with $^{176}\text{Hf}/^{177}\text{Hf} = 0.282134 \pm 5$ ($n=13$, ~35ng Hf runs). All data are reported relative to the accepted JMC value of $^{176}\text{Hf}/^{177}\text{Hf} = 0.282160$. Hf blanks are typically <50 pg.

Sr and Nd isotopic compositions were obtained at the University of Vienna, Department of Lithospheric Research. About 50 mg of separated clinopyroxene fractions were leached in hot 6N HCl for 4 hours before being dissolved in a HF:HNO₃ 4:1 mixture, followed by dissolution in 1 ml of HNO₃ and subsequent transfer to 6N HCl. Element extraction (Sr, REE) was performed using AG 50W-X8 (200-400 mesh, Bio-Rad) resin and 2.5 N and 4.0 N HCl as eluents. Nd was separated from the REE group using teflon-coated HdEHP and 0.24 N HCl as eluent. Maximum total procedural blanks were < 1 ng for Sr and 50 pg for Nd, and were taken as negligible. The pure element fractions were evaporated using a Re double filament assembly and run in static mode on a Thermo-Finnigan Triton TIMS machine. A mean $^{87}\text{Sr}/^{86}\text{Sr}$ ratio of 0.710280 ± 0.000006 ($n = 7$) was determined for NBS987 (Sr) and a mean $^{143}\text{Nd}/^{144}\text{Nd}$ ratio of 0.511850 ± 0.000003 ($n = 7$) for La Jolla (Nd) international standards during the period of investigation. Within-run mass fractionation was corrected using

$^{88}\text{Sr}/^{86}\text{Sr} = 8.3752$, and $^{146}\text{Nd}/^{144}\text{Nd} = 0.7219$, respectively.

Clinopyroxene trace elements were analyzed with a LA-ICP-MS system (Laser ablation unit: ESI NWR 193; ICP-MS: Agilent 7500) at the Central Lab for Water, Minerals and Rocks, NAWI Graz, Karl-Franzens-University of Graz and Graz University of Technology. The material was ablated by using a 193 nm laser pulsed at 10 Hz, 50 to 75 μm spot size with an energy of $\sim 7 \text{ J/cm}^2$. Helium was used as carrier gas at $\sim 0.7 \text{ l/min}$ flow and data were acquired in time resolved mode. For each analysis a 30 second gas blank was obtained for background correction. A laser warmup for 30 seconds was done prior to ablation, then it was active for 60 seconds followed by 60 seconds washout time. The standard glasses NIST610 or NIST612 were routinely analyzed for standardization using values of Pearce *et al.* (1997) and drift correction while standards NIST614 and BCR-2 were analyzed as unknowns to monitor the accuracy of the measurements. Both standards could be reproduced within $\pm 10\%$ of the certified values. Silicon or calcium was used as internal standard.

RESULTS

Sample description and petrography

Mantle xenolith samples for this study were collected at 4 different outcrops in Rio Negro Province, North Patagonian Massif (Fig. 1). Sample localities are Comallo (COM), located $\sim 300 \text{ Km}$ east of the subduction zone front, Puesto Diaz (PD) and Cerro

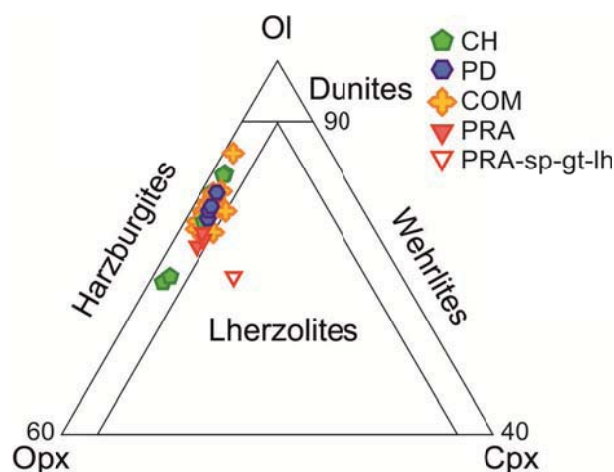


Fig. 2. Modal compositions of north Patagonian mantle xenoliths calculated using mineral and bulk rock major element compositions or determined by point counting method. With the exception of sample PRA74 (spinel-garnet-lherzolite) and CH48 (spinel-dunite), all samples plot in the harzburgite field. Abbreviations as in Fig. 1.

Chenque (CH), $\sim 130 \text{ Km}$ NE and Prahuaniyeu (PRA), $\sim 200 \text{ Km}$ ESE of Comallo. Studied COM samples were brought to the surface by lava flows, while mantle xenoliths from PD and CH were sampled from basaltic necks. In Prahuaniyeu, mantle xenoliths are found in nephelinites and tuffs. Host basalts from PD, CH and COM are of trachy-basaltic composition (Table 2). K/Ar ages of a Prahuaniyeu lava flow indicate an eruption $22.2 \pm 0.6 \text{ Ma}$ ago (unpublished data). The mantle xenolith carrying lava flow from Comallo yields K/Ar ages of $1.3 \pm 0.4 \text{ Ma}$ (unpublished data). No age determination for host rocks from Puesto Diaz and Cerro Chenque are available at this point. However, K/Ar data from the basaltic neck of Trafal, located 7-8 Km southeast of PD and CH, suggest eruption ages of $24.2 \pm 0.7 \text{ Ma}$ (unpublished data).

The studied sample suite comprises 28 new spinel-harzburgites and 2 new spinel-dunites. Modal compositions (Table 1 and Fig. 2) were determined by mass balance

Table 1: Modal compositions of north Patagonian mantle xenoliths calculated using bulk rock and mineral compositions.

	Puesto Diaz										Cerro Chenque					
	PDI*	PD2	PD28	PD32	PD51	PD61*	PD64	CH1	CH17	CH25	CH26	CH42	CH43	CH48	CH63	
OI	75.5	75.6	75.5	78.4	76.3	73.4	77.5	76.4	64.0	78.5	65.0	81.5	81.1	92.7	73.8	
Opx	20.3	21.6	21.6	19.1	21.0	22.1	19.4	21.2	33.6	19.9	32.2	16.5	16.8	1.2	23.3	
Cpx	2.4	2.1	2.3	1.9	2.3	2.7	2.1	1.8	1.5	1.2	2.0	1.5	1.4	2.4	2.3	
Spl	1.7	0.7	0.7	0.7	0.4	1.8	0.9	0.7	0.9	0.4	0.7	0.6	0.7	3.7	0.6	
Gt	-	-	-	-	-	-	-	-	-	-	-	-	-	-	-	
Rock type	H	H	H	H	H	H	H	H	H	H	H	H	H	D	H	

	Comallo										Prahuaniyeu					
	COM101	COM103	COM108	COM110	COM118	COM139	COM140	COM141	COM142	PR474	PR494	PR4301	PR4303	PR4306		
OI	76.1	75.7	75.5	75.8	75.2	72.0	72.7	73.6	84.6	64.6	77.8	69.8	70.8	72.1		
Opx	21.2	21.2	22.0	19.9	19.3	22.7	24.5	23.3	13.7	23.3	19.5	26.1	24.6	24.3		
Cpx	1.9	2.1	1.7	3.3	4.6	4.6	1.9	2.5	1.0	10.8	2.2	3.4	3.8	3.1		
Spl	0.9	1.0	0.8	0.9	0.9	0.7	0.9	0.6	0.8	<i>tr</i>	0.5	0.5	0.5	0.5		
Gt	-	-	-	-	-	-	-	-	-	1.6	-	-	-	-		
Rock type	H	H	H	H	H	H	H	H	H	L	H	H	H	H		

*modes determined by point counting method (1000 points/thin section).

H – harzburgite; D – dunite; L – lherzolite; OI – olivine; Opx – orthopyroxene; Cpx – clinopyroxene; Spl – spinel; Grt – garnet; tr – traces. Samples in italic: Data from Bjerg *et al.* (2009)

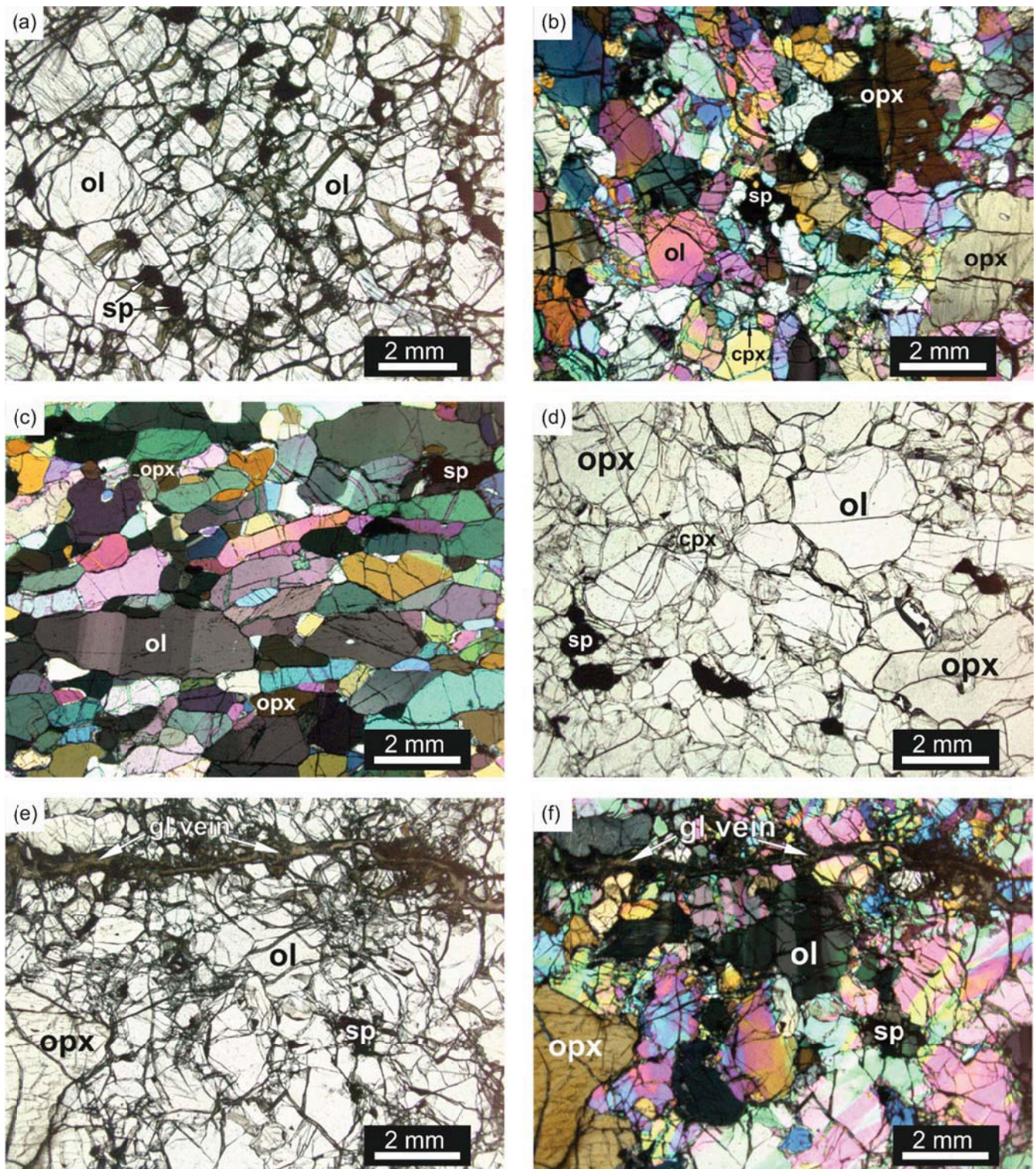


Fig. 3. Microphotographs of north Patagonian mantle xenoliths. (a) cumulate texture of dunite sample CH48 in plane-polarized light. (b) protogranular texture of harzburgite CH25 under cross-polarized light; notice kinked orthopyroxene and olivine. (c) foliated texture of sample COM108 under cross-polarized light; ol exhibit kink bands. (d) protogranular texture of sample COM141 in plane-polarized light. (e) protogranular harzburgite PD64; notice thick devitrified glass vein. (f) same as (e) under cross-polarized light. ol – olivine; opx – orthopyroxene; cpx – clinopyroxene; sp – spinel; gl vein – devitrified glass vein.

calculations of whole rock and mineral compositions or by point counting method (PD1 and PD61). Six additional spinel-harzburgites and 1 spinel-garnet lherzolite (PRA74) were chosen from

the large PRA sample suite previously studied by Bjerg *et al.* (2009) for further investigation. COM and PRA samples are fresh, while samples from PD and CH have experienced minor

serpentinization. Textures are mainly protogranular to porphyroclastic for PD and CH and protogranular to equigranular that often exhibit foliation, defined by aligned elongated orthopyroxene and olivine, in COM and PRA samples. See Fig. 3a-f for microphotographs of thin sections. Even though at COM sample locality many peridotites contain disseminated amphibole and/or phlogopite, only anhydrous samples were chosen to be analyzed for this work. Hence, none of the samples exhibit obvious modal metasomatism. However, many samples show thick melt veins (up to 100 μ m) cutting through the peridotites (Fig. 3e and 3f). These melt veins are dominantly filled with devitrified glass that sometimes contain tiny (\sim 1 μ m) Ni-Fe sulphides. In some samples, veins are filled with silica glass and secondary minerals, such as apatite, rutile and feldspars. Many samples show secondary textures, such as spongy rims around clinopyroxene, reaction rims around orthopyroxene and/or sieve textured spinel. Deformation textures, such as kink bands in olivine or bent exsolution lamellae in orthopyroxene, are a common feature in north Patagonian mantle xenoliths.

Bulk rock chemistry

Major and trace element concentrations are given in Table 2.

Major elements

Bulk rock Al_2O_3 and CaO compositions of the studied samples lie within a narrow range of 0.68 to 1.31 wt. % and 0.36 to 1.25 wt. %, respectively. With the exception of sample PRA74, a

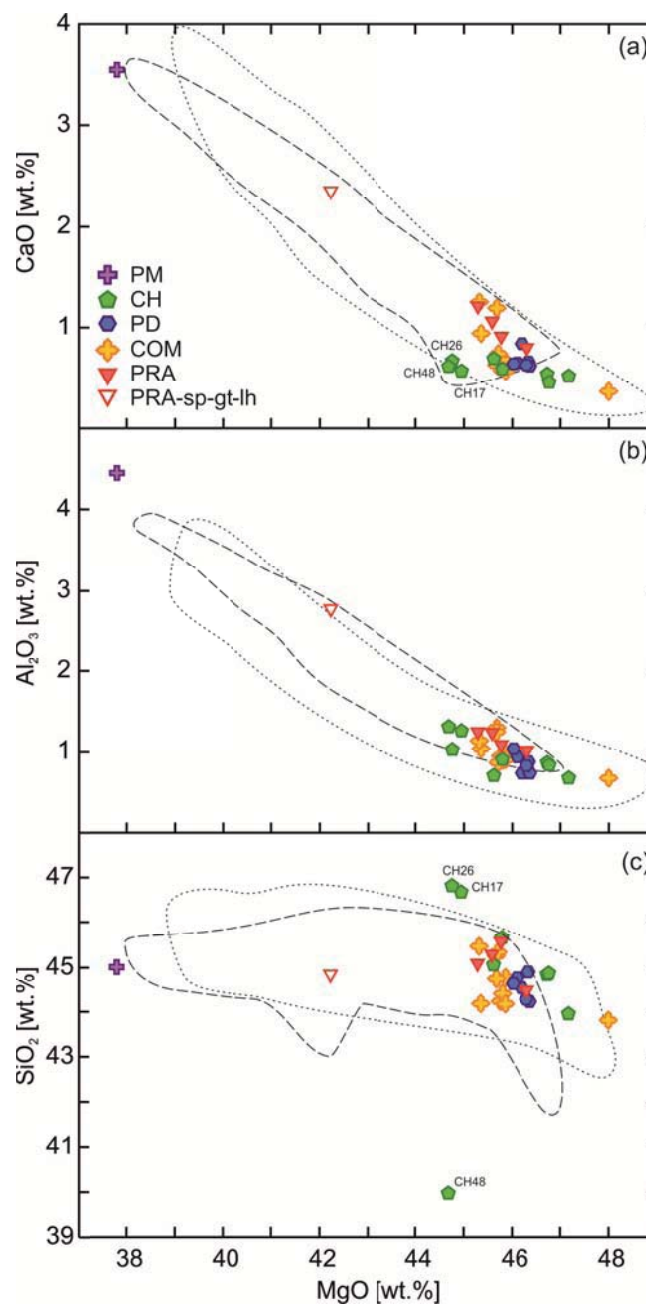


Fig. 4. Bulk rock MgO vs. Al_2O_3 (a), CaO (b) and SiO_2 (c) contents, respectively. Dashed line covers all Prahuaniyeu mantle xenoliths from Bjerg *et al.*, 2009; dotted line represents bulk rock compositions of southern Patagonian mantle xenoliths from Mundl *et al.* (2014). Samples CH48 (cumulate dunite), CH17 and CH26 deviate from the melting trends in (a) and (c). Legend and abbreviations as in Fig. 2; PM – primitive mantle from McDonough & Sun (1995).

spinel-garnet-lherzolite with Al_2O_3 and CaO contents of 2.78 and 2.35 wt. %, respectively, the studied samples represent an overall strongly depleted sample suite. Generally, there is a visible co-variation between major

Table 2: Bulk rock major and trace element compositions of PD, CH, COM and PRA samples

	Mantle Xenoliths									
	PD2 ^I	PD12 ^I	PD28 ^I	PD32 ^{II}	PD51 ^I	PD64 ^I	CH1 ^I	CH17 ^I	CH25 ^I	CH26 ^I
wt.%										
SiO ₂	44.9	44.5	44.8	44.2	44.6	44.3	44.8	46.7	44.9	46.8
TiO ₂	0.005	0.001	0.002	0.013	0.023	0.003	0.003	0.003	0.006	0.007
Al ₂ O ₃	0.877	0.736	0.937	0.736	1.039	0.827	0.867	1.259	0.837	1.028
FeO	7.110	7.275	7.101	7.586	7.897	7.632	7.192	6.498	7.585	6.918
MnO	0.111	0.111	0.121	0.121	0.121	0.121	0.111	0.111	0.121	0.121
MgO	46.3	46.2	46.1	46.4	46.0	46.3	46.7	45.0	46.8	44.8
CaO	0.655	0.837	0.645	0.615	0.636	0.625	0.534	0.564	0.454	0.665
Na ₂ O	<0.01	<0.01	<0.01	<0.01	<0.01	<0.01	<0.01	<0.01	<0.01	<0.01
K ₂ O	0.006	0.020	0.007	0.023	0.017	0.012	0.007	0.005	0.008	0.010
P ₂ O ₅	0.009	0.007	0.007	0.016	0.011	0.008	0.012	0.013	0.010	0.012
Total	100.01	99.74	99.70	99.72	100.41	99.82	100.29	100.08	100.65	100.34
Mg#	0.92	0.92	0.92	0.92	0.91	0.92	0.92	0.92	0.92	0.92
LOI%	0.69	0.53	0.70	0.60	1.01	0.45	0.46	0.39	0.60	0.56
ppm										
Sr	0.582	1.920	1.859	2.926	1.824	<0.1	0.019	<0.1	<0.1	0.108
Ga	2.3	2.3	2.8	2.9	2.6	2.2	2.0	2.9	2.8	4.1
Zn	63.5	75.7	66.2	68.6	74.2	69.9	65.3	61.3	60.2	63.6
Ni	2985	3055	2923	3026	2669	3035	3034	2702	2849	2690
Co	184	188	183	199	195	197	187	165	190	168
Cr	3335	2986	3303	3212	2770	3916	3091	4036	3113	3982
Sc	6.2	8.2	8.6	8.9	7.0	9.7	7.7	9.9	5.5	8.6
V	45.3	48.4	29.4	38.2	40.7	43.8	34.8	49.2	40.4	41.5
Y	<0.1	<0.1	<0.1	0.104	0.190	<0.1	0.010	<0.1	0.028	<0.1
Nb	0.006	<0.1	<0.1	0.562	0.126	0.008	0.066	0.001	0.027	0.050
La	0.102	0.073	0.137	0.947	0.211	0.121	0.100	0.117	0.153	0.129
Ce	0.182	0.109	0.254	1.595	0.412	0.215	0.202	0.207	0.297	0.209
Pr	0.019	0.009	0.018	0.155	0.050	0.023	0.018	0.020	0.033	0.020
Nd	0.060	0.032	0.050	0.529	0.181	0.074	0.081	0.070	0.126	0.063
Sm	n.d.	0.012	n.d.	0.089	0.047	n.d.	0.031	n.d.	0.038	n.d.
Eu	n.d.	0.001	n.d.	0.023	0.012	n.d.	0.008	n.d.	0.008	n.d.
Gd	n.d.	0.010	n.d.	0.095	0.057	n.d.	0.031	n.d.	0.037	n.d.
Tb	0.001	0.001	0.001	0.010	0.010	0.002	0.004	0.001	0.005	0.002
Dy	0.006	0.002	0.004	0.054	0.058	0.014	0.026	0.006	0.029	0.010
Ho	0.002	0.001	0.002	0.010	0.015	0.003	0.007	0.002	0.007	0.003
Er	0.006	0.001	0.006	0.033	0.040	0.010	0.017	0.006	0.024	0.009
Tm	0.001	0.001	0.002	0.004	0.007	0.003	0.003	0.002	0.005	0.002
Yb	0.015	0.010	0.020	0.034	0.063	0.020	0.028	0.016	0.036	0.019
Lu	0.003	0.002	0.003	0.005	0.010	0.003	0.005	0.002	0.007	0.002
Hf	0.04	0.03	0.05	0.06	0.08	0.05	0.04	0.03	0.04	0.04
Ta	<0.1	0.059	<0.1	<0.1	<0.1	<0.1	<0.1	<0.1	<0.1	0.069
Pb	0.402	0.412	0.328	0.564	0.365	0.361	0.382	0.356	0.329	0.413
Th	0.028	0.034	0.067	0.152	0.046	0.038	0.214	0.032	0.041	0.055
U	0.047	0.077	0.031	0.042	0.034	0.037	0.059	0.017	0.019	0.029

PD: Puesto Diaz; CH: Cerro Chenque; COM: Comallo; PRA: Prahuaniyeu; Italic values: ICP-MS analyses; others: XRF analyses; n.d.: not determined; ^{I, II, III}: Group affiliations according to PM-normalized REE patterns (Fig. 5); * Bjerg *et al.* (2009), § Ntaflos *et al.* (2000).

Table 2: continued

Mantle Xenoliths										
	CH42 ^I	CH43 ^I	CH48 ^{III}	CH63 ^I	COM101 ^{II}	COM103 ^{II}	COM108 ^I	COM110 ^{III}	COM118 ^{II}	COM139 ^{II}
wt. %										
SiO ₂	44.0	45.7	40.0	45.1	44.2	44.8	44.2	44.2	44.7	45.5
TiO ₂	0.007	0.002	0.057	0.008	0.030	0.020	0.027	0.043	0.070	0.036
Al ₂ O ₃	0.676	0.907	1.310	0.706	0.948	0.978	0.907	1.038	1.300	1.139
FeO	7.366	6.818	14.155	7.650	7.856	7.476	7.711	7.729	7.174	7.439
MnO	0.111	0.111	0.173	0.121	0.121	0.121	0.121	0.121	0.121	0.121
MgO	47.2	45.8	44.7	45.6	45.8	45.9	45.9	45.4	45.7	45.3
CaO	0.514	0.584	0.609	0.686	0.605	0.645	0.565	0.938	1.189	1.250
Na ₂ O	<0.01	<0.01	<0.01	<0.01	0.001	<0.01	0.001	0.001	<0.01	<0.01
K ₂ O	0.012	0.005	0.004	0.007	0.005	0.015	0.010	0.009	0.060	0.014
P ₂ O ₅	0.014	0.011	0.031	0.009	0.017	0.026	0.012	0.019	0.013	0.009
Total	99.84	99.89	100.99	99.85	100.21	100.80	100.04	100.09	101.15	101.63
Mg#	0.92	0.92	0.85	0.91	0.91	0.92	0.91	0.91	0.92	0.92
LOI%	0.27	0.69	0.82	1.07	-0.40	-0.41	-0.39	-0.42	-0.30	-0.22
ppm										
Sr	0.871	<0.1	3.935	<0.1	4.488	5.409	4.112	7.140	15.018	7.933
Ga	9.0	2.6	4.4	3.4	1.0	2.7	0.6	1.3	2.8	2.8
Zn	66.7	66.6	139.7	65.0	46.9	69.4	46.2	47.8	65.7	67.9
Ni	3145	2820	2869	3005	2362	2972	2371	2367	2933	2956
Co	198	172	336	194	118	193	116	117	185	191
Cr	3093	3564	6355	3094	2186	3417	2228	2322	2923	3148
Sc	7.7	10.4	9.6	12.1	4.2	7.9	4.2	6.0	9.5	8.7
V	40.4	43.4	50.5	47.8	25.5	40.8	20.2	22.5	43.1	55.7
Y	<0.1	<0.1	0.228	<0.1	0.238	0.294	0.115	0.378	0.484	0.236
Nb	0.138	<0.1	0.213	0.174	0.037	0.119	0.094	<0.1	0.292	0.078
La	0.235	0.082	0.174	0.111	0.303	0.418	0.257	0.198	0.495	0.308
Ce	0.458	0.142	0.428	0.147	0.721	0.872	0.655	0.670	1.076	0.793
Pr	0.051	0.015	0.063	0.014	0.101	0.110	0.085	0.131	0.154	0.096
Nd	0.200	0.036	0.332	0.053	0.431	0.487	0.366	0.721	0.717	0.416
Sm	0.043	n.d.	0.096	n.d.	0.114	0.123	0.089	0.174	0.178	0.101
Eu	0.009	n.d.	0.028	n.d.	0.033	0.032	0.026	0.057	0.059	0.029
Gd	0.044	n.d.	0.096	n.d.	0.103	0.106	0.084	0.140	0.185	0.104
Tb	0.004	0.001	0.014	0.002	0.014	0.014	0.010	0.023	0.025	0.015
Dy	0.021	0.009	0.081	0.013	0.084	0.085	0.052	0.116	0.135	0.090
Ho	0.004	0.002	0.017	0.003	0.018	0.018	0.010	0.022	0.026	0.018
Er	0.011	0.006	0.046	0.008	0.051	0.050	0.030	0.059	0.073	0.050
Tm	0.003	0.001	0.007	0.003	0.009	0.008	0.006	0.009	0.012	0.007
Yb	0.021	0.013	0.055	0.019	0.059	0.055	0.036	0.056	0.070	0.052
Lu	0.003	0.002	0.009	0.004	0.010	0.009	0.006	0.010	0.010	0.008
Hf	0.05	0.03	0.10	0.05	0.17	0.15	0.09	0.12	0.10	0.08
Ta	0.003	<0.1	0.318	0.004	0.028	<0.1	0.046	<0.1	0.066	<0.1
Pb	0.353	0.372	0.482	0.543	0.932	0.406	0.532	0.444	0.364	5.904
Th	0.046	0.040	0.036	0.042	0.054	0.070	0.052	0.034	0.047	0.039
U	0.034	0.026	0.026	0.062	0.031	0.044	0.023	0.022	0.027	0.027

PD: Puesto Diaz; CH: Cerro Chenque; COM: Comallo; PRA: Prahuanique; Italic values: ICP-MS analyses; others: XRF analyses; n.d.: not determined; ^{I, II, III}: Group affiliations according to PM-normalized REE patterns (Fig. 5); * Bjerg *et al.* (2009), [§] Ntaflos *et al.* (2000).

Table 2: continued

Mantle Xenoliths								
	COM140 ^{III}	COM141 ^I	COM142 ^{II}	PRA74 ^{III*}	PRA94 ^{I*}	PRA301 ^{I*}	PRA303 ^{I*}	PRA306 ^{II*}
wt. %								
SiO ₂	45.3	45.3	43.8	44.8	44.5	45.3	45.1	45.6
TiO ₂	0.027	0.003	0.018	0.089	0.037	0.024	0.033	0.079
Al ₂ O ₃	1.250	0.867	0.675	2.760	1.019	1.240	1.251	1.089
FeO	7.467	7.129	7.138	9.010	8.061	7.732	7.787	7.439
MnO	0.121	0.121	0.111	0.130	0.131	0.121	0.121	0.121
MgO	45.7	45.7	48.0	42.2	46.3	45.6	45.3	45.8
CaO	0.625	0.736	0.363	2.350	0.797	1.059	1.210	0.907
Na ₂ O	<0.01	<0.01	<0.01	0.186	0.045	0.023	0.064	0.118
K ₂ O	0.003	0.003	0.012	0.013	0.068	0.005	0.027	0.019
P ₂ O ₅	0.015	0.009	0.015	0.017	0.026	0.082	0.048	0.169
Total	101.28	100.80	101.03	100.77	100.99	101.15	100.91	101.28
Mg#	0.92	0.92	0.92	0.89	0.91	0.91	0.91	0.92
LOI%	-0.34	-0.33	-0.30	<i>n.d.</i>	<i>n.d.</i>	<i>n.d.</i>	<i>n.d.</i>	<i>n.d.</i>
ppm								
Sr	2.581	7.777	2.970	<i>n.d.</i>	<i>n.d.</i>	<i>n.d.</i>	<i>n.d.</i>	<i>n.d.</i>
Ga	3.4	2.1	2.5	5.10	4.00	3.00	4.00	4.00
Zn	69.9	65.0	66.6	67	62	59	61	61
Ni	2844	2924	3173	11.00	<i>n.d.</i>	<i>n.d.</i>	<i>n.d.</i>	<i>n.d.</i>
Co	190	185	194	2155	2353	2340	2372	2198
Cr	3303	3487	3229	100	111	106	207	100
Sc	11.5	8.2	7.2	2952	2448	2820	2682	2780
V	44.6	45.2	29.4	8.30	6.00	6.20	6.30	7.10
Y	0.241	<0.1	0.127	<i>n.d.</i>	<i>n.d.</i>	<i>n.d.</i>	<i>n.d.</i>	<i>n.d.</i>
Nb	<0.1	<0.1	0.038	<i>n.d.</i>	<i>n.d.</i>	<i>n.d.</i>	<i>n.d.</i>	<i>n.d.</i>
La	0.130	0.397	0.295	0.412	0.414	0.237	1.024	1.474
Ce	0.388	0.901	0.503	0.591	0.852	0.46	1.229	2.965
Pr	0.062	0.114	0.073	0.141	0.101	0.061	0.121	0.313
Nd	0.330	0.443	0.312	0.673	0.402	0.241	0.462	1.361
Sm	0.103	0.077	0.071	0.205	0.1	0.06	0.131	0.311
Eu	0.031	0.023	0.020	0.067	0.03	0.016	0.04	0.1
Gd	0.094	0.061	0.072	0.229	0.083	0.041	0.1	0.321
Tb	0.013	0.007	0.009	0.039	0.011	0.006	0.013	0.055
Dy	0.079	0.027	0.049	0.237	0.06	0.039	0.07	0.305
Ho	0.017	0.006	0.012	0.052	0.011	0.009	0.013	0.078
Er	0.050	0.017	0.035	0.14	0.048	0.03	0.042	0.231
Tm	0.009	0.003	0.006	0.022	0.009	0.006	0.009	0.039
Yb	0.060	0.026	0.035	0.13	0.067	0.048	0.05	0.264
Lu	0.010	0.004	0.006	0.02	0.011	0.01	0.01	0.04
Hf	0.09	0.09	0.08	<i>n.d.</i>	<i>n.d.</i>	<i>n.d.</i>	<i>n.d.</i>	<i>n.d.</i>
Ta	<0.1	<0.1	0.641	<i>n.d.</i>	<i>n.d.</i>	<i>n.d.</i>	<i>n.d.</i>	<i>n.d.</i>
Pb	0.426	0.540	0.398	<i>n.d.</i>	<i>n.d.</i>	<i>n.d.</i>	<i>n.d.</i>	<i>n.d.</i>
Th	0.035	0.044	0.052	<0.01	0.11	0.06	0.15	0.02
U	0.016	0.022	0.026	<i>n.d.</i>	<i>n.d.</i>	<i>n.d.</i>	<i>n.d.</i>	<i>n.d.</i>

PD: Puesto Diaz; CH: Cerro Chenque; COM: Comallo; PRA: Prahuaniyeu; Italic values: ICP-MS analyses; others: XRF analyses; *n.d.*: not determined; ^{I, II, III}: Group affiliations according to PM-normalized REE patterns (Fig. 5); * Bjerg *et al.* (2009), § Ntaflos *et al.* (2000).

Table 2: continued

Host basalts				
	PD	CH	COM [§]	PRA*
wt. %				
SiO ₂	47.5	48.8	48.2	39.74
TiO ₂	2.20	2.22	2.09	3.25
Al ₂ O ₃	14.3	15.9	15.7	9.7
FeO	11.4	10.8	11.0	14.5
MnO	0.16	0.14	0.16	0.22
MgO	9.63	6.72	8.31	13.63
CaO	8.81	7.11	9.07	11.39
Na ₂ O	3.23	4.07	3.82	4.29
K ₂ O	2.17	2.73	1.49	1.20
P ₂ O ₅	0.68	0.81	0.40	1.40
Total	100.07	99.26	100.17	99.26
Mg#	0.60	0.53	0.57	0.63
LOI%	1.35	1.25	<i>n.d.</i>	0.47
ppm				
<i>Sr</i>	911	930	550	1503
<i>Ga</i>	18	20	20	23
<i>Zn</i>	89	83	90	130
<i>Ni</i>	218	111	122	376
<i>Co</i>	45	35	40	55
<i>Cr</i>	328	131	212	467
<i>Sc</i>	8.1	5.7	23	17
<i>V</i>	195	141	190	170
<i>Y</i>	20	23	24	43
<i>Nb</i>	59	63	25	123
<i>La</i>	58	60	14	106
<i>Ce</i>	89	110	41	219
<i>Pr</i>	<i>n.d.</i>	<i>n.d.</i>	<i>n.d.</i>	<i>n.d.</i>
<i>Nd</i>	43	42	15	83
<i>Sm</i>	<i>n.d.</i>	<i>n.d.</i>	4.4	16
<i>Eu</i>	<i>n.d.</i>	<i>n.d.</i>	1.6	4.9
<i>Gd</i>	<i>n.d.</i>	<i>n.d.</i>	<i>n.d.</i>	<i>n.d.</i>
<i>Tb</i>	<i>n.d.</i>	<i>n.d.</i>	0.90	1.77
<i>Dy</i>	<i>n.d.</i>	<i>n.d.</i>	<i>n.d.</i>	<i>n.d.</i>
<i>Ho</i>	<i>n.d.</i>	<i>n.d.</i>	<i>n.d.</i>	<i>n.d.</i>
<i>Er</i>	<i>n.d.</i>	<i>n.d.</i>	<i>n.d.</i>	<i>n.d.</i>
<i>Tm</i>	<i>n.d.</i>	<i>n.d.</i>	<i>n.d.</i>	<i>n.d.</i>
<i>Yb</i>	<i>n.d.</i>	<i>n.d.</i>	1.9	2.56
<i>Lu</i>	<i>n.d.</i>	<i>n.d.</i>	0.19	0.28
<i>Hf</i>	2.4	4.6	2.9	16.1
<i>Ta</i>	3.2	4.3	<i>n.d.</i>	<i>n.d.</i>
<i>Pb</i>	1.2	1.7	0.53	<i>n.d.</i>
<i>Th</i>	7.4	9.0	3.0	<i>n.d.</i>
<i>U</i>	4.600	4.600	<i>n.d.</i>	<i>n.d.</i>

PD: Puesto Diaz; CH: Cerro Chenque; COM: Comallo; PRA: Prahuanieyu; *Italic values*: ICP-MS analyses; others: XRF analyses; *n.d.*: not determined; ^{I, II, III}: Group affiliations according to PM-normalized REE patterns (Fig. 5); * Bjerg *et al.* (2009), [§] Ntaflos *et al.* (2000).

elements. Al_2O_3 and CaO decrease with increasing MgO ranging from 44.7 to 48.0 wt. %, and 42.2 wt. % for PRA74 (Fig. 4a and 4b). CaO contents of samples CH17, CH26 and CH48 are lower at given MgO and slightly deviate from the apparent melt depletion trend defined by the remaining samples. Samples CH17 and CH26 have a high orthopyroxene/olivine ratio (~ 0.5), whereas sample CH48 likely represents a cumulate spinel-dunite. A deviation of these three samples from the rest of the sample suite is also illustrated in SiO_2 vs. MgO (Fig. 4c). While the cumulate dunite CH48 has low bulk rock SiO_2 contents (40.0 wt. %), samples CH17 and CH26 show higher SiO_2 at given MgO contents relative to the rest of the sample suite resulting from the high orthopyroxene/olivine ratio. For comparison, fields for the Prahuaniyeu sample suite studied by Bjerg *et al.* (2009) and bulk rock compositions of southern Patagonian mantle xenoliths from Mundl *et al.* (2014) are added to Fig. 4a-c.

Trace elements

Primitive mantle (PM) normalized rare earth element (REE) patterns divide the spinel-peridotite sample suite into 3 distinct groups (Fig. 5a-c). Group I is defined by a U-shaped REE pattern with a strong enrichment in LREE and a minor enrichment in MREE relative to HREE ($(\text{La}/\text{Yb})_N=2-14$; $(\text{Sm}/\text{Yb})_N<1-3$). Group II samples exhibit a roughly linear enrichment from HREE to LREE ($(\text{La}/\text{Sm})_N=2-7$; $(\text{Sm}/\text{Yb})_N=1-3$) and samples from Group III display a hump in MREE over HREE and LREE ($(\text{La}/\text{Sm})_N<1$; $(\text{Sm}/\text{Yb})_N=2-3$). The sole spinel-garnet-lherzolite sample PRA74

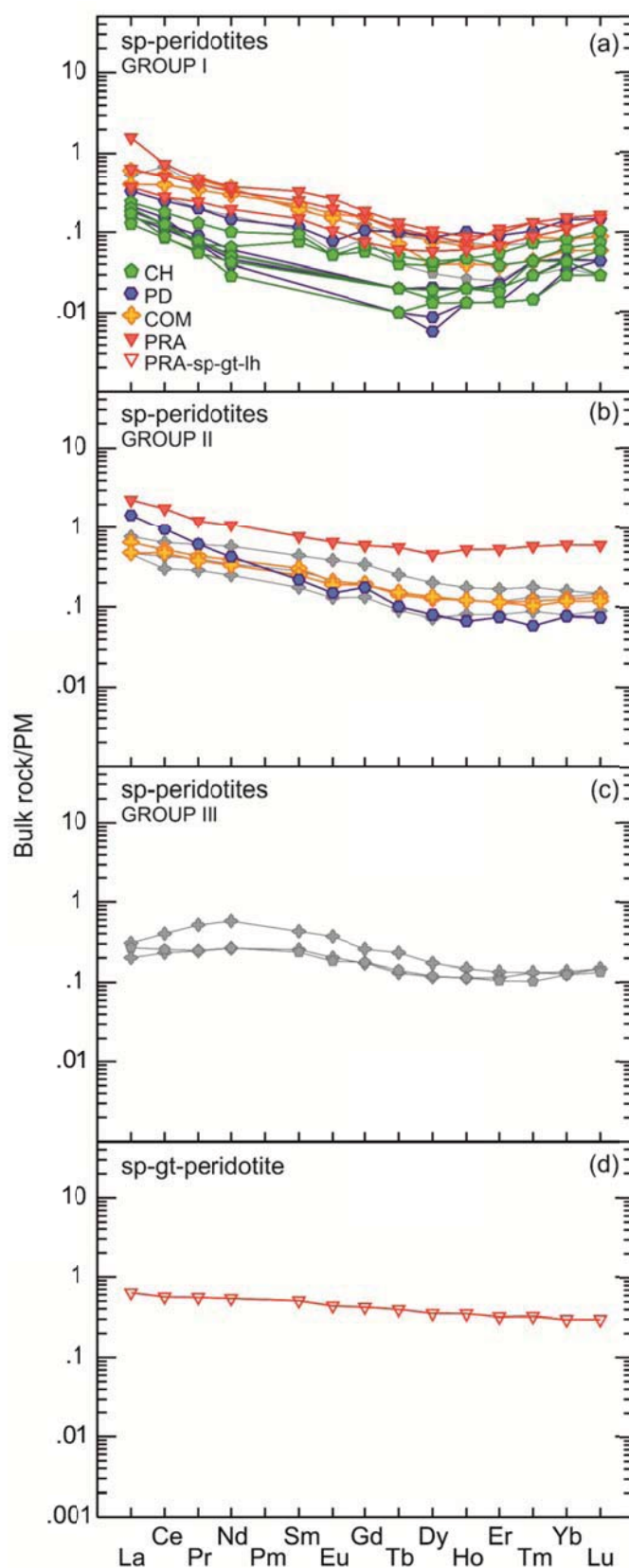


Fig. 5. Primitive mantle (PM) normalized bulk rock rare earth element (REE) distribution patterns. (a), (b) and (c) represent different groups and (d) represents spinel-garnet-lherzolite. Highlighted are samples further investigated for Re-Os isotopic compositions and HSE contents: in (a) Group I: CH1, CH25, CH26, CH43, CH63, COM108, COM141, PD28, PD51, PD64, PRA94, PRA301, PRA303; in (b) Group II: COM103, COM139, PD32, PRA306. (c) None of Group III samples has been analyzed for Re-Os or HSE compositions; Group I, Group II and Group III are represented by spinel-peridotites, Group IV comprises spinel-garnet-peridotite PRA74. Legend and abbreviations as in Fig. 2. PM from McDonough & Sun (1995).

shows a nearly flat PM-normalized pattern from HREE to MREE with a minor enrichment in La ($(La/Sm)_N=1.3$) (Fig. 5d). All studied samples exhibit elevated LREE and/or MREE. These enrichments contrast the strong depletions recorded in the major element systematics described above and therefore suggest variable enrichment process(es) after the initial melt depletion event.

Mineral chemistry

Olivine

Olivine major element analyses are given in Table 3. Forsterite (Fo) contents in all samples fall within a narrow range between $Fo_{90.8-91.9}$ for spinel-harzburgites and $Fo_{90.5}$ for the spinel-garnet-lherzolite PRA74. Two cumulate dunites, PD and CH, yield distinctly lower Fo contents of 85.9. The NiO and CaO compositions range from 0.37 to 0.45 wt. % and 0.03 to 0.15 wt. %, respectively in mantle peridotites and from 0.30 to 0.32 wt. % and 0.7 wt. %, respectively in cumulate dunites.

Orthopyroxene

Orthopyroxene microprobe analyses are given in Table 4. Orthopyroxenes in spinel-harzburgites with compositions $En_{89-91}Wo_{1-3}Fs_{8-9}$ yield narrow mg# $[Mg/(Mg+Fe_{tot})]$ between 0.91 and 0.92. The spinel-garnet-lherzolite and the cumulate spinel-dunites have orthopyroxene compositions of $En_{89}Wo_2Fs_9$ with mg# 0.91 and $En_{85}Wo_1Fs_{14}$ with mg# 0.87, respectively. Orthopyroxenes in spinel-garnet lherzolite PRA74 has with 5.7 wt. % the highest Al_2O_3 content of all analyzed orthopyroxenes.

Clinopyroxene

Major elements: Clinopyroxene major element results are given in Table 5. Clinopyroxene in spinel-harzburgites are Cr-diopsides with mean compositions $En_{48-54}Wo_{42-49}Fs_{3-5}$ and mg# 0.91-0.95. Clinopyroxenes in the two cumulate dunites are augites with mean $En_{46}Wo_{47}Fs_7$ and mg# 0.86. Cr_2O_3 contents vary between 0.71 and 1.24 wt. % in PD, CH and COM samples. Clinopyroxenes in PRA samples have generally higher Cr_2O_3 compositions with 1.11 to 1.53 wt. % in spinel-peridotites. Na_2O and TiO_2 compositions in north Patagonian mantle xenolith clinopyroxenes range from 0.27 to 1.48 wt. % and from 0.01 to 0.86 wt. %, respectively.

Trace elements: According to their clinopyroxene trace element compositions (Table 6), the samples were divided into 4 different groups (Fig. 6). Clinopyroxene PM-normalized patterns of those samples further analyzed for Sr-Nd-Hf isotopic compositions are highlighted. **Group I** is represented by samples with PM-normalized REE patterns showing a hump in MREE over HREE and LREE elements. Thus, $(La/Sm)_N < 1$ and $(Sm/Yb)_N = 1.3-5.4$. All samples of this group exhibit negative Zr and Ti anomalies relative to the adjacent elements in a PM-normalized extended trace element diagram. While some clinopyroxenes show either positive Pb (CH1) or positive Sr anomalies (COM108, COM118, COM142), the two cumulate dunites PD48 and CH48 exhibit both, an enrichment in Sr as well as in Pb. The remaining clinopyroxenes from this Group exhibit negative Sr and

Table 3: Average olivine major element compositions determined using microprobe analysis

	PD1	PD2	PD7	PD27	PD28	PD32	PD48	PD51	PD61	PD64	CHI	CHI2	CHI7	CH25	CH26	CH42	CH43	CH48	CH63
n	6	2	6	4	4	4	6	4	6	7	6	4	5	4	7	5	3	5	5
SiO ₂	41.4	41.4	41.4	41.2	41.2	41.2	40.1	41.1	41.1	41.0	41.1	41.2	41.2	41.2	41.1	41.1	41.1	40.1	40.9
TiO ₂	0.002	0.000	0.002	0.010	0.009	0.000	0.014	0.002	0.010	0.008	0.003	0.006	0.009	0.000	0.006	0.006	0.021	0.006	0.006
Al ₂ O ₃	0.001	0.002	0.001	0.012	0.009	0.006	0.012	0.001	0.000	0.005	0.013	0.006	0.000	0.002	0.005	0.022	0.000	0.005	0.005
Cr ₂ O ₃	0.014	0.031	0.027	0.006	0.014	0.030	0.003	0.000	0.026	0.033	0.002	0.008	0.013	0.004	0.011	0.013	0.013	0.016	0.004
FeO*	8.50	8.09	8.01	8.08	8.22	8.55	13.27	8.99	8.60	8.75	8.20	8.42	7.95	8.64	8.37	8.44	8.19	13.46	8.78
MnO	0.125	0.115	0.107	0.119	0.125	0.132	0.193	0.140	0.129	0.132	0.120	0.112	0.116	0.131	0.125	0.1235	0.129	0.178	0.123
NiO	0.393	0.416	0.394	0.395	0.413	0.404	0.298	0.373	0.392	0.395	0.403	0.408	0.413	0.373	0.409	0.423	0.411	0.322	0.409
MgO	50.0	50.2	50.0	50.0	50.3	50.0	45.5	49.7	49.0	49.7	50.2	50.2	50.5	49.5	49.8	49.7	50.0	45.9	49.7
CaO	0.052	0.028	0.044	0.041	0.058	0.068	0.071	0.039	0.070	0.061	0.062	0.087	0.100	0.045	0.063	0.082	0.118	0.075	0.045
P ₂ O ₅	0.001	0.002	0.003	0.005	0.008	0.012	0.030	0.001	0.006	0.003	0.000	0.012	0.001	0.006	0.005	0.001	0.004	0.038	0.006
Total	100.51	100.27	100.02	99.87	100.44	100.42	99.54	100.32	99.41	100.07	100.14	100.44	100.31	99.86	99.88	99.89	100.03	100.15	99.92
Mg#	0.91	0.92	0.92	0.92	0.92	0.91	0.86	0.91	0.91	0.91	0.92	0.91	0.92	0.91	0.91	0.91	0.92	0.86	0.91

	COM101	COM103	COM108	COM110	COM118	COM139	COM140	COM141	COM142	PRA1	PRA74	PRA94	PRA301	PRA303	PRA306
n	>10	>10	>10	>10	>10	>10	>10	>10	>10	>10	>10	>10	>10	>10	>10
SiO ₂	41.0	41.2	41.0	41.0	41.1	40.9	41.0	41.2	41.3	41.1	41.0	40.9	40.9	41.0	41.2
TiO ₂	0.011	0.003	0.005	0.011	0.007	0.006	0.007	0.002	0.009	<i>n.d.</i>	<i>n.d.</i>	<i>n.d.</i>	<i>n.d.</i>	<i>n.d.</i>	<i>n.d.</i>
Al ₂ O ₃	0.035	0.008	0.032	0.02	0.03	0.012	0.014	0.009	0.012	0.020	0.060	0.040	0.020	0.040	0.020
Cr ₂ O ₃	0.016	0.013	0.021	0.018	0.028	0.017	0.022	0.035	0.045	0.050	0.010	0.050	0.050	0.040	0.030
FeO*	8.52	8.52	8.41	8.53	8.39	8.56	8.59	8.30	7.84	8.70	9.30	8.60	8.4	8.2	8.8
MnO	0.131	0.128	0.126	0.129	0.13	0.128	0.123	0.12	0.122	0.140	0.150	0.130	0.130	0.110	0.140
NiO	0.412	0.399	0.422	0.415	0.388	0.392	0.393	0.396	0.395	0.380	0.380	0.380	0.450	0.380	0.410
MgO	49.9	49.6	50.2	49.7	49.8	49.6	49.6	49.7	50.0	49.9	49.8	49.7	50.1	50.3	50.3
CaO	0.058	0.058	0.057	0.073	0.074	0.069	0.068	0.066	0.079	0.080	0.100	0.110	0.150	0.130	0.070
P ₂ O ₅	<i>n.d.</i>	0.023	<i>n.d.</i>	<i>n.d.</i>	0.008	0.006	0.01	0.011	0.008	<i>n.d.</i>	<i>n.d.</i>	<i>n.d.</i>	<i>n.d.</i>	<i>n.d.</i>	<i>n.d.</i>
Total	100.11	99.93	100.24	99.90	99.90	99.79	99.81	99.92	99.84	100.35	100.69	99.98	100.24	100.21	100.97
Mg#	0.91	0.91	0.91	0.91	0.91	0.91	0.91	0.91	0.92	0.91	0.91	0.91	0.91	0.92	0.91

*Total Fe as FeO; *n.d.* - not determined; samples in *italic*: Bjerg *et al.* (2009); n - number of analyses

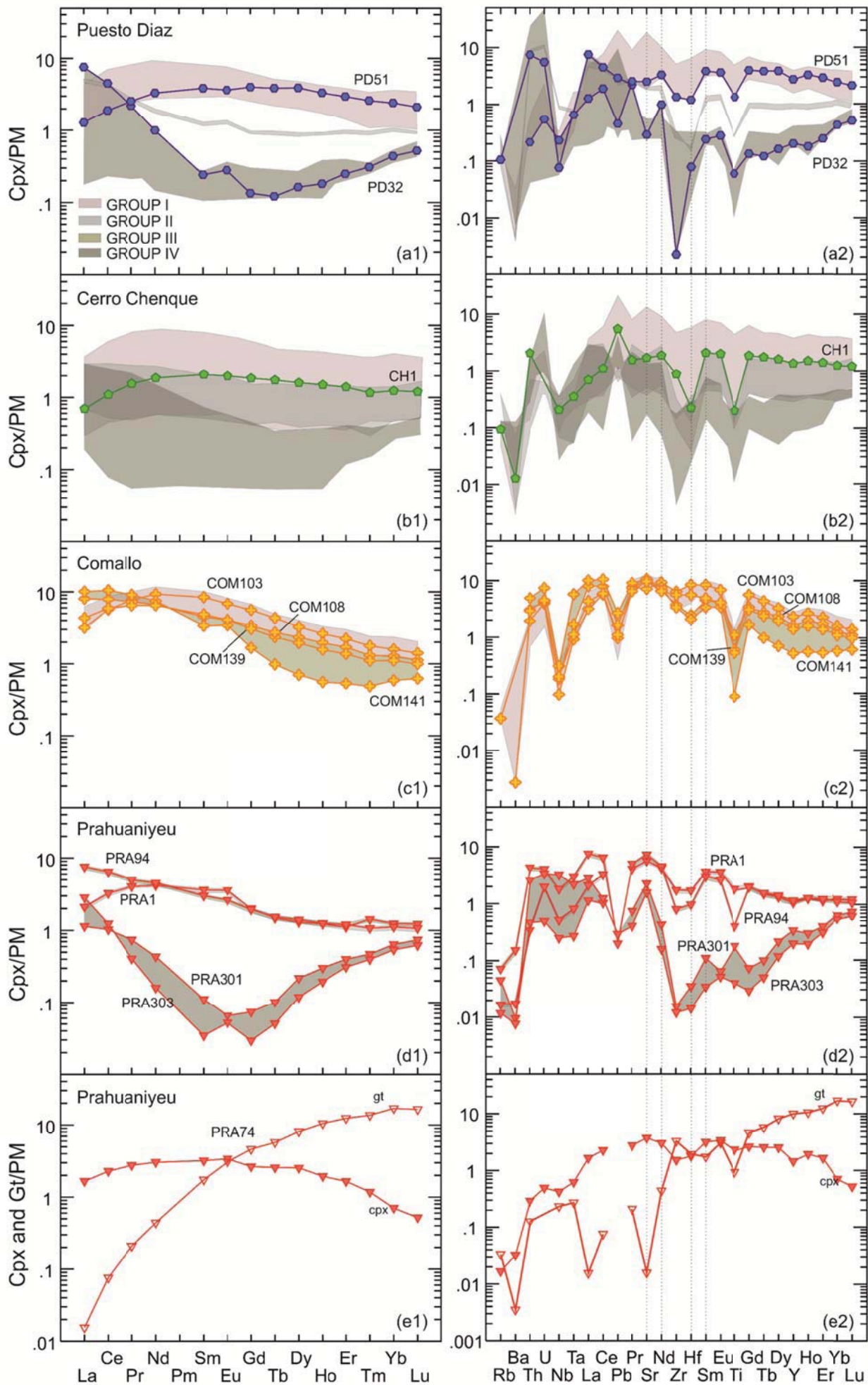


Fig. 6. PM normalized clinopyroxene and garnet REE and spider diagrams subdivided into respective sampling localities Puesto Diaz (a1 and a2), Cerro Chenque (b1 and b2), Comallo (c1 and c2) and Prahuanieyu (d1 and d2). Different shaded areas represent 4 separate groups. Each group contains samples with distinct PM-normalized REE and other trace element patterns. Group I: LREE>MREE>HREE; Group II: LREE>MREE<<HREE; Group III: LREE>>MREE<<HREE; Group IV: LREE>>MREE<<HREE. Samples further used for clinopyroxene isotopic investigations are highlighted. (e1) and (e2) display PM-normalized patterns of spinel-garnet-ilmenite PRA74. Legend and abbreviations as in Fig. 2.

Table 4: Average orthopyroxene major element compositions determined using microprobe analysis

	PD1	PD2	PD7	PD27	PD28	PD32	PD48	PD51	PD61	PD64	CH1	CH12	CH17
n	4	4	3	6	4	6	3	4	8	6	4	5	5
SiO ₂	57.2	56.9	57.2	57.2	56.9	56.8	55.4	55.8	56.7	57.1	56.7	56.7	56.9
TiO ₂	0.098	0.007	0.005	0.013	0.008	0.008	0.187	0.136	0.024	0.005	0.025	0.006	0.005
Al ₂ O ₃	2.49	2.33	2.10	2.11	2.24	2.11	2.61	3.44	2.16	1.83	2.22	2.27	2.21
Cr ₂ O ₃	0.373	0.550	0.437	0.444	0.413	0.523	0.310	0.514	0.494	0.404	0.455	0.470	0.467
FeO*	5.46	5.41	5.24	5.29	5.22	5.53	8.81	5.96	5.45	5.53	5.30	5.47	5.21
MnO	0.128	0.131	0.132	0.142	0.131	0.155	0.192	0.152	0.131	0.130	0.128	0.140	0.130
NiO	0.091	0.078	0.092	0.075	0.111	0.096	0.059	0.062	0.109	0.092	0.088	0.087	0.085
MgO	34.7	35.0	34.6	34.8	34.7	34.6	32.0	34.0	34.2	34.9	34.6	34.6	35.0
CaO	0.337	0.365	0.517	0.327	0.580	0.634	0.436	0.406	0.621	0.416	0.510	0.569	0.432
Na ₂ O	0.035	0.015	0.014	0.016	0.094	0.011	0.043	0.012	0.070	0.016	0.023	0.018	0.016
Total	100.94	100.79	100.32	100.38	100.37	100.47	100.09	100.46	100.01	100.41	100.09	100.40	100.47
Mg#	0.92	0.92	0.92	0.92	0.92	0.92	0.87	0.91	0.92	0.92	0.921	0.919	0.92
en	91.1	91.2	91.1	91.4	91.0	90.5	85.6	90.1	90.5	90.9	91.1	90.4	91.4
wo	0.6	0.7	1.0	0.6	1.1	1.2	0.8	0.8	1.2	0.8	0.9	1.5	0.8
fs	8.2	8.1	7.9	8.0	7.9	8.3	13.5	9.1	8.3	8.3	8.0	8.2	7.8

	CH25	CH26	CH42	CH43	CH48	CH63	COM101	COM103	COM108	COM110	COM118	COM139
n	7	4	5	5	3	6	>10	>10	>10	>10	>10	>10
SiO ₂	56.4	57.1	57.0	56.9	55.3	57.3	56.6	56.7	56.5	56.4	56.4	56.0
TiO ₂	0.072	0.018	0.010	0.007	0.211	0.011	0.032	0.041	0.028	0.073	0.077	0.063
Al ₂ O ₃	2.87	1.96	1.85	2.19	2.61	1.45	2.40	2.17	2.34	2.56	2.65	2.63
Cr ₂ O ₃	0.497	0.455	0.462	0.496	0.295	0.278	0.51	0.436	0.438	0.453	0.446	0.425
FeO*	5.75	5.53	5.31	5.22	8.92	5.64	5.48	5.51	5.52	5.39	5.34	5.65
MnO	0.139	0.142	0.133	0.120	0.189	0.131	0.137	0.13	0.136	0.139	0.133	0.134
NiO	0.077	0.100	0.091	0.090	0.079	0.113	0.104	0.097	0.109	0.108	0.1	0.1
MgO	34.1	34.7	34.9	34.8	32.0	35.1	34.4	34.2	34.5	34.2	34.3	34.1
CaO	0.475	0.364	0.566	0.562	0.598	0.388	0.636	0.615	0.627	0.656	0.635	0.632
Na ₂ O	0.034	0.021	0.020	0.018	0.037	0.027	0.016	0.054	0.132	0.01	0.064	0.043
Total	100.35	100.34	100.32	100.33	100.25	100.45	100.25	99.96	100.37	100.06	100.09	99.79
Mg#	0.91	0.92	0.92	0.92	0.86	0.92	0.918	0.917	0.9175	0.919	0.92	0.915
en	90.3	91.0	91.0	91.1	85.2	90.9	90.5	90.5	90.5	90.5	90.7	90.2
wo	0.9	0.7	1.1	1.1	1.1	0.7	1.2	1.2	1.2	1.2	1.2	1.2
fs	8.8	8.4	8.0	7.8	13.6	8.4	8.3	8.4	8.3	8.2	8.1	8.6

*Total Fe as FeO; samples in italic: Bjerg *et al.* (2009); n – number of analyzes

Table 4: continued

	COM140	COM141	COM142	<i>PRA1</i>	<i>PRA74</i>	<i>PRA94</i>	<i>PRA301</i>	<i>PRA303</i>	<i>PRA306</i>
n	>10	>10	>10						
SiO ₂	56.0	56.8	57.0	<i>55.1</i>	<i>54.5</i>	<i>55.3</i>	<i>56.1</i>	<i>55.4</i>	<i>55.9</i>
TiO ₂	0.061	0.006	0.049	<i>0.15</i>	<i>0.15</i>	<i>0.04</i>	<i>0.01</i>	<i>0.03</i>	<i>0.10</i>
Al ₂ O ₃	2.83	2.05	1.97	<i>3.80</i>	<i>5.70</i>	<i>3.70</i>	<i>3.40</i>	<i>3.40</i>	<i>4.10</i>
Cr ₂ O ₃	0.441	0.447	0.456	<i>0.81</i>	<i>0.65</i>	<i>0.92</i>	<i>0.66</i>	<i>1.04</i>	<i>0.59</i>
FeO*	5.63	5.40	5.02	<i>5.30</i>	<i>5.80</i>	<i>5.40</i>	<i>5.30</i>	<i>5.20</i>	<i>5.60</i>
MnO	0.122	0.128	0.124	<i>0.12</i>	<i>0.10</i>	<i>0.13</i>	<i>0.15</i>	<i>0.11</i>	<i>0.13</i>
NiO	0.097	0.099	0.101	<i>0.12</i>	<i>0.13</i>	<i>0.11</i>	<i>0.1</i>	<i>0.08</i>	<i>0.1</i>
MgO	33.9	34.4	34.5	<i>33.4</i>	<i>32.4</i>	<i>33.1</i>	<i>34.0</i>	<i>33.3</i>	<i>33.4</i>
CaO	0.621	0.582	0.623	<i>0.95</i>	<i>1.21</i>	<i>1.3</i>	<i>0.93</i>	<i>1.47</i>	<i>0.83</i>
Na ₂ O	0.056	0.036	0.08	<i>0.14</i>	<i>0.19</i>	<i>0.11</i>	<i>0.02</i>	<i>0.08</i>	<i>0.08</i>
Total	99.84	99.94	99.89	<i>99.87</i>	<i>100.73</i>	<i>100.12</i>	<i>100.67</i>	<i>100.08</i>	<i>100.84</i>
Mg#	0.915	0.919	0.924	<i>0.9</i>	<i>0.9</i>	<i>0.9</i>	<i>0.9</i>	<i>0.9</i>	<i>0.9</i>
en	90.2	90.7	91.2	<i>90.1</i>	<i>88.7</i>	<i>89.3</i>	<i>90.3</i>	<i>89.4</i>	<i>90.0</i>
wo	1.2	1.1	1.2	<i>1.8</i>	<i>2.4</i>	<i>2.5</i>	<i>1.8</i>	<i>2.8</i>	<i>1.6</i>
fs	8.6	8.2	7.6	<i>8.1</i>	<i>9.0</i>	<i>8.2</i>	<i>7.9</i>	<i>7.8</i>	<i>8.4</i>

*Total Fe as FeO; samples in italic: Bjerg *et al.* (2009); n – number of analyzes

Pb anomalies. Samples from **Group II** display a roughly flat pattern from HREE to MREE with $(\text{Sm}/\text{Yb})_N \sim 1$ and an enrichment in LREE with $(\text{La}/\text{Sm})_N = 1.3-4.1$. All samples from within this group exhibit negative Ti, Zr and Pb, and positive Sr anomalies. **Group III** samples are characterized by a continuous enrichment in MREE and LREE over HREE with $(\text{Sm}/\text{Yb})_N = 2.7-5.9$ and $(\text{La}/\text{Yb})_N = 6.6-18.1$, respectively. Spider diagrams show positive as well as negative Pb and Sr and exclusively negative Zr anomalies in this clinopyroxene group. Clinopyroxenes from **Group IV** have U-shaped PM-normalized REE patterns that are defined by $(\text{Ho}/\text{Yb})_N < 1$, an occasional minor enrichment in MREE with $(\text{Sm}/\text{Yb})_N = 0.1-1.7$ and a strong enrichment in LREE with $(\text{La}/\text{Yb})_N$ of up to 84.1. All Group IV clinopyroxenes show negative Zr anomalies and with

the exception of sample PRA301, mantle xenoliths from this group exhibit negative Ti anomalies. Sample PRA74, the only spinel-garnet-peridotite within the sample suite, exhibits REE patterns expected for a fertile lherzolite and shows now enrichment in either MREE or LREE (Fig. 6e1 and e2). All groups are displayed in Fig. 6a-d as 4 differently shaded areas separated according to their respective areas of origin.

Spinel

Representative spinel analyses are given in Table 7. Cr# $[\text{Cr}/(\text{Cr}+\text{Al})]$ and mg# in spinel are in the range from 0.23 to 0.49 and from 0.64 to 0.78, respectively in spinel-harzburgites. The cumulate dunites have spinels with cr# between 0.28 and 0.29. Mg# are with 0.51 to 0.54 much lower in cumulates relative to mantle xenoliths. Spinel in

Table 5: Average clinopyroxene major element compositions determined using microprobe analysis

	PD1	PD2	PD7	PD27	PD28	PD32	PD48	PD51	PD61	PD64	CH1	CH12	CH17
n	4	3	3	7	4	5	3	4	6	5	8	4	3
SiO ₂	53.1	53.7	53.7	53.7	54.5	53.7	51.3	52.7	54.0	54.1	53.4	53.7	53.6
TiO ₂	0.300	0.011	0.007	0.005	0.018	0.011	0.786	0.642	0.042	0.017	0.040	0.027	0.006
Al ₂ O ₃	3.45	2.50	2.56	2.48	2.81	2.27	5.24	3.96	2.69	1.97	2.81	2.36	2.31
Cr ₂ O ₃	0.914	1.009	0.990	0.964	1.052	0.961	0.988	0.814	1.068	0.707	1.117	0.852	0.807
FeO*	1.94	1.60	1.66	1.73	2.18	1.95	4.14	1.99	2.06	1.99	2.25	1.77	1.95
MnO	0.047	0.068	0.058	0.060	0.069	0.061	0.098	0.071	0.073	0.070	0.057	0.058	0.055
NiO	0.043	0.045	0.052	0.034	0.053	0.053	0.038	0.048	0.025	0.045	0.058	0.023	0.042
MgO	16.8	16.9	17.0	17.2	16.9	17.4	14.8	16.5	16.8	17.7	17.3	17.4	17.7
CaO	23.3	23.8	23.8	23.5	21.6	23.5	20.9	23.1	22.1	23.6	22.3	23.5	23.4
Na ₂ O	0.563	0.562	0.480	0.454	1.264	0.379	1.305	0.746	0.941	0.359	0.676	0.574	0.266
Total	100.54	100.18	100.21	100.16	100.47	100.26	99.56	100.50	99.86	100.60	100.00	100.17	100.14
Mg#	0.94	0.95	0.95	0.95	0.93	0.94	0.86	0.94	0.94	0.94	0.93	0.95	0.94
en	48.4	48.4	48.4	49.1	50.2	49.0	45.9	48.1	49.6	49.4	50.1	49.2	49.7
wo	48.4	49.0	48.8	48.1	46.1	47.8	46.7	48.5	46.9	47.4	46.1	47.9	47.1
fs	3.2	2.7	2.8	2.9	3.7	3.2	7.4	3.4	3.5	3.5	3.8	2.9	3.2

	CH25	CH26	CH42	CH43	CH48	CH63	COM101	COM103	COM108	COM110	COM118	COM139
n	5	4	5	4	3	6	>10	>10	>10	>10	>10	>10
SiO ₂	53.0	53.6	53.7	53.9	51.2	53.7	53.3	53.5	53.2	53.1	52.7	52.5
TiO ₂	0.250	0.043	0.013	0.008	0.861	0.051	0.098	0.104	0.095	0.202	0.277	0.215
Al ₂ O ₃	4.03	2.32	2.15	2.28	5.04	2.26	3.02	2.95	3.22	3.33	4.17	3.31
Cr ₂ O ₃	1.211	0.930	0.891	0.918	0.915	0.990	0.925	1.011	1.060	0.996	1.226	0.884
FeO*	1.85	1.80	2.08	1.89	4.19	1.85	2.38	2.41	2.55	2.41	2.40	2.59
MnO	0.081	0.060	0.068	0.072	0.095	0.064	0.078	0.069	0.073	0.078	0.073	0.074
NiO	0.033	0.051	0.040	0.061	0.033	0.047	0.053	0.049	0.053	0.042	0.056	0.055
MgO	15.9	17.1	17.8	17.4	14.7	17.1	16.9	16.7	16.7	16.8	16.2	16.7
CaO	22.8	23.5	22.9	23.0	21.5	23.6	22.5	22.0	22.1	22.5	21.7	22.5
Na ₂ O	0.944	0.505	0.403	0.514	1.278	0.560	0.744	0.958	1.109	0.747	1.113	0.711
Total	100.16	99.95	100.05	100.04	99.82	100.23	99.95	99.79	100.19	100.18	99.93	99.57
Mg#	0.94	0.94	0.94	0.94	0.86	0.94	0.93	0.93	0.92	0.93	0.92	0.92
en	47.6	48.8	50.2	49.6	45.2	48.7	49.1	49.2	49.1	48.9	48.9	48.6
wo	49.2	48.2	46.4	47.3	47.5	48.3	46.9	46.7	46.6	47.0	46.9	47.1
fs	3.3	3.0	3.4	3.1	7.4	3.1	4.0	4.1	4.3	4.1	4.2	4.4

*Total Fe as FeO; samples in italic: Bjerg *et al.* (2009); n – number of analyzes

Table 5: continued

	COM140	COM141	COM142	<i>PRA1</i>	<i>PRA74</i>	<i>PRA94</i>	<i>PRA301</i>	<i>PRA303</i>	<i>PRA306</i>
n	>10	>10	>10						
SiO ₂	52.6	53.5	53.9	<i>52.9</i>	<i>51.9</i>	<i>52.8</i>	<i>53.2</i>	<i>53.0</i>	<i>52.8</i>
TiO ₂	0.227	0.011	0.136	<i>0.310</i>	<i>0.460</i>	<i>0.080</i>	<i>0.040</i>	<i>0.100</i>	<i>0.290</i>
Al ₂ O ₃	4.11	2.96	3.24	<i>4.80</i>	<i>7.00</i>	<i>4.30</i>	<i>3.50</i>	<i>3.70</i>	<i>5.50</i>
Cr ₂ O ₃	1.119	1.197	1.243	<i>1.500</i>	<i>1.080</i>	<i>1.530</i>	<i>1.110</i>	<i>1.510</i>	<i>1.220</i>
FeO*	2.57	2.30	2.24	<i>2.44</i>	<i>3.30</i>	<i>2.90</i>	<i>2.26</i>	<i>2.80</i>	<i>2.70</i>
MnO	0.073	0.070	0.068	<i>0.090</i>	<i>0.100</i>	<i>0.100</i>	<i>0.070</i>	<i>0.110</i>	<i>0.090</i>
NiO	0.054	0.050	0.049	<i>0.060</i>	<i>0.040</i>	<i>0.050</i>	<i>0.040</i>	<i>0.060</i>	<i>0.020</i>
MgO	16.1	16.6	16.3	<i>16.4</i>	<i>17.1</i>	<i>17.8</i>	<i>17.7</i>	<i>18.0</i>	<i>15.9</i>
CaO	21.7	22.1	21.1	<i>20.0</i>	<i>17.5</i>	<i>19.8</i>	<i>22.2</i>	<i>19.7</i>	<i>20.6</i>
Na ₂ O	1.107	0.973	1.460	<i>1.420</i>	<i>1.460</i>	<i>0.910</i>	<i>0.470</i>	<i>0.810</i>	<i>1.460</i>
Total	99.72	99.72	99.77	<i>99.96</i>	<i>99.89</i>	<i>100.24</i>	<i>100.50</i>	<i>99.77</i>	<i>100.59</i>
Mg#	0.92	0.93	0.93	<i>0.92</i>	<i>0.90</i>	<i>0.92</i>	<i>0.93</i>	<i>0.92</i>	<i>0.91</i>
en	48.6	49.0	49.8	<i>51.0</i>	<i>54.3</i>	<i>52.9</i>	<i>50.6</i>	<i>53.6</i>	<i>49.3</i>
wo	47.0	47.0	46.3	<i>44.7</i>	<i>39.9</i>	<i>42.2</i>	<i>45.7</i>	<i>42.0</i>	<i>46.1</i>
fs	4.5	3.9	4.0	<i>4.3</i>	<i>5.9</i>	<i>4.8</i>	<i>3.6</i>	<i>4.6</i>	<i>4.6</i>

*Total Fe as FeO; samples in italic: Bjerg *et al.* (2009); n – number of analyzes

spinel-garnet-lherzolite PRA74 has the lowest cr# (0.19) and the highest mg# (0.81) of the entire sample suite.

Sulphides

Representative sulphide analyses are provided in Table 8. Sulphide occurrences in 15 mantle peridotite samples, further used for Re-Os isotope analyses, were investigated. All those samples contain sulphides, which occur either as interstitial or enclosed, sometimes enclosed in form of sulphide trails in silicate minerals, primarily in olivine and orthopyroxene (Fig. 7a-f). In some samples, sulphides only occur as tiny (<2µm) phases in intergranular devitrified glass, too small to be analyzed. Sulphides from 8 samples were large enough to get good results using microprobe analyses (Table 8). The most abundant sulphide phases are monosulphide solid solutions (Mss), pentlandite (Pn) and

chalcopyrite (Cp). Other, less common phases identified are pyrrhotite (Po – Fe_{1-x}S_(x=0 to 0.17)), bornite (Bn – Cu₅FeS₄), cubanite (Cb – CuFe₂S₃), pyrite (Py – FeS₂), heazlewoodite (Hz – Ni₃S₂) and millerite (Mi – NiS). In sample PD28, laurite, a rare ruthenium sulphide (RuS₂) was found (Fig. 7c). No compositional differences between enclosed and interstitial sulphide phases of the same type can be recognized. Sulphides found in devitrified glass are commonly rich in Ni (up to 65 wt. %) and can, wherever applicable, be identified as heazlewoodite or millerite. Enclosed as well as interstitial sulphides often exhibit rims or patches of secondary Fe-hydroxides, probably resulting from sulphur loss during weathering processes (Lorand, 1990).

Table 6: Cpx and gt trace element compositions determined using ICP-MS laser ablation analysis

sp-peridotites	PD1 ^I	PD7 ^{IV}	PD27 ^{IV}	PD28 ^{IV}	PD32 ^{IV}	PD48 ^I	PD 51 ^I	PD61 ^{II}	PD64 ^{IV}	CH1 ^I	CH12 ^{IV}	CH17 ^{IV}	CH25 ^{II}	CH26 ^{IV}	CH42 ^{IV}	CH43 ^{IV}	CH48 ^I	CH63 ^{II}
Co	20.3	19.7	21.0	20.4	19.6	21.5	20.5	18.5	17.5	19.7	20.4	20.9	19.2	17.0	19.9	20.9	18.0	31.4
Zn	18.40	10.27	16.45	8.24	8.30	13.83	14.54	8.61	8.62	7.27	8.87	7.57	6.02	15.86	7.39	8.09	14.86	11.96
Cu	2.478	3.655	1.905	3.170	3.970	1.580	0.606	1.168	0.959	1.498	0.919	1.157	0.972	0.969	1.500	1.748	1.037	1.421
V	271	143	156	133	167	245	224	183	180	175	188	146	204	124	196	158	229	197
Rb	<0.025	0.147	0.085	0.057	0.063	0.074	<0.028	0.056	0.059	0.056	0.079	0.035	<0.030	<0.023	<0.026	0.077	0.030	0.225
Sr	34.5	4.5	7.0	4.0	5.8	333.0	50.2	37.5	10.1	33.8	14.5	0.9	38.4	6.8	26.9	3.4	265.2	10.9
Y	6.22	1.01	0.66	0.80	0.87	15.68	11.91	4.15	1.62	5.81	1.18	0.22	5.94	1.58	0.95	0.54	16.36	1.58
Zr	12.21	0.03	0.13	3.15	0.02	49.05	14.20	3.05	0.84	9.19	0.96	0.02	3.38	1.84	0.50	0.10	49.88	1.56
Ba	0.027	0.046	1.046	<0.068	<0.074	0.198	<0.068	0.030	<0.023	0.084	0.158	0.146	<0.084	0.098	<0.076	0.841	0.020	0.461
Nb	0.197	0.034	0.098	0.114	0.050	0.069	0.152	0.624	0.135	0.135	0.467	0.012	0.205	0.027	0.237	0.018	0.056	0.237
La	1.031	0.115	0.242	3.710	4.900	2.838	0.826	3.395	0.761	0.450	0.818	0.120	1.789	0.597	1.907	0.121	2.390	0.462
Ce	3.650	0.387	0.659	5.760	7.560	11.818	3.165	7.480	1.770	1.836	1.890	0.129	5.045	0.778	4.440	0.152	10.105	0.877
Pr	0.619	0.054	0.084	0.364	0.560	2.107	0.649	0.724	0.200	0.395	0.228	<0.007	0.740	0.077	0.551	0.015	2.040	0.124
Nd	3.483	0.281	0.354	0.708	1.241	11.880	4.150	2.515	0.633	2.337	1.172	<0.033	3.455	0.330	1.758	0.093	11.425	0.727
Sm	1.178	0.071	0.084	0.120	0.098	3.440	1.566	0.526	0.111	0.846	0.290	<0.048	0.866	0.127	0.312	0.059	3.260	0.210
Eu	0.456	0.026	0.032	0.017	0.043	1.181	0.561	0.212	0.056	0.307	0.089	<0.013	0.305	0.053	0.090	<0.013	1.080	0.071
Gd	1.374	0.076	0.074	0.054	0.073	3.445	2.174	0.531	0.164	1.008	0.248	<0.049	0.900	0.192	0.182	0.052	3.455	0.228
Tb	0.217	0.019	0.011	0.012	0.012	0.511	0.383	0.096	0.028	0.173	0.034	<0.006	0.159	0.027	0.020	0.007	0.467	0.045
Dy	1.353	0.141	0.098	0.052	0.110	3.248	2.630	0.622	0.182	1.079	0.212	<0.023	1.022	0.256	0.154	0.071	3.100	0.262
Ho	0.258	0.037	0.024	0.017	0.027	0.632	0.496	0.139	0.057	0.224	0.041	0.008	0.219	0.055	0.027	0.015	0.659	0.061
Er	0.624	0.123	0.088	0.101	0.109	1.691	1.297	0.441	0.174	0.613	0.136	0.052	0.634	0.175	0.112	0.091	1.741	0.175
Tm	0.073	0.022	0.017	0.021	0.021	0.232	0.177	0.066	0.024	0.079	0.024	0.010	0.095	0.025	0.024	0.017	0.241	0.020
Yb	0.493	0.216	0.157	0.239	0.193	1.603	1.064	0.476	0.232	0.547	0.188	0.115	0.627	0.209	0.199	0.133	1.780	0.214
Lu	0.069	0.034	0.029	0.049	0.035	0.234	0.143	0.065	0.044	0.081	0.032	0.020	0.111	0.032	0.033	0.024	0.250	0.034
Hf	0.318	<0.009	0.006	<0.025	0.023	1.681	0.340	0.047	0.012	0.063	0.007	0.020	0.035	0.084	<0.024	0.022	1.652	0.101
Ta	0.056	0.006	0.023	0.021	<0.006	0.011	0.024	0.030	0.019	0.013	0.031	<0.008	0.024	0.002	0.049	<0.006	0.013	0.026
Pb	0.072	0.176	0.046	1.293	0.439	2.760	0.068	0.371	0.035	0.821	0.061	0.147	0.096	0.613	0.162	0.314	3.160	0.165
Th	0.034	0.003	0.013	1.689	0.594	0.045	0.017	0.741	0.006	0.164	0.144	<0.009	0.039	0.127	0.057	0.023	0.104	0.056
U	0.013	<0.002	0.007	0.859	0.113	0.042	0.011	0.228	0.006	0.027	0.052	<0.001	0.020	0.210	0.026	0.061	0.046	0.013

Samples in italic: Bjerg *et al.* (2009); I,II,III,IV: Group affiliations according to PM-normalized REE patterns (Fig. 6)

Table 6: continued

	sp-peridotites													sp-gt-lherzolite		
	COM103 ^I	COM108	COM118 ^I	COM139 ^{III}	COM140 ^I	COM141 ^{III}	COM142 ^I	PRA1 ^I	PRA94 ^{III}	PRA301 ^{IV}	PRA303 ^{IV}	PRA74 cpx	PRA74 gt			
Co	19.9	20.8	19.5	21.0	19.8	18.6	18.9	22.1	n.d.	18.8	n.d.	25.8	43.5			
Zn	8.72	9.72	8.92	9.51	9.13	7.21	7.80	n.d.	n.d.	n.d.	n.d.	n.d.	n.d.			
Cu	0.754	0.609	1.018	0.661	1.701	0.257	2.246	n.d.	n.d.	n.d.	n.d.	n.d.	n.d.			
V	191	203	223	229	250	234	190	193	n.d.	163	n.d.	193	98			
Rb	0.022	<0.035	0.025	<0.029	0.033	<0.023	<0.025	0.010	0.043	0.027	0.007	0.010	0.020			
Sr	141.5	192.4	253.3	203.6	202.6	211.6	225.3	112.3	144.6	45.1	31.3	74.9	0.313			
Y	9.86	5.95	10.64	6.84	11.95	2.23	10.17	4.47	4.88	1.46	0.86	6.26	42.87			
Zr	67.19	58.28	37.42	39.17	48.34	35.16	30.13	18.23	8.39	0.16	0.13	16.03	34.83			
Ba	<0.053	0.018	<0.075	<0.066	0.071	<0.062	0.066	0.115	1.009	0.063	0.050	0.213	0.023			
Nb	0.064	0.132	0.229	0.120	0.075	0.202	0.113	0.340	1.191	0.165	2.118	0.278	0.153			
La	2.052	2.804	4.060	5.183	3.223	6.530	1.886	1.367	4.880	0.737	1.840	1.075	0.010			
Ce	9.497	9.900	14.530	13.190	13.147	17.630	10.075	5.457	10.773	1.720	2.075	3.835	0.127			
Pr	1.966	1.643	2.553	1.851	2.583	2.306	2.056	1.027	1.265	0.188	0.103	0.703	0.053			
Nd	11.640	8.094	12.647	8.290	14.700	9.327	11.730	5.233	5.663	0.543	0.200	3.810	0.550			
Sm	3.417	1.969	3.027	1.825	4.100	1.367	3.030	1.473	1.223	0.045	0.014	1.300	0.707			
Eu	1.052	0.628	1.004	0.625	1.305	0.526	1.028	0.550	0.404	0.010	0.008	0.525	0.473			
Gd	3.037	1.661	2.760	1.841	3.653	0.907	3.095	1.090	1.056	0.040	0.016	1.443	2.520			
Tb	0.428	0.233	0.414	0.270	0.486	0.097	0.403	0.147	0.152	0.010	0.005	0.255	0.570			
Dy	2.186	1.314	2.321	1.573	2.718	0.472	2.292	0.877	0.941	0.147	0.080	1.715	5.483			
Ho	0.391	0.235	0.431	0.292	0.494	0.083	0.414	0.183	0.187	0.045	0.029	0.290	1.563			
Er	0.978	0.603	1.114	0.748	1.323	0.233	0.993	0.487	0.527	0.175	0.136	0.725	5.427			
Tm	0.121	0.075	0.145	0.089	0.165	0.033	0.120	0.097	0.073	0.032	0.027	0.080	0.930			
Yb	0.701	0.490	0.877	0.567	1.040	0.259	0.779	0.547	0.493	0.283	0.238	0.310	7.487			
Lu	0.095	0.067	0.115	0.076	0.138	0.042	0.099	0.083	0.072	0.050	0.042	0.035	1.110			
Hf	2.383	1.583	1.282	0.692	1.590	0.584	1.132	0.483	0.273	0.010	0.004	0.508	0.553			
Ta	0.034	0.041	0.044	0.062	0.034	0.212	0.030	0.030	0.110	0.010	0.081	0.023	0.010			
Pb	0.145	0.165	0.220	0.243	0.100	0.400	0.067	n.d.	0.030	n.d.	0.044	<0.010	<0.010			
Th	0.154	0.232	0.192	0.243	0.278	0.389	0.053	0.027	0.338	0.037	0.205	0.023	0.010			
U	0.080	0.091	0.089	0.086	0.079	0.150	0.033	0.040	0.082	0.010	0.068	0.010	n.d.			

Samples in italic: Bjerg *et al.* (2009); I, II, III, IV; Group affiliations according to PM-normalized REE patterns (Fig. 6)

Table 7: Average spinel major element compositions determined using microprobe analysis

n	PDI	PD2	PD7	PD27	PD28	PD32	PD48	PD51	PD61	PD64	CHI	CHI2	CHI7	CH25	CH26	CH42	CH43	CH48	CH63
	2	3	2	2	2	2	3	4	4	3	5	5	4	3	3	3	2	5	4
SiO ₂	0.065	0.022	0.065	0.064	0.023	0.073	0.092	0.031	0.043	0.027	0.044	0.036	0.025	0.013	0.034	0.055	0.050	0.049	0.029
TiO ₂	0.581	0.022	0.009	0.000	0.013	0.042	0.739	0.155	0.214	0.020	0.039	0.142	0.035	0.140	0.037	0.704	0.008	2.093	0.067
Cr ₂ O ₃	28.4	34.4	34.6	36.4	32.6	34.7	21.3	21.0	38.0	35.9	32.5	34.5	32.3	27.5	38.3	38.1	37.7	21.4	37.8
Al ₂ O ₃	39.6	35.7	34.5	33.8	37.2	33.9	37.6	47.5	29.6	33.5	36.5	34.4	37.1	41.0	30.6	28.1	31.2	35.0	31.2
FeO	10.3	11.3	11.6	10.8	10.5	10.8	15.1	9.8	11.2	11.6	10.2	10.6	10.0	9.9	11.1	12.1	11.2	16.9	12.1
Fe ₂ O ₃	1.43	0.62	1.10	0.47	0.90	2.43	8.77	1.22	2.95	1.37	2.28	1.90	1.19	1.67	2.15	3.77	2.25	8.76	1.69
MgO	18.2	17.0	16.6	17.0	17.6	17.1	15.0	19.2	16.4	16.5	17.8	17.3	17.9	18.5	16.6	16.0	16.6	14.3	16.0
MnO	0.127	0.111	0.107	0.097	0.104	0.138	0.137	0.103	0.133	0.139	0.110	0.115	0.099	0.125	0.123	0.128	0.122	0.165	0.126
NiO	0.21	0.16	0.17	0.16	0.20	0.18	0.29	0.22	0.17	0.18	0.20	0.21	0.20	0.14	0.15	0.20	0.17	0.30	0.17
Total	98.97	99.42	98.72	98.79	99.16	99.36	99.05	99.21	98.67	99.25	99.63	99.24	98.89	98.89	99.10	99.29	99.18	98.91	99.05
Cr#	0.32	0.39	0.40	0.42	0.37	0.41	0.28	0.23	0.46	0.42	0.37	0.40	0.37	0.31	0.46	0.48	0.45	0.29	0.45

n	COM101	COM103	COM108	COM110	COM118	COM139	COM140	PRA1	PRA74	PRA94	PRA301	PRA303	PRA306
	>5	>5	>5	>5	>5	>5	>5	>5	>5	>5	>5	>5	>5
SiO ₂	0.030	0.025	0.041	0.037	0.037	0.037	0.045	0.060	0.150	0.150	0.020	0.100	0.070
TiO ₂	0.100	0.122	0.094	0.200	0.183	0.248	0.158	0.360	0.300	0.130	0.050	0.200	0.210
Cr ₂ O ₃	34.2	37.6	36.9	31.2	32.8	29.7	26.4	29.3	17.2	35.1	29.6	40.3	20.6
Al ₂ O ₃	34.6	29.6	29.7	37.0	35.6	35.5	40.0	39.5	50.5	33.3	39.5	28.4	46.8
FeO	10.6	11.4	11.4	10.3	10.8	10.7	10.0	10.0	8.4	10.9	9.1	10.4	9.4
Fe ₂ O ₃	2.95	4.08	5.52	3.27	2.62	5.83	4.29	1.15	2.70	2.50	1.89	2.80	2.70
MgO	17.6	16.4	16.6	18.0	17.5	17.5	18.3	18.4	20.7	17.1	18.8	17.0	19.5
MnO	0.123	0.133	0.132	0.115	0.110	0.130	0.108	0.050	0.150	0.070	0.060	0.080	0.080
NiO	0.20	0.19	0.22	0.26	0.20	0.26	0.27	0.24	0.34	0.24	0.23	0.15	0.28
Total	100.44	99.60	100.59	100.39	99.81	99.93	99.66	99.06	100.44	99.49	99.25	99.43	99.64
Cr#	0.40	0.46	0.46	0.36	0.38	0.36	0.31	0.33	0.19	0.41	0.33	0.49	0.23

Samples in italic: Bjerg *et al.* (2009); n – number of analyzes

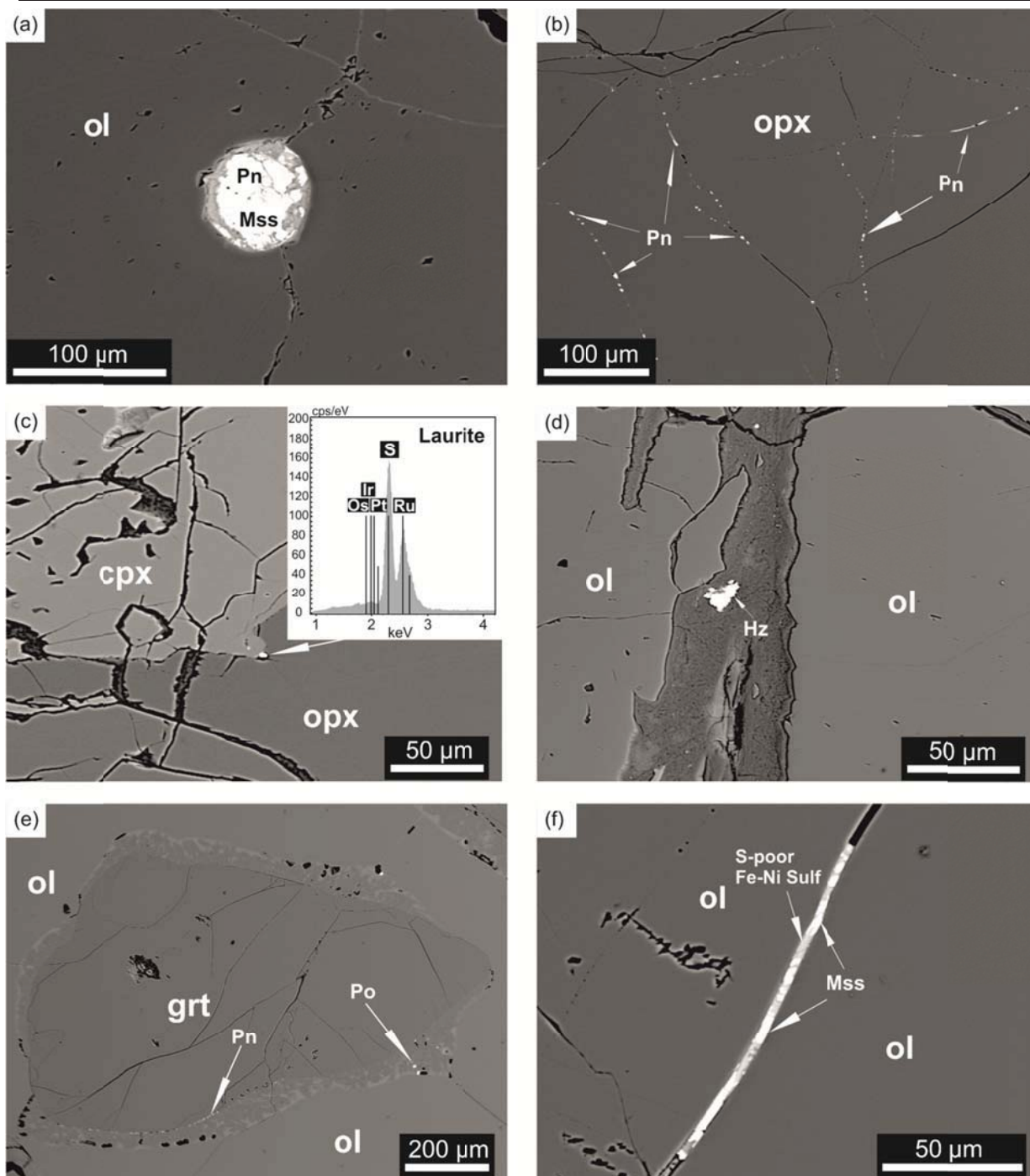


Fig. 7. Backscattered electron images of sulphide occurrences in north Patagonian mantle xenoliths. (a) COM103: rounded sulphide inclusion in ol. Pn and Mss with light grey rim composed of altered, S-poor Fe-Ni phase. (b) COM108: sulphide (Pn) trails in orthopyroxene. (c) PD28: Laurite at clinopyroxene-orthopyroxene grain boundary. Microprobe EDS peaks for platinum group elements in the upper right corner. (d) PD51: sulphide (Hz) in devitrified glass vein. (e) PRA74: sulphides in symplectitic rim around garnet. Po and Pn. (f) PRA306: intergranular elongated sulphide between two olivine grains. Mss and S-poor Fe-Ni-phase. Mss – monosulphide solid solution; Pn – pentlandite; Po – pyrrhotite; Hz – heazlewoodite; ol – olivine; opx – orthopyroxene; cpx – clinopyroxene; grt – garnet.

P-T conditions

Equilibrium temperatures (Table 9), calculated using the 2-pyroxene thermometer of Brey & Köhler (1990), at

an assumed pressure of 15 kbar, yield core temperatures of up to ~950 °C for samples from PD, CH and COM. Equilibration temperatures in PRA samples were determined by Bjerg *et*

Table 8: Sulfide microprobe analyses

Sulfide phase	Pn					Mss						
	Sample	PD51	COM103	COM139	PRA74	PRA306	COM103				COM139	
<i>e/i</i>	<i>e</i>	<i>i</i>	<i>e</i>	<i>e</i>	<i>i</i>	<i>i</i>	<i>e</i>	<i>e</i>	<i>i</i>	<i>i</i>	<i>e</i>	<i>e</i>
Fe	31.9	28.4	28.4	29.5	31.4	29.0	49.7	38.6	45.3	36.8	37.7	39.5
Co	0.422	0.657	0.835	0.285	0.394	0.004	0.114	0.252	0.213	0.213	0.678	0.408
Ni	33.8	37.2	37.8	33.8	30.9	32.6	11.1	22.4	15.0	23.0	22.8	20.8
Cu	0.000	0.002	0.027	2.36	3.09	0.008	0.010	0.004	0.004	0.000	0.013	0.005
Cr	0.007	0.007	0.003	0.050	0.028	0.004	0.027	0.000	0.348	0.769	0.000	0.044
S	33.6	32.8	33.0	33.2	33.3	38.9	39.1	39.6	38.7	39.0	39.3	39.1
Total	99.74	99.06	100.13	99.20	99.05	100.52	100.09	100.81	99.62	99.83	100.45	99.88

Sulfide phase	Mss										Cp	
	Sample	COM141	PRA74			PRA306					COM139	PRA306
<i>e/i</i>	<i>e</i>	<i>e</i>	<i>e</i>	<i>i</i>	<i>e</i>	<i>e</i>	<i>e</i>	<i>e</i>	<i>e</i>	<i>e</i>	<i>e</i>	
Fe	40.4	36.7	34.1	33.5	29.4	25.5	23.7	36.6	37.9	32.8	29.6	
Co	0.357	0.246	0.291	0.186	0.331	0.327	0.313	0.311	0.330	0.007	0.015	
Ni	20.9	24.5	27.5	26.5	28.5	40.4	40.5	24.1	22.9	0.677	0.367	
Cu	0.281	0.372	0.093	0.031	0.164	0.151	1.409	0.262	0.192	30.9	33.5	
Cr	0.018	0.020	0.004	0.122	0.075	0.052	0.046	0.064	0.055	0.004	0.054	
S	37.6	38.4	38.3	37.8	41.6	33.7	33.3	38.4	37.8	34.8	34.7	
Total	99.55	100.21	100.19	98.28	100.06	100.15	99.32	99.73	99.19	99.12	98.34	

Sulfide phase	Po		Hz		Bo	Cb	Py
	Sample	PD51	PRA306	PD51	PD51	PRA74	COM103
<i>e/i</i>	<i>e</i>	<i>i</i>	<i>i</i>	<i>i</i>	<i>e</i>	<i>e</i>	<i>e</i>
Fe	62.6	58.6	2.54	2.13	15.328	37.840	43.060
Co	0.000	0.124	0.092	0.155	0.010	0.083	2.81
Ni	0.536	1.33	65.4	62.7	0.18	3.71	1.80
Cu	0.008	0.147	0.000	0.003	54.8	22.8	0.853
Cr	0.010	0.028	0.005	0.014	0.029	0.000	0.008
S	36.4	39.2	30.4	30.7	28.6	34.8	52.5
Total	99.61	99.49	98.38	95.68	99.07	99.18	101.00

Sample	Laurite core*	Laurite rim*
	PD28	PD28
<i>e/i</i>	<i>i</i>	<i>i</i>
Os	2.28	1.57
Ir	4.94	2.92
Ru	56.5	59.2
S	36.3	36.3
Total	100.0	100.0

e/i – enclosed/interstitial; Mss – monosulphide solid solution; Pn – pentlandite; Cp – chalcopyrite; Po – pyrrhotite; Hz – heazlewoodite; Bn – bornite; Cb – cubanite; Py – pyrite. *standardless microprobe EDS analyses of laurite.

al. (2009) using the same method, yielding higher temperatures of up to ~1190 °C relative to our studied mantle xenolith samples. Pressure estimated using the Al-in-opx geobarometer by Brey & Köhler (1990) for the only studied spinel-garnet-lherzolite is 22.4 kbar (Bjerg *et al.*, 2009).

Isotopic compositions and PGE+Re systematics

Hf-Sr-Nd isotopic ratios

All Hf, Sr and Nd isotopic results obtained from leached clinopyroxene separates are given in Table 10 and plotted in Fig. 8. The 11 studied samples are exclusively spinel-harzburgites. For comparison, Sr-Nd isotopic ratios from Bjerg *et al.* (2009) of sample PRA74, a spinel-garnet-lherzolite are also given. In addition, COM host basalt Sr-Nd results from Ntaflos *et al.* (2000) are added to Table 10 and Fig. 8, respectively.

Sr-Nd isotopic compositions of Puesto Diaz, Cerro Chenque and Comallo xenoliths range from 0.703287 to 0.704835 and 0.512761 to 0.512952, respectively and fall between the bulk silicate Earth (BSE) and PREMA model composition after Zindler & Hart (1986). Prahuanियeu samples have slightly lower $^{143}\text{Nd}/^{144}\text{Nd}$ (0.512620 to 0.513029) at given $^{87}\text{Sr}/^{86}\text{Sr}$ (0.702663 to 0.703886) compared to our other studied sample suites. One sample, PRA301, has higher $^{143}\text{Nd}/^{144}\text{Nd}$ and lower $^{87}\text{Sr}/^{86}\text{Sr}$ than all other samples and plots within the MORB field after Hofmann (1997).

Hf isotopic results given in Table 10 show a wide range in radiogenic $^{176}\text{Hf}/^{177}\text{Hf}$ ratios. Samples from

Comallo show narrow ϵHf values between +7.3 and +14.0 and yield unrealistic future T_{MAS} . The only Cerro Chenque sample analyzed for Hf isotopic ratios yields an ϵHf value of +37.8 and a T_{MA} of 0.38 Ga. Puesto Diaz spinel-harzburgite PD32 shows the highest $^{176}\text{Hf}/^{177}\text{Hf}$ ratio of the whole sample suite with 0.28744 leading to

Table 9: Estimated equilibrium T (and P) conditions after Brey & Köhler (1990).

	T [°C]	P [kbar]
<i>sp-peridotites</i>		
CH1	930	
CH12	789	
CH17	833	
CH25	748	
CH26	748	
CH42	946	
CH43	829	
CH63	767	
PD1	813	
PD7	800	
PD28	861	
PD32	830	
PD51	776	
PD61	882	
PD64	787	
COM101	905	
COM103	872	
COM108	875	
COM110	860	
COM118	911	
COM139	846	
COM140	878	
COM141	854	
COM142	867	
PRA1*	1061	
PRA94*	1160	
<i>sp-grt-peridotite</i>		
PRA74*	1192	22.4

Core temperature estimates of spinel-peridotites at an assumed pressure of 15 kbar.

*Bjerg *et al.* (2009)

ϵ_{Hf} of +164.8. The determined T_{MA} of sample PD32 is 1.09 Ga. Analyzed $^{176}\text{Hf}/^{177}\text{Hf}$ of sample PD51 leads to ϵ_{Hf} +21.9 and results in a calculated T_{MA} of 1.25 Ga. The ϵ_{Hf} values calculated from Prahuanieyu clinopyroxene separates are between +8.8 and +92.1 with determined T_{MA} s ranging from unrealistic future to impossibly old ages. Overall, Hf isotopes show a strong decoupling from Nd and Sr. The compositions extend to highly

radiogenic $^{176}\text{Hf}/^{177}\text{Hf}$ at a relatively narrow Nd (and Sr) isotope range (Fig. 8b and 8c). This variance has also been observed in samples from the present day oceanic mantle (Hawaii: Bizimis et al., 2003, 2007; Gakkel Ridge: Stracke et al., 2011), and has been taken to suggest that Hf isotopes better retain a record of older depletion events than Nd and Sr isotopes in pyroxenes.

Fig. 8. Clinopyroxene $^{143}\text{Nd}/^{144}\text{Nd}$ vs. $^{87}\text{Sr}/^{86}\text{Sr}$ (a); ϵ_{Hf} vs. ϵ_{Nd} (b); and $^{87}\text{Sr}/^{86}\text{Sr}$ (c). Fields in (a) for EMI, HIMU, PREMA and DMM from Zindler & Hart (1986), OIB and MORB fields from Hofmann (1997). Fields in (b) and (c) mantle array including field for MORB and OIB from Nowell et al. (1998). Legend: Abbreviations as in Fig.1, BSE – bulk silicate earth.

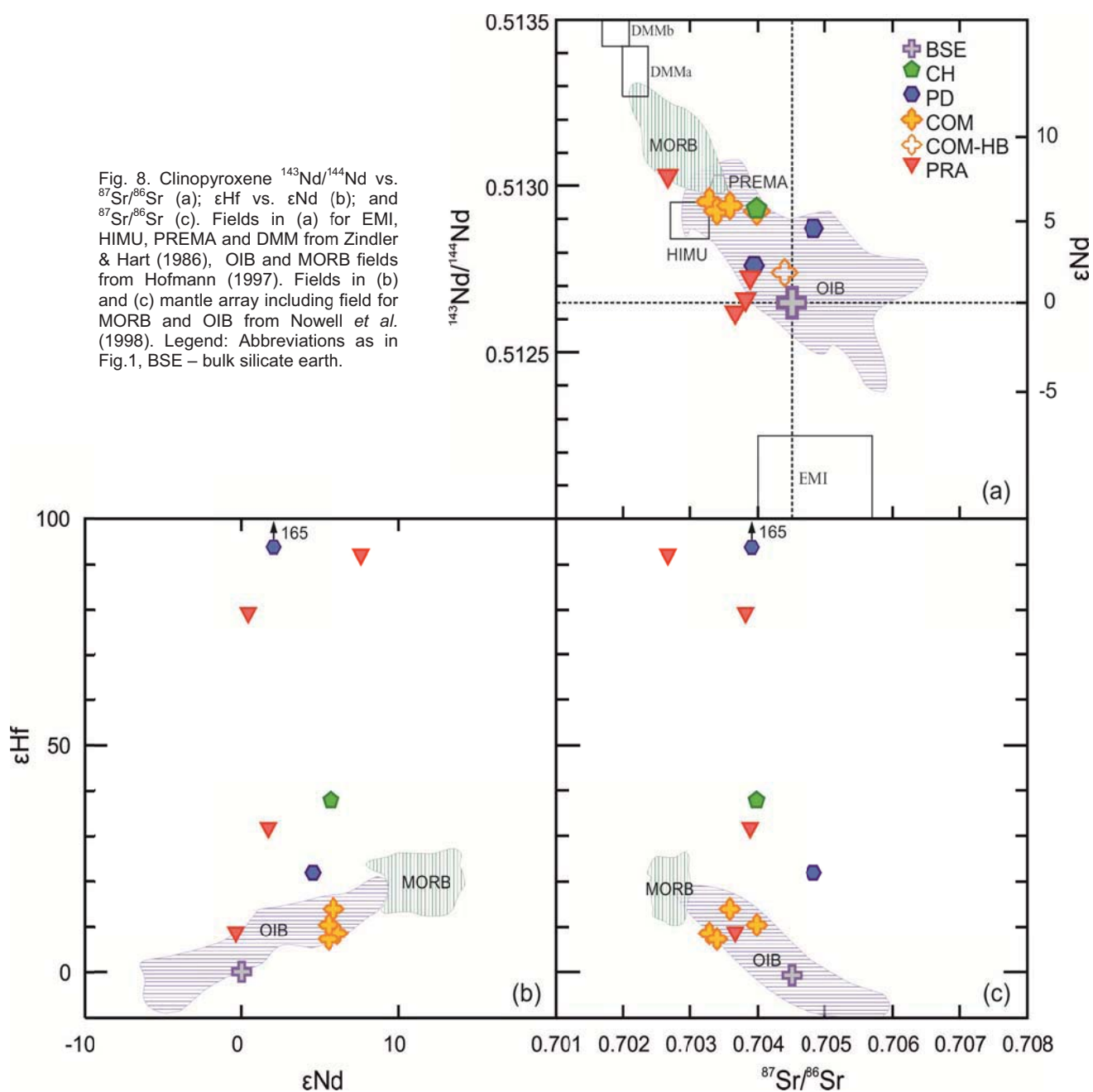


Table 10: Hf-Sr-Nd isotopic results

Sample	$^{176}\text{Lu}/^{177}\text{Hf}$	$^{176}\text{Hf}/^{177}\text{Hf}$	$2\sigma^*10^{-7}$	ϵHf	T_{MA}	$^{87}\text{Sr}/^{86}\text{Sr}$	$2\sigma^*10^{-7}$	$^{147}\text{Sm}/^{144}\text{Nd}$	$^{143}\text{Nd}/^{144}\text{Nd}$	$2\sigma^*10^{-7}$	ϵNd	T_{MA}
CHI	0.1835	0.283854	9	37.8	0.4	0.703978	4	0.2189	0.512930	4	5.7	2.0
PD32	0.2605	0.287444	49	164.8	1.1	0.703945	21	0.1751	0.512761	4	2.4	-0.9
PD51	0.0598	0.283406	7	21.9	1.2	0.704835	4	0.2284	0.512871	4	4.5	1.1
COM103	0.0057	0.283179	4	13.9	-0.8	0.703588	4	0.1775	0.512939	4	5.9	-2.4
COM108	0.0060	0.283027	4	8.5	-0.5	0.703287	4	0.1471	0.512952	4	6.1	-1.0
COM139	0.0157	0.282992	4	7.3	-0.6	0.703399	3	0.1331	0.512923	4	5.6	-0.7
COM141	0.0102	0.283079	4	10.4	-0.7	0.703984	4	0.0886	0.512923	4	5.6	-0.4
PRA1	0.0328	0.283034	3	8.8	-27.0	0.703667	4	0.1702	0.512620	4	-0.3	0.1
<i>PRA1</i>	<i>n.d.</i>	<i>n.d.</i>	<i>n.d.</i>	<i>n.d.</i>	<i>n.d.</i>	<i>n.d.</i>		<i>0.1693</i>	<i>0.512637</i>	<i>50</i>	<i>0.0</i>	<i>0.0</i>
<i>PRA 74 cpx</i>	<i>n.d.</i>	<i>n.d.</i>	<i>n.d.</i>	<i>n.d.</i>	<i>n.d.</i>	<i>n.d.</i>		<i>0.2146</i>	<i>0.513144</i>	<i>4</i>	<i>9.9</i>	<i>4.3</i>
<i>PRA 74 opx</i>	<i>n.d.</i>	<i>n.d.</i>	<i>n.d.</i>	<i>n.d.</i>	<i>n.d.</i>	<i>n.d.</i>		<i>0.3328</i>	<i>0.513145</i>	<i>47</i>	<i>9.9</i>	<i>0.6</i>
<i>PRA 74 grt</i>	<i>n.d.</i>	<i>n.d.</i>	<i>n.d.</i>	<i>n.d.</i>	<i>n.d.</i>	<i>n.d.</i>		<i>0.8259</i>	<i>0.513187</i>	<i>26</i>	<i>10.7</i>	<i>0.1</i>
PRA94	0.0373	0.283683	4	31.7	11.2	0.703886	3	0.1306	0.512726	3	1.7	-0.2
PRA301	0.7100	0.285390	24	92.1	0.2	0.702663	4	0.0501	0.513029	32	7.6	-0.4
PRA303	1.5558	0.285029	15	79.3	0.1	0.703820	5	0.0430	0.512660	11	0.4	0.0
<i>COM-HB</i>	<i>n.d.</i>	<i>n.d.</i>	<i>n.d.</i>	<i>n.d.</i>	<i>n.d.</i>	<i>0.704390</i>		<i>n.d.</i>	<i>0.512740</i>		<i>n.d.</i>	<i>n.d.</i>

$^{176}\text{Lu}/^{177}\text{Hf}$ and $^{147}\text{Sm}/^{144}\text{Nd}$ were calculated using Lu and Hf and Sm and Nd concentrations of clinopyroxenes from LA-ICP-MS analyses (Table 6); ϵHf , ϵNd and T_{MA} for Hf and Nd calculated with reference to CHUR values $^{176}\text{Lu}/^{177}\text{Hf} = 0.0334$, $^{176}\text{Hf}/^{177}\text{Hf} = 0.282785$, $^{147}\text{Sm}/^{144}\text{Nd} = 0.1967$ and $^{143}\text{Nd}/^{144}\text{Nd} = 0.512638$ (Bouvier *et al.*, 2008). Samples in italic from Bjerg *et al.*, 2009 (PRA) and Ntaflos *et al.*, 2000 (COM-HB). cpx – clinopyroxene; opx – orthopyroxene; grt – garnet; HB – host basalt.

Re-Os isotopic composition

The Os isotopic results are given in Table 11. All bulk rock Os isotopic compositions determined in this study are less radiogenic than those of primitive mantle estimates (Meisel *et al.*, 2001) and range from 0.1171 to 0.1257. Osmium isotopic ratios were recalculated to the average eruption age of the mantle xenoliths (10 Ma). These $^{187}\text{Os}/^{188}\text{Os}_{(\text{EA})}$ ratios lead to γ_{Os} values between -1.0 and -7.8. Rhenium depletion ages (T_{RDs} ; Walker *et al.*, 1989), calculated using primitive mantle values by Meisel *et al.* (2001), yield early Paleozoic (0.5 Ga) to late Paleoproterozoic ages (1.7 Ga) for the stabilization of the SCLM underneath the North Patagonian Massif (Fig. 9). $^{187}\text{Re}/^{188}\text{Os}$ compositions range from subchondritic 0.005 to suprachondritic 0.803. The majority of samples however, yield $^{187}\text{Re}/^{188}\text{Os}$ ratios that are considerably lower than the chondritic estimate (0.40186; Shirey & Walker, 1998). Generally, analyzed Os isotopic ratios do not correlate with $^{187}\text{Re}/^{188}\text{Os}$ (Fig. 10a) or indices of melt

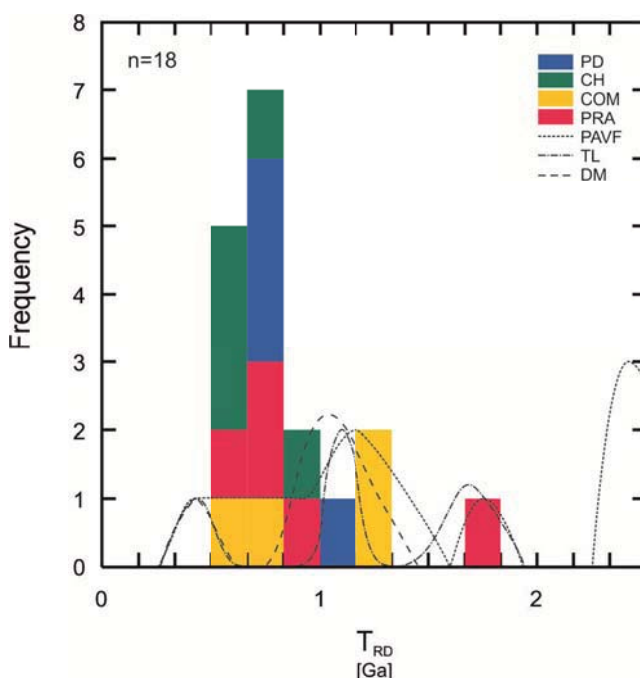


Fig. 9. T_{RD} of north Patagonian mantle xenoliths calculated using primitive mantle values from Meisel *et al.* (2001). For comparison, different grey dashed lines represent south Patagonian mantle xenoliths from Mundl *et al.* (2014). Legend and abbreviations as in Fig. 1; PAVF – Pali Aike Volcanic Field, TL – Tres Lagos, DM – Deseado Massif.

depletion, such as bulk rock Al_2O_3 (Fig. 10b).

Highly siderophile element concentrations

Eighteen samples were chosen for Re-Os isotopic analyses. Of those

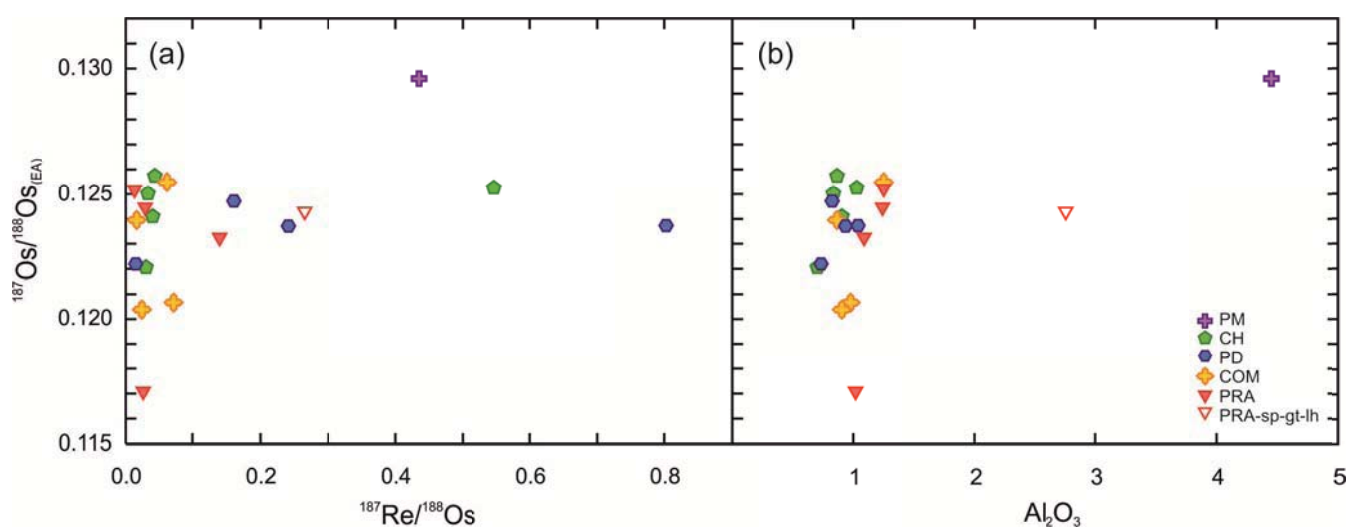


Fig. 10. (a) lacking correlation of $^{187}\text{Os}/^{188}\text{Os}_{(\text{EA})}$ with $^{187}\text{Re}/^{188}\text{Os}$ and (b) with bulk rock Al_2O_3 contents. $^{187}\text{Os}/^{188}\text{Os}_{(\text{EA})}$ = calculated value at time of eruption (10 Ma). Legend: Abbreviations as in Fig. 1; PM values from Meisel *et al.* (2001); $^{187}\text{Re}/^{188}\text{Os}$ = 0.4353 and $^{187}\text{Os}/^{188}\text{Os}$ = 0.1296 and McDonough & Sun (1995), respectively.

Table 11: Osmium isotopic results

Sample	Re [ppb]	Os [ppb]	Ir [ppb]	Ru [ppb]	Pt [ppb]	Pd [ppb]	$^{187}\text{Re}/^{188}\text{Os}$	$^{187}\text{Os}/^{188}\text{Os}_{(m)}$	$^{187}\text{Os}/^{188}\text{Os}_{(EA)}$	$2\sigma \cdot 10^{-6}$	γ_{Os}	T_{MA}^* [Ga]	$T_{\text{RD(EA)}}^*$ [Ga]
GH1	0.034	3.83	3.27	4.60	1.50	0.002	0.043	0.12573	0.12572	12	-1.0	0.6	0.5
CH25	0.026	3.76	2.02	3.72	0.48	0.003	0.033	0.12502	0.12501	4	-1.5	0.7	0.6
CH26	0.067	0.59	1.09	3.97	0.35	1.430	0.547	0.12525	0.12516	16	-1.4	-2.3	0.6
CH43	0.040	4.81	5.39	4.73	0.28	0.080	0.040	0.12410	0.12409	2	-2.3	0.8	0.8
CH63	0.024	3.82	3.02	7.21	4.65	1.050	0.030	0.12205	0.12204	18	-3.9	1.1	1.0
PD28	0.015	0.30	0.69	3.40	0.27	0.020	0.241	0.12371	0.12367	72	-2.6	1.8	0.8
PD32	0.009	2.90	2.07	3.12	3.93	0.580	0.015	0.12219	0.12219	6	-3.8	1.1	1.0
PD51	0.015	0.09	0.22	2.29	0.05	0.150	0.803	0.12373	0.12360	24	-2.6	-1.0	0.8
PD64	0.089	2.66	0.24	5.80	0.24	0.300	0.161	0.12472	0.12469	24	-1.8	1.1	0.7
COM103	0.008	0.54	1.25	3.65	1.47	0.030	0.071	0.12066	0.12065	14	-5.0	1.5	1.2
COM108	0.012	2.38	2.25	3.90	6.20	1.060	0.024	0.12038	0.12038	10	-5.2	1.3	1.3
COM139	0.026	2.04	3.08	5.09	1.31	0.170	0.061	0.12548	0.12547	4	-1.2	0.7	0.6
COM141	0.003	2.97	2.48	4.49	2.94	0.160	0.005	0.12395	0.12395	2	-2.4	0.8	0.8
PRA74	0.081	1.47	2.49	4.52	3.81	2.710	0.265	0.12429	0.12425	10	-2.1	1.9	0.7
PRA94	0.009	1.68	2.05	3.25	3.72	0.670	0.026	0.11708	0.11708	10	-7.8	1.8	1.7
PRA301	0.017	2.87	2.43	1.99	6.04	0.130	0.029	0.12446	0.12446	24	-2.0	0.8	0.7
PRA303	0.005	2.74	2.10	2.71	4.84	0.680	0.009	0.12522	0.12522	6	-1.4	0.6	0.6
PRA306	0.020	0.69	2.75	3.36	3.70	0.730	0.140	0.12325	0.12322	44	-2.9	1.3	0.9

*Re-Os model ages (T_{MA} and T_{RD}) were calculated using primitive upper mantle values from Meisel *et al.* (2001): $^{187}\text{Re}/^{188}\text{Os} = 0.4353$ and $^{187}\text{Os}/^{188}\text{Os} = 0.1296$, $\lambda^{187}\text{Re} = 1.666 \cdot 10^{-11}$ from Smoliar *et al.* (1996); $^{187}\text{Os}/^{188}\text{Os}_{(m)}$ = measured value, $^{187}\text{Os}/^{188}\text{Os}_{(EA)}$ = calculated value at time of eruption (10 Ma); $^{187}\text{Re}/^{188}\text{Os}$ determined using Re and Os concentrations; $T_{\text{RD(EA)}} =$ Rhenium depletion age at time of eruption assuming Re = 0.

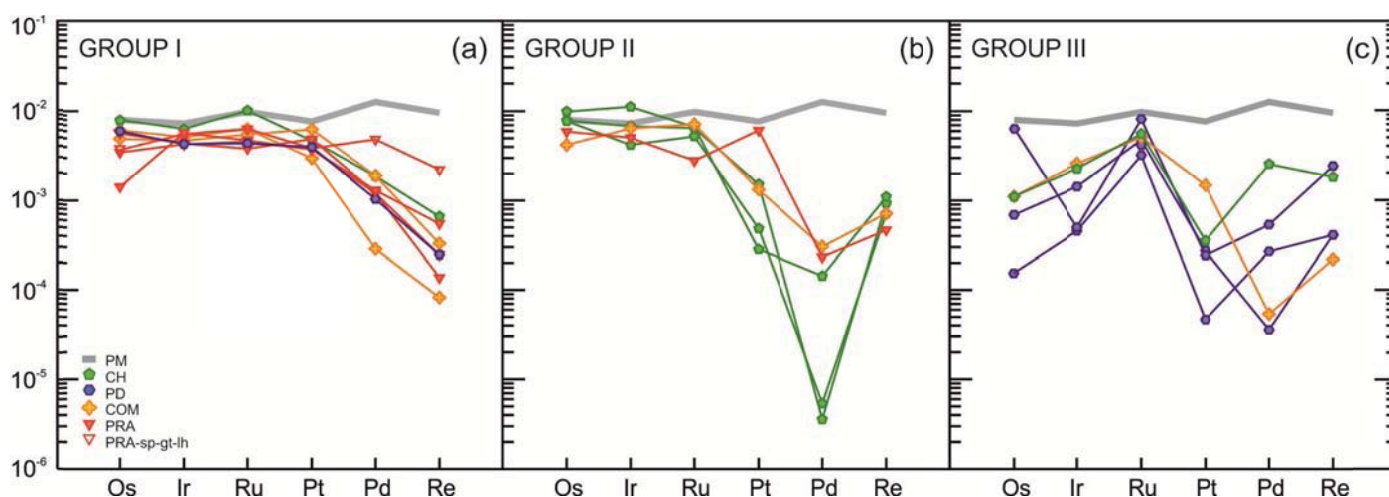


Fig. 11. Chondrite normalized highly siderophile element patterns. Three Groups can be distinguished (see text for detailed explanation). CI from Anders & Grevesse, (1989). Grey line represents primitive mantle of Becker *et al.*, (2006).

samples also platinum group element (PGE) and Re concentrations were determined (Table 11). Rhenium contents in north Patagonian mantle peridotites range from 0.003 to 0.089 ppb. The scatter in Os concentrations is much higher ranging from as low as 0.09 (PD51) to 4.81 ppb (CH43). Sample CH43 is the only sample with Os contents higher than fertile mantle estimates (3.9 ppb, Becker *et al.*, 2006). Analyzed mantle xenoliths also exhibit quite variable contents in Ir (0.22-5.39 ppb), Ru (1.99-7.21 ppb), Pt (0.012-6.200 ppb) and Pd (0.002-2.710 ppb). Based on CI-normalized highly siderophile element (HSE) patterns (Fig. 11a-c), three distinct groups can be recognized. GROUP I (Fig. 11a) is represented by samples with unfractionated iridium-group PGE (IPGE) and depleted palladium-group PGE (PPGE) correlating with melt extraction estimates. However, all but sample CH63 are generally IPGE depleted with reference to the PM (Becker *et al.*, 2006). GROUP II samples exhibit a strong depletion in PPGEs with a relative enrichment in Re

(Fig. 11b). Two samples (CH1 and CH25) exhibit a pronounced Pd depletion. One sample (PRA301) slightly deviates from that group as it exhibits a positive Pt anomaly. Samples from GROUP III show a distinct Ir-Ru fractionation. Ruthenium exhibits a strong positive peak relative to Ir and Pt. One sample, PD64, slightly deviates from this Group as its Os content is with 2.66 ppb much higher than those of the rest of Group III. Rhenium, and in most cases also Pd are enriched relative to Pt (Fig. 11c). With the exception of sample PD64, HSE variation diagrams reveal a good correlation of Ir with Os in Group III (Fig. 12a). Ru is weakly correlated with Ir in Groups I and II, but yields higher Ru at given Ir concentrations in Group III (Fig. 12b). This suggests that in Groups I and II Ru and Ir might be controlled by the same mineral phases, while in Group III Ir and Os are likely hosted in the same phases. There is no visible correlation of Re, Pt or Pd with Ir in any of the three groups (Fig. 12c-e).

DISCUSSION

Melt extraction estimates

With the exception of spinel-garnet-lherzolite PRA74, all samples are harzburgites and have undergone

extensive melt extraction, as is recognizable in bulk rock major and trace element compositions (Table 2; Fig. 4 and 5). The majority of our north Patagonian mantle xenoliths have clinopyroxenes with very low HREE (Fig. 6). The only possible way to model

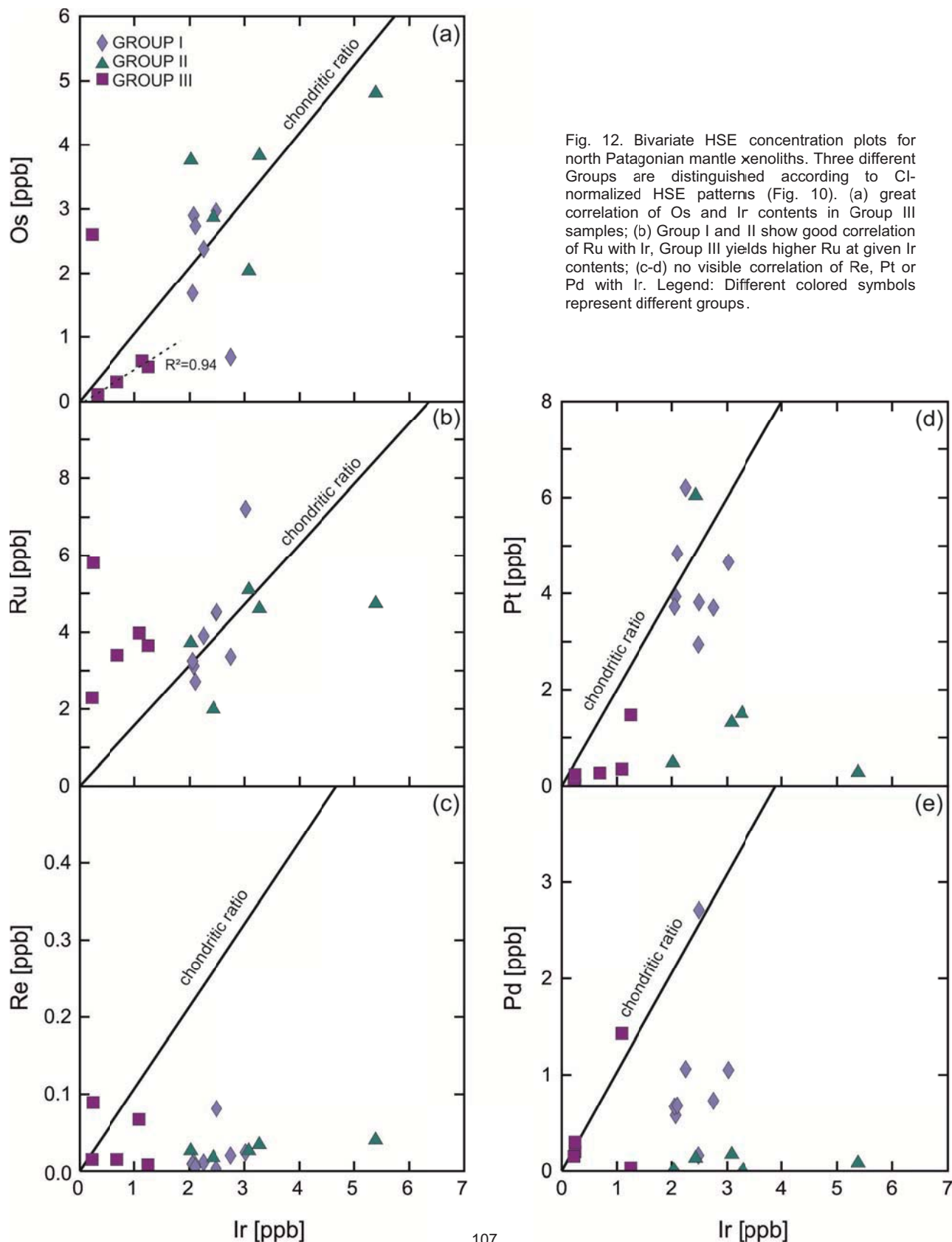


Fig. 12. Bivariate HSE concentration plots for north Patagonian mantle xenoliths. Three different Groups are distinguished according to CI-normalized HSE patterns (Fig. 10). (a) great correlation of Os and Ir contents in Group III samples; (b) Group I and II show good correlation of Ru with Ir, Group III yields higher Ru at given Ir contents; (c-d) no visible correlation of Re, Pt or Pd with Ir. Legend: Different colored symbols represent different groups.

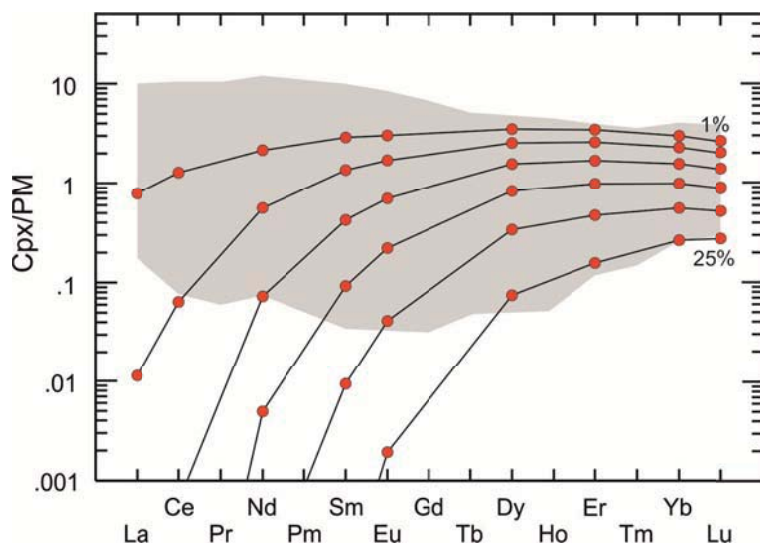
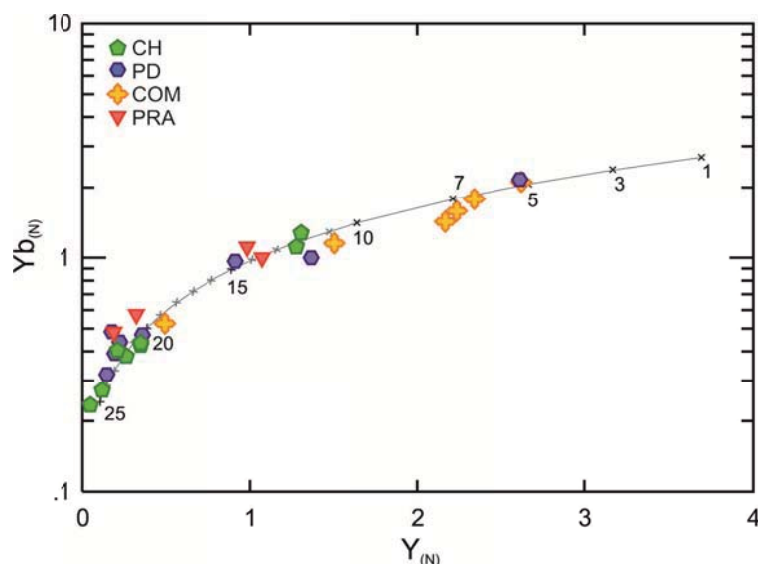


Fig. 13. Partial melting degrees modeled using method by Bizimis *et al.* (2003), mineral-melt distribution coefficients used from Norman (1998), source modes and melt modes by Kinzler (1997), DMM (Salters & Stracke, 2004) as starting source. Orange PM-normalized clinopyroxene REE patterns after 1%, 5%, 10%, 15%, 20% and 25% melt extraction, respectively. Grey field represents north Patagonian mantle xenoliths from this study. All samples exhibit an extensive metasomatic enrichment of LREE and/or MREE relative to the strong depletion expected for these elements after large amounts of melt extraction.

these low REE and still have remaining clinopyroxenes in the residue is to use the melting model by Bizimis *et al.* (2003) based on incremental melt removal, clinopyroxene distribution coefficients by Norman (1998), source and melt modes by Kinzler (1997) and DMM values from Salters & Stracke (2004) as starting source composition. Modeling of clinopyroxene trace element compositions after various degrees of melt extraction (Fig. 13.) yield melting estimates for Prahuaniyeu and Comallo spinel-harzburgites of up to 21% and 19% partial melting, respectively. See Table 11 and Fig. 14 for melt extraction estimates of all samples. Cerro Chenque and Puesto Diaz mantle xenoliths have experienced up to 25% melt extraction. Samples PD1 and PD51 yield melting

Fig. 14. Clinopyroxene PM-normalized Yb versus PM-normalized Y of north Patagonian mantle xenoliths from this study. Line indicates melt increments modeled using method by Bizimis *et al.* (2003). Parameters used for modeling: as in Fig. 13. Black x with numbers are degrees of partial melting (1 – 25 %); grey x represent 1 % melting steps. Legend: Abbreviations as in Fig. 1.



estimates of “only” 12% and 5%, respectively. Modal compositions however indicate a similar depletion as the other PD samples. Modal composition determination of samples PD1 and PD51 yield 2.3 and 2.1 mode % clinopyroxene, respectively and are within the average clinopyroxene composition (2.3 mode %) of Puesto Diaz samples (Table 1). Using bulk rock major element compositions to model melt depletion (i.e. MgO vs. Al₂O₃; Fig. 15) results in melt extraction estimates for the majority of the north Patagonian spinel-harzburgites, including all Puesto Diaz samples, between 20 and 30 %. This is in good agreement with the

determined partial melting estimates from the majority of north Patagonian clinopyroxene trace elements. Hence, the differences within the sample suite are only recognized in trace element concentrations at similar bulk rock and modal compositions.

Host basalt infiltration

All analyzed bulk rock samples exhibit enrichment in highly incompatible elements (Fig. 5). PM-normalized bulk rock REE patterns show elevated LREE even in those samples where clinopyroxenes are not enriched in LREE (clinopyroxene Group I, Fig. 6). No accessory mantle minerals able to host highly incompatible elements could be detected in those samples. Hence, these elements must be bound in interstitial phases. As these elements have not been incorporated in clinopyroxene, these processes probably took place not too long before the transport to the surface. Hence, interstitial host basalt glass is likely responsible for the bulk rock enrichment of highly incompatible elements.

Metasomatism

Evidence from clinopyroxene and bulk rock trace element compositions

It is obvious from clinopyroxene and bulk rock LREE enrichment in most of the north Patagonian samples, that melt/fluid-rock reaction processes have taken place. According to clinopyroxene trace element compositions, most of our studied samples indicate melt(s) percolating through the peridotites. Ionov *et al.* (2002), after Vernières *et al.* (1997), attributed variable trace element enrichment patterns of clinopyroxenes to chromatographic effects during reactive porous melt flow. A progressing percolation of a melt through the mantle xenoliths can be illustrated by looking at 4 different mantle samples from Puesto Diaz that reflect different stages of reaction with an advancing percolating melt (Fig. 16). As melt rises within a melt conduit, it infiltrates the surrounding wall rocks. Consequently, this melt, probably strongly enriched in LREE>MREE>HREE, reacts with the harzburgite it percolates and changes its composition. This reaction with our

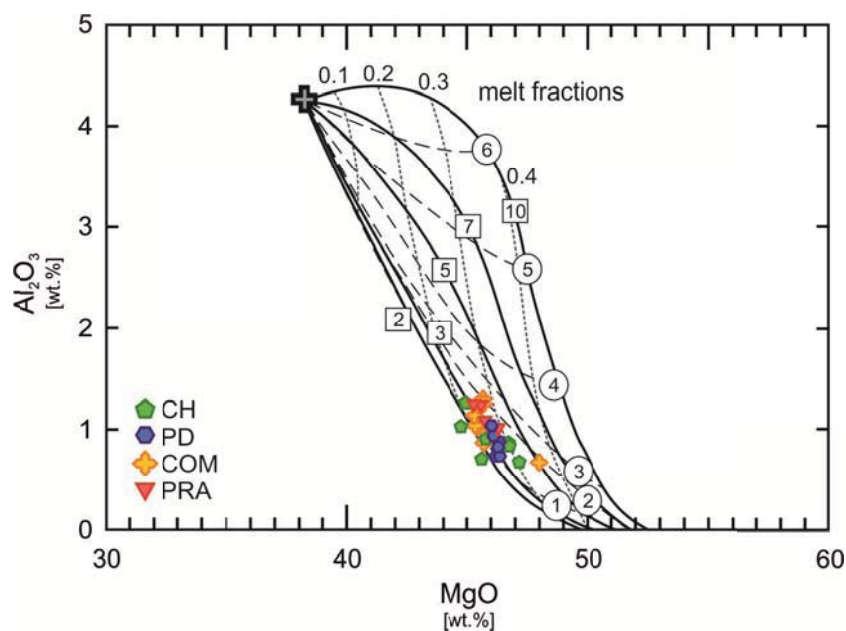


Fig. 15. Fractional melting estimates using bulk rock Al_2O_3 versus MgO model by Herzberg (2004). The majority of north Patagonian spinel-harzburgites plot between 20 and 30 % melt extraction at final melting pressures between 1 and 2 GPa. Narrow dashed lines represent different melt fractions; bold lines labelled with numbers in squares are initial melting pressures [GPa]; dashed lines labelled with circled numbers represent final melting pressures [GPa]. Legend: Abbreviations as in Fig. 1; starting composition from Herzberg (2004).

samples is mainly reflected by clinopyroxene trace element compositions and to a far lesser extent by major elements. None of the samples have been modally altered. Hence, this melt percolation affected the composition of the already existent minerals, especially clinopyroxene, but did not form or precipitate a new generation of silicate minerals. Al_2O_3 and TiO_2 contents in clinopyroxene are slightly higher in samples PD1 (3.45 wt. % and 0.30 wt. %, respectively) and PD51 (3.96 wt. % and 0.64 wt. %, respectively) compared to the average Al_2O_3 and TiO_2 composition of Puesto Diaz harzburgites (2.74 wt. % and 0.12 wt. %, respectively) (Table 5). Mg# in clinopyroxene and orthopyroxene, as well as Fo contents in olivine of samples PD1 and PD51 do not differ from the rest of the sample suite and hence, have not been affected by the percolating melt. On the other hand, samples PD1 and PD51 yield slightly lower cr# in spinel (0.32 and 0.23, respectively) relative to the average cr# in PD spinels (0.38). This suggests that an interaction of spinel with melt caused an increase in Al_2O_3 in spinel which consequently lowered its cr#. It is obvious from major element compositions of minerals that sample PD51 was affected the most by this percolating melt, followed by sample PD1. PD64 and PD32, interpreted to be the samples furthest away from the melt conduit, have not been affected in terms of major elements. Trace element compositions show a continuous reaction with the harzburgites as the melt propagates through the rocks. As mentioned above, the melt source is assumed to be enriched in LREE,

MREE and to a lesser extent in HREE. A reaction of this percolating melt results in refertilization of the harzburgite closest to the melt conduit. This is reflected in PM-normalized clinopyroxene REE patterns that exhibit enriched HREE<MREE>LREE (Fig. 16 I). As the melt reacts with the harzburgite closest to the melt source, it subsequently changes its composition as a result of chromatographic fractionation of the melt (e.g. Navon & Stolper, 1987; Takazawa *et al.*, 1992). This “new” melt then continues to intergranularly propagate through the mantle section further away from the melt conduit where it again reacts with the next section of rock (Fig. 16 II). These PM-normalized REE patterns are characterized by a small enrichment in HREE and a hump in MREE suggesting that while melt, likely enriched in HREE<MREE and more so in LREE, percolated through this mantle section, HREE and MREE were incorporated into clinopyroxene while LREE, the more incompatible elements, largely remained in the melt. This LREE enriched and HREE depleted melt then advanced through the mantle and likely reacted with a different mantle section further along its way, resulting in peridotites showing a stronger LREE than MREE enrichment (Fig. 16 III). The last reaction is represented by sample PD32, where LREE are strongly enriched. The budget of MREE in the melt at this stage is nearly exhausted and hence enrichment in the harzburgite PD32 is minor (Fig. 16 IV). We suggest that the samples closest to the melt conduit have experienced the strongest refertilization in terms of their trace element compositions. Our model

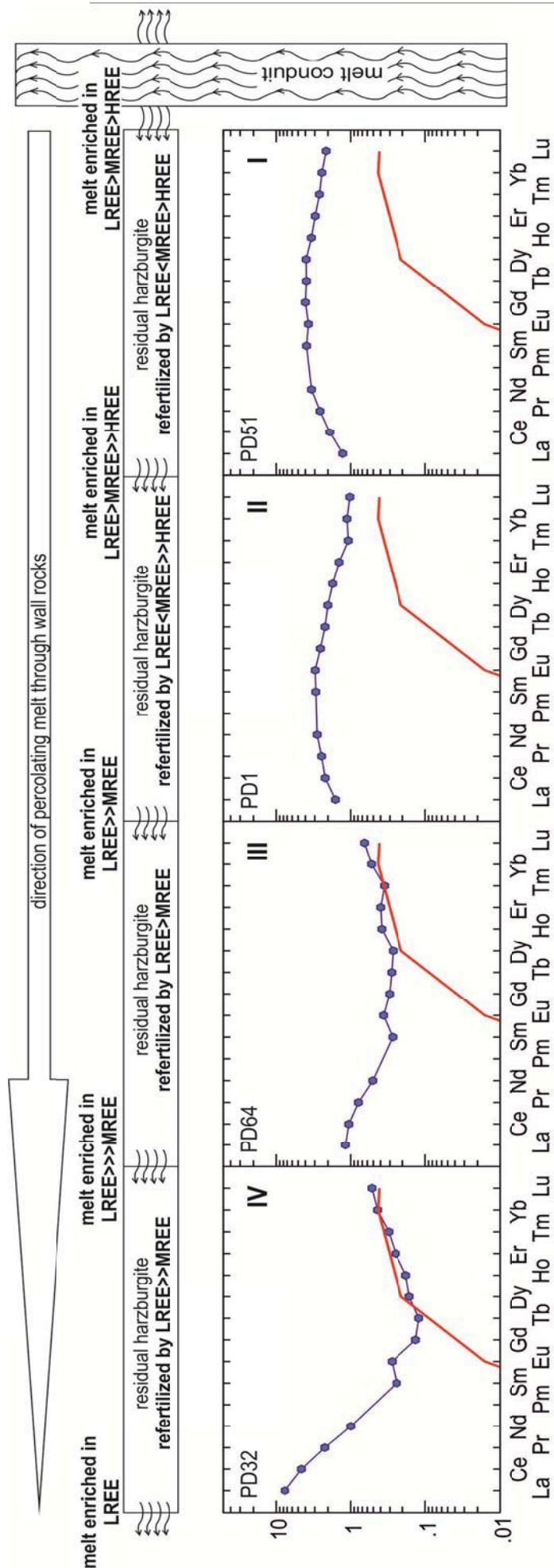


Fig. 16. Schematic drawing of a percolating melt model, similar to model by Ionov *et al.* (2002). Melt infiltrates horizontally from a close melt conduit. I, II, III, IV represent clinopyroxene PM-normalized REE patterns of Puesto Diaz samples PD51, PD1, PD64 and PD32, respectively. Red line represents modeled clinopyroxene composition after 22 % melt extraction, using the same parameters as in Fig. 13. Melt advances from right to left and changes its composition as it reacts with each mantle section (from I to IV).

calculations for melt extraction estimates (Fig. 14) suggest that sample PD51 has “only” experienced 5 % partial melting (Table 12). However, bulk rock and mineral major element and modal compositions reflect a much stronger depletion. Hence, addition of HREE to clinopyroxene concentration by percolating melts after the initial melt depletion results in misleading clinopyroxene melt extraction estimates.

Sr-Nd-Hf isotope systematics and implications for metasomatism

In the diagram $^{143}\text{Nd}/^{144}\text{Nd}$ vs. $^{87}\text{Sr}/^{86}\text{Sr}$ (Fig. 8a), all spinel-harzburgites from COM, CH and PD plot within the OIB field (Hoffmann, 1997). One sample from Prahuaniyeu (PRA301) plots beyond the OIB field, in the MORB field, while the other 3 PRA samples exhibit less radiogenic Nd and more radiogenic Sr and plot just outside or on the edge to the OIB field. All four COM samples yield very homogeneous present day ϵNd values between +5.6 and +6.1. Contrary, Sr isotopic ratios vary between 0.703287 and 0.703984 in the same four samples. This weak decoupling of Sr isotopes from Nd isotopes can be attributed to metasomatism by slab derived fluid/melts as these melts commonly have high $^{87}\text{Sr}/^{86}\text{Sr}$ and moderate Nd compositions (e.g. Zanetti *et al.*, 1999). A second model to decouple Sr from Nd

Table 12: Estimated melt extraction determined using clinopyroxene trace element compositions (Fig. 14).

<i>sp-peridotites</i>	
CH1	12.0%
CH12	22.0%
CH17	25.0%
CH25	12.0%
CH26	21.0%
CH42	22.0%
CH43	24.0%
CH63	21.0%
PD1	12.0%
PD27	23.5%
PD28	21.5%
PD32	22.0%
PD51	5.0%
PD61	15.0%
PD64	20.5%
COM 103	7.5%
COM108	12.0%
COM 118	6.5%
COM 139	11.0%
COM 140	5.0%
COM 141	19.0%
COM 142	7.0%
PRA1	14.0%
PRA94	13.5%
PRA301	20.0%
PRA303	21.5%

isotopes in mantle xenoliths are melt percolation processes (Ionov *et al.*, 2002; Conceição *et al.*, 2005) which have been observed in our samples. These authors argue for a decoupling of

Sr from Nd isotopes due to the “chromatographic effect” of a percolating melt rather than a reaction of a peridotite with high $^{87}\text{Sr}/^{86}\text{Sr}$ ratio carrying subduction related melts as proposed in the first model. However, in mantle samples studied from the Comallo area, a subduction related metasomatism can be considered likely as Comallo is located only ~300 km away from the subduction front. Also, the majority of samples from COM are modally metasomatized mantle peridotites comprising high abundances of amphibole and/or phlogopite, whose existence can probably be attributed to subduction-related fluid/rock interaction (Papadopoulou *et al.*, 2014; Ntaflou *et al.*, 2000).

Hf isotopic compositions vary strongly within the studied sample suite with ϵHf values ranging from +7 to +165. While all COM samples plot within the Nd-Hf mantle array (Fig. 8b), samples from PD, CH and PRA yield highly radiogenic $^{176}\text{Hf}/^{177}\text{Hf}$ ratios leading to ϵHf values of up to +165 and plot above the fields for OIB and MORB. These samples form an almost vertical trend in Fig. 8b and Fig. 8c and show a strong decoupling of Hf with Nd and Sr isotopic compositions. High radiogenic Hf ratios could reflect ancient melt depletion of those mantle sections, while decoupled $^{143}\text{Nd}/^{144}\text{Nd}$ and $^{87}\text{Sr}/^{86}\text{Sr}$ ratios indicate a metasomatic disturbance of the same samples. All harzburgites plotting within the OIB field (Fig. 8b and Fig. 8c) yield future Hf T_{MAs} . These future T_{MAs} of samples from COM and PRA1 suggest a recent disturbance of the Lu-Hf system. This disturbance is also reflected in very low $^{176}\text{Lu}/^{177}\text{Hf}$ ratios resulting from elevated

Hf concentrations in COM clinopyroxene (Table 6). Hf concentrations are very low in samples PRA301 and PRA303 (Table 6), as is expected for samples that have experienced high degrees of melt extraction. However, despite their high ϵ_{Hf} values of +92 and +79, respectively and hence, high $^{176}\text{Hf}/^{177}\text{Hf}$ ratios, calculated model ages yield very young T_{MAS} of 80 to 210 Ma. This suggests that the Lu-Hf system in those samples has been significantly disturbed as T_{RDS} calculated from Os isotopic ratios suggest an initial melt extraction event taking place at least 1.7 Ga ago. The oldest Hf T_{MAS} of north Patagonian mantle xenoliths have been determined in samples from Puesto Diaz. Sample PD51 yields with 1.25 Ga the oldest T_{MA} of the entire sample suite. From trace element analyses in clinopyroxene, we suggested that this sample was severely affected by melt percolation processes and as a consequence thereof was refertilized in terms of trace elements. Hence, the Lu-Hf system has been disturbed significantly. Sample PD32 yields a T_{MA} of 1.09 Ga. However, this age is distinctly younger than the suggested ages for the initial basement formation of the North Patagonian Massif (1.7 – 2.1 Ga; Martínez Dopico *et al.*, 2011).

Metasomatic processes inferred from HSE compositions

Many authors have studied the effects of melt percolation processes on highly siderophile elements (e.g. Büchl *et al.*, 2002; Lorand *et al.*, 2004, 2010; Ackerman *et al.*, 2009; Wang *et al.*, 2009). In mantle rocks, HSE reside mainly in base metal sulphides (Alard *et*

al., 2000; Luguet *et al.*, 2001) and HSE-bearing alloys (Luguet *et al.*, 2007; Lorand *et al.*, 2008; Lorand *et al.*, 2010; Lorand *et al.*, 2013; Ackerman *et al.*, 2013). At large degrees of partial melting (>20%) these base metal sulphides should be fully exhausted in the melt (Luguet *et al.*, 2003). This results in a strong depletion of the residual mantle in Pd and Re (and partially in Pt) as these elements are more incompatible relative to the IPGEs (Os, Ir, Ru) (Pearson *et al.*, 2004). The remaining HSE Os, Ir and Ru (and Pt) are subsequently redistributed into microphases, such as minerals of the laurite (RuS_2) – erlichmanite (OsS_2) series and Pt-Ir-Os and/or Ru-Ir-Os alloys (Luguet *et al.*, 2007; Lorand *et al.*, 2010; Fonseca *et al.*, 2012). Melting degree estimates of our north Patagonian harzburgites inferred from clinopyroxene trace element and bulk rock major element compositions yield between 20 and 30 % of melt extraction. Hence, the compatible HSEs are expected to reside in such microphases. However, as these minerals are rare and very small in mantle xenoliths, they are difficult to be detected. In one sample, PD28, a laurite could be identified using EDS peaks (Fig. 7c, right upper corner). A standard-less microprobe EDS-analyses revealed no significant Os or Ir concentrations in the laurite (Table 8). Hence, these elements are likely being hosted by (Pt)-Ir-Os alloys. A lack of correlation of Ir and Ru in HSE GROUP III samples (Fig. 12b) also suggests that these elements do not reside in the same phases. With the exception of sample PD64, all other harzburgites from GROUP III show a good

correlation of Os with Ir (Fig. 12a). This indicates that these elements are hosted by the same phases, i.e. Pt-Ir-Os alloys.

Information from bulk rock and clinopyroxene trace element concentrations suggests at least one metasomatic event where melts percolated through mantle sections sampled by some of our studied xenoliths. Due to the multi-stage magmatic history of northern Patagonia since the Precambrian as previously mentioned in the geological settings, several melt-rock reaction processes could have likely taken place in the underlying subcontinental lithospheric mantle. Samples from Group III of the PGE patterns exhibit a strong fractionation of Ru from Os, Ir and PPGEs. This fractionation cannot be due to melting processes, but rather results from percolating melts removing phases that host Os, Ir and probably Pt. While laurite remains in the mantle section affected by melt percolation, Pt-Ir-Os alloys must have been physically removed as a result thereof. Lorand *et al.* (2004) suggested that IPGEs can behave incompatibly during melt percolation events at high melt/rock ratios. They also proposed that Pt-Ir-Os alloys may be stripped or dissolved by a silicate melt flowing through a mantle section (Lorand *et al.*, 2004, 2010). Why laurite remained in the peridotite and was not dissolved or removed from it like Pt-Ir-Os alloys, remains uncertain. Brenan & Andrews (2001) suggest a high temperature stability of laurite. However, this high stability also applies to IPGE-rich alloys and hence cannot be responsible for a fractionation of Ru with Ir, Os and Pt. One explanation

could be that the percolating melt was already S-saturated and hence, picked up Os, Ir and Pt residing as alloys, but left laurite, a Ru-sulphide, behind. Our proposed scenario therefore suggests that under certain conditions, laurite can be more stable during melt percolation processes than Pt-Ir-Os alloys.

Generally, most of our studied samples from HSE Group I and II exhibit a slight deficit in compatible HSE which is evidenced by low IPGE concentrations relative to primitive mantle values (Becker *et al.*, 2006) (Fig. 10). This can also be attributed to melt percolation processes removing some of the primary sulphides and hence decreasing the abundance of Os, Ir and Ru at high melt-rock ratios (e.g. Becker *et al.*, 2001; Büchl *et al.*, 2002, Lorand *et al.*, 2003). Percolating melts likely are responsible for the precipitation of secondary sulphides. Minor amounts of base metal sulphides were found in most of north Patagonian mantle xenoliths. As they should be completely consumed during extensive partial melt extraction (>20 %) (Luguet *et al.*, 2003), their existence in our highly depleted samples, predominantly on or close to grain boundaries, hints their addition from a percolating melt. Elevated Re and in some cases also Pd contents support this assumption. Whether the removal of Pt-Ir-Os alloys and the precipitation of secondary sulphides from the percolating melt was a single event or these processes took place separately, cannot be answered at this time. Elevated Re concentrations could also be the result of host basalt infiltration, hence late stage enrichment in Re. The mantle xenolith carrying host basalts erupted between 1 and 25 Ma

ago. An enrichment in Re from host basalt infiltration therefore, would not have affected the Os isotopic compositions, as the decay of Re to radiogenic Os is much too long to significantly elevate the $^{187}\text{Os}/^{188}\text{Os}$ ratio. A combination of suprachondritic $^{187}\text{Re}/^{188}\text{Os}$ and subchondritic $^{187}\text{Os}/^{188}\text{Os}$ ratios in two north Patagonian samples (CH26 and PD51) suggests that the addition of Re must have taken place rather recently.

Timing of the stabilization of the SCLM underneath the North Patagonian Massif

Analyzed $^{187}\text{Os}/^{188}\text{Os}$ ratios of our studied sample suite are comparable to off-cratonic mantle samples (Pearson *et al.*, 2002; Reisberg *et al.*, 2005 and references therein) and are much higher than average osmium ratios reported for Archean cratonic peridotites (Pearson *et al.*, 1995 a,b; Carlson *et al.*, 1999). As mentioned above, Os isotopic ratios do not correlate with either $^{187}\text{Re}/^{188}\text{Os}$ or indices of melt depletion, such as bulk rock Al_2O_3 (Fig. 9). This indicates a disturbance of the Re-Os system of the majority of the studied north Patagonian mantle xenoliths after the initial melting event, which is in agreement with our previously proposed theory of melt percolation affecting HSE systematics which in turn impacts the Os isotopic results. An important fact to keep in mind is that after the melt percolation event that removed most of Os residing in Pt-Ir-Os alloys (HSE Group III), the concentration of Os was significantly lowered. Hence, the production of ^{187}Os from Re introduced into the rocks by

melt, easily elevates the $^{187}\text{Os}/^{188}\text{Os}$ ratio resulting in much younger T_{RDs} than expected and in some cases in suprachondritic $^{187}\text{Re}/^{188}\text{Os}$ ratios. Rhenium depletion model ages (T_{RD}) calculated using primitive mantle values (Meisel *et al.*, 2001) yield a late Paleoproterozoic formation age of the SCLM underneath the North Patagonian Massif. However, our oldest calculated T_{RD} (1.7 Ga; PRA94) is clearly younger than the oldest model ages determined by Schilling *et al.* (2008), who suggest an at least early Paleoproterozoic (2.1 Ga) stabilization of the SCLM underneath Prahuanieyu. Sample PRA74 yields a T_{RD} of only 0.7 Ga. However, since this spinel-garnet-lherzolite is fertile and hence, most of the Re remained in the sample after the initial melting event, this age must be considered absolute minimum. In contrast to T_{RD} , Re-Os model age (T_{MA}) calculations also include the analyzed $^{187}\text{Re}/^{188}\text{Os}$ ratios and assume that this ratio is representative of the long-term history of the mantle, hence that it has not been affected by Re and/or Os alteration processes (Shirey & Walker, 1998). From the HSE systematics and the bulk rock and mineral compositions, we can assume that sample PRA74 has not been affected by metasomatic processes or significant host basalt infiltration which altered the Re/Os ratios. Therefore, the calculated 1.9 Ga T_{MA} (Table 11) can be considered reasonable. This T_{MA} is still younger but similar to the suggested formation age of 2.1 Ga for the oldest North Patagonian Massif basement rocks (Martínez Dopico *et al.* 2011). The COM mantle xenoliths suggest a SCLM stabilization in that area around 1.3 Ga

ago. The oldest determined T_{RD} of samples from Puesto Diaz and Cerro Chenque indicate a formation of the SCLM at least 1.0 Ga ago. This is in good agreement with the T_{MA} determined from Hf isotopic analyses of clinopyroxenes from Puesto Diaz sample PD32 (1.1 Ga). This sample is interpreted to not have been affected by percolating melts in terms of clinopyroxene Hf concentrations. Also, Re-Os and HSE systematics reveal no obvious disturbance in this sample. Hence, calculated Os T_{RD} of 1.0 Ga, as well as Hf T_{MA} of 1.1 Ga may provide a good estimate for the timing of the stabilization of the SCLM underneath Puesto Diaz.

Implications for more than one SCLM fragment beneath the North Patagonian Massif

Bulk rock and mineral major and trace element compositions (Tables 2 – 7) reveal a strongly depleted nature of the whole studied sample suite. However, it is important to mention that the four PRA spinel-harzburgites were specifically chosen for isotopic analyses from a large sample suite studied by Bjerg *et al.* (2009) because of their refractory character enabling the comparison of the isotopic ratios with those from the highly depleted COM, PD and CH samples. Generally, the Prahuanieyu sample suite from Bjerg *et al.* (2009) is represented by mantle xenoliths ranging from fertile lherzolites to highly depleted harzburgites (Fig. 4). This clearly distinguishes Prahuanieyu from the sample suites of Puesto Diaz and Cerro Chenque. All PD and CH samples are spinel-harzburgites and

hence, the SCLM underneath Puesto Diaz and Cerro Chenque is strongly depleted in basaltic components. A lack of fertile samples from Puesto Diaz and Cerro Chenque could be attributed to biased sampling methods. However, the large amount (>100) of mantle xenoliths collected from the north Patagonian area around Puesto Diaz and Cerro Chenque point to a strongly depleted character of the SCLM. Therefore, the samples leading to our results and interpretations can be considered representative.

Furthermore, as mentioned in the previous chapter, Re-Os isotopic systematics suggest a SCLM formation beneath Prahuanieyu at least 1.7 Ga ago. This is in good agreement with a presented T_{RD} of 1.7 Ga for the oldest PRA sample from Schilling *et al.* (2008). Mantle xenoliths from Puesto Diaz and Cerro Chenque yield oldest T_{RDs} of 1.0 Ga, hence significantly younger than PRA.

These obvious disparities in the character of the mantle xenolith samples (range of fertility and age) from Prahuanieyu and Puesto Diaz – Cerro Chenque suggest different geological origins and evolutions. This could imply that the SCLM beneath the North Patagonian Massif possibly consist of at least 2 separate mantle domains.

CONCLUSIONS

The majority of north Patagonian mantle xenolith analyzed in this study has experienced extensive melt extraction between 20 and 30 % melt removal. This is reflected in very low HREE concentrations of clinopyroxene as well as in bulk rock compositions.

The fact that the majority of north Patagonian mantle xenoliths is represented by highly depleted spinel-harzburgites distinctly distinguishes them from south Patagonian mantle xenoliths. In contrast, samples from southern Patagonia cover the whole range of fertile lherzolites to strongly depleted harzburgites and dunites.

All studied north Patagonian mantle xenoliths have experienced cryptic metasomatic processes resulting in refertilization of the samples. We suggest an advancing percolating melt to have reacted with our highly depleted harzburgite samples as it propagated through the wall rock and subsequently changed its composition. This reaction of a chromatographically fractionated melt with the mantle rocks at various stages is evidenced by enriched bulk rock and clinopyroxene trace element abundances of different degrees. However, these melt-rock reactions have overall not affected bulk rock major element or modal contents. Disturbed isotopic and HSE compositions confirm that metasomatic processes have taken place. Trace element analyses, HSE systematics and Os-Hf-Nd-Sr isotopic results suggest melt percolation processes and commonly host basalt infiltration to have affected the SCLM underneath north Patagonia.

The oldest T_{RD} (1.7 Ga) and T_{MA} (1.9 Ga) determined from Os isotopic results of sample PRA94 and PRA74, respectively, suggest a stabilization of the SCLM underneath northern Patagonia of at least late Paleoproterozoic age. The oldest calculated T_{RD} from Comallo and Puesto Diaz/Cerro Chenque yield with

1.3 Ga and 1.0 Ga, respectively, younger stabilization ages for the SCLM underneath these regions. However, HSE concentrations of most north Patagonian mantle xenoliths have been significantly modified by metasomatic processes and hence, most samples are not suitable for determining exact estimates of the timing of SCLM formation. Thus, the majority of T_{RD} ages obtained in this study must be considered minimum.

ACKNOWLEDGEMENTS

This study was financed by the FWF grant P 23557-N19 (PI: Th. Ntaflou). We gratefully acknowledge Peter Nagl (University of Vienna) for his help with XRF analyses. We thank Vojtech Erban (Czech Geological Survey) for Os isotope analyses and Jana Ďurišová (Czech Academy of Sciences) for the ICP-MS analyses of highly siderophile elements. We are grateful to Martha Papadopoulou for conducting some of the Comallo microprobe analyses. L. Ackerman acknowledges the Scientific Programme CEZ: RVO67985831 of the Institute of Geology, Academy of Sciences of the Czech Republic (Os isotopic and PGE analyses). M. Bizimis acknowledges support from award NSF-EAR-1347890 (Hf isotopic analyses). We especially want to thank Suzanne Kay, Michel Grégoire and Charles Stern for their constructive reviews and Marjorie Wilson for the editorial handling.

REFERENCES

Ackerman, L., Walker, R.J., Puchtel, I.S., Pitcher, L., Jelínek, E. & Strnad, L. (2009). Effects of melt

- percolation on highly siderophile elements and Os isotopes in subcontinental lithospheric mantle: A study of the upper mantle profile beneath Central Europe. *Geochimica et Cosmochimica Acta* 73, 2400-2414.
- Ackerman, L., Pitcher, L., Strnad, L., Puchtel, I. S., Jelínek, E., Walker, R. J. & Rohovec, J. (2013). Highly siderophile element geochemistry of peridotites and pyroxenites from Horní Bory, Bohemian Massif: Implications for HSE behavior in subduction-related upper mantle. *Geochimica et Cosmochimica Acta* 100, 158-175.
- Alard, O., Griffin, W.L., Lorand, J.-P., Jackson, S.E. & O'Reilly, S.Y. (2000). Non-chondritic distribution of the highly siderophile elements in mantle sulfides. *Nature* 407, 891-894.
- Anders, E. & Grevesse, N. (1989). Abundances of the elements: Meteoritic and solar. *Geochimica et Cosmochimica Acta* 59, 197-214.
- Ardolino, A., Franchi, M., Remersal, M. & Salani, F. (1999). El volcanismo en la Patagonia Extraandina. In: Haller, M.J. (ed.), "Geología Argentina", *Anales SEGEMAR* 29, 579-612.
- Becker, H., Shirey, S.B. & Carlson, R.W. (2001). Effects of melt percolation on the Re-Os systematics of peridotite from a Paleozoic convergent plate margin. *Earth and Planetary Science Letters* 188, 107-121.
- Becker, H., Horan, M.F., Walker, R.J., Gao, S., Lorand, J.-P. & Rudnick, R.L. (2006). Highly siderophile element composition of the Earth's primitive upper mantle: Constraints from new data on peridotite massifs and xenoliths. *Geochimica et Cosmochimica Acta* 70, 4528-4550.
- Birck, J.L., Roy Barman, M. & Capmas, F. (1997). Re-Os isotopic measurements at the femtomole level in natural samples. *Journal of Geostandards and Geoanalysis* 20, 19-27.
- Bizimis, M., Sen, G. & Salters, V.J.M. (2003). Hf-Nd isotope decoupling in the oceanic lithosphere: constraints from spinel peridotite from Oahu, Hawaii. *Earth and Planetary Science Letters* 217, 43-58.
- Bizimis, M., Griselein, M., Lassiter, J.C., Salters, V.J.M. & Sen, G. (2007). Ancient recycled mantle lithosphere in the Hawaiian plume: Osmium-Hafnium isotopic evidence from peridotite mantle xenoliths. *Earth and Planetary Science Letters* 257, 259-273.
- Bizimis, M., Salters, V.J.M., Garcia, M.O. & Norman, M.D. (2013). The composition and distribution of rejuvenated component across the Hawaiian plume: Hf-Nd-Sr-Pb isotope systematics of Kuala lavas and pyroxenite xenoliths. *Geochemistry, Geophysics, Geosystems* 14, 4458-4478.
- Bjerg, E.A., Ntaflos, T., Kurat, G., Dobosi, G. & Labudía, C.H. (2005). The upper mantle beneath Patagonia, Argentina, documented by xenoliths from alkali basalts. *Journal of South American Earth Sciences* 18, 125-145.
- Bjerg, E.A., Ntaflos, T., Thöni, M., Aliani, P. & Labudía, C.H. (2009). Heterogeneous Lithospheric Mantle beneath Northern Patagonia: Evidence from Prahuaníyey Garnet- and Spinel-Peridotites. *Journal of Petrology* 50, 1267-1298.
- Bouvier, A., Vervoort, J.D. & Patchett, P.J. (2008). The Lu-Hf and Sm-Nd isotopic composition of CHUR: constraints from unequilibrated chondrites and implications for the bulk composition of terrestrial planets. *Earth and Planetary Science Letters* 273, 48-57.
- Brenan, J.M. & Andrews, D. (2001). High-temperature stability of laurite and Ru-Os-Ir alloy and their role in PGE fractionation in mafic magmas. *The Canadian Mineralogist* 39, 341-360.
- Brey, G.P. & Köhler, T. (1990). Geothermobarometry in four-phase Iherzolites II. New thermobarometers and practical assessment of existing thermobarometers. *Journal of Petrology* 31, 1353-1378.
- Büchl, A., Brüggmann, G.E., Muenker, C. & Hofmann, A.W. (2002). Melt percolation monitored by Os-isotopes and PGE abundances: a case study from the mantle section of the Troodos ophiolite. *Earth and Planetary Science Letters* 204, 385-402.
- Carlson, R.W., Pearson, D.G., Boyd, F.R., Shirey, S.B., Irvine, G., Menzies, A.H. & Gurney, J.J. (1999). Re-Os systematics of lithospheric peridotites: Implications for lithosphere formation and preservation. In: Gurney, J.J., Gurney, J.L., Pascoe, M.D. & Richardson, S.H. (Eds.), *Proceedings of the VIIIth International Kimberlite Conference. Red Roof Design, Cape Town*, 99-108.
- Cohen, A.S. & Waters, F.G. (1996). Separation of osmium from geological materials by solvent extraction for analysis by thermal ionization mass spectrometry. *Analytica Chimica Acta* 332, 269-275.

- Conceição, R.V., Mallmann, G., Koester, E., Schilling, M., Bertotto, G.W. & Rodriguez-Vargas, A. (2005). Andean subduction-related mantle xenoliths: Isotopic evidence of Sr-Nd decoupling during metasomatism. *Lithos* 82, 273-287.
- Creaser, R.A., Papanastassiou, D.A. & Wasserburg, G.J. (1991). Negative thermal ion mass spectrometry of osmium, rhenium, and iridium. *Geochimica et Cosmochimica Acta* 55, 397-401.
- Fonseca, R.O.C., Laurenz, V., Mallmann, G., Luguët, A., Hoehne, N. & Jochum, K.P. (2012). New constraints on the genesis and long term stability of Os-rich alloys in the Earth's mantle. *Geochimica et Cosmochimica Acta* 87, 227-242.
- Herzberg, C. (2004). Geodynamic Information in Peridotite Petrology. *Journal of Petrology* 45, 2507-2530.
- Hofmann, A.W. (1997). Mantle geochemistry: the message from oceanic volcanism. *Nature* 385, 219-229.
- Gorring, M.L. & Kay, S.M. (2000). Carbonatite metasomatized peridotite xenoliths from southern Patagonia: implications for lithospheric processes and Neogene plateau magmatism. *Contributions to Mineralogy and Petrology* 140, 55-72.
- Ionov, D.A., Bodinier, J.-L., Mukasa, S.B. & Zanetti, A. (2002). Mechanisms and sources of mantle metasomatism: major and trace element compositions of peridotite xenoliths from Spitsbergen in the context of theoretical modeling. *Journal of Petrology* 43, 2219-2259.
- Ionov, D.A., Mukasa, S.B. & Bodinier, J.-L. (2002). Sr-Nd-Pb Isotopic Compositions of Peridotite Xenoliths from Spitsbergen: Numerical Modeling Indicates Sr-Nd Decoupling in the Mantle by Melt Percolation Metasomatism. *Journal of Petrology* 43, 2261-2278.
- Kay, S.M., Ramos, V.A., Mpodozis, C. & Sruoga, P. (1989). Late Paleozoic to Jurassic silicic magmatism at the Gondwana margin: analogy to the Middle Proterozoic in North America?. *Geology* 17, 324-328
- Kay, S.M., Ardolino, A.A., Gorring, M.L. & Ramos, V.A. (2007). The Somuncura Large Igneous Province in Patagonia: Interaction of a Transient Mantle Thermal Anomaly with a Subducting Slab. *Journal of Petrology* 48, 53-77.
- Kempton, P.D., Hawesworth, C.J., Lopez-Escobar, L., Pearson, D.G. & Ware, A.G. (1999a). Spinel \pm garnet lherzolite xenoliths from Pali Aike, Part 2: trace element and isotopic evidence on the evolution of lithospheric mantle beneath southern Patagonia. In: Gurney, J.J., Gurney, J.L., MD Pascoe, M.D. & Richardson, S.H. (eds) *T.J.B. Dawson Volume, Proceedings of the 7th International Kimberlite Conference*. Cape Town: Red Roof Design, 415-428.
- Kempton, P.D., Hawesworth, C.J., Lopez-Escobar, L., Pearson, D.G. & Ware, A.G. (1999b). Spinel \pm garnet lherzolite xenoliths from Pali Aike, Part 1: Petrography, mineral chemistry and geothermobarometry. In: Gurney, J.J., Gurney, J.L., MD Pascoe, M.D. & Richardson, S.H. (eds) *T.J.B. Dawson Volume, Proceedings of the 7th International Kimberlite Conference*. Cape Town: Red Roof Design, 415-428.
- Kinzler, R.J. (1997). Melting of mantle peridotite at pressures approaching the spinel to garnet transition: application to mid-ocean ridge basalt petrogenesis. *Journal of Geophysical Research* 102(B1), 853-874.
- Labudía, C.H., Bjerg, E. A. & Ntaflos, T. (2011). Nuevas dataciones del vulcanismo del noroeste de la Meseta de Somuncurá, Argentina. *XVIII Congreso Geológico Argentino, Simposio Evolución tectono-magmática cenozoica del Macizo Norpatagónico*, 356-357.
- Lorand, J.P. (1990). Are spinel lherzolite xenoliths representative of abundance of sulfur in the upper mantle? *Geochimica et Cosmochimica Acta* 54, 1487-1492.
- Lorand, J.-P., Reisberg, L. & Bedini, L.M. (2003a). Platinum-group elements and melt percolation processes in Sidamo spinel peridotite xenoliths, Ethiopia, East African Rift. *Chemical Geology* 196, 58-75.
- Lorand, J.-P., Delpech, G., Grégoire, M., Moine, B., O'Reilly, S.Y. & Cottin, J.-Y. (2004). Platinum-group elements and the multistage metasomatic history of Kerguelen lithospheric mantle, South Indian Ocean. *Chemical geology* 208, 195-214.
- Lorand, J.-P., Luguët, A., Alard, O., Bezos, A. & Meisel, T. (2008). Abundance and distribution of platinum-group elements in orogenic lherzolites; a case study in a Fontete Rouge lherzolite (French Pyrénées). *Chemical Geology* 248, 174-194.
- Lorand, J.-P., Alard, O. & Luguët, A. (2010). Platinum-group element micronuggets and refertilization process in the Lherz peridotite. *Earth and Planetary Science Letters* 289, 298-310.

- Lorand, J.-P., Luguët, A. & Alard, O. (2013). Platinum-group element systematics and petrogenetic processing of the continental upper mantle: A review. *Lithos* 164-167, 2-21.
- Luguët, A., Lorand, J.-P. & Seyler, M. (2003). Sulfide petrology and highly siderophile element geochemistry of abyssal peridotites: a coupled study of sulfide petrology and highly siderophile element geochemistry in abyssal peridotites from the Kane Fracture Zone (MARK area, Mid-Atlantic ridge). *Geochimica et Cosmochimica Acta* 67, 1553-1570.
- Luguët, A., Shirey, S., Lorand, J.-P., Horan, M.F. & Carlson, R.C. (2007). Residual platinum group minerals from highly depleted harzburgites of the Lherz massif (France) and their role in HSE fractionation of the mantle. *Geochimica et Cosmochimica Acta* 71, 3082-3097.
- Mallick, S., Standish, J.J. & Bizimis, M. (in press). Constraints on the mantle mineralogy of an ultra-slow ridge: Hafnium isotopes in abyssal peridotites and basalts from the 9-25°E Southwest Indian Ridge. *Earth and Planetary Science Letters* (2014), <http://dx.doi.org/10.1016/j.epsl.2014.10.048>
- Martínez Dopico, C.I., López de Luchi, M.G., Rapalini, A.E. & Kleinhanns, I.C. (2011). Crustal segments in the North Patagonian Massif, Patagonia: An integrated perspective based on Sm-Nd isotope systematics. *Journal of South American Earth Sciences* 31, 324-341.
- McDonough, W.F. & Sun, S. (1995). The composition of the Earth. *Chemical Geology* 120, 223-253.
- Meisel, T., Walker, R.J., Irving, A.J. & Lorand, J.-P. (2001). Osmium isotopic compositions of mantle xenoliths: A global perspective. *Geochimica et Cosmochimica Acta* 65, 1311-1323.
- Mundl, A., Ntaflou, T., Ackerman, L., Bizimis, M., Bjerg, E.A. & Hauzenberger, C.A. (2014). Meso- and Paleoproterozoic subcontinental lithospheric mantle domains beneath southern Patagonia: Isotopic evidence for its connection to Africa and Antarctica. *Geology*, published online on 21 November 2014. Doi: 10.1130/G36344.1
- Munker, C., Weyer, S., Scherer, E. & Mezger, K. (2001). Separation of high field strength elements (Nb, Ta, Zr, Hf) and Lu from rock samples for MC-ICPMS measurements. *Geochemistry, Geophysics, Geosystems* 2.
- Munoz, J., Troncoso, R., Duhart, P., Crignola, P., Ramer, L. & Stern, C.R. (2002). The relation of the mid-Tertiary coastal magmatic belt in south-central Chile to the late Oligocene increase in plate convergence rate. *Revista Geologica de Chile* 27(2), 177-204.
- Navon, O. & Stolper, E. (1987). Geochemical consequences of melt percolation - the upper mantle as a chromatographic column. *Journal of Geology* 95, 285-307.
- Ntaflou, T., Günther, M., Labudia, H.C., Bjerg, E.A., Kurat G. & Dingeldey, C. (2000). Isotopic and Geochemical Evolution of the Cenozoic Basalts from Rio Negro, Patagonia, Argentina. *31st International Geological Congress, Extended Abstract #SD603s, Electronic version, Rio de Janeiro*.
- Ntaflou, T., Bjerg, E.A., Labudia, C.H. & Kurat, G. (2007). Depleted lithosphere from the mantle wedge beneath Tres Lagos, southern Patagonia, Argentina. *Lithos* 94, 46-65.
- Norman, M.D. (1998). Melting and metasomatism in the continental lithosphere: laser ablation ICPMS analysis of minerals in spinel lherzolites from eastern Australia. *Contributions to Mineralogy and Petrology* 130, 240-255.
- Nowell, G.M., Kempton, P.D., Noble, S.R., Fitton, J.G., Saunders, A.D., Mahoney, J.J. & Taylor, R.N. (1998). High precision Hf isotope measurements of MORB and OIB by thermal ionization mass spectrometry: insights into the depleted mantle. *Chemical Geology* 149 (3-4), 211-233.
- Pankhurst, R.J. & Rapela, C.R. (1995). Production of Jurassic rhyolite by anatexis of the lower crust of Patagonia. *Earth and Planetary Science Letters* 134(1-2), 23-36.
- Pankhurst, R.J., Rapela, C.W., Fanning, C.M. & Márquez, M. (2006). Gondwanide continental collision and the origin of Patagonia. *Earth-Science Reviews* 76, 235-257.
- Papadopoulou, M., Ntaflou, T., Bjerg, E.A. & Grégoire, M. (2014). Hydrous metasomatism and melt percolation in the lithospheric mantle wedge underneath Comallo, Rio Negro, Argentina. *EGU 2014 Conference Abstract*.
- Pearce, N.J.G., Perkins, Westgate, J.A., Gorton, M.P., Jackson, S.E., Neal, C.R. & Chenery, S.P. (1997). A compilation of new and published major and trace element data for NIST SRM 610 and NIST SRM 612 glass reference materials. *Geostandards Newsletter* 21, 115-144.

- Pearson, D.G., Carlson, R.W., Shirey, S.B., Boyd, F.R. & Nixon, P.H. (1995a). The stabilization of Archaean lithospheric mantle: a Re-Os isotope study of peridotite xenoliths from the Kaapvaal craton. *Earth and Planetary Science Letters* 134, 341-357.
- Pearson, D.G., Carlson, R.W., Shirey, S.B., Boyd, F.R., Pokhilenko, N.P. & Shimizu, N. (1995b). Re-Os, Sm-Nd and Rb-Sr isotope evidence for thick Archaean lithospheric mantle beneath the Siberia craton modified by multi-stage metasomatism. *Geochimica et Cosmochimica Acta* 59, 959-977.
- Pearson, D.G., Irvine, G.J., Carlson, R.W., Kopylova, M.G. & Ionov, D.A. (2002). *The development of lithospheric keels beneath the earliest continents: time constraints using PGE and Re-Os systematics*. In: Fowler, C.M.R., Ebinger, C.J., Hawkesworth, C.J. (Eds.) *The Early Earth: Physical, Chemical and Biological Development*. Geological Society of London, *Special Publications* 199, 65-90.
- Pearson, D.G., Irvine, G.J., Ionov, D.A., Boyd, F.R. & Dreibus, G.E. (2004). Re-Os isotope systematics and platinum group element fractionation during mantle melt extraction: a study of massif and xenolith peridotite suites. *Chemical Geology* 208, 29-59.
- Ramos, V.A. (1999). Plate tectonic setting of the Andean Cordillera. *Episodes* 22(3), 183-190.
- Ramos, V.A. (2008). Patagonia: A paleozoic continent adrift? *Journal of South American Earth Sciences* 26, 235-251.
- Rapalini, A., López de Luchi, M., Martínez Dopico, C., Lince Klinger, F., Giménez, M. & Martínez, P. (2010). Did Patagonia collide with Gondwana in the Late Paleozoic? Some insights from a multidisciplinary study of magmatic units of the North Patagonian Massif. *Geológica Acta* 8, 349-371.
- Rapalini, A., López de Luchi, M., Tohver, E. & Cawood, P.A. (2013). The South American ancestry of the North Patagonian Massif: geochronological evidence for an autochthonous origin? *Terra Nova* 25, 337-342.
- Rapela, C.W. & Kay, S.M. (1988). Late Paleozoic to Recent Magmatic Evolution of Northern Patagonia. *Episodes* 11(3), 175-182.
- Rapela, C.W., Spalletti, L.A., Merodio, J.C. & Aragón, E. (1988). Temporal evolution and spatial variation of early tertiary volcanism in the Patagonian Andes (40°S-42°30'S). *Journal of South American Earth Sciences* 1(1), 75-88.
- Reisberg, L., Zhi, X., Lorand, J.-P., Wagner, C., Peng, Z. & Zimmermann, C. (2005). Re-Os and S systematics of spinel peridotite xenoliths from east central China: Evidence for contrasting effects of melt percolation. *Earth and Planetary Science Letters* 239, 286-308.
- Rivalenti, G., Mazzucchelli, M., Laurora, A., Ciuffi, S.I.A., Zanetti, A., Vannucci, R. & Cingolani, C.A. (2004). The backarc mantle lithosphere in Patagonia, South America. *Journal of South American Sciences* 17, 121-152.
- Salters, V.J.M. & Stracke, A. (2004). Composition of the depleted mantle. *Geochemistry, Geophysics, Geosystems* 5.
- Shaw, C.S.J. & Klügel, A. (2002). The pressure and temperature conditions and timing of glass formation in mantle-derived xenoliths from Baarley, West Eifel, Germany: the case for amphibole breakdown, lava infiltration and mineral-melt reaction. *Mineralogy and Petrology* 74, 163-187.
- Shaw, C.S.J. & Dingwell, D.B. (2008). Experimental peridotite-melt reaction at one atmosphere: a textural and chemical study. *Contributions to Mineralogy and Petrology* 155, 199-214.
- Schilling, M., Conceição, R.V., Mallmann, G., Koester, E., Kawashita, K., Hervé, F., Morata, D. & Motoki A. (2005). Spinel-facies mantle xenoliths from Cerro Redondo, Argentina Patagonia: Petrographic, geochemical, and isotopic evidence of interaction between xenoliths and host basalt. *Lithos* 82, 485-502.
- Schilling, M.E., Carlson, R.W., Conceição, R.V., Dantas, C., Bertotto, G.W. & Koester, E. (2008). Re-Os isotope constraints on subcontinental lithospheric mantle evolution of southern South America. *Earth and Planetary Science Letters* 268, 89-101.
- Shirey S.B. & Walker, R.J. (1995). Carius tube digestion for low blank rhenium-osmium analysis. *Analytical Chemistry* 67(34), 2136-2141.
- Shirey S.B. & Walker, R.J. (1998). The Re-Os isotope system in cosmochemistry and high-temperature geochemistry. *Annual Review of Earth and Planetary Sciences* 26, 423-500.
- Skewes, M.A. & Stern, C.R. (1979). Petrology and geochemistry of alkali basalts and ultramafic inclusions from the Palei-Aike volcanic field in southern Chile and the origin of the Patagonian plateau lavas. *Journal of Volcanology and Geothermal Research* 6, 3-25.

- Smoliar, M.I., Walker, R.J. & Morgan, J.W. (1996). Re-Os ages of Group IIA, IIIA, IVA and IVB iron meteorites. *Science* 271, 1099-1102.
- Stern, C.R., Saul, S., Skewes, M.A. & Futa, K. (1989). Garnet peridotite xenoliths from the Pali-Aike alkali basalts of southernmost South America. In: Rossi, J. (ed.) *Kimberlites and Related Rocks. Geological Society of Australia Special Publication* 14, 735-744.
- Stern, C.R., Kilian, R., Olker, B., Hauri, E.H. & Kyser, T.K. (1999). Evidence from mantle xenoliths for relatively thin (<100 km) continental lithosphere below the Phanerozoic crust of southernmost South America. *Lithos* 48, 217-235.
- Stracke, A., Snow, J.E., Hellebrand, E., von der Handt, A., Bourdon, B., Kirbaum, K. & Günther, D. (2011). Abyssal peridotite Hf isotopes identify extreme mantle depletion. *Earth and Planetary Science Letters* 308, 359-368.
- Takazawa, E., Frey, F. A., Shimizu, N., Obata, M. & Bodinier, J. L. (1992). Geochemical evidence for melt migration and reaction in the upper mantle. *Nature* 359, 55-58.
- Vernières, J., Godard, M. & Bodinier, J.-L. (1997). A plate model for the simulation of trace element fractionation during partial melting and magma transport in the Earth's upper mantle. *Journal of Geophysical Research* 102, 24771-24784.
- Völkening, J., Walczyk, T. & Heumann, K.G. (1991). Osmium isotope ratio determinations by negative thermal ionization mass spectrometry. *International Journal of Mass Spectrometry and Ion Processes*, 105, 147-159.
- Walker, R.J., Carlson, R.W., Shirey, S.B. & Boyd, F. R. (1989). Os, Sr, Nd, and Pb isotope systematics of southern African peridotite xenoliths: Implications for the chemical evolution of subcontinental mantle. *Geochimica et Cosmochimica Acta* 53, 1583-1595.
- Wang, K.-L., O'Reilly, S.Y., Griffin, W.L., Pearson, N.J. & Zhang, M. (2009). Sulphides in mantle peridotites from Penghu Islands, Taiwan: melt percolation, PGE fractionation, and the lithospheric evolution of the South China block. *Geochimica et Cosmochimica Acta* 73, 4531-4557.
- Wang, J., Hattori, K.H., Li, J. & Stern, C.R. (2008). Oxidation state of Paleozoic subcontinental lithospheric mantle below the Pali Aike volcanic field in southernmost Patagonia. *Lithos* 105, 98-110.
- Zindler, A. & Hart, S. (1986). Chemical Geodynamics. *Annual Review of Earth and Planetary Sciences* 14, 493-571.

MUNDL Andrea

Date of birth 12th January 1982
Nationality Austrian
Contact details Hernalser Hauptstrasse 20/21, 1170 Vienna, Austria
 Email: andrea.mundl@univie.ac.at / andrea_mundl@yahoo.com
 Tel: +43 699 170 57 633 / +43 1 4277 53318

PROFESSIONAL EXPERIENCE

Since 04/2012 **University of Vienna, Department of Lithospheric Research, Austria**
 Research Assistant
 FWF-Project P 23557 "The Geochemical and Petrological Evolution of the Lithospheric Earth Mantle beneath Patagonia"
 Project leader: Prof. Theodoros Ntaflos

10/2010 – 12/2011 **TPA Gesellschaft für Qualitätssicherung und Innovation GmbH, Austria**
 Project collaborator
 EU-Project ROCARE - Roman Cements for Architectural Restoration to New High Standards

11/2007 – 10/2008 **Austrian Airlines**
 Passenger Service Agent

EDUCATION

Since 04/2012 **University of Vienna, Department of Lithospheric Research, Austria**
 PhD studies in Earth Sciences (anticipated date of graduation: 05/2015)
 Advisor: Prof. Theodoros Ntaflos
Thesis: "Petrological, geochemical and Os-Hf-Nd-Sr isotopic characterization of the Subcontinental Lithospheric Earth Mantle beneath Patagonia"

03/2006 – 11/2008 **University of Vienna, Austria**
 Master studies in Earth Sciences
Thesis: "Petrology and Geochemistry of the lithospheric mantle beneath Las Heras, South Patagonia, Argentina"

10/2002 – 02/2006 **University of Vienna, Austria**
 Bachelor studies in Earth Sciences
Thesis: "Magmatic Evolution of La Palma, Canary Islands"

INTERNATIONAL EXPERIENCE

01/2013; 05/2013
 03/2014 **Academy of Sciences, Prague, Czech Republic (Dr. Lukas Ackerman)**
 10 weeks lab work – Os isotope and PGE+Re chemistry and analyses (TIMS, ICP-MS)

10/2013 – 11/2013 **University of South Carolina, Columbia, USA (Ass. Prof. Michael Bizimis)**
 6 weeks lab work – Hf and Pb isotope chemistry and analyses (MC-ICP-MS)

02/2013 Field work **Patagonia, Argentina**
 2 weeks sample collection

11/2008 – 05/2009 Travel around the world

09/2006 – 06/2007 Academic exchange year at **University of Washington, Seattle, USA**
 Joint Study fellowship

08/2001 – 08/2002 Au Pair in St. Louis, MO, USA

SKILLS AND EXPERTISE

Earth Sciences	Igneous Petrology, (Isotope) Geochemistry, Volcanology, Geochronology
Analytical Methods	Microprobe (good), TIMS (fair), (LA-/MC-)ICP-MS (fair)
Languages	German (native), English (fluent), French (basic), Italian (basic)

PUBLICATIONS**Conference abstracts**

EGU 2015	Mundl, A. , Ntaflos, T., Ackerman, L., Bizimis, M., Bjerg, E.A., and Hauzenberger, C.A. "Geochemical and isotopic characterization of mantle xenoliths from the back arc region of north Patagonia" – oral presentation
6 th Orogenic Lherzolite Conference 2014	Mundl, A. , Ntaflos, T., Ackerman, L., Bizimis, M., and Bjerg, E.A. "Os and Hf isotopes in mantle xenoliths from Southern Patagonia: Evidence for Proterozoic SCLM fragments" – oral presentation
EGU 2014	Mundl, A. , Ntaflos, T., Ackerman, L., Bizimis, M., and Bjerg, E.A. "Proterozoic SCLM domains beneath Southern Patagonia" – oral presentation
MinPet 2013	Mundl, A. , Ntaflos, T., Bjerg, E.A., Hauzenberger, C.A., and Ackerman, L. "Lithospheric mantle heterogeneities beneath Southern Patagonia" – oral presentation
Goldschmidt 2013	Mundl, A. , Ntaflos, T., Bjerg, E.A., Hauzenberger, C.A., and Ackerman, L. "Lithospheric mantle heterogeneities beneath Southern Patagonia" – poster presentation
Basalt 2013	Mundl, A. , Ntaflos, T., and Bjerg, E.A. "Major element whole rock and mineral chemistry of Southern Patagonian Mantle Xenoliths" – oral presentation
EGU 2013	Mundl, A. , Ntaflos, T., Bjerg, E.A., and Hauzenberger, C.A. "Major and trace element whole rock and mineral chemistry of Southern Patagonian Mantle Xenoliths" – oral presentation Mundl, A. , Ntaflos, T., Bjerg, E.A., and Kosler, J. "Lithospheric mantle heterogeneities beneath northern Santa Cruz province, Argentina" – poster presentation

Peer-reviewed articles

Mundl, A., Ntaflos, T., Ackerman, L., Bizimis, M., Bjerg, E.A. & Hauzenberger, C.A. (2015). Mesoproterozoic and Paleoproterozoic subcontinental lithospheric mantle domains beneath southern Patagonia: Isotopic evidence for its connection to Africa and Antarctica. *Geology*, v. 43, p. 39-42. doi:10.1130/G36344.1, first published online 21 November 2014.

Mundl, A., Ntaflos, T., Ackerman, L., Bizimis, M., Bjerg, E.A., Wegner, W. & Hauzenberger, C.A. (accepted). Geochemical and Os-Hf-Nd-Sr isotopic characterization of north Patagonian mantle xenoliths: Implications for extensive melt extraction and percolation processes. *Journal of Petrology, Thematic Issue – 6th Orogenic Lherzolite Conference*.